ISSN en trámite

instituto de astronomía

unam

revista mexicana de astronomía y astrofísica

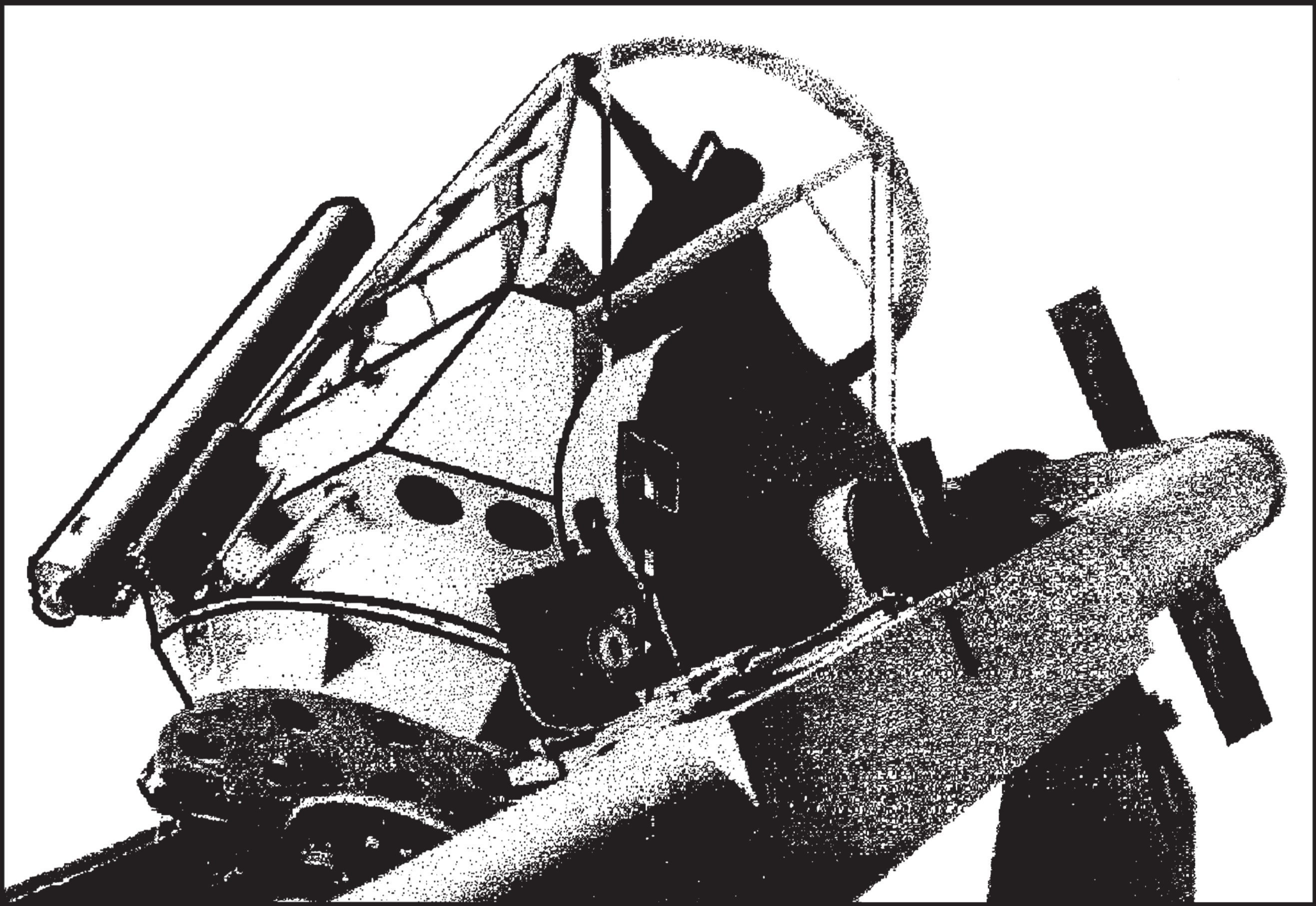

volumen 59
número 1
octubre 2023

volumen 59, número 1, abril 2023

revista mexicana de astronomía y astrofísica

Instituto de Astronomía
Universidad Nacional Autónoma de México

revista
mexicana de
astronomía
y astrofísica

ISSN en trámite

URL de DOI: https://doi.org/10.22201/ia.01851101p.2023.59.01

rmaa@astro.unam.mx

http://www.astroscu.unam.mx/RMxAA/

La *RMxAA* aparece indexada en Current Contents, Science Citation Index, Astronomy and Astrophysics Abstracts, Physics Briefs, Publicaciones Científicas en América Latina, Astronomy and Astrophysics Monthly Index, PERIODICA, RedALyC, Latindex y SciELO.

Revista Mexicana de Astronomía y Astrofísica, volumen 59, número 1, abril 2023, es una publicación semestral, editada y distribuida por el Instituto de Astronomía, UNAM, Circuito Exterior, Ciudad Universitaria, 04510, Alcaldía Coyoacán, Ciudad de México, Teléfono: 5556223906, Correo Electrónico: rmaa@astro.unam.mx, ISSN en trámite. Editora responsable: Christine Patricia Allen Armiño. Distribución: Bienes y Servicios del Instituto de Astronomía, UNAM. Impresa por Grupo Edición, S.A. de C.V., Xochicalco 619, Colonia Letrán Valle, 03650, Alcaldía Benito Juárez, Ciudad de México. Fecha de impresión: 27 de marzo de 2023. Número de ejemplares impresos: 500 en papel Couché de 100 gramos los interiores y en cartulina Couché de 250 gramos los forros. Precio de la publicación: gratuito.

Revista Mexicana de Astronomía y Astrofísica, **59**, 3–10 (2023)

https://doi.org/10.22201/ia.01851101p.2023.59.01.01

RR LYRAE STARS IN THE GLOBULAR CLUSTER PALOMAR 2

A. Arellano Ferro[1], I. Bustos Fierro[2], S. Muneer[3], and S. Giridhar[3]

Received July 8 2022; accepted August 20 2022

ABSTRACT

A CCD *VI* imaging time-series over 11-year is employed to explore the light curves of stars in the field of Palomar 2. We discovered 20 RRab and 1 RRc variables. A revision of *Gaia*-DR3 data enabled us to identify 10 more variables and confirm the RRab nature of 6 of them and one RGB. The cluster membership is discussed, and 18 variables are most likely cluster members. The Fourier light curve decomposition for the 11 best quality light curves of cluster member stars leads to independent estimates of the cluster distance 27.2 ± 1.8 kpc and $[\mathrm{Fe/H}]_{\mathrm{ZW}} = -1.39 \pm 0.55$. We confirm the cluster as of the Oo I type.

RESUMEN

Empleando una serie temporal de más de 11 años de imágenes CCD *VI*, exploramos las curvas de luz de estrellas en el campo del cúmulo. Descubrimos 20 RRab y 1 RRc. Una revisión de los datos de *Gaia*-DR3 permitió identificar 11 variables más y confirmar la naturaleza RRab de 6 de ellas y una RGB. Presentamos un análisis de membresía y concluimos que al menos 18 de estas variables pertenecen al cúmulo. La descomposición de Fourier de las curvas de luz de mejor calidad de 11 RR Lyrae miembros conduce a estimaciones independientes de la distancia 27.2 ± 1.8 kpc y metalicidad $[\mathrm{Fe/H}]_{\mathrm{ZW}} = -1.39 \pm 0.55$ medias para el cúmulo. Confirmamos que el cúmulo es del tipo Oo I.

Key Words: globular clusters: individual: Pal 2 — stars: variables: RR Lyrae

1. INTRODUCTION

The globular cluster Palomar 2 is a distant (30 kpc) stellar system in the direction of the Galactic anticenter and close to the Galactic plane ($l = 170.53°$, $b = -9.07°$). It is buried in dust with $E(B - V) \approx 0.93$ and shows evidence of differential reddening (Bonatto & Chies-Santos 2020). It is, therefore, a faint cluster with the HB at about $V \approx 21.5$ (Harris 1996). Most likely due to its faintness no variables in the cluster have ever been reported.

In the present paper we take advantage of an 11-year long time-series of CCD *VI* data, analyzed in the standard Differential Imaging Approach (DIA), to explore the light curves of nearly 500 stars in the field of view (FoV) of the cluster. We have found 21 new RR Lyrae stars (V1-V14 and SV1-SV7 in Table 1). In conjunction with the *Gaia*-DR3 variability index, we confirm the RRab nature of 6 more stars (G3, G11, G12, G13, G18 and G23), plus 1 RGB (G17), for a total of 28 variables in the field of view of our images. In what follows, we argue in favour of the membership of 18 of them and present their light curves and ephemerides. The mean distance and [Fe/H] of the cluster shall be calculated by the Fourier decomposition of RRab stars with the best quality light curves.

[1]Instituto de Astronomía, Universidad Nacional Autónoma de México, Ciudad Universitaria, México.
[2]Observatorio Astronómico, Universidad Nacional de Córdoba, Córdoba, Argentina.
[3]Indian Institute of Astrophysics, Bangalore, India.

2. OBSERVATIONS AND DATA REDUCTIONS

The data were obtained between December 12, 2010 and February 12, 2021 with the 2.0-m telescope at the Indian Astronomical Observatory (IAO), Hanle, India. The detector used was a SITe ST-002 2Kx4K with a scale of 0.296 arcsec/pix, for a field of view of approximately 10.1×10.1 arcmin^2. From October 14, 2018 and February 17, 2020 the detector used was a Thompson grade 0 E2V CCD44-82-0-E93 2Kx4K with a scale of 0.296 arcsec/pix, or a FoV of approximately 10.1×10.1 arcmin^2. A total of 197 and 240 images were obtained in the V and I filters, respectively.

2.1. *Difference Imaging Analysis*

The image reductions were performed employing the software Difference Imaging Analysis (DIA) with its pipeline implementation DanDIA (Bramich 2008; Bramich et al. 2013, 2015) to obtain high-precision photometry of all the point sources in the field of view (FoV) of our CCD. This allowed us to construct an instrumental light curve for each star. For a detailed explanation of the use of this technique, the reader is referred to the work by Bramich et al. (2011).

2.2. *Transformation to the Standard System*

Since two different detectors were used to achieve the observations as described in the previous section, we treated the transformation to the standard system as two independent instruments. Otherwise, the procedure was the standard one described in detail in previous publications, in summary; we used local standard stars taken from the catalog of Photometric Standard Fields (Stetson 2000) to set our photometry into the VI Johnson-Kron-Cousin standard photometric system (Landolt 1992).

The transformation equations carry a small but mildly significant colour term and are of the form: $V - v = A(v - i) + B$ and $I - i = C(v - i) + D$ for each filter, respectively. The interested reader can find the details of this transformation approach in Yepez et al. (2022).

3. STAR MEMBERSHIP USING *GAIA*-EDR3

We have made use of the latest data release *Gaia*-DR3 (Gaia Collaboration 2021) to perform a membership analysis of the stars in the field of Pal 2. To this end, we employed the method of Bustos Fierro & Calderón (2019), which is based on the Balanced Iterative Reducing and Clustering using Hierarchies (BIRCH) algorithm developed by Zhang et al. (1996). The method and our approach to it have been described in a recent paper by Deras et al. (2022). We recall here that our method is based on a clustering algorithm at a first stage and a detailed analysis of the residual overdensity at a second stage; member stars extracted in the first stage are labeled M1, and those extracted in the second stage are labeled M2. Stars without proper motions were retained, labeled as "unknown membership status" or UN.

The analysis was carried out for a 10 arcmin radius field centered in the cluster. We considered 1806 stars with measured proper motions, of which 407 were found to be likely members. Out of them, only 288 were in the FoV of our images, for which we could produce light curves.

From the distribution of the field stars in phase space we estimated the number expected to be located in the same region of the sky and the vector point diagram (VPD) of the extracted members; therefore, they could have been erroneously labelled as members. Within the M1 stars the resulting expected contamination is 36 (11%), and within the M2 stars it is 87 (7%); therefore, for a given extracted star its probability of being a cluster member is 89% if it is labelled M1, or 93% if it is labelled M2.

4. DIFFERENTIAL REDDENING AND THE CMD

Palomar 2 is a heavily reddened cluster subject to substantial differential reddening, as it is evident in the crowded and deep HST color magnitude diagram (CDM) shown by Sarajedini et al. (2007). A thorough treatment of the differential reddening in the cluster enabled Bonatto & Chies-Santos (2020) to produce a reddening map, which these authors have kindly made available to us. In Figure 2 the observed CMD and the dereddened versions are shown. To deredden the CMD, the differential reddening map was added to a foreground reddening of $E(B - V) = 0.93$.

5. THE VARIABLE STARS IN PAL 2

No variable stars in Pal 2 have been reported thus far. The case of Pal 2 is a particularly challenging one since the cluster is not only distant, but it is also behind a heavy dust curtain; its horizontal branch (HB) is located below 21 mag. We have occasionally taken CCD VI images of Pal 2 since 2010 and until 2021 and we have attempted to take advantage of this image collection to search for variables in the FoV of the cluster. We were able to measure 400-500 point sources in the V and I images that span a range in magnitude and colour shown in the left panel of Figure 2. The HB being located at the bottom of the stellar distribution, we are in fact working at the very limit of our photometry in order to detect cluster member RR Lyrae.

To search for variability we proceeded as follows. By using the string-length method (Burke et al. 1970, Dworetsky 1983), we phased each light curve in our data with a period varying between 0.2 d and 1.0 d, a range adequate for RR Lyrae stars, in steps of 10^{-6} d. For each phased light curve, the length of the line joining consecutive points, called the string-length and represented by the parameter S_Q, was calculated. The best phasing occurs when S_Q is minimum, and corresponds to the best period

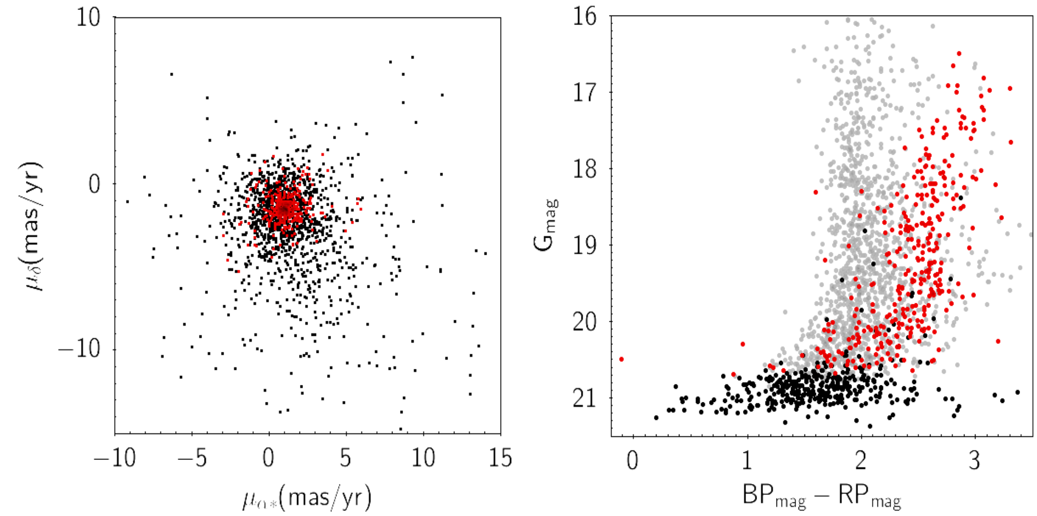

Fig. 1. VPD and Gaia CMD of Pal 2. In the left panel, black and red points represent field and member stars respectively, as extracted by our analysis of the *Gaia*DR3 proper motions. In the right panel gray and red symbols are used for non-member and member stars, while black dots represent stars without proper motion information; hence their membership status cannot be assigned (UN). The colour figure can be viewed online.

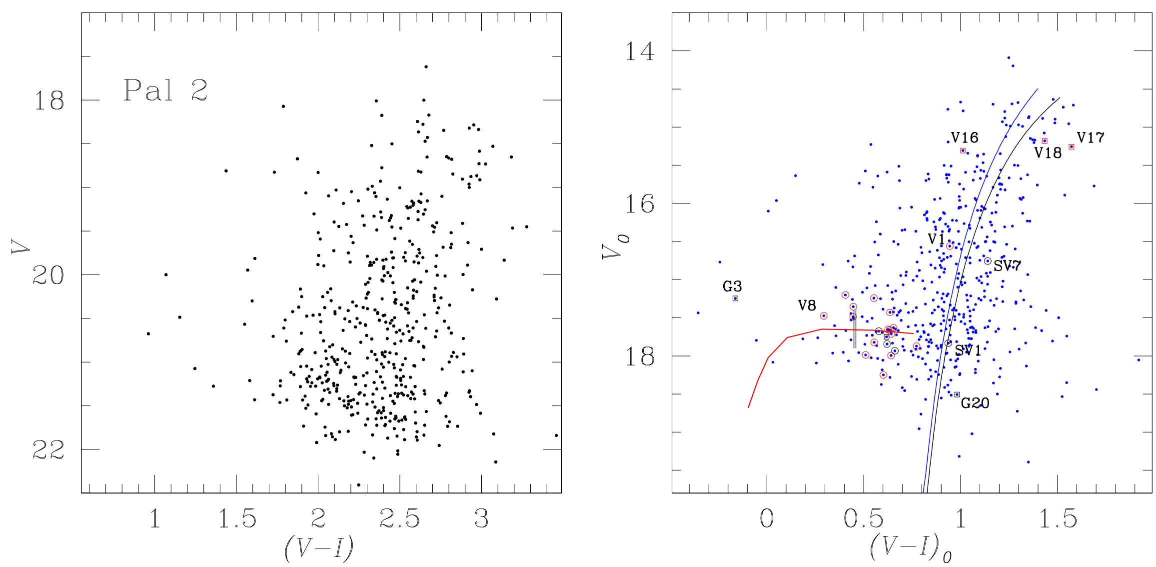

Fig. 2. The colour-magnitude diagram of Pal 2. The left panel shows all the stars measured in the FoV of our images and illustrates the magnitude and colour ranges of our data. The right panel has been diferentially dereddened by adopting the reddening map of Bonatto & Chies-Santos (2020). We adopted from these authors an average foreground reddening of $E(B-V) = 0.93$. As a reference we included two isochrones from the models of VandenBerg et al. (2014) for [Fe/H]=-1.6 and -2.0 and a theoretical horizontal branch built by Yepez et al. (2022). Isochrones and HB have been placed at a distance of 26.1 kpc (Bonatto & Chies-Santos 2020). Variable stars are indicated and discussed in § 5. The vertical black lines are the empirical first overtone red edge (FORE) from Arellano-Ferro et al. (2015, 2016). The colour figure can be viewed online.

that our data can provide. A detailed visual inspection of the best phased light curve helped to confirm the variability of some stars. We noticed, however, that the seasonal scatter of the light curve could vary depending mainly on the prevailing seeing conditions and crowdedness of a particular star, a situation that worsens near the core of the cluster. Therefore, it may happen that in some seasons the light curve

TABLE 1

DATA OF VARIABLE STARS IN THE FOV OF OUR PAL 2 IMAGES

ID	Gaia variable	Type	P (d)	E_0 (+2450000)	V (mag)	V Amp (mag)	RA (J2000.0)	DEC (J2000.0)	$P_{\rm Gaia}$ (d)	Membership status	Gaia number
V1		RRab	0.542848	6312.3363	20.534	0.805	4:46:03.57	+31:22:45.8		M1	159504640014524672
V2	G5	RRab	0.551396	5542.2114	21.342	1.056	4:46:04.60	+31:23:41.5	0.5513624	M1	159504747388302336
V3		RRab	0.554363	6948.4976	21.792	0.951	4:46:05.53	+31:23:29.0		M1	159504747388520064
V4	G14	RRab	0.651889	5912.2228	21.413	0.814	4:46:05.61	+31:23:43.2	0.6518656	M1	159504747387726464
V5	G4	RRab	0.511639	8896.2470	21.382	0.997	4:46:07.02	+31:23:13.5	0.5067667	M2	159504678667943552
V6	G21	RRab	0.553259	9258.3356	21.461	1.168	4:46:07.82	+31:23:07.7	0.5532034	M2	159504678668831872
V7	G16	RRab	0.655812	8407.3827	20.925	0.914	4:46:08.11	+31:23:37.1	–	M1	159504678667937024
V8	G7	RRc	0.373408	5542.2114	20.757	0.548	4:46:08.06	+31:22:21.7	–	M1	159501689370744192
V9	G6	RRab	0.629619	8896.1493	21.521	0.787	4:46:08.24	+31:23:09.3	0.6129630	M1	159504674373384320
V10	G8	RRab	0.685890	5912.3072	20.700	0.512	4:46:09.11	+31:22:38.0	0.6858277	M1	159501723731340288
V11	G19	RRab	0.575280	6222.3870	20.673	0.842	4:46:10.58	+31:22:35.0	0.5752915	M1	159501719435472896
V12	G9	RRab	0.583630	6633.3246	20.894	0.603	4:46:12.82	+31:22:26.3	0.5953860	M1	159501650715992064
V13		RRab	0.546972	6948.4441	21.327	0.887	4:46:07.17	+31:23:15.5		M2	159504678668829184
V14	G1	RRab	0.574697	6948.4591	21.842	1.610	4:46:07.21	+31:22:47.2	0.5513435	M2	159504678667961856
V15	G12	RRab	0.508471	8781.4301	20.918	0.323	4:46:05.00	+31:22:52.9	–	M1	159504644308236672
V16	G13	RR?	0.490213	5912.1144	19.179	0.330	4:46:04.64	+31:22:42.0	–	M1	159504644308250624
V17	G17	RGB			19.0	0.9	4:46:02.96	+31:23:09.2	–	M1	159504708733123200
V18	G11	RR?	0.510211	5912.1144	18.876	0.768	4:46:05.85	+31:23:03.3	–	M1	159504644308215808
SV1		RRab	0.588566	6634.1554	21.267	1.024	4:46:04.22	+31:22:34.8		UN	159504644309111808
SV2		RRab	0.537325	8406.4629	21.876	1.299	4:46:06.39	+31:23:54.0		UN	159504747388298112
SV3		RRab	0.661914	5868.4136	21.517	1.077	4:46:03.96	+31:23:16.2		FS	159504713028573696
SV4		RRab	0.587210	8407.3175	21.585	1.363	4:46:06.56	+31:23:27.2		FS	159504674373556992
SV5	G15	RRab	0.490941	6221.4206	21.312	1.391	4:46:09.04	+31:23:12.8	0.4909349	FS	159504678668828160
SV6	G10	RRab	0.570669	6946.4683	20.840	0.960	4:46:12.31	+31:22:45.3	0.5706582	FS	159501723731332480
SV7		RRab	0.551215	6634.1714	19.274	1.371	4:46:13.65	+31:24:11.5		FS	159506190497880832
	G3	RRab	0.531512	6633.3479	20.486	0.769	4:45:57.72	+31:24:19.0	0.5242873	FS	159504987906469248
	G18	RRab	0.562320	6223.3662	20.700	0.576	4:46:09.50	+31:23:01.9	0.5623196	FS	159501723732926208
	G23	RRab	0.595453	6633.3810	21.178	1.104	4:45:59.23	+31:22:53.4	0.56065912	FS	159504609949939072
	G2[1]										159501655012584064
	G20[2]				21.513		4:45:56.77	+31:21:09.0	0.59148323	FS	159504128913233536
	G22[1]										

[1] Out of our FoV. [2] Not measured by our photometry.

variation is dubious, but extremely clear in the runs of best quality, which turned out to be from the 2013 and 2018-2020 seasons.

With the above method we discovered 21 RR Lyrae variables, mostly of the RRab type. Confronting with the membership analysis described in § 3, we concluded that 14 of them were likely cluster members. The latest *Gaia*-DR3 enabled us to search for stellar variability flags in the field of Pal 2. In fact, Gaia flags 22 variables. A cross-match with our variables list shows 12 matches; we found some variables not marked by *Gaia* and *a posteriori* we confirmed the variability of a few *Gaia* sources not previously detected by us.

In Table 1 we list the 32 variables in the field of Pal 2. The table is organized as follows. We have given the name with the prefix "V" only to those stars that seem likely cluster members (status M1 or M2), 18 in total, V1-V18. Arbitrarily, we identified the *Gaia* variables as G1-G22. This identification is listed in Column 2. In the bottom 14 rows of Table 1 we list the likely non-members (status FS). For non-member variables detected by us, we used the nomenclature with the prefix "SV".

5.1. *Variables in the CMD*

In the right panel CMD of Figure 2, all variable stars have been marked with a red circle if they are cluster members or a black circle otherwise. As a reference we included two isochrones from the models of VandenBerg et al. (2014) for [Fe/H]=−1.6 and −2.0 and a theoretical horizontal branch built by Yepez et al. (2022). Isochrones and HB were placed at a distance of 26.1 kpc Bonatto & Chies-Santos (2020). It is heartening to see nearly all the RR Lyrae stars fall in the whereabouts of the HB. In the following section we address some peculiar individual cases.

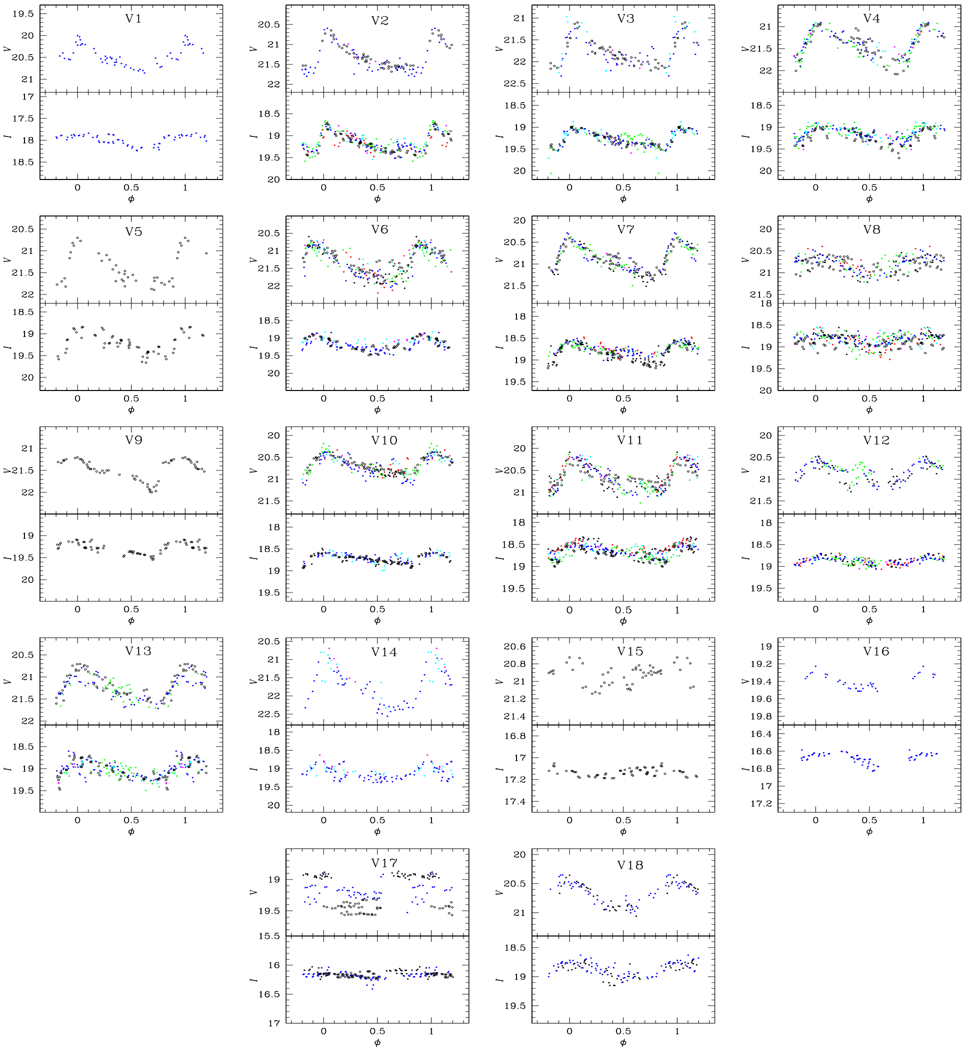

Fig. 3. Light curves of cluster member variables in Pal 2. Different colors are used for yearly seasons. From the plots, it is obvious that the best quality data are from the 2013 (blue dots) and 2018-2020 (open circles) seasons. The rest, although more scattered, do follow and confirm the variations. The colour figure can be viewed online.

5.2. *Individual Cases*

V1. Its position on the CMD above the HB and in the mid-RGB is intriguing since the light curve and period suggest this star to be a member RRab star. An alternative possibility is that the star is a binary. Our data are not sufficient to explore this possibility.

V16, V17 and V18. Their position on the CMD near the tip of the RGB suggests these stars are red giant variables. However, our photometry was not extensive enough to confirm a long-term variability. Alternatively, we were able to identify short-therm variations in V16 and V18 (see Figure 3). The V17 light curve is, in fact, consistent with that of a long-term RGB.

SV1. It is a clear RRab star, falling much to the red of the HB. The star is not a cluster member.

SV7. We have detected clear RRab-like variations in our V data. However, no variation is seen in the I data. While variations might be spurious, we retain the star as a candidate variable to be confirmed.

SV4, SV5, SV6 and G23. These are the four non-member stars, hence identified by black circles or squares in the DCM. However, they lie very near the HB. Their non-membership status was assigned by the statistical approach to their proper motions, but they might be cluster members.

G3 and G20. G3 is a clear RRab star, not a cluster member. For G20 we got a very noisy light curve

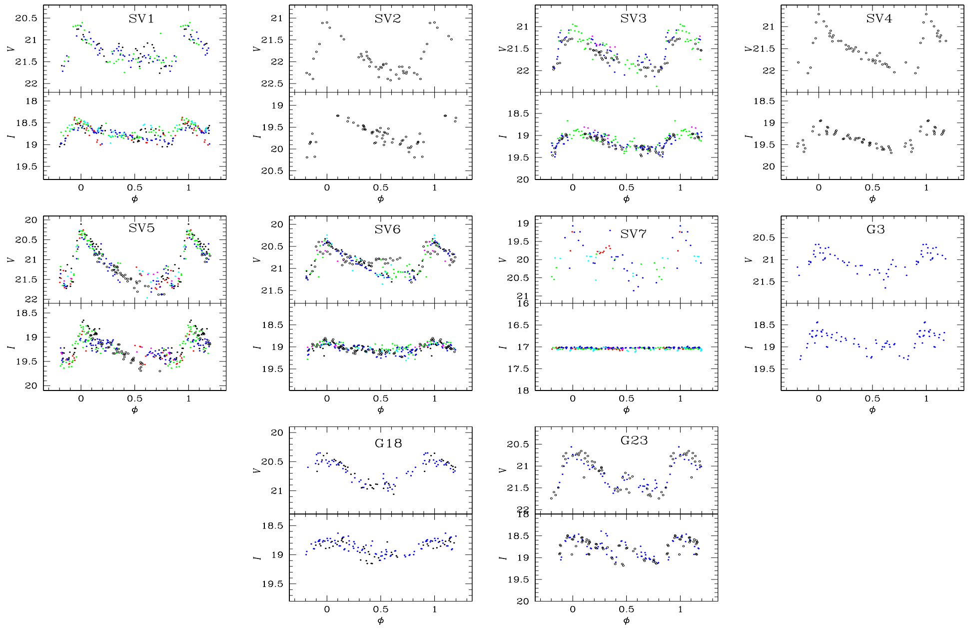

Fig. 4. Light curves of variables in the field of Pal 2. They are most likely field stars, see § 5 for a discussion. The colour code is as in Figure 3. The colour figure can be viewed online.

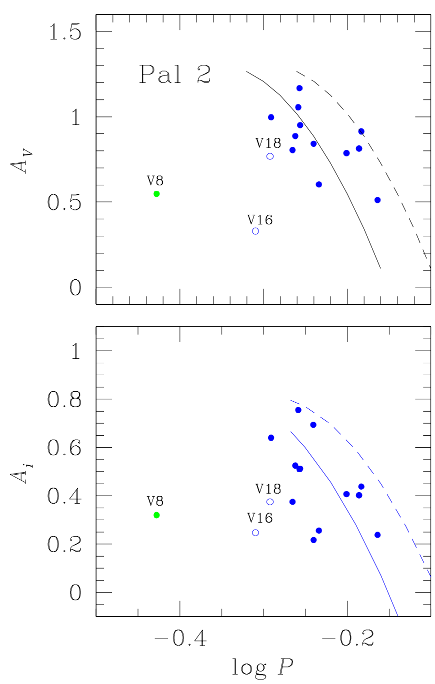

Fig. 5. Distribution of RR Lyrae stars in the amplitude-period diagram. The solid sequences correspond to the unevolved stars typical of Oo I type clusters (Cacciari et al. 2005). The dashed sequence corresponds to evolved stars of the Oo II clusters (Kunder et al. 2013). V8 is a RRc star. See § 6 for a discussion on V16 and V18. The colour figure can be viewed online.

that makes its classification very difficult; however, the star is likely a non-member.

6. THE OOSTERHOFF TYPE OF PAL 2

The average period of the member RRab star listed in Table 1 is 0.55 days which indicates that Pal 2 is of the Oo I type. We can further confirm this from the distributions of the RRab stars in the Amplitude-Period or Bailey diagram, shown in Figure 5. Given the dispersion of the light curves, the amplitude distribution is also scattered. However, it is clear that the RRab stars follow the expected sequence for unevolved stars typical of OoI clusters (Cacciari et al. 2005), in both the V and I bands. The upper sequence corresponds to evolved stars of the Oo II clusters (Kunder et al. 2013). Hence, Pal 2 is an Oo I type cluster. We note that the stars V16 and V18, whose nature is not clear due to their position in the RGB and short period (§ 5), do not follow the general trend, rather confirming that they are not field RR Lyrae stars. Alternatively, they may be binary stars. Further observations may be required to provide a proper classification.

7. CLUSTER DISTANCE AND METALLICITY FROM MEMBER RR LYRAE STARS

Although the scatter of all these faint cluster member stars may be large, we attempted an estimation of the mean distance and [Fe/H] via the Fourier light curve decomposition. This approach

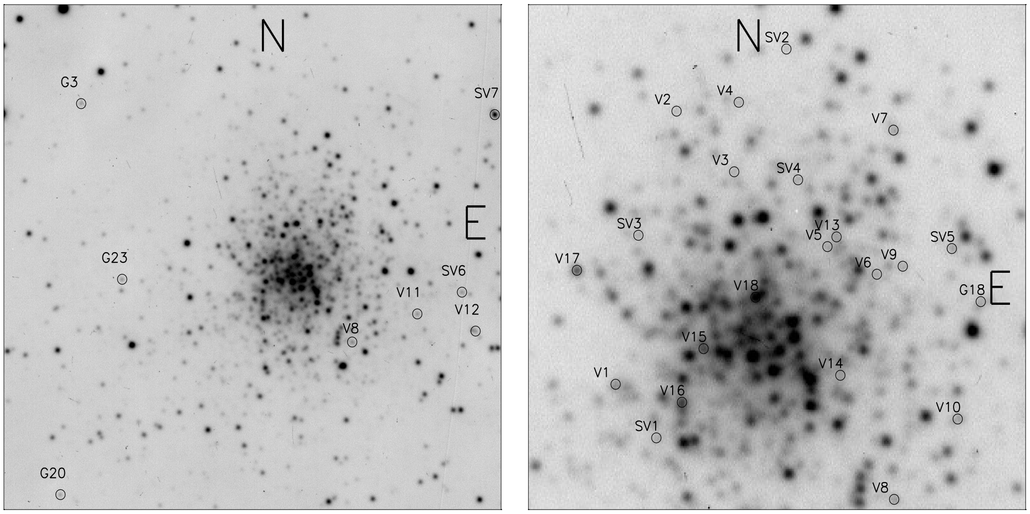

Fig. 6. Identification chart of variables in our FoV of Pal 2. The left panel shows a field of 4.1×4.1 arcmin^2. The right panel is about 1.7×1.7 arcmin^2. Expansion of the digital version is recommended for clearness.

has been amply described in previous papers. Both the method details and the specific calibrations for M_V and [Fe/H] for RRab stars can be found in a recent paper by Arellano Ferro (2022).

We selected the RRab members with the best quality light curves and restricted the Fourier approach to this sample. These are the variables V2-V13 shown in Figure 3. The mean values for the distance modulus $(V - M_V)_o$=17.18 and $\mathrm{[Fe/H]_{ZW}} = -1.39 \pm 0.55$ were found. The corresponding distance is 27.2 ± 1.8 kpc for a foreground reddening of $E(B-V) = 0.93$ plus the differential values according to the reddening map of Bonatto & Chies-Santos (2020). The quoted errors are the standard deviation of the mean; they are a bit too large but given the faintness of the stars and their consequent photometric scatter, the results are in remarkably good agreement with independent determinations: $(V - M_V)_o = 17.1 \pm 0.1$ and [Fe/H]=-1.3 (Harris et al. 1997); $\mathrm{Fe/H]_{ZW}} = -1.68 \pm 0.04$ (Ferraro et al. 1999); or $d = 27.2$ kpc and [Fe/H]=-1.42 listed by Harris (1996) (2010 update).

8. SUMMARY

We have found and identified 32 variables in the field of the globular cluster Palomar 2. A membership analysis based on *Gaia*-DR3 proper motions and the positioning of the variables in the corresponding intrinsic CMD, demonstrates that at least 18 of these variables are cluster members. Most of the detected variables are of the RRab type but one RRc and at least one RGB were identified.

The mean cluster distance and metallicity, estimated from the Fourier light curve decomposition of 11 cluster member RRab stars with the best quality available data, lead to $d = 27.2 \pm 1.8$ kpc and metallicity -1.39 ± 0.55, in reasonable agreement with the previous estimates. A detailed finding chart of all these variables is provided.

This project was partially supported by DGAPA-UNAM (Mexico) via grants IG100620. AAF is thankful to Mr. G.A. García Pérez and Mr. G. Ríos Segura for computational help. The facilities at IAO and CREST are operated by the Indian Institute of Astrophysics, Bangalore, we are grateful for the observing time allocated and for the valuable help of the support staff.

REFERENCES

Arellano Ferro, A., Mancera Piña, P. E., Bramich, D. M., et al. 2015, MNRAS, 452, 727, `https://doi.org/10.1093/mnras/stv1299`

Arellano Ferro, A., Luna, A., Bramich, D. M., et al. 2016, Ap&SS, 361, 175, `https://doi.org/10.1007/s10509-016-2757-5`

Arellano Ferro, A. 2022, RMxAA, 58, 257, `https://doi.org/10.22201/ia.01851101p.2022.58.02.08`

Bonatto, C. & Chies-Santos, A. L. 2020, MNRAS, 493, 2688, `https://doi.org/mnras/staa510`

Bramich, D. M. 2008, MNRAS, 386, 77, `https://doi.org/10.1111/j.1745-3933.2008.00464.x`

Bramich, D. M., Bachelet, E., Alsubai, K. A., Mislis, D., & Parley, N. 2015, A&A, 577, 108, `https://doi.org/10.1051/0004-6361/201526025`

Bramich, D. M., Figuera Jaimes, R., Giridhar, S., & Arellano Ferro, A. 2011, MNRAS, 413, 1275, https://doi.org/10.1111/j.1365-2966.2011.18213.x

Bramich, D. M., Horne, K., Albrow, M. D., et al. 2013, MNRAS, 428, 2275, https://doi.org/10.1093/mnras/sts184

Burke, Edward W., J., Rolland, W. W., & Boy, W. R. 1970, JRASC, 64, 353

Bustos Fierro, I. H. & Calderón, J. H. 2019, MNRAS, 488, 3024, https://doi.org/10.1093/mnras/stz1879

Cacciari, C., Corwin, T. M., & Carney, B. W. 2005, AJ, 129, 267, https://doi.org/10.1086/426325

Deras, D., Arellano Ferro, A., Bustos Fierro, I., & Yepez, M. A. 2022, RMxAA, 58, 121, https://doi.org/10.22201/ia.01851101p.2022.58.01.10

Dworetsky, M. M. 1983, MNRAS, 203, 917, https://doi.org/10.1093/mnras/203.4.917

Ferraro, F. R., Messineo, M., Fusi Pecci, F., et al. 1999, AJ, 118, 1738, https://doi.org/10.1086/301029

Gaia Collaboration, Brown, A. G. A., Vallenari, A. et al. 2021, A&A, 649, 1, https://doi.org/10.1051/0004-6361/202039657

Harris, W. E. 1996, AJ, 112, 1487, https://doi.org/10.1086/118116

Harris, W. E., Durrell, P. R., Petitpas, G. R., Webb, T. M., & Woodworth, S. C. 1997, AJ, 114, 1043, https://doi.org/10.1086/118534

Kunder, A., Stetson, P. B., Catelan, M., Walker, A. R., & Amigo, P. 2013, AJ, 145, 33, https://doi.org/10.1088/0004-6256/145/2/33

Landolt, A. U. 1992, AJ, 104, 340, https://doi.org/10.1086/116242

Sarajedini, A., Bedin, L. R., Chaboyer, B., et al. 2007, AJ, 133, 1658, https://doi.org/10.1086/511979

Stetson, P. B. 2000, PASP, 112, 925, https://doi.org/10.1086/316595

VandenBerg, D. A., Bergbusch, P. A., Ferguson, J. W., & Edvardsson, B. 2014, ApJ, 794, 72, https://doi.org/10.1088/0004-637x/794/1/72

Yepez, M. A., Arellano Ferro, A., Deras, D., et al. 2022, MNRAS, 511, 1285, https://doi.org/10.1093/mnras/stac054

Zhang, T., Ramakrishnan, R., & Livny, M. 1996, SIGMOD Rec., 25, 103, http://doi.org/10.1145/235968.233324

A. Arellano Ferro: Instituto de Astronomía, Universidad Nacional Autónoma de México, Ciudad Universitaria, C.P. 04510, México.

I. Bustos Fierro: Observatorio Astronómico, Universidad Nacional de Córdoba, Laprida 854, X5000BGR, Córdoba, Argentina.

S. Giridhar and S. Muneer: Indian Institute of Astrophysics, Bangalore, India.

Revista Mexicana de Astronomía y Astrofísica, **59**, 11–43 (2023)

https://doi.org/10.22201/ia.01851101p.2023.59.01.02

OPTIMAL TWO-IMPULSE INTERPLANETARY TRAJECTORIES: EARTH-VENUS AND EARTH-MARS MISSIONS

L. A. Gagg Filho[1] and S. da Silva Fernandes[2]

Received March 18 2022; accepted August 23 2022

ABSTRACT

This work describes several models to design optimal interplanetary trajectories. The transfer problem consists in transferring a space vehicle from a circular low Earth orbit (LEO) to a circular low orbit around a destiny planet (Venus or Mars). Models based on the two-body, four-body, and five-body problems are considered. Also, several versions of the patched-conic approximation are utilized including a detailed version that designs a lunar swing-by maneuver. The results show that the optimal trajectories for Earth-Mars and Earth-Venus missions collide with the Moon if a lunar swing-by maneuver with an unspecified altitude of the closest approach is included in the trajectory design; however, sub-optimal trajectories that do not collide with the Moon exist, presenting a smaller fuel consumption than the trajectories without lunar swing-by and with no greater changes in the time of flight.

RESUMEN

Se describen varios modelos para diseñar trayectorias interplanetarias óptimas. El problema consiste en la transferencia de un vehículo espacial de una órbita circular baja alrededor de la Tierra (LEO) a una órbita circular baja alrededor de un planeta (Venus o Marte). Se consideran modelos basados en el problema de dos cuerpos, el de cuatro cuerpos y el de cinco cuerpos. También se utilizan versiones de la aproximación cónica parchada, incluyendo una que utiliza una maniobra de impulso lunar. Los resultados muestran que las trayectorias óptimas para misiones Tierra-Marte y Tierra-Venus colisionan con la Luna si se incluye la maniobra lunar sin especificar la distancia mínima de acercamiento. Sin embargo, existen trayectorias sub-óptimas que no colisionan con la Luna, no implican cambios en los tiempos de vuelo, y permiten un menor consumo de combustible que aquellas sin la maniobra lunar.

Key Words: Earth — interplanetary medium — Moon — space vehicles

1. INTRODUCTION

Private companies together with governmental agencies are scheduling spectacular missions to Moon. NASA, for instance, has contracts with Boeing and SpaceX to take humans to Low-Earth Orbit as part of the Commercial Crew Development program (Weinzierl 2018). This governmental agency has also envisioned the Artemis program for bringing human back to Moon (Foust 2019). The building of the Orion spacecraft with partnership of Lockheed Martin (Petrescu et al. 2017) is part of this program. The development and building of the European Service Module of Orion is a partnership with ESA and the Airbus (Meiss et al. 2016). The success of these programs, which also intend to build a space station in the cislunar space, represents a huge step to achieve a greater accomplishment: a manned mission to Mars and its future colonization. NASA and Lockheed Martin company have revealed a tight schedule of activities (Cichan et al. 2016) to establish a spacecraft in Martian orbit in order to explore Deimos and Phobos (Martian moons) and the surface of Mars (O'Dell et al. 2018). There

[1]Flight Mechanics Department, Instituto Tecnológico de Aeronáutica, Praça Marechal Eduardo Gomes 50, Vila das Acácias, 12228-900, São José dos Campos, SP, Brazil.

[2]Mathematics Department, Instituto Tecnológico de Aeronáutica, Praça Marechal Eduardo Gomes 50, Vila das Acácias, 12228-900, São José dos Campos, SP, Brazil.

are several others companies involved in commercial space activities like Blue Origin and Virgin Galactic for space tourism, Astrobotic for transportation to the Moon, Astroscale for space debris removal, Deep Space Industries for asteroid mining, and many others (Weinzierl 2018).

While manned missions are still not performed in interplanetary space, unmanned missions are exploring the Solar System for several reasons: economic (asteroid mining), colonization perspective (Mars colonization), survival purpose (the studying of dangerous asteroids that could impact Earth), and scientific purposes (life search). The Hayabusa-2 mission embraces two of these reasons: scientific and planetary defense, since it intends to return a sample of the asteroid 162173 Ryugu back to Earth and to test a kinetic impactor (Tsuda et al. 2018). In the context of asteroid missions, NASA proposes a mission to the 16 Psyche asteroid, the largest metal asteroid in the main belt (Shepard et al. 2017). Concerning life search, Europa (Jupiter's moon) is believed to be the best place in the Solar System to sustain life; in this way, NASA has proposed the Europa mission in which a space vehicle will perform several flybys around this moon in order to study it (Bayer et al. 2017). Titan, the largest moon of Saturn, is the target of a mission in which the Dragonfly, a rotorcraft lander, will explore its surface (Lorenz et al. 2018). Despite several future plans, unmanned missions are limited to the Solar System, and the manned missions are still limited to the low orbits around the Earth. A few cogitate about interstellar missions: the Breakthrough Starshot project (Daukantas 2017) intends to send a probe to reach Proxima Centauri, but several technological advances are needed.

For all these missions, trajectory determinations must be accomplished considering a mathematical model as realistic as possible. Moreover, these trajectories must be minimum-time trajectories or minimum-fuel trajectories (Prussing and Chiu 1986) or a trade-off between these two performance index as the Apollo missions. In order to perform these optimization, an initial guess is necessary, which can be a solution trajectory in a more simple model. Dei Tos and Topputo (2019), however, develop a method to optimize impulsive trajectories in a complex model that is based on a real ephemeris model. Izzo et al. (2019) utilizes machine learning based on artificial neural networks, an heuristic method, to represent the optimal guidance profile of an interplanetary mission. Abdelkhalik and Mortari (2007) utilize a genetic algorithm to solve the transfer between noncoplanar elliptical orbits utilizing impulsive maneuvers. On the other hand, Ellison et al. (2018) develop analytical methods to compute partial-derivatives of two bounded-impulsive trajectories with multiple swing-by maneuvers. Gagg Filho and da Silva Fernandes (2018) build patched-conic approximations to obtain geometrical details of interplanetary missions. Genta and Maffione (2019) state that the parameters and constraints of a trajectory are important to define the launch date, which is vital for the feasibility of the mission. Once a good initial approximation of the trajectory is obtained, a simple optimization method can be utilized as, for instance, the gradient method (Addis et al. 2011).

In the context of space missions, the present work proposes models based on the two-body, four-body, and five-body problems for trajectory determination in a preliminary mission analysis from Earth to inner planets (Venus) and outer planets (Mars) considering planar models. Among the models based on the two-body problem there are the well-known interplanetary patched-conic approximation based on the Hohmann transfer, which solves the heliocentric phase; and the interplanetary patched-conic approximation based on the Gauss problem (Bate et al. 1971), also known as Lambert's problem (Battin et al. 1978; Prussing 1979; Battin and Vaughan 1984; Gooding 1990). The characterization of the trajectory phases by the patched-conic approximations is accomplished by the definition of the sphere of influence (SOI), in a way that when the motion of the space vehicle occurs, for instance, inside the Earth's SOI, the geocentric phase is characterized.

Despite the patched-conic approximations based on the Hohmann transfer and the one based on the Gauss problem being usually used for preliminary mission analysis, these models patch the trajectory phases in an independent way. In this way, the visualization of the complete trajectory has discontinuities and information related to the complete trajectory is lost. In this sense, the present work also utilizes a patched-conic approximation based on a detailed geometry of the transfer problem (Gagg Filho and da Silva Fernandes 2018) which determines the complete trajectory by means of a two-point boundary value problem (TPBVP) and it includes a swing-by maneuver with the Moon. Broucke (1988) qualitatively mentions that the Moon is a weak gravitational accelerator; however, the present work extends the conclusion of Broucke (1988) by quantifying the saving of fuel consumption, represented by the sum of the velocity increments, when a lunar swing-by maneuver is performed in an interplanetary mission. The work of Faria Venditti et al. (2010) optimizes interplanetary trajectories considering swing-by maneuvers by using a patched-conic approximation in such way that no discontinuity exist for the velocity vector. Yang et al. (2019) solve a powered swing-by maneuver by using a pseudostate theory and, next, a patching technique matches the segments of the swing-by maneuver with the interplanetary trajectory in order to determine a more realistic trajectory. Lavagna et al. (2005) adopt a multi-objective strategy to minimize both fuel consumption and trip time by considering aero-gravity assist maneuvers. An evolutionary algorithm is used in this last work to avoid trapped solutions in local minima. In the present work, the patched-conic approximations with detailed geometry, and the models based on the four and five-body problem determine the complete interplanetary trajectory without any discontinuity not only in the velocity vector, but also in the position vector; moreover, the swing-by maneuver is solved together with the complete trajectory in an unique TPBVP providing an initial guess to determine the local minimum by means of a gradient technique.

In the context of the interplanetary transfer model based on the planar restricted four-body problem (PCR4BP, Sun-Earth-destiny planet-space vehicle), the present work formulates the same transfer problem with a different approach from the one described by Miele and Wang (1999b) but similar to Miele et al. (2004b), i.e, the differential equations that govern the motion of the space vehicle are written, in the present work, utilizing Cartesian coordinates (Miele and Wang 1999b utilize polar coordinates) in three distinct forms. Each form defines the differential equations for the relative motion of the space vehicle with respect to Earth, Sun, and destiny planet, respectively. The choice of the proper version of the differential equations is dependent on the predominant gravitational field acting on the space vehicle. A two-point boundary value problem (TPBVP), involving prescribed values of the initial phase angle between the space vehicle and the Earth, and the initial phase angle (rendezvous angle) of the destiny planet, is formulated. Based on this TPBVP, an one-degree of freedom optimization problem concerning the minimization of the total fuel consumption, with a prescribed rendezvous angle, is proposed. A two-degree of freedom optimization problem is also formulated, in which the rendezvous angle is taken as additional unknown. Next, the Moon's gravitational influence is included in the set of differential equations that describes the relative motion of the space vehicle to Earth; thus, the four-body problem is converted into a five-body problem in the neighborhood of Earth and a three-degree of freedom optimization problem is formulated. Therefore, this last model enables the lunar swing-by maneuver before the leaving of the space vehicle from the Earth's SOI.

The objective of this work is to analyze Earth-Mars and Earth-Venus transfers from a circular low Earth orbit (LEO) to a circular low orbit around the destiny planet (Venus or Mars) by using bi-impulsive optimal trajectories that minimize the fuel consumption in the context of the two-body, four-body, or five-body problems. This work also investigates the saving of fuel if a lunar swing-by maneuver is performed in these missions. Note that only planar problems are taken into account in the present work, which provides a good approximation for a preliminary analysis. In this case, the patched-conic approximations based on the Hohmann transfer and on the Gauss problem must already provide relevant results. The planar circular restricted four-body model is similar to the one used by Miele and Wang (1997), Miele and Wang (1999a), Miele and Wang (1999b), and by Miele et al. (2004a). In this way, the present paper extends the four-body model used by Miele by including the Moon in a planar circular restricted five-body model, and an analysis for the Earth-Venus mission is also considered.

2. MATHEMATICAL FORMULATION

This section formulates the interplanetary transfer based on the two-body problem, the restricted four-body problem, and the restricted five-body problem. The interplanetary mission consists in transferring a space vehicle from a low Earth orbit (LEO) to a low Mars orbit - LM_tO(or, to a low Venus orbit - LVO) by applying two impulses tangential to the terminal orbits. The first velocity increment Δv_{LEO} inserts the space vehicle into a transfer trajectory, and the second velocity increment Δv_{LM_tO} (or, Δv_{LVO}) brakes the vehicle circularizing its motion at the LM_tO (or, LVO). The fuel consumption is represented by the total characteristic velocity $\Delta v_{Total} = \Delta v_{LEO} + \Delta v_{LM_tO}$ (or, $\Delta v_{LEO} + \Delta v_{LVO}$) (Marec 1979). The terminal orbits, the planet orbits and the Moon orbit are considered circular and coplanar, in a way that the motion of the space vehicle occurs in the plane of these orbits. Table 1 shows the approximate eccentricity and inclination of the celestial body orbits.

Note in Table 1 that the inclinations of the celestial body orbits used in the present paper are small (the largest is that of the Moon and it is equal to

TABLE 1

INCLINATION AND ECCENTRICITY OF THE MAIN BODY ORBITS (JPL/NASA)

	Eccentricity	Inclination to the mean ecliptic
Venus	0.0067	3.3977°
Earth-Moon barycenter	0.0167	0.0005°
Moon	0.0554	5.1600°
Mars	0.0933	1.8518°

5.6°), so the orbital motion of the Moon, Earth, Mars, Venus and space vehicle is simplified on the ecliptic plane. In the same way, the orbits of the celestial bodies are considered circular as their eccentricities are small (the largest is that of Mars and it is equal to 0.0933).

Among the models based on the two-body problem there are: the classic patched-conic approximation based on the Hohmann transfer, the patched-conic approximation based on the Gauss problem, the patched-conic approximation with detailed geometry, and the patched-conic approximation with a lunar swing-by maneuver. For all the models based on patched-conic approximations, the interplanetary trajectory is divided in phases, which are defined by the sphere of influence (SOI) of the main bodies. In this way, the patched-conic approximations have, at least, three phases: the geocentric phase, where only the gravitational field of the Earth is considered; the heliocentric phase, where only the gravitational field of the Sun is considered; and, the planetocentric phase, where only the gravitation field of the destiny planet is considered. These models are briefly discussed below. In order to simplify the notation, Mars is considered to be the destiny planet without loss of generality.

2.1. *Patched-Conic Approximation Based on the Hohmann Transfer*

For the patched-conic approximation based on the Hohmann transfer, the heliocentric phase is solved first (Bate et al. 1971). For this phase, the Hohmann transfer (Bate et al. 1971; Prussing and Conway 1993) is utilized to estimate the parameters of the elliptic transfer trajectory that defines the heliocentric phase, which includes the Hohmann velocity increments $\Delta v_{0,Hohmann}$ and $\Delta v_{f,Hohmann}$. Next, the geocentric and the planetocentric trajectories are simultaneously determined by considering them as hyperbolic, with their excess velocities, $\Delta v_{\infty,geo}$ and $\Delta v_{\infty,pla}$, equal to the Hohmann velocity increments, $\Delta v_{0,Hohmann}$ and $\Delta v_{f,Hohmann}$ respectively. By using well-known results of the two-body problem, it is now possible to determine the initial velocity, v_0, of the space vehicle right after the application of Δv_{LEO}, and the final velocity, v_f, of the space vehicle right before the application of Δv_{LM_tO} (or Δv_{LVO}). The velocity increments are calculated as:

$$\Delta v_{LEO} = v_0 - \sqrt{\frac{\mu_E}{r_0}}, \qquad (1)$$

$$\Delta v_{LM_tO} = v_f - \sqrt{\frac{\mu_{M_t}}{r_f}}, \qquad (2)$$

where μ_E and μ_{M_t} are the Earth and Mars gravitational parameters, respectively; r_0 is the radius of the circular LEO, and, r_f is the radius of the circular LM_tO.

2.2. *Patched-Conic Approximation Based on the Gauss Problem*

According to the Hohmann transfer in the previous section, the space vehicle describes an elliptic heliocentric trajectory making a 180° arc in true anomaly (the transfer ellipse is tangent simultaneously to the terminal orbits). However, if it is desired to reach the SOI of Mars with a smaller travel time, a smaller arc of true anomaly must be prescribed. In this way, the vectors of the excess velocities must be obtained by another procedure. To achieve this goal, the heliocentric phase is solved with the Gauss problem (also known as Lambert problem [1]) (Bate et al. 1971; Battin et al. 1978; Prussing 1979; Battin and Vaughan 1984; Gooding 1990). To apply the Gauss problem, the magnitude of two position vectors of the space vehicle must be provided, as well as the time of flight and the true anomaly variation Δf between these two vectors and the direction of motion. Since the elliptic trajectory is defined from the boundary of the Earth's SOI to the boundary of Mars' SOI, the magnitudes of these two vectors are the Earth-Sun distance, D_E, and the Mars-Sun distance, D_{M_t}. Once the excess velocities, $\Delta v_{0,Gauss}$ and $\Delta v_{f,Gauss}$, are obtained based on the Gauss problem, the initial velocity v_0 and the final velocity

[1] In the classic Lambert problem, the two position vectors (or equivalently the magnitude of the position vectors and the variation of the true anomaly) are provided together with the time of flight. Then, the velocity vectors are calculated without any optimization. However, if the variation of the true anomaly or the time of flight is not prescribed, that is, it is taken as unknown, then one can formulate an one-degree optimization problem (Problem 1 and Problem 2).

v_f of the space vehicle are calculated; and the velocity increments, Δv_{LEO} and Δv_{LM_tO}, applied to the space vehicle, are determined using equations (1) and (2), respectively.

Note that the Gauss problem is solved for a prescribed value of time of flight; therefore, an optimization problem is enunciated below by setting the time of flight as an unknown to be determined in order to obtain the solution with minimum Gauss velocity increment $\Delta v_{Total,Gauss}$.

Problem 1 *"Given the value of Δf, the direction of motion, and prescribing the magnitudes of two position vectors (D_E and D_{M_t}, for instance), determine the time of flight Δt between these two vectors that minimizes the function*

$$F(\Delta t): \quad \Delta v_{Total,Gauss} = \Delta v_{0,Gauss} + \Delta v_{f,Gauss}.\text{"} \tag{3}$$

An equivalent optimization problem can be also enunciated with a prescribed time of flight by setting the true anomaly variation Δf as unknown to minimize the fuel consumption. This second optimization problem is enunciated below.

Problem 2 *"Given the value of time of flight, the direction of motion, and prescribing the magnitudes of two position vectors (D_E and D_{M_t}, for instance), determine the true anomaly Δf between these two vectors that minimizes the function*

$$F(\Delta f): \quad \Delta v_{Total,Gauss} = \Delta v_{0,Gauss} + \Delta v_{f,Gauss}.\text{"} \tag{4}$$

2.3. *Patched-Conic Approximation with Detailed Geometry*

In the patched-conic approximation based on the Hohmann transfer and the one based on the Gauss problem, the heliocentric phase is first solved to determine the excess velocities. For these models, it is not possible to build the complete Earth-Mars trajectory without discontinuity between the points that connect the phases. This section shortly comments about a new patched-conic approximation in which the excess velocities are determined through a detailed geometry; it is based on an extension of the lunar patched-conic approximation, as described by Arthur Gagg Filho and da Silva Fernandes (2016). For this model, the geocentric phase is solved first, followed by the heliocentric phase, and finally, the planetocentric is determined. The inertial reference frame S_{XY} is taken with the Sun at origin, the X-axis

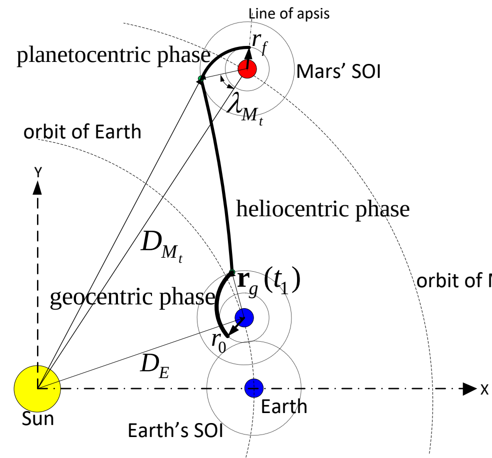

Fig. 1. Geometry of the patched-conic approximation. The color figure can be viewed online.

pointing towards Earth at the initial time, and with the Y-axis orthogonal to the X-axis according to Figure 1. Therefore, when the complete trajectory, Figure 1, is determined, one must compare the calculated arrival condition of the space vehicle with the prescribed arrival condition. In this way, the complete trajectory is obtained by solving a two-point boundary value problem (TPBVP) as enunciated below

Problem 3 *"Given the terminal altitudes h_{LEO} and h_{LM_tO}, and prescribing the initial phase angle $\theta_{EP}(0)$ of the space vehicle with the Earth and the phase angle λ_{Mt}, which describes the arrival geometry at the Mars' SOI, determine the initial velocity v_0 subjected to the final constraint:*

$$g(v_0): \quad r_{p_{pla}} - r_f = 0, \tag{5}$$

where $r_{p_{pla}}$ is the calculated pericenter distance of the planetocentric phase, and r_f is the prescribed radius of the LM_tO."

The velocity increments, Δv_{LEO} and Δv_{LM_tO}, applied to space vehicle are determined using equations (1) and (2), respectively. Note that an optimization problem can be enunciated in order to determine the value of λ_{Mt} that minimizes the fuel consumption Δv_{Total}.

2.4. *Patched-Conic Approximation with a Lunar Swing-by Maneuver*

This patched-conic model is similar to the patched-conic approximation presented in § 2.3, but with two more phases in order to include a lunar swing-by maneuver, and with the inertial reference frame S_{XY} centered on the Sun with the X-axis parallel to the Earth-Moon line at the initial time (see Figure 2). In this way, the complete trajectory is described by five phases: a first elliptic geocentric phase is characterized from the departure of the space vehicle from the LEO until it reaches the boundary of the Moon's SOI; next, an hyperbolic selenocentric phase models the lunar swing-by maneuver; a second, but hyperbolic geocentric phase is defined from the departure from the Moon's SOI until the reaching of the boundary of the Earth's SOI; next, an elliptic heliocentric phase is defined from the departure of the Earth's SOI until the space vehicle reaches the Mars' SOI; finally, the hyperbolic planetocentric phase is characterized from the boundary of the Mars' SOI until the arrival at the LM_tO. The complete formulation of this patched-conic approximation can be found in Gagg Filho and da Silva Fernandes (2018). Since there is a lunar swing-by maneuver in this model, an intermediary constraint is included. This constraint defines the pericenter altitude of the selenocentrinc phase. Therefore, the TPBVP can be enunciated as it follows:

Problem 4 *"Given the terminal altitudes h_{LEO} and h_{LM_tO}, and prescribing the phase angle λ_1, which describes the arrival geometry at the Moon's SOI, and the phase angle λ_{Mt}, which describes the arrival geometry at the Mars' SOI, determine the initial velocity v_0 and the phase angles λ_S, which describes the departure geometry from the Earth's SOI, subjected to the final constraint:*

$$g\left(\lambda_S\right): \quad r_{p_{pla}} - r_f = 0, \tag{6}$$

and subject to the intermediary constraint:

$$g_0\left(v_0\right): \quad r_{pM} - r_{sP} = 0, \tag{7}$$

where r_{sP} is the prescribed distance of close encounter with the Moon, and r_{pM} is the calculated pericenter distance of the selenocentric phase."

The velocity increments, Δv_{LEO} and Δv_{LM_tO}, applied to the space vehicle are determined using equations (1) and (2), respectively. Note that an optimization problem with two-degree of freedom can be enunciated in order to determine the values of λ_{Mt} and λ_1 which minimize the fuel consumption Δv_{Total}.

2.5. *Interplanetary Transfer Problem Based on the Four-Body Problem*

In this section, the interplanetary transfer problem based on the planar circular restricted four-body problem (PCR4BP), in which the three primaries are the Earth, the Sun and Mars, and the fourth body is the space vehicle, is formulated. A mathematical development can be found in Miele and Wang (1999b), which utilizes polar coordinates to formulate the problem; however, the present work formulates the differential equations in Cartesian coordinates similar to Miele et al. (2004b). To solve the interplanetary transfer problem, consider an inertial reference frame S_{XY} centered on the Sun with the X-axis pointing to Earth at the initial time t_0, and with the Y-axis orthogonal to the X-axis at the direction of orbital motion of the Earth around the Sun (Figure 3). Despite the space vehicle being subjected to

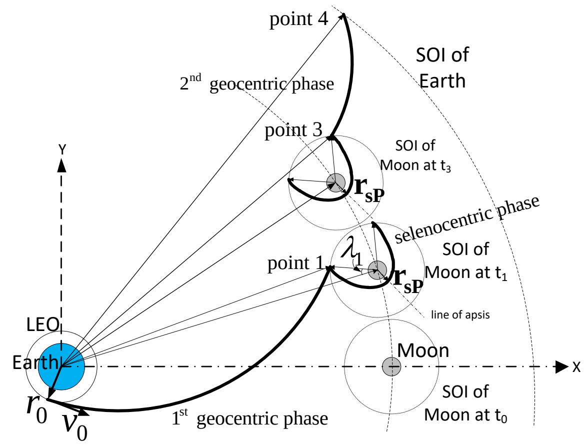

(a) Geocentric and selenocentric phases.

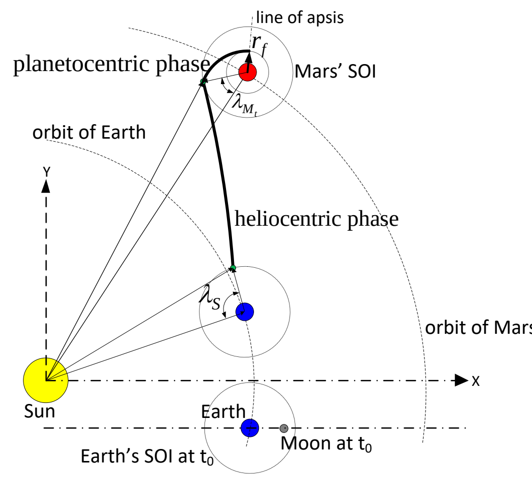

(b) Heliocentric and planetocentric phases.

Fig. 2. Patched-conic approximation with swing-by. Modified from Gagg Filho and da Silva Fernandes (2018). The color figure can be viewed online.

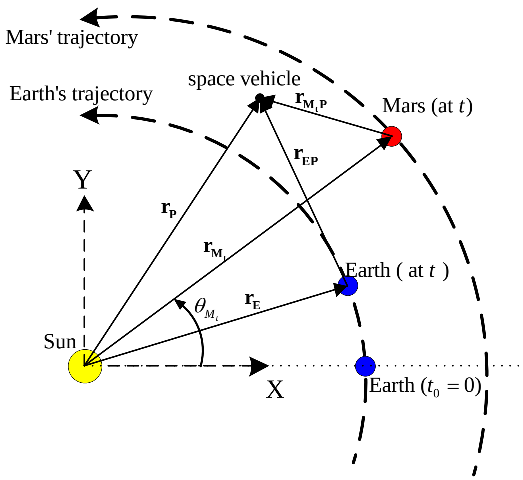

Fig. 3. Inertial reference frame S_{XY} for the PCR4BP. The color figure can be viewed online.

the gravitational fields of the three primaries during the whole trajectory, three phases of the trajectories are considered to formulate the problem: the geocentric phase, the heliocentric phase, and the planetocentric phase. This procedure provides a better accuracy in the numerical integration of the differential equations because a suitable normalization is used in each phase. For example, when the space vehicle is in the neighborhood of Earth, the gravitational field of this body is predominant; thus, the system of differential equations is written based on the relative motion of the space vehicle with respect to Earth. In this case, the normalization is performed by utilizing the Earth's parameters. On the other hand, when the space vehicle is far from Earth and Mars, the gravitational field of the Sun is predominant; therefore, the system of differential equations is written based on the relative motion of the space vehicle with respect to Sun. The same explanation follows when the space vehicle is in the neighborhood of Mars. In order to characterize the different phases, the concept of SOI is utilized. In this model, the concept of SOI is only applied to separate the phases; thus, the space vehicle is still subjected to the gravitational fields of the primaries along the whole trajectory.

2.5.1. *Geocentric Phase*

At the initial time, the space vehicle is at the *LEO*. After applying the first velocity increment Δv_{LEO}, the space vehicle is inserted into an interplanetary transfer trajectory. So, at the beginning of the mission, the space vehicle is in the neighborhood of the Earth and its motion is described by the following system of differential equations:

$$\ddot{x}_{EP} = -\frac{\mu_S}{r_P^3}(x_{EP}+x_E) - \frac{\mu_E}{r_{EP}^3}(x_{EP}) - \frac{\mu_{M_t}}{r_{M_tP}^3}(x_{EP}+x_E-x_{M_t}) + \frac{\mu_S}{r_E^3}(x_E)\,, \tag{8}$$

$$\ddot{y}_{EP} = -\frac{\mu_S}{r_P^3}(y_{EP}+y_E) - \frac{\mu_E}{r_{EP}^3}(y_{EP}) - \frac{\mu_{M_t}}{r_{M_tP}^3}(y_{EP}+y_E-y_{M_t}) + \frac{\mu_S}{r_E^3}(y_E)\,, \tag{9}$$

where (x_{EP}, y_{EP}) are the components of the position vector of the space vehicle with respect to Earth; r_P, r_{EP}, and, r_{M_tP} are the magnitude of the position vector of the space vehicle with respect to, respectively, Sun, Earth, and the destiny planet (Mars); and μ_S is the gravitational parameter of the Sun. (x_E, y_E) and (x_{M_t}, y_{M_t}) define the components of the position vectors of the Earth and Mars, respectively, and are calculated as follows:

$$x_E = D_E\cos(\omega_E t), \tag{10}$$

$$y_E = D_E\sin(\omega_E t), \tag{11}$$

$$x_{M_t} = D_{M_t}\cos[\omega_{M_t}t + \theta_{M_t}(0)], \tag{12}$$

$$y_{M_t} = D_{M_t}\sin[\omega_{M_t}t + \theta_{M_t}(0)], \tag{13}$$

where ω_E and ω_{M_t} are the angular velocities (mean motions) of Earth and Mars, respectively, around Sun (see Table 2); D_E and D_{M_t} are, respectively, the Sun-Earth distance and the Sun-Mars distance; $\theta_{M_t}(0)$ is the initial phase angle, also called the rendezvous angle, of Mars in the S_{XY} reference frame.

The time derivative expressions of equations 10 – 13 provide the velocity vector components:

$$\dot{x}_E(t) = -\omega_E D_E\sin(\omega_E t), \tag{14}$$

$$\dot{y}_E(t) = \omega_E D_E\cos(\omega_E t), \tag{15}$$

$$\dot{x}_{M_t}(t) = -\omega_{M_t}D_{M_t}\sin[\omega_{M_t}t + \theta_{M_t}(0)], \tag{16}$$

$$\dot{y}_{M_t}(t) = \omega_{M_t}D_{M_t}\cos[\omega_{M_t}t + \theta_{M_t}(0)]. \tag{17}$$

Initial Conditions

The initial conditions that define the beginning of integration of the differential equation system (equations 8 and 9), are given by the components of the position and velocity vectors of the space vehicle with respect to Earth at t_0, i.e, at the time right after the application of Δv_{LEO}:

$$x_{EP}(0) = r_{EP}(0)\cos[\theta_{EP}(0)]\,, \tag{18}$$

TABLE 2

PLANETARY DATA

Planet	Distance to the Sun (km)	Radial Distance (km)	gravitational parameter μ (km^3/s^2)	mean motion (rad/s)	SOI radius (km)
Venus[1]	1.0815×10^8	6051.8	32.4776×10^4	$3.23861161 \times 10^{-7}$	615976.52
Earth[2]	1.4960×10^8	6378.2	39.8600×10^4	$1.99177621 \times 10^{-7}$	923502.24
Mars[2]	2.2790×10^8	3397.0	4.2830×10^4	$1.05850987 \times 10^{-7}$	577723.87

[1]Calculated distance from the data of JPL/NASA.

[2]Calculated distance from the data found in Miele and Wang (1999b).

$$y_{EP}(0) = r_{EP}(0) \sin\left[\theta_{EP}(0)\right], \tag{19}$$

$$\dot{x}_{EP}(0) = -\left[\sqrt{\frac{\mu_E}{r_{EP}(0)}} + \Delta v_{LEO}\right] \sin\left[\theta_{EP}(0)\right], \tag{20}$$

$$\dot{y}_{EP}(0) = \left[\sqrt{\frac{\mu_E}{r_{EP}(0)}} + \Delta v_{LEO}\right] \cos\left[\theta_{EP}(0)\right], \tag{21}$$

where $r_{EP}(0) = r_{EP_0}$ is the Earth-space vehicle distance at t_0 given by $R_E + h_{LEO}$ with R_E denoting the mean equatorial radius of Earth and h_{LEO} denoting the altitude of the LEO; and, $\theta_{EP}(0)$ is the initial phase angle of the space vehicle with respect to Earth in the S_{XY} reference frame. The LEO is assumed in the counterclockwise direction (direct orbit).

The numerical integration of equations 8 and 9 is performed from $t = t_0$ to $t = t_1$, at which the following constraint becomes true:

$$g_{0_{GEO}} : r_{EP}(t_1) > R_{ST}, \tag{22}$$

where R_{ST} is the radius of the SOI of the Earth. The heliocentric phase initiates when the constraint $g_{0_{GEO}}$ is satisfied.

2.5.2. *Heliocentric Phase*

In this phase, the gravitational field of the Sun is predominant and it initiates when the space vehicle leaves the Earth's SOI. In this way, the system of differential equations that describes the motion of the space vehicle is written with its position and velocity vectors with respect to the inertial frame as following:

$$\ddot{x}_P = -\frac{\mu_S}{r_P^3}\left(x_P\right) - \frac{\mu_E}{r_{EP}^3}\left(x_P - x_E\right) - \frac{\mu_{M_t}}{r_{M_tP}^3}\left(x_P - x_{M_t}\right), \tag{23}$$

$$\ddot{y}_P = -\frac{\mu_S}{r_P^3}\left(y_P\right) - \frac{\mu_E}{r_{EP}^3}\left(y_P - y_E\right) - \frac{\mu_{M_t}}{r_{M_tP}^3}\left(y_P - y_{M_t}\right), \tag{24}$$

where (x_P, y_P) are the components of the position vector of the space vehicle with respect to Sun (origin of the inertial reference system).

Initial Conditions

The initial conditions of the system defined by equations (23) and (24) are the components of the position and velocity vectors of the space vehicle with respect to Sun at time t_1. In this way, one has

$$x_P(t_1) = x_E(t_1) + x_{EP}(t_1), \tag{25}$$

$$y_P(t_1) = y_E(t_1) + y_{EP}(t_1), \tag{26}$$

$$\dot{x}_P(t_1) = \dot{x}_E(t_1) + \dot{x}_{EP}(t_1), \tag{27}$$

$$\dot{y}_P(t_1) = \dot{y}_E(t_1) + \dot{y}_{EP}(t_1). \tag{28}$$

For the calculation of these initial conditions it is enough to determine the components of the position and velocity vectors of the Earth at t_1 by utilizing equations 10, 11, 14 and 15; and to utilize the components of position and velocity vectors of the space vehicle with respect to Earth at t_1, which are provided as the state variables by the end of the integration of the geocentric phase. Once the initial conditions are established, the differential equation system, equations 23 and 24, is integrated from $t = t_1$ to $t = t_2$, when the space vehicle reaches the boundary of the SOI of Mars (or Venus) defined by the following constraint:

$$g_{0_{HELIO}} : r_{M_tP}(t_2) < R_{SM_t}, \tag{29}$$

where R_{SM_t} is the radius of the SOI of Mars. The planetocentric phase initiates when the constraint $g_{0_{HELIO}}$ is satisfied.

2.5.3. *Planetocentric Phase*

The planetocentric phase initiates when the space vehicle reaches the boundary of Mars' SOI; thus, the gravitational field of Mars becomes predominant.

The system of differential equations is expressed with the components of the position and velocity vectors of the space vehicle with respect to Mars as below:

$$\ddot{x}_{M_tP}=-\frac{\mu_S}{r_P^3}(x_{M_tP}+x_{M_t})-\frac{\mu_E}{r_{EP}^3}(x_{M_tP}+x_{M_t}-x_E)-\frac{\mu_{M_t}}{r_{M_tP}^3}(x_{M_tP})+\frac{\mu_S}{r_{M_t}^3}(x_{M_t}), \tag{30}$$

$$\ddot{y}_{M_tP}=-\frac{\mu_S}{r_P^3}(y_{M_tP}+y_{M_t})-\frac{\mu_E}{r_{EP}^3}(y_{M_tP}+y_{M_t}-y_E)-\frac{\mu_{M_t}}{r_{M_tP}^3}(y_{M_tP})+\frac{\mu_S}{r_{M_t}^3}(y_{M_t}), \tag{31}$$

where (x_{M_tP}, y_{M_tP}) are the components of the position vector of the space vehicle with respect to Mars.

Initial Conditions

The initial conditions of the system defined by equations (30) and (31) are the components of the position and velocity vectors of the space vehicle to Mars at time t_2. These components are expressed by:

$$x_{M_tP}(t_2) = x_P(t_2) - x_{M_t}(t_2), \tag{32}$$

$$y_{M_tP}(t_2) = y_P(t_2) - y_{M_tP}(t_2), \tag{33}$$

$$\dot{x}_{M_tP}(t_2) = \dot{x}_P(t_2) - \dot{x}_{M_tP}(t_2), \tag{34}$$

$$\dot{y}_{M_tP}(t_2) = \dot{y}_P(t_2) - \dot{y}_{m_tP}(t_2). \tag{35}$$

For the calculation of these initial conditions it is enough to determine the components of the position and velocity vectors of Mars at t_2 by utilizing equations 12, 13, 16 and 17; and to utilize the components of position and velocity vectors of the space vehicle with respect to Sun at t_2, which are provided as the state variables by the end of the integration of the heliocentric phase. Once the initial conditions are established, the differential equation system, equations (30) and (31), is integrated from $t = t_2$ to $t = T$, the moment right before the application of the second velocity increment that circularizes the space vehicle in the low orbit of the destiny planet according to the final constraints. Note that, in order to switch between the phases, the position vector of the primaries must be monitored.

2.5.4. *Two-Point Boundary Value Problem*

According to § 2.5.1 and § 2.5.3, one can determine the trajectory by integrating the system of differential equations of each phase if the initial conditions of equations (8) and (9) are given. However, the final conditions must agree with the terminal constraints at the LM_tO. Therefore, a TPBVP is enunciated as it follows:

Problem 5 *"Given the terminal altitudes h_{LEO} and h_{LM_tO}, and prescribing the initial phase angle $\theta_{EP}(0)$ of the space vehicle with respect to Earth and the initial phase angle of Mars $\theta_{M_t}(0)$, determine the set of variables $(\Delta v_{LEO}, \Delta v_{LM_tO}, T)$ subject to the final constraints:*

$$g_1: \quad (x_{M_tP}(T))^2 + (y_{M_tP}(T))^2 - (r_{M_tP}(T))^2 = 0, \tag{36}$$

$$g_2: \quad (\dot{x}_{M_tP}(T))^2 + (\dot{y}_{M_tP}(T))^2 - \left[\sqrt{\frac{\mu_{M_t}}{r_{M_tP}(T)}} + \Delta v_{LM_tO}\right]^2 = 0, \tag{37}$$

$$g_3: \quad (x_{M_tP}(T))(\dot{y}_{M_tP}(T)) - (y_{M_tP}(T))(\dot{x}_{M_tP}(T)) \pm r_{M_tP}(T)\left[\sqrt{\frac{\mu_{M_t}}{r_{M_tP}(T)}} + \Delta v_{LM_tO}\right] = 0, \text{”} \tag{38}$$

where the upper (lower) sign in equation (38) indicates a clockwise (counterclockwise) arrival at the $LMtO$. This problem is solved by means of the Newton-Raphson algorithm.

Note also that the angles $\theta_{EP}(0)$ and $\theta_{M_t}(0)$ are prescribed. By taking advantage of this fact, two optimization problems are next enunciated.

2.5.5. *One-Degree of Freedom Optimization Problem*

If there is a solution of the TPBVP for each value of $\theta_{EP}(0)$ with $\theta_{M_t}(0)$ prescribed; then there must exist an optimal value of $\theta_{EP}(0)$ that minimizes the fuel consumption. Therefore, the following one-degree of freedom optimization problem is enunciated:

Problem 6 *"Given the terminal altitudes h_{LEO} and h_{LM_tO}, and prescribing $\theta_{M_t}(0)$, determine the set of variables $(\Delta v_{LEO}, \Delta v_{LM_tO}, T, \theta_{EP}(0))$ that minimizes the function*

$$F: \quad \Delta v_{Total} = \Delta v_{LEO} + \Delta v_{LM_tO}, \tag{39}$$

subject to the final constraints g_1, g_2 and g_3 defined by equations (36), (37) and (38), respectively. "

2.5.6. *Two-Degree of Freedom Optimization Problem*

According to Problem 5, the phase angles $\theta_{EP}(0)$ and $\theta_{M_t}(0)$ must be prescribed in order to solve the TPBVP. However, one can take both angles as unknowns to solve a two-degree optimization problem as enunciated below:

Problem 7 *"Given the terminal altitudes h_{LEO} and h_{LM_tO}, determine the set of variables (Δv_{LEO}, Δv_{LM_tO}, T, $\theta_{EP}(0)$, $\theta_{M_t}(0)$) that minimizes the function*

$$F: \quad \Delta v_{Total} = \Delta v_{LEO} + \Delta v_{LM_tO}, \tag{40}$$

subject to the final constraints g_1, g_2 and g_3 defined by equations (36), (37) and (38), respectively."

2.6. *Interplanetary Transfer Problem Based on the Five-Body Problem*

This model extends the formulation of the interplanetary transfer based on the PCR4BP (§ 2.5) by including a lunar swing-by maneuver. In this sense the system of differential equations of the geocentric phase, equations (8) and (9), is modified by adding the gravitational attraction of the Moon, converting the PCR4BP into a planar circular restricted five-body problem (PCR5BP). Thus, the new system of differential equations that describes the motion of the space vehicle at the neighborhood of Earth is described as below:

$$\ddot{x}_{EP} = -\frac{\mu_S}{r_P^3}(x_{EP} + x_E) - \frac{\mu_E}{r_{EP}^3}(x_{EP}) - \frac{\mu_{M_t}}{r_{M_tP}^3}(x_{EP} + x_E - x_{M_t}) - \frac{\mu_M}{r_{PM}^3}(x_{EP} - x_{ME}) + \frac{\mu_S}{r_E^3}(x_E), \tag{41}$$

$$\ddot{y}_{EP} = -\frac{\mu_S}{r_P^3}(y_{EP} + y_E) - \frac{\mu_E}{r_{EP}^3}(y_{EP}) - \frac{\mu_{M_t}}{r_{M_tP}^3}(y_{EP} + y_E - y_{M_t}) - \frac{\mu_M}{r_{PM}^3}(y_{EP} - y_{ME}) + \frac{\mu_S}{r_E^3}(y_E), \tag{42}$$

where r_{PM} is the magnitude of the position vector of the space vehicle with respect to Moon, and, (x_{ME}, y_{ME}) are the components of the position vector of the Moon with respect to Earth determined as it follows

$$x_{ME} = D_M \cos(\theta_M(0) + \omega_M t), \tag{43}$$

$$y_{ME} = D_M \sin(\theta_M(0) + \omega_M t). \tag{44}$$

The Earth-Moon mean distance is denoted by D_M in equations 43 and 44, ω_M is the angular velocity (mean motion) of the Moon around the Earth, and $\theta_M(0)$ is the initial phase angle of the Moon with respect to the X-axis of the inertial reference frame S_{XY}.

When the space vehicle leaves the Earth's SOI, the system of differential equation must be rewritten with the position vector of the space vehicle with respect to Sun in a similar way to equations (41) and (42). In the same way, when the space vehicle enters the SOI of the destiny planet, another system of differential equations is used with the position vector of the space vehicle with respect to the destiny planet. To simplify numerical computation, the gravitational field of the Moon is neglected in the heliocentric and planetocentric phases. If the initial condition for the integration of the equations of motion (equations 41 and 42) is accurate enough, the lunar swing-by maneuver will occur naturally; therefore, there is no intermediary constraint that defines the swing-by maneuver.

2.6.1. *The Two-Point Boundary Value Problem (TPBVP)*

The TPBVP of this interplanetary transfer problem is similar to the one based on the four-body problem, but with an additional parameter: the initial phase angle of the Moon $\theta_M(0)$ with respect to the X-axis of the inertial reference frame S_{XY}. Therefore, the TPBVP is enunciated as:

Problem 8 *"Given the terminal altitudes h_{LEO} and h_{LM_tO}, and, prescribing the phase angles $\theta_{EP}(0)$, $\theta_{M_t}(0)$, and $\theta_M(0)$, determine the set of variables (Δv_{LEO}, Δv_{LM_tO}, T), subject to the final constraints g_1, g_2 and g_3 defined by equations (36), (37) and (38), respectively."*

Note that an optimization problem of two-degree of freedom is also formulated as Problem 7 but with $\theta_M(0)$ as a prescribed parameter. Moreover, one can prescribe two of the three angles [$\theta_{EP}(0)$, $\theta_{M_t}(0)$, and $\theta_M(0)$] to solve an one-degree optimization problem; or, one can set $\theta_M(0)$ as also an unknown to be determined in a three-degree optimization problem enunciated as:

Problem 9 *"Given the terminal altitudes h_{LEO} and h_{LM_tO}, determine the set of variables ($\Delta v_{LEO}, \Delta v_{LM_tO}, T, \theta_{EP}(0)$, $\theta_{M_t}(0), \theta_M(0)$), that minimizes the function*

$$F: \quad \Delta v_{Total} = \Delta v_{LEO} + \Delta v_{LM_tO}, \tag{45}$$

subject to the final constraints g_1, g_2 and g_3 defined by equations (36), (37) and (38), respectively."

3. RESULTS

This section is divided in two topics. The first one presents results about interplanetary missions without a lunar swing-by maneuver. The second one presents interplanetary missions with an intermediary lunar swing-by maneuver. In the first part, a study is performed by solving TPBVPs by using the interplanetary patched-conic approximations and the model based on the PCR4BP. Next, the one and the two-degree of freedom optimization problems are solved in the context of the PCR4BP to determine the optimal trajectories. Penalties on the fuel consumption are quantified if the space vehicle does not depart specifically from the optimal geometry. In the second part, the trajectories determined by the patched-conic approximation are utilized as an initial guesses to solve the TPBVP (Problem 8) based on the PCR5BP. By using this last solution, the three-degree optimization problem is solved to determine the optimal interplanetary trajectories with a lunar swing-by maneuver in the context of the PCR5BP.

All the TPBVPs are solved by means of a Newton-Raphson algorithm (Press et al. 1997), and the optimization problems are solved by means of the Sequential Gradient Restoration Algorithm (Miele et al. 1969). The computational codes are implemented using FORTRAN 90.

3.1. *Interplanetary Missions Without Swing-by Maneuver*

This section studies interplanetary missions without a lunar swing-by maneuver. For this study, the patched-conic with detailed geometry, § 2.3, and the problem based on the four-body problem, § 2.5, are used. An inner transfer, Earth-Venus, and an outer transfer, Earth-Mars, are utilized to exemplify the results. The terminal altitudes are: $h_{LEO} = 463\,\text{km}$, $h_{M_tO} = 200\,\text{km}$ for Mars mission and $h_{LVO} = 200\,\text{km}$ for Venus mission. The eccentricities of the main body orbits are neglected as already discussed. The Earth-Moon mean distance is $D_M = 384400\,\text{km}$, the SOI radius of the Moon is 66300 km, and the mean motion of the Moon's orbit around Earth is $\omega_M = 2.6653 \times 10^{-6}\,\text{rad/s}$. The gravitational parameter of the Sun is $\mu_S = 1.327 \times 10^{11}$ (Miele and Wang 1999b). The data for Earth, Venus and Mars are presented in Table 2.

3.1.1. *Interplanetary Patched-Conic Approximations*

According to Problem 3, the TPBVP is solved by setting two parameters: $\theta_{EP}(0)$ and λ_{Mt} (or, λ_V for the Venus mission). However, solutions may not exist for some values of these parameters. With this in mind, the patched-conic approximation based on Hohmann transfer (§ 2.1) and the patched-conic approximation based on the Gauss problem (§ 2.2) help to glimpse solutions for Problem 3 providing values for $\theta_{EP}(0)$. Figures 4 and 5 plot the solutions of the main parameters: Δv_{LEO}, Δv_{LM_tO}, Δv_{Total}, T and $\theta_{M_t}(T)$ for Mars mission or $\theta_V(T)$ for the Venus mission against $\theta_{EP}(0)$ and λ_{Mt}. These figures are the solution of several TPBVPs, in which different sets of $\theta_{EP}(0)$ and λ_{Mt} are used. In this way, for each value of $\theta_{EP}(0)$, solutions are searched for λ_{Mt} within the interval $[0°, 180°]$ with a 1° step; and, solutions for λ_V within the interval $[0°, -180°]$ with a $-1°$ step. Observe that, according to the Hohmann transfer, the solutions for the Earth-Mars mission are to be found with an arrival ahead the SOI of Mars $\lambda_{Mt} \in [0°, 180°]$, and the solutions for the Earth-Venus mission are to be found with an arrival behind the SOI of Venus, $\lambda_V \in [-180°, 0°]$. For the parametrization of $\theta_{EP}(0)$, the interval is indirectly specified by the Gauss problem: for the Earth-Mars mission the time of flight in the Gauss problem is specified within the interval $[215, 265]$ days with a 1 day step. Then, the Gauss problem is solved by prescribing the time of flight and using the true anomaly as an unknown to minimize the fuel consumption (Problem 2). Therefore, there is a relation between the time of flight and $\theta_{EP}(0)$ given by the Gauss problem. The same procedure is performed for the Earth-Venus transfer in which the time of flight is specified within the interval $[70, 180]$ days. In order to illustrate only the practical results, Figures 4 and 5 show only results in which Δv_{Total} does not exceed 10 km/s. Both clockwise and counterclockwise arrivals are considered.

The model based on the interplanetary patched-conic approximation with detailed geometry also sets the motion direction at the final terminal orbit (LM_tO or LVO) which can be clockwise or counterclockwise. In terms of fuel consumption, the motion direction almost does not change the velocity increments for the Earth-Mars mission (Figures 4a–4c). In fact, the results of both direction are overlapping each other in these figures. The same occurs for the Earth-Venus mission (Figures 5a–5c). Moreover, the phase angles $\theta_{M_t}(T)$ and $\theta_V(T)$ (Figures 4e and 5e) and the time of flight (Figures 4d and 5d) do not change with respect to the arrival direction. For the Earth-Mars mission, the best set $(\theta_{EP}(0), \lambda_{Mt})$ for small fuel consumption impacts mainly on the reduction of Δv_{LM_tO}: while Δv_{LEO} can decrease

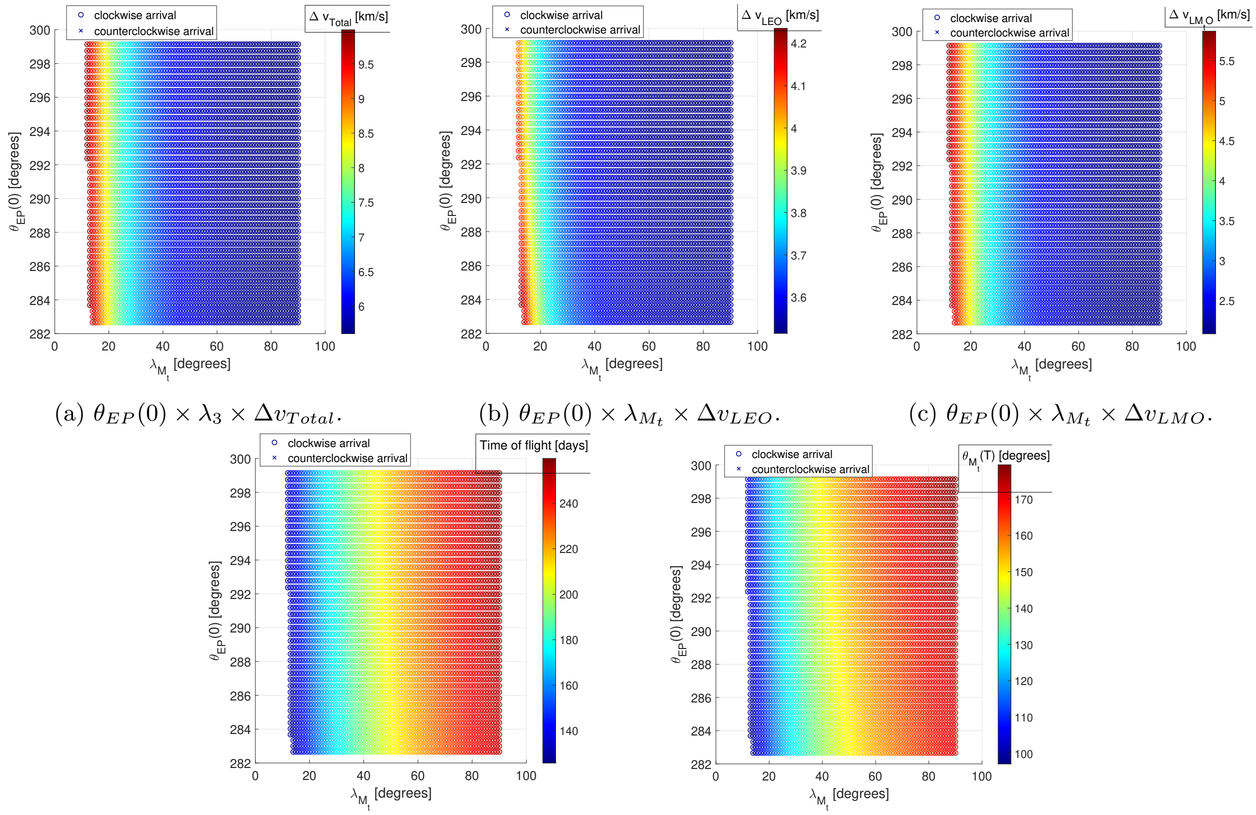

(a) $\theta_{EP}(0) \times \lambda_3 \times \Delta v_{Total}$.
(b) $\theta_{EP}(0) \times \lambda_{M_t} \times \Delta v_{LEO}$.
(c) $\theta_{EP}(0) \times \lambda_{M_t} \times \Delta v_{LMO}$.
(d) $\theta_{EP}(0) \times \lambda_{M_t} \times Time\ of\ flight$.
(e) $\theta_{EP}(0) \times \lambda_{M_t} \times \theta_{M_t}(T)$.

Fig. 4. Main parameters of the patched-conic approximation with detailed geometry. Earth-Mars mission. The color figure can be viewed online.

about 720.824 m/s (Figure 4b), Δv_{LM_tO} can decrease 3.779155 km/s (Figure 4c). As for the Earth-Venus mission the decreasing of fuel consumption is due to both velocity increments: while Δv_{LEO} can decrease to about 1.258184 km/s (Figure 5b), Δv_{LVO} can decrease to 2.769650 km/s (Figure 5c). The decreasing of fuel consumption is strongly related to the angle λ_{Mt} for the Earth-Mars mission or λ_V for the Earth-Venus mission. To illustrate this fact, observe in Figures 4a and 5a that Δv_{Total} has small changes for same values of λ_{Mt} or λ_V. This same remark is also true for the time of flight and for the final phase angle of the destiny planet $\theta_{EP}(T)$ or $\theta_V(T)$. By comparing Figure 4a with Figure 4d, and Figure 5a with Figure 5d, one can conclude that the solutions of minimum consumption correspond to the trajectories with larger time of flight for both Earth-Mars and Earth-Venus missions. The main parameters of the solutions with the smallest fuel consumption are highlighted in Tables 3 and 4, and, the trajectories are plotted in Figures 6 and 7, in which the rendezvous angles are also shown. For the Earth-Mars mission the rendezvous angle, $\theta_{M_t}(0)$, is positive, i.e, Mars is ahead the Earth at t_0; and for the Earth-Venus mission the rendezvous angle $\theta_V(0)$, is negative, which means that Venus is behind the Earth at t_0.

Note that for all the trajectories with the smallest fuel consumption, the arrival at the SOI of the destiny planet is nearly parallel to the orbital motion of the destiny planet around the Sun; thus, the angles λ_{Mt} and λ_V are about 90° for an ahead arrival or −90° for an arrival trajectory from behind. Therefore, these smallest fuel consumption trajectories present an heliocentric phase close to the Hohmann transfer. One can also classify the quadrant of the arrival trajectory in the SOI of the destiny planet as illuminated or non illuminated by the Sun. In this way, the smallest fuel consumption trajectories for the Earth-Mars mission with counterclockwise and clockwise arrival occur, respectively, in the illuminated quadrant and in the non-illuminated quadrant (see Figure 8). Both trajectories have the same fuel consumption and the same value of λ_{M_t} and they are very close to each other. The only difference is the phase angle that defines the arrival

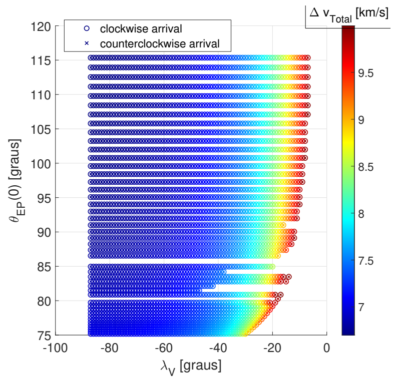

(a) $\theta_{EP}(0) \times \lambda_V \times \Delta v_{Total}$.

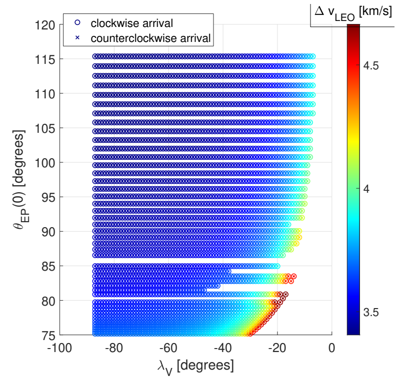

(b) $\theta_{EP}(0) \times \lambda_V \times \Delta v_{LEO}$.

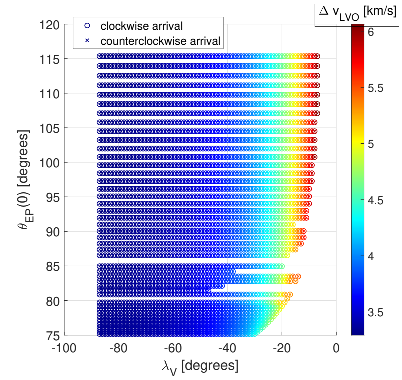

(c) $\theta_{EP}(0) \times \lambda_V \times \Delta v_{LVO}$.

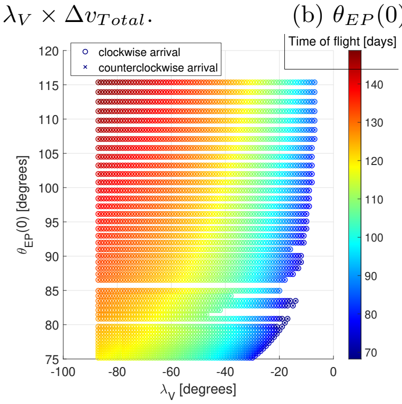

(d) $\theta_{EP}(0) \times \lambda_V \times Time\ of\ flight$.

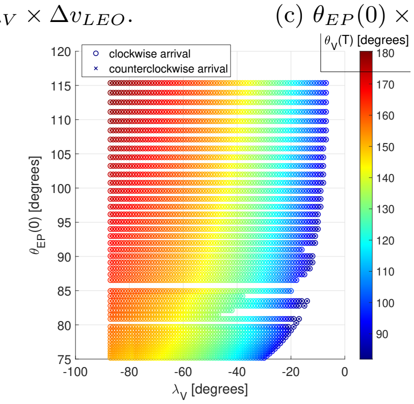

(e) $\theta_{EP}(0) \times \lambda_V \times \theta_V(T)$.

Fig. 5. Main parameters of the patched-conic approximation with detailed geometry. Earth-Venus mission. The color figure can be viewed online.

TABLE 3

MAIN PARAMETERS FOR THE SMALLEST FUEL CONSUMPTION TRAJECTORIES FOR EARTH-MARS MISSION

Model	Δv_{LEO} (km/s)	Δv_{LM_tO} (km/s)	Δv_{Total} (km/s)	Time of Flight (days)	$\theta_{M_t}(T)$ (degrees)	$\theta_{EP}(0)$ (degrees)
PCR4BP[1]	3.551905	2.100124	5.652029	257.861	179.075	298.382
Miele[2]	3.552000	2.100000	5.652000	257.880	179.020	298.150
Patched-conic based on Hohmann	3.555746	2.101260	5.657006	264.430	182.928	299.474
Patched-conic based on Gauss	3.555572	2.101454	5.657026	263.579	182.429	299.139
Patched-conic detailed geometry[3]	3.514668	2.087434	5.602101	257.965	179.353	297.573

[1] Results from a two degree-of-freedom optimization problem.

[2] Results based on the PR4CP calculated by Miele and Wang (1999b).

[3] Smallest fuel consumption trajectory found for $\lambda_{Mt} = 89°$ (arrival ahead the SOI).

at the LM_tO (see Figure 8b). For the Earth-Venus mission, the results are inverted: the smallest fuel consumption trajectories with counterclockwise and clockwise arrival occur, respectively, in the non illuminated quadrant and in the illuminated quadrant (see Figure 9). Both trajectories have the same fuel

TABLE 4

MAIN PARAMETERS FOR THE SMALLEST FUEL CONSUMPTION TRAJECTORIES FOR EARTH-VENUS MISSION

Model	Δv_{LEO} (km/s)	Δv_{LVO} (km/s)	Δv_{Total} (km/s)	Time of Flight (days)	$\theta_V(T)$ (degrees)	$\theta_{EP}(0)$ (degrees)
PCR4BP[1]	3.449138	3.337284	6.786422	139.628	173.795	105.084
Patched-conic based on Hohmann	3.447245	3.339810	6.787055	151.822	189.273	115.420
Patched-conic based on Gauss	3.447417	3.339550	6.786967	151.771	189.197	115.355
Patched-conic detailed geometry [2]	3.406312	3.294024	6.700336	147.976	183.519	113.934

[1] Results from a two degree-of-freedom optimization problem.

[2] Smallest fuel consumption trajectory found for $\lambda_V = -87°$ (arrival behind the SOI).

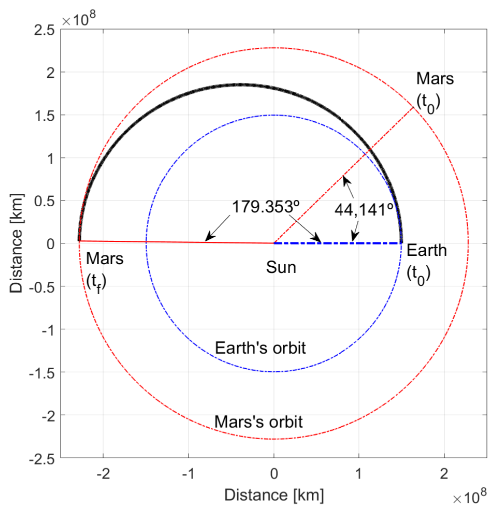

Fig. 6. Smallest fuel consumption trajectory for an Earth-Mars mission based on the patched-conic approximation. Arrival ahead the SOI of Mars. The color figure can be viewed online.

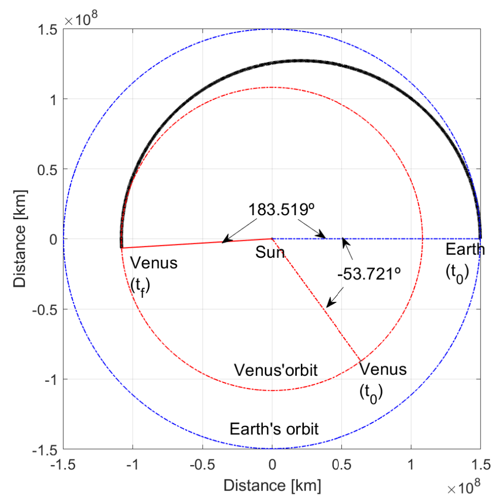

Fig. 7. Smallest fuel consumption trajectory for an Earth-Venus mission based on the patched-conic approximation. Arrival behind the SOI of Venus. The color figure can be viewed online.

consumption and the same value of λ_V. The only difference between them is the phase angle that defines the arrival at the LVO (see Figure 9b).

Therefore, in a real navigation problem for both Earth-Mars and Earth-Venus missions, one can define the direction of arrival at the final orbit when the space vehicle reaches the boundary of the SOI of the target planet because the clockwise and counterclockwise arrival trajectories are very close to each other.

Table 3 also shows the good agreement between the results for the smallest fuel consumption trajectory computed by: the patched-conic approximation; the optimal trajectory obtained by solving Problem 7 which is based on the PCR4BP; and the optimal results determined by Miele and Wang (1999b) for the Earth-Mars mission. Also, Tables 3 and 4 highlight the optimal results of the patched-conic based on the Gauss problem (Problem 2) and the results of the patched-conic based on the Hohmann transfer. For these last two models, the velocity increments are more compatible with the results provided by Miele and Wang (1999b) for the Earth-Mars mission (Table 3); however, a larger discrepancy occurs in the time of flight, which is 6 to 7 days longer than the one calculated by the PCR4BP. The detailed patched-conic approximation, on the other hand, presents

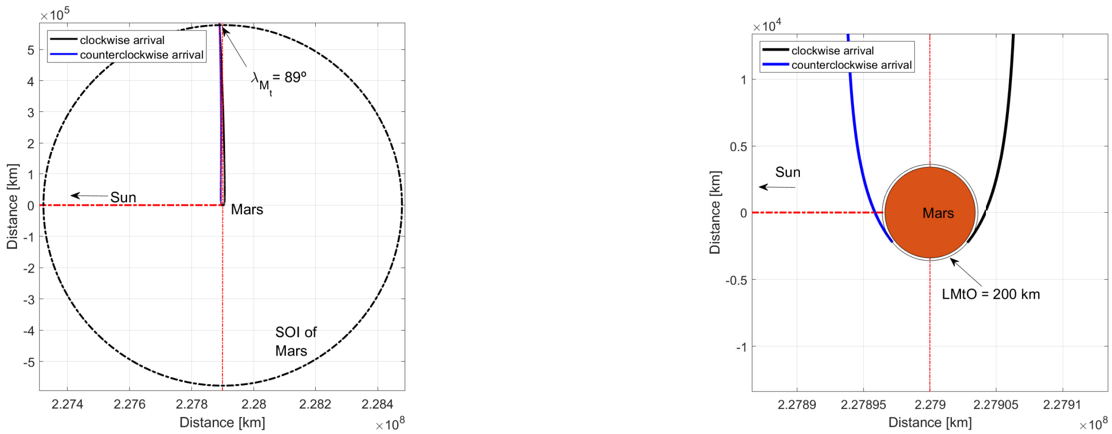

(a) Mars rotating reference frame.

(b) Zoom at the LM_tO.

Fig. 8. Smallest fuel consumption trajectories with clockwise and counterclockwise arrivals at the LM_tO. The color figure can be viewed online.

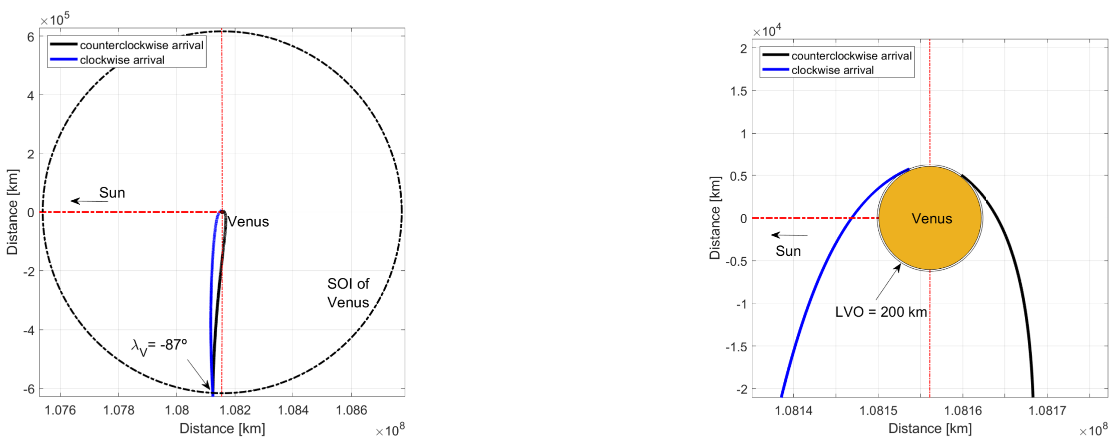

(a) Venus rotating reference frame.

(b) Zoom at the LVO.

Fig. 9. Smallest fuel consumption trajectories with clockwise and counterclockwise arrivals at the LVO. The color figure can be viewed online.

values of time of flight, final phase angle $\theta_{M_t}(T)$, and, initial phase angle $\theta_{EP}(0)$ closer to the values of the model based on the PCR4BP.

In the Venus mission, the discrepancy of the time of flight is even greater, reaching 12 to 13 days when one compares the patched-conic based on Gauss or based the Hohmann transfer with the model based on the PCR4BP. Similar to the Earth-Mars mission, the detailed patched-conic approximation for the Earth-Venus mission presents values of time of flight, final phase angle $\theta_V(t)$, and initial phase angle $\theta_{EP}(0)$ closer to the values of the model based on the PCR4BP.

Therefore, even though the patched-conic approximation with detailed geometry presents a fuel consumption slightly different from the other models, it presents more detailed and accurate geometric information than the other patched-conic approximations (based on Gauss and based on the Hohmann transfer) allowing the visualization of the complete trajectory without discontinuity and with a time of flight compatible with the trajectory based on the PCR4BP. Moreover, one can include swing-by maneuver in this patched-conic approximation, whose results are presented later in this work.

3.1.2. *Planar Circular Restricted Three-Body Problem*

By now, one can use this patched-conic approximation to provide initial guesses for Problem 5 based on the PCR4BP. In this way, Figures 10 and 11 plot the fuel consumption determined by

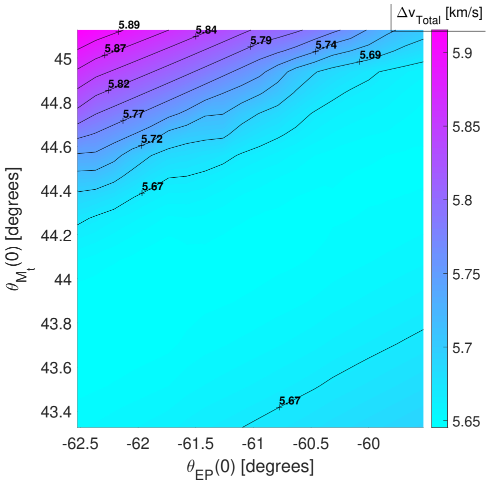

Fig. 10. Results of the TPBVP based on the PCR4BP for the Earth-Mars mission. The color figure can be viewed online.

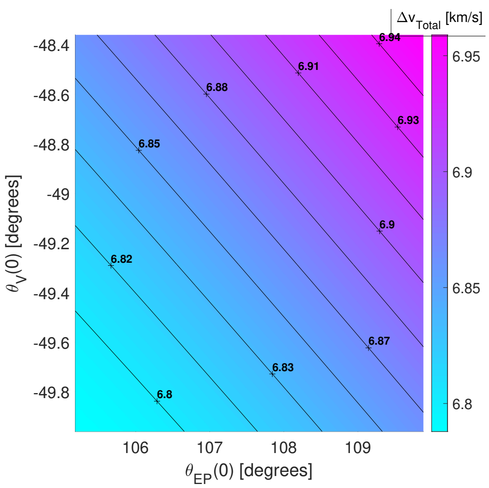

Fig. 11. Results of the TPBVP based on the PCR4BP for the Earth-Venus mission. The color figure can be viewed online.

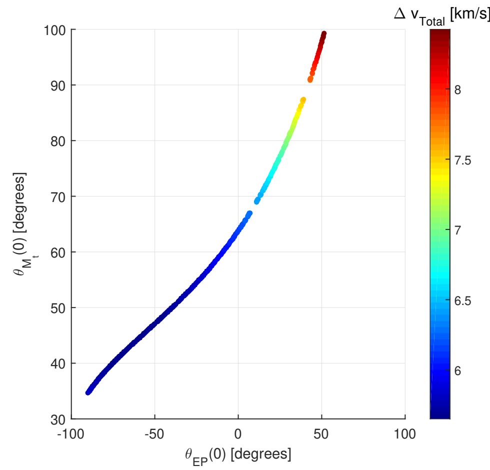

Fig. 12. Optimal curve $\theta_{EP}(0) \times \theta_{M_t}(0)$. Earth-Mars mission. The color figure can be viewed online.

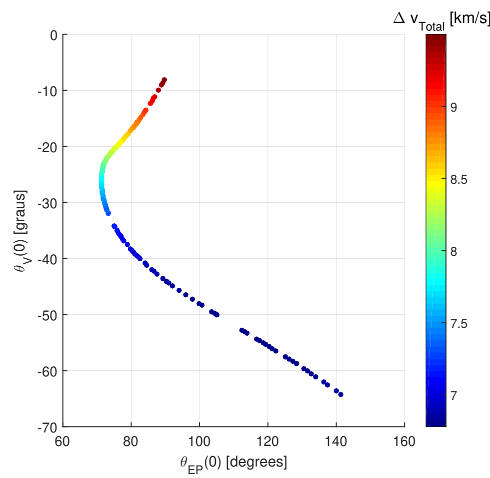

Fig. 13. Optimal curve $\theta_{EP}(0) \times \theta_{V_t}(0)$. Earth-Venus mission. The color figure can be viewed online.

the TPBVP (Problem 5) considering several sets of $\theta_{EP}(0), \theta_{M_t}(0)$, or $\theta_{EP}(0), \theta_V(0)$.

Figures 10 and 11 illustrate interpolated surfaces in which the results of Problem 5 are found, and, where one can observe that there is a minimum Δv_{Total} for each value of $\theta_{EP}(0)$. One can glimpse on Figures 10 and 11 that Δv_{Total} for the Earth-Venus mission is 1 km/s larger than the one of the Earth-Mars mission (see the color bars beside the figures). In order to determine the minimum consumption solutions in Figures 10 and 11, the one-degree optimization problem that prescribes $\theta_{M_t}(0)$, or $\theta_V(0)$, is solved (Problem 6). For this case, the results are shown in Figures 12 – 17.

Indeed, the rendezvous angles $\theta_{M_t}(0)$ and $\theta_V(0)$ have a huge influence on the fuel consumption. The proper choice of these angles can lead to a saving of fuel consumption of order of 3 km/s (or even greater) for both missions. Moreover, these angles define the initial phase angle of the space vehicle, $\theta_{EP}(0)$, and, consequently, the time of flight. Generally, for the Earth-Mars mission, the higher the angle $\theta_{M_t}(0)$, the higher the value of $\theta_{EP}(0)$ (Figure 12). The decreasing of $\theta_{EP}(0)$ is followed by the decreasing of the time of flight (Figure 14). Therefore, except for the trajectories with times of flight larger than 285 days approximately, the decreasing of the time of flight is followed by the decreasing of Δv_{Total}, which does not agree with the common sense that the time of flight must increase. On the other hand, for the Earth-Venus mission, the behavior of the parame-

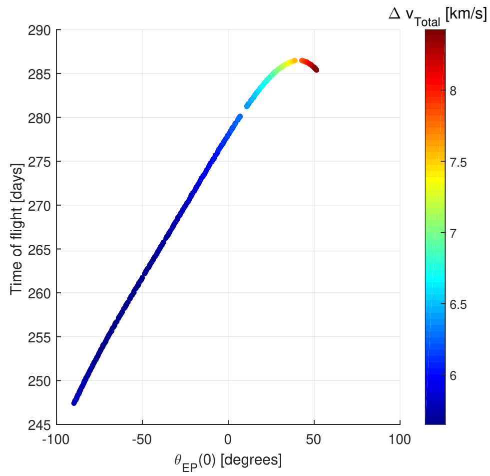

Fig. 14. Optimal curve $\theta_{EP}(0)\times$Time of flight. Earth-Mars mission. The color figure can be viewed online.

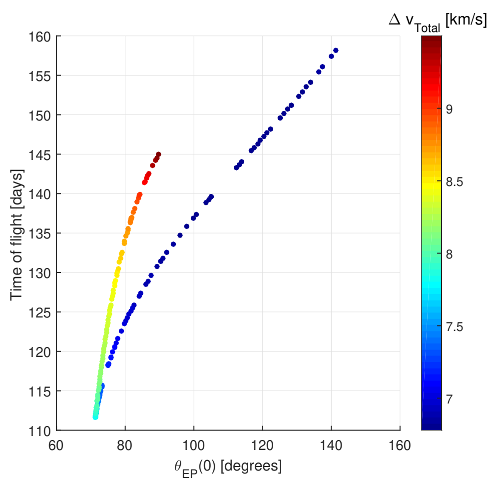

Fig. 15. Optimal curve $\theta_{EP}(0)\times$Time of flight. Earth-Venus mission. The color figure can be viewed online.

ters is inverted: the smaller the value of $\theta_V(0)$, the higher the angle $\theta_{EP}(0)$, for which Δv_{Total} is of order of 7 km/s (Figure 13). The increasing of $\theta_{EP}(0)$ is followed by an increasing of the time of flight (Figure 15), i.e, the decreasing of Δv_{Total} is achieved with an increasing of the time of flight, which agrees with common sense. A remark is necessary for the Earth-Venus trajectories that present larger Δv_{Total} (close to 8 km/s): for Δv_{Total} larger than 8 km/s, the trajectories obtained have increasing times of flight, reaching 145 days (Figure 15) with $\theta_V(0)$ increasing approximately until near $-10°$. This remark is better visualized in Figure 17, where an inversion of the curve behavior is observed for Δv_{Total}. All these behaviors are due to the two possibilities of solutions with approximately the same time of flight but with different fuel consumption. Figures 18 and 19 are an

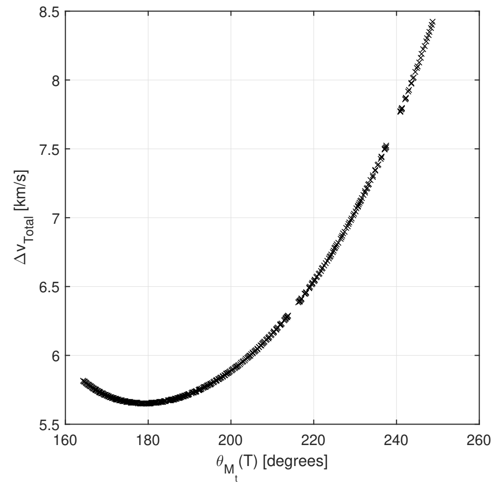

Fig. 16. Optimal curve $\theta_{M_t}(T)\times\Delta v_{Total}$. Earth-Mars mission. The color figure can be viewed online.

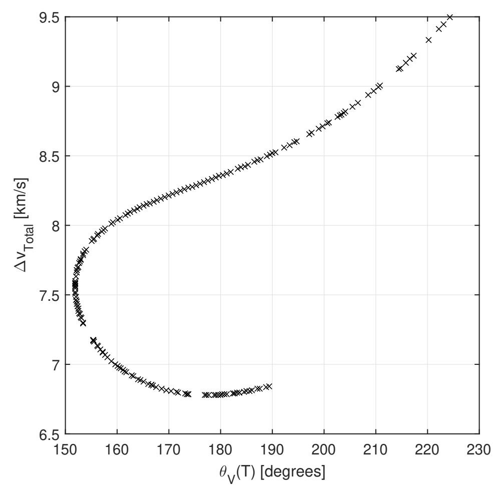

Fig. 17. Optimal curve $\theta_V(T)\times\Delta v_{Total}$. Earth-Venus mission.

example of these two possibility of trajectories: the trajectory in Figure 18 has a Δv_{Total} 2.218063 km/s larger than the one of Figure 19, but both present a time of flight of 139 days. Observe that the minimum fuel consumption trajectory of Earth-Venus mission has a value of $\theta_V(T)$ between 170° and 180° (Figure 17), and it is not the solution of minimum time, which is the singular point of the curve in Figure 15. This singular point (minimum time) makes the convergence of the two-degree of freedom optimization problem harder for the Earth-Venus mission because the numerical derivative expressions become sensitive. For the Earth-Mars, on the contrary, there is no singular point as the curve is well behaved in Figure 14. Moreover, the best optimal values of $\theta_{M_t}(T)$ and $\theta_V(T)$ are close to 180° (Figures 16 and 17).

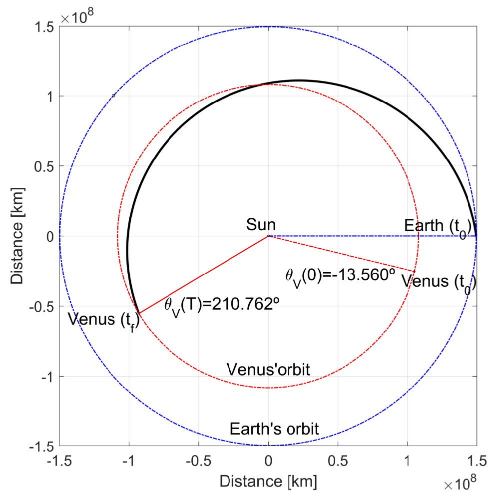

Fig. 18. Earth-Venus mission. Time of flight = 139.917 days, $\Delta v_{Total} = 9.004485$ km/s. The color figure can be viewed online.

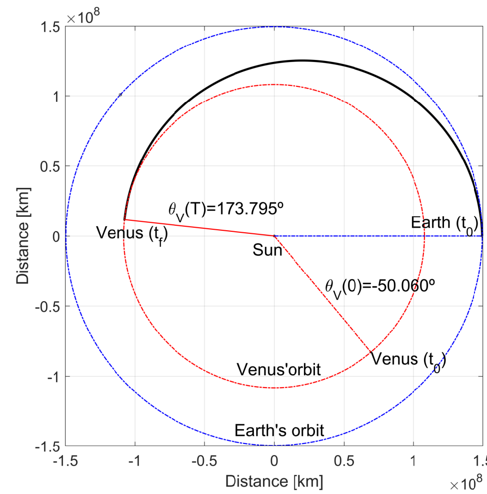

Fig. 19. Earth-Venus mission. Time of flight = 139.628 days, $\Delta v_{Total} = 6.786422$ km/s. The color figure can be viewed online.

In order to determine the best optimal initial phase angle of the destiny planet with higher accuracy, one can use the two-degree optimization problem (Problem 7) whose results have already been presented in Tables 3 and 4.

Note in Figure 6 that the value of the initial phase angle for the outer transfer means that the destiny planet is ahead of Earth ($\theta_{M_t}(0) > 0°$) with the initial position of the space vehicle underneath the line Sun-Earth ($180° < \theta_{EP}(0) < 360°$, Table 3). On the other hand, at the initial time of the inner transfer, the destiny planet is behind the Earth ($\theta_V(0) < 0°$), Figure 7, and the space vehicle is above the Sun-Earth line ($0° < \theta_{EP}(0) < 180°$, Table 4) for the minimum consumption trajectory.

The result of Problem 7 (based on the PCR4BP) for the Earth-Mars mission (Table 3) practically coincides with the result found by Miele and Wang (1999b), and it presents the optimal Δv_{Total} of nearly 50 m/s larger than the one of the patched-conic with detailed geometry. Despite this difference, the trajectories of these models are practically the same (Figure 20). The Mars rotating frame depicted in Figure 20d is a Sun centered reference frame with the X-axis pointing towards Mars at all times; thus, it rotates following the motion of Mars. For the Earth-Venus trajectory (Table 4), the optimal Δv_{Total} determined by Problem 7 (based on the PCR4BP) practically coincides with the one computed by the patched-conic approximation based on Hohmann and based on Gauss; however, the times of flight differ by nearly 12 days. By comparing the results of Problem 7 with the patched-conic with the detailed geometry, the difference in Δv_{Total} is about 86 m/s and the difference in time of flight is about 8.35 days with patched-conic approximation presenting the smaller fuel consumption and the larger time of flight for the Earth-Venus mission. This difference of results changes a little the shape of the trajectory as shown in Figure 21. The Venus rotating frame depicted in Figure 21d is a Sun centered reference frame with the X-axis pointing towards Venus at all time; thus, it rotates following the motion of Venus. For the Earth-Mars mission, however, the trajectories of both models coincide. The larger difference between the shapes of trajectories of the Earth-Venus mission occurs because this transfer problem is more sensitive as the orbital velocity of the target planet Venus is greater than the orbital velocity of the target planet Mars.

3.1.3. *Penalty on Fuel Consumption*

For more realistic models, in which one uses the ephemeris of the celestial bodies, it is not possible to find the proper geometrical set of the bodies in a given epoch that corresponds to the geometrical set of minimum fuel consumption determined by Problem 7 (two-degree of freedom optimization problem based on the PCR4BP). In this case, one can perform a correspondence of the geometrical set given by the ephemeris with a geometrical set determined by Problem 6 (one-degree of freedom optimization problem) by adjusting the initial phase angle of the destiny planet (rendezvous angle) in this last Problem. In this way, a penalty in the fuel consumption can be determined due to the deviations from the geometrical set determined by the two-degree of freedom

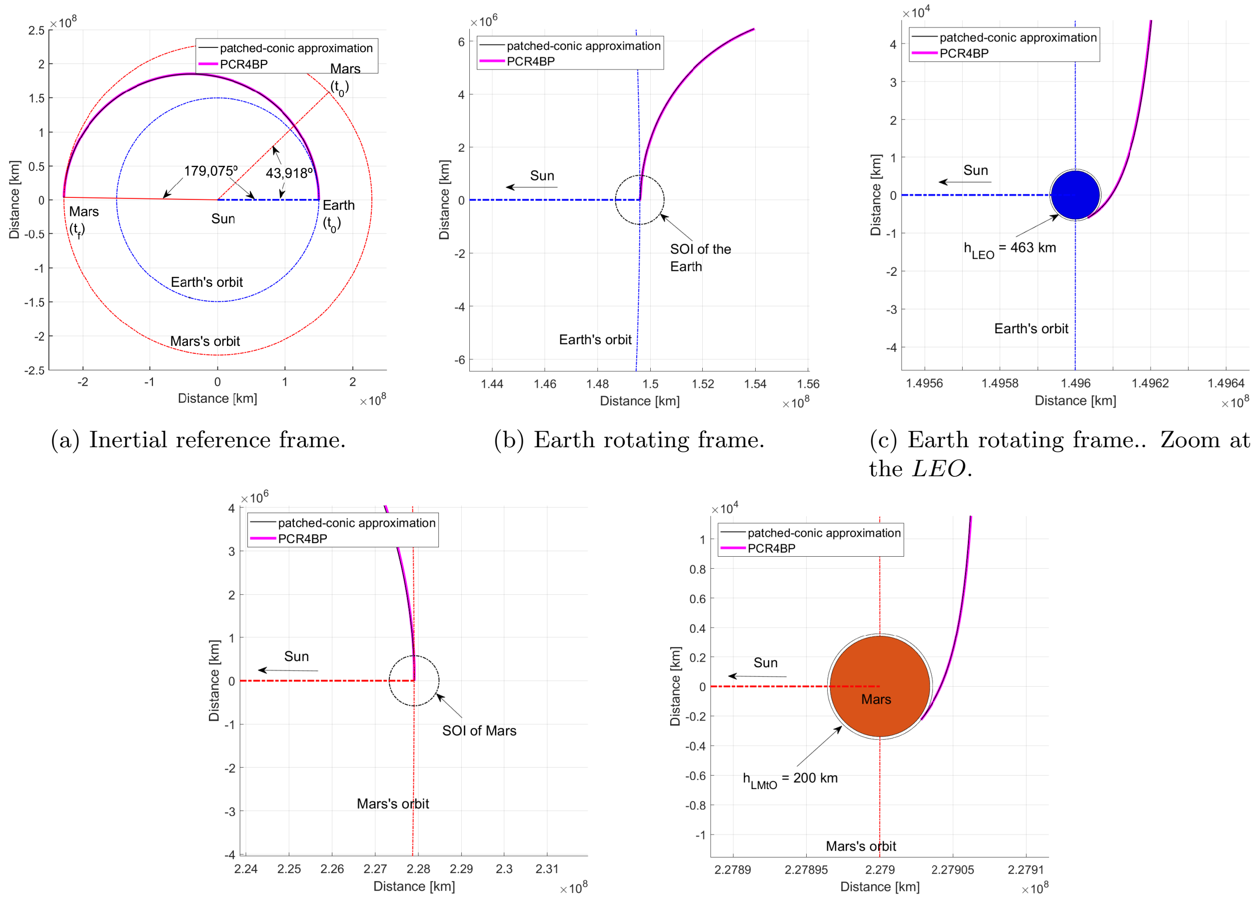

(a) Inertial reference frame.

(b) Earth rotating frame.

(c) Earth rotating frame.. Zoom at the LEO.

(d) Mars rotating frame.

(e) Mars rotating frame. Zoom at LM_tO.

Fig. 20. Optimal Earth-Mars trajectory. Phase angles are computed by PCR4BP. The color figure can be viewed online.

TABLE 5

PENALTY IN THE MAIN PARAMETERS DUE TO EARLY AND DELAYED DEPARTURES. EARTH-MARS MISSION

$\theta_{M_t}(0) - \theta_{M_t}(0)^*$	$(-)9.0°$	$\theta_{M_t}(0)^* = 43.918°$	$(+)15.0°$	$(+)30.0°$	$(+)40.0°$
Δv_{LEO} (km/s)	(+)0.123037	3.551905	(+)0.240781	(+)0.800470	(+)1.306203
Δv_{LM_tO} (km/s)	(+)0.036667	2.100124	(+)0.058534	(+)0.200583	(+)0.340452
Δv_{Total} (km/s)	(+)0.159705	5.652029	(+)0.299315	(+)1.001053	(+)1.646655
Time (*days*)	(-)10.417	257.861	(+)16.377	(+)25.752	(+)28.356
$\theta_{EP}(0)$ (*degrees*)	(-)28.055	298.382	(+)49.801	(+)81.454	(+)96.600

optimization problem. Figures 22a and 22b show the penalty in Δv_{Total}, respectively, for the Earth-Mars and Earth-Venus missions, when the rendezvous angle does not agree with its optimal value, denoted by the subscript $*$. The resulting change in the time of flight due to this advance or delay of the rendezvous angle is shown in Figures 22c and 22d, and the launch window, which is defined by the variation of $\theta_{EP}(0)$, is visualized in Figures 22e and 22f. Note that the curves highlighted by Figure 22 are the results of the one-degree of freedom optimization problem (Problem 6). Tables 5 and 6 exemplify some points of Figure 22 to better quantify the penalty on the parameters due to advance or delay of the ren-

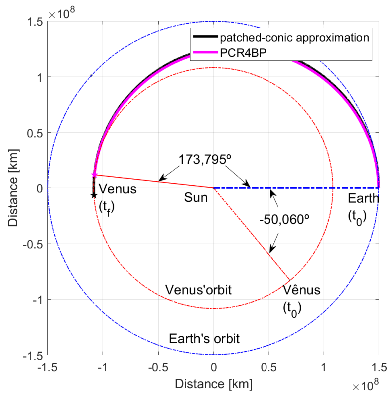

(a) Inertial reference frame.

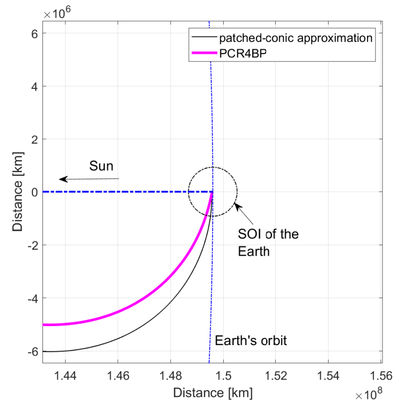

(b) Earth rotating frame.

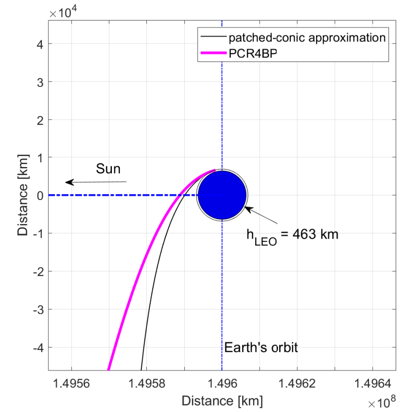

(c) Earth rotating frame.. Zoom at the *LEO*.

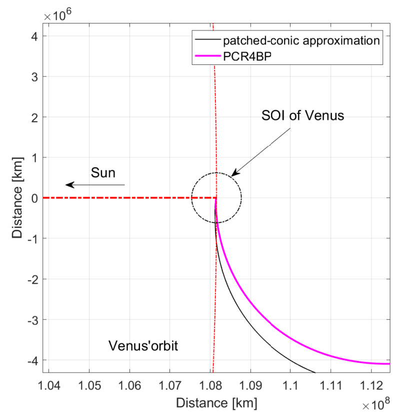

(d) Venus rotating frame.

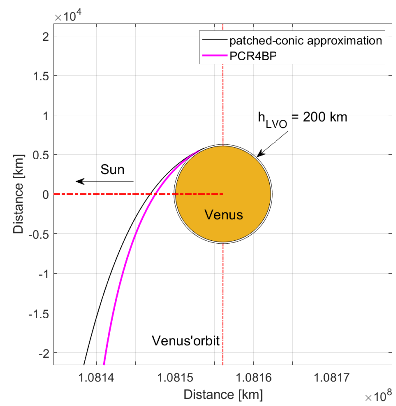

(e) Venus rotating frame. Zoom at LM_tO.

Fig. 21. Optimal Earth-Venus trajectory. Phase angles are computed by PCR4BP. The color figure can be viewed online.

TABLE 6

PENALTY IN THE MAIN PARAMETERS DUE TO EARLY AND DELAYED DEPARTURES. EARTH-VENUS MISSION

$\theta_V(0) - \theta_V(0)^*$	$(-)9.0°$	$\theta_V(0)^* = -50.060°$	$(+)15.0°$	$(+)30.0°$	$(+)40.0°$
Δv_{LEO} (km/s)	(+)0.013842	3.449138	(+)0.278435	(+)0.752205	(+)0.643154
Δv_{LVO} (km/s)	(+)0.002513	3.337284	(+)0.063947	(+)0.835651	(+)1.901170
Δv_{Total} (km/s)	(+)0.016355	6.786422	(+)0.342381	(+)1.587856	(+)2.544324
Time (*days*)	(+)12.731	139.628	(-)20.312	(-)14.062	(+)3.935
$\theta_{EP}(0)$ (*degrees*)	(+)25.454	105.084	(-)29.212	(-)29.382	(-)17.101

dezvous phase angle. The following comments are noted for these results:

1. Positive values of $\theta_{M_t}(0) - \theta^*_{M_t}(0)$, which are denoted by (+) for the Earth-Mars mission indicate early departures of the space vehicle from the LEO, while negative values, which are denoted by (-), indicate delayed departures. For the Earth-Venus mission, positive values of $\theta_V(0) - \theta^*_V(0)$ indicate delayed departures, and negative values indicate early departures.

2. Both delayed and early departures in both missions increase the fuel consumption: an early departure corresponding to a change in the rendezvous angle of 40° in the Earth-Mars mission increases Δv_{Total} in 1.646566 km/s (Ta-

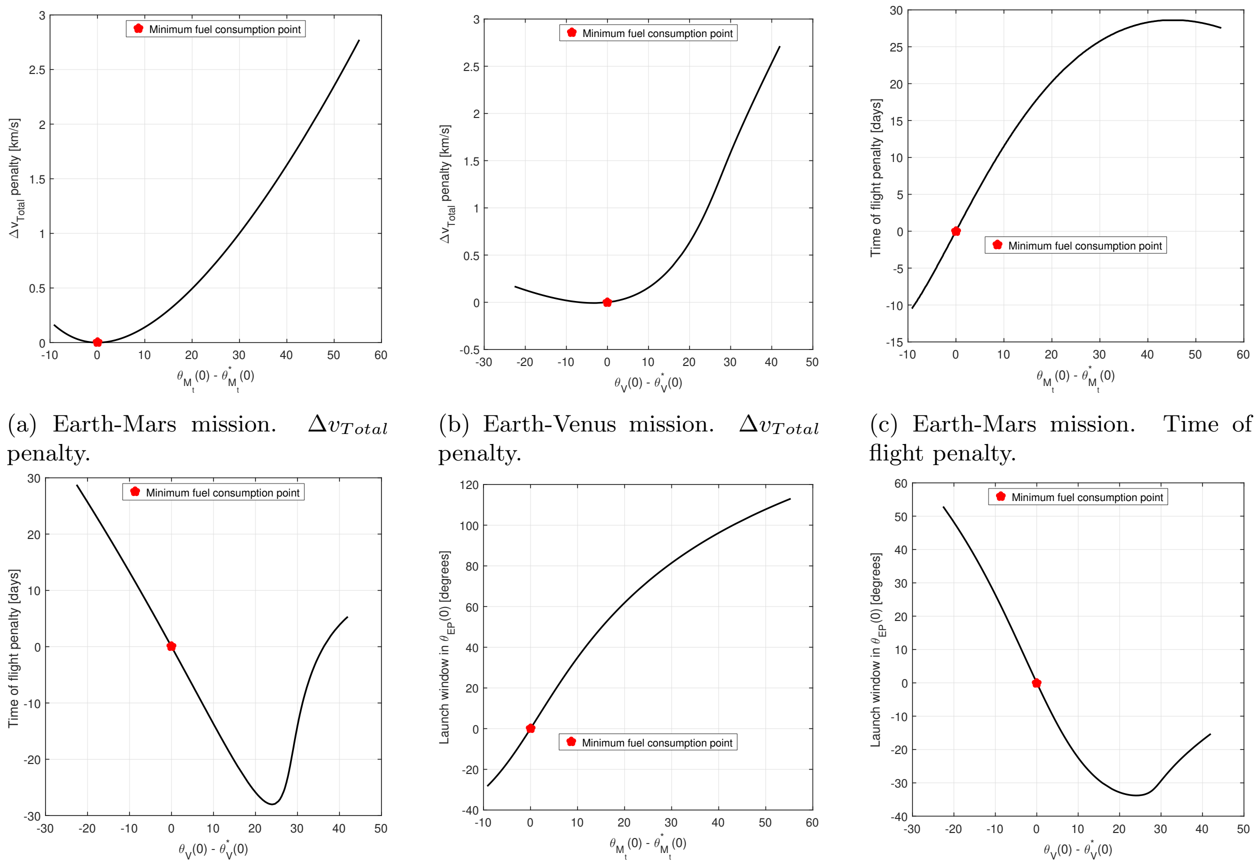

(a) Earth-Mars mission. Δv_{Total} penalty.

(b) Earth-Venus mission. Δv_{Total} penalty.

(c) Earth-Mars mission. Time of flight penalty.

(d) Earth-Venus mission. Time of flight penalty.

(e) Earth-Mars mission. $\theta_{EP}(0)$ penalty.

(f) Earth-Venus mission. $\theta_{EP}(0)$ penalty.

Fig. 22. Penalty in the main parameters with respect to minimum fuel consumption trajectory (Problem 7). The color figure can be viewed online.

ble 5), while a delayed departure corresponding to the same value of the rendezvous angle in the Earth-Venus mission increases Δv_{Total} by 2.544324 km/s (Table 6). The increase in Δv_{Total} is an effect of the increase of both velocity increments Δv_{LEO} and Δv_{LM_tO} or Δv_{LVO} (Tabs. 5 and 6). For the Earth-Venus mission (Table 6), there is a slight decrease of Δv_{LEO} between the delayed departures corresponding to a variation of the rendezvous angle of 30° and 40°; however, Δv_{LVO} more than doubles its value culminating in an significant increase of Δv_{Total}.

3. The early departures for the Earth-Mars mission $(\theta_{M_t}(0) - \theta^*_{M_t}(0) > 0)$ and for the Earth-Venus mission $(\theta_V(0) - \theta^*_V(0) < 0)$ increase the time of flight (see Figures 22c and 22d). For example, the early departure corresponding to a variation of the rendezvous angle of 15° for the Earth-Mars mission increases the time of flight by 16.377 days with a penalty on Δv_{total} of 299.315 m/s (Table 5); and the delayed departure corresponding to a variation of the rendezvous angle of $-9°$ for the Earth-Venus mission increases the time of flight by 12.731 days with a penalty on Δv_{total} of 16.355 m/s (Table 6).

4. Delaying the departure for both Earth-Mars and Earth-Venus mission decreases the time of flight; however, there is a delayed departure that minimizes the time of flight in the Earth-Venus mission. Observe in Table 6 that a delayed departure corresponding to a variation of the rendezvous angle of 15° for the Earth-Venus mission decreases the time of flight by 20.312 days with a penalty on Δv_{total} of 342.381 m/s, while a delayed departure of 40° for the same mission increases the time of flight by 3.935 days, with a penalty on Δv_{total} of 2544.324 m/s, which shows that there is a minimum time of flight.

5. The launch window, which is defined by the change in $\theta_{EP}(0)$, is larger for the Earth-Mars mission: assuming a variation of the rendezvous angles within the interval of $-10°$ and $40°$, the launch window for the Earth-Mars mission is, approximately, between $-30°$ and $100°$ (angular range of $130°$). On the other hand, for the Earth-Venus mission, the launch window is defined between $-35°$ and $25°$ (angular range of $60°$) for the same variation of the rendezvous angle. As an example, the early departure of the space vehicle corresponding to a variation of the rendezvous angle of $30°$ increases $\theta_{EP}(0)$ by $81.454°$ (Table 5) for the Earth-Mars mission and decreases $\theta_{EP}(0)$ by only $29.382°$ (Table 6) for the Earth-Venus mission.

In general, by observing Figures 22, delayed and early departures increase the fuel consumption (Figures 22a and 22b) in both missions; however, the minimum fuel consumption solution for the Earth-Venus mission lies on a flatter region of the Δv_{Total} penalty curve (Figure 22b) than the one for the Earth-Mars mission (Figure 22a) making the optimization algorithm convergence harder. The minimum fuel consumption solution for both missions does not correspond to the maximum or minimum time of flight solution (Figure 22c and Figure 22d); moreover, the Earth-Mars mission presents a maximum time of flight solution (Figure 22c) in contrast to the Earth-Venus mission, which presents a minimum time of flight solution (Figure 22d). Finally, the launch window is larger for the Earth-Venus mission, as already discussed (Figure 22e and Figure 22f).

The penalty on the main parameters for the Earth-Mars mission was also observed by Miele and Wang (1999b); part of their results are given in Table 7. A good agreement is observed between the results of Table 5 and the ones of Table 7. This fact is better observed in the columns with $\theta_{M_t}(0) - \theta^*_{M_t}(0) > 0$; the values practically coincide.

The next section studies the possibility of saving fuel consumption without increasing significantly the time of flight for both missions, Earth-Mars and Earth-Venus, by including a lunar swing-by maneuver.

3.2. *Interplanetary Missions with Swing-by Maneuver*

Firstly, this section studies the solutions of interplanetary trajectories for Earth-Mars and Earth-Venus missions by solving only the TPBVPs with a lunar swing-by maneuver (Problems 4 and 8). Next, the optimal solutions of the three-degree of freedom optimization problem (Problem 9) are presented.

3.2.1. *Non-Optimal Solutions*

Tables 8 and 9 compare the interplanetary trajectories for Earth-Mars and Earth-Venus missions with lunar swing-by maneuvers. The results of the patched-conic approximation with detailed geometry (Problem 4) that includes a lunar swing-by maneuver, Table 8, have already explained by Gagg Filho and da Silva Fernandes (2018). These results are used as initial guess to solve the TPBVP defined by Problem 8 in the context of the PCR5BP, which is highlighted in Table 9. In this last model, the gravitational attraction of the Moon is neglected during the interplanetary and planetocentric phases. If the initial condition for Problem 8 is accurate enough, the lunar swing-by maneuver will occur naturally during the integration of the equations of motion (equations 41 and 42).

By comparing both models that include the lunar swing-by maneuver, i.e., the patched-conic approximation and the PCR5BP, a difference is observed between the results of Table 8 and Table 9: the patched-conic approximation presents a fuel consumption, Δv_{Total}, distinct from the one of the PCR5BP. For the Earth-Venus mission, for instance, the trajectory based on the patched-conic approximation has Δv_{Total} about 224.373 m/s smaller than the one of the trajectory based on the PCR5BP. This difference between models has been already observed for the interplanetary missions without swing-by maneuvers (Table 4), where this difference reaches 86.086 m/s. This discrepancy between the models is also observed for the Earth-Mars mission with lunar swing-by: the trajectory based on the patched-conic approximation presents a Δv_{Total} about 121.718 m/s smaller than the one of the trajectory based on the PCR5BP. For the Earth-Mars mission without swing-by maneuver, this difference is 50 m/s (Table 3).

In the context of the patched-conic approximation, the Earth-Mars mission with a lunar swing-by (Table 8) shows a saving of fuel consumption of 153 m/s with approximately the same time of flight as the one of the patched-conic without lunar swing-by maneuver; and the Earth-Venus mission presents a saving of fuel consumption of 33.21 m/s with a time of flight only 1.5 days larger than the one of the patched-conic without lunar swing-by maneuver. The results in the context of the PCR5BP only reinforce these remarks: the Earth-Mars mission with lunar swing-by shows a saving of fuel consumption

TABLE 7

PENALTY IN THE MAIN PARAMETERS DUE TO EARLY AND DELAYED DEPARTURES (MIELE & WANG 1999b). EARTH-MARS MISSION

$\theta_{M_t}(0) - \theta_{M_t}(0)^*$	$(-)14.86°$	$\theta_{M_t}(0)^* = 43.860°$	$(+)15.14°$	$(+)30.14°$
Δv_{LEO} (km/s)	(+)0.341	3.552	(+)0.240	(+)0.803
Δv_{LM_tO} (km/s)	(+)0.127	2.100	(+)0.058	(+)0.201
Δv_{Total} (km/s)	(+)0.468	5.652	(+)0.298	(+)1.004
Time (*days*)	(-)13.29	257.88	(+)16.48	(+)25.74
$\theta_{EP}(0)$ (*degrees*)	(-)37.73	298.15	(+)49.97	(+)81.80

TABLE 8

MINIMUM FUEL CONSUMPTION SOLUTION*

Parameter	Earth-Mars	Earth-Venus
Δv_{LEO} (km/s)	3.362211	3.376566
Δv_{LMtO} or Δv_{LVO} (km/s)	2.086891	3.289849
Δv_{Total} (km/s)	5.449101	6.666415
Time of flight (days)	257.443	149.440
$\theta_E(0)$ (degrees)	-46.188	86.040
Rendezvous angle (degrees)	43.368	-56.269
$\theta_{M_t}(T)$ or $\theta_V(T)$ (degrees)	132.079	269.358
h_{sP} (km)	1400.0	9100.0
$\theta_{EP}(0)$ (degrees)	-141.035	-151.321
λ_1 (degrees)	-17.0	4.0
λ_S (degrees)	91.845	90.170
λ_{M_t} or λ_V	90.0	-90.0

*Patched-conic approximation with a lunar swing-by maneuver.

of 81.21 m/s with a time of flight only 0.418 days smaller than the mission without lunar swing-by maneuver (PCR4BP); and the Earth-Venus mission with lunar swing-by presents a fuel consumption of 104.366 m/s smaller than the one without swing-by maneuver (PCR4BP) with a time of flight only 1.931 days larger than the mission without lunar swing-by maneuver.

This comparison using Table (8) and Table (9) is limited because, even considering different models, they do not shown exactly the same trajectory. The only correspondence between Tables (8) and Table (9) is that the result of trajectory of Table (8) is used to glimpse an initial guess to solve the TPBVP (Problem 8), whose solutions are presented in Table (9). During the convergence of the algorithm that solves this TPBVP, the solution can move away from the initial guess. A better comparison can be made if an optimization problem is solved considering both models; however, the intention of this paper is to illustrate that the patched-conic approximation with lunar swing-by maneuver can be well utilized as an initial guess for the model based on the PCR5BP. Since the objective of this paper is also to study the saving of fuel consumption due to the lunar swing-by maneuver on interplanetary missions, and, considering that there is a potential of saving fuel consumption as illustrated in Table (9), the optimization problem with a three-degree of freedom is conducted to obtain more solid conclusions.

Figures 23 and 24 plot the trajectories described by Tables 8 and 9. Since the trajectories based on the PCR5BP are obtained by solving Problem 8, there is no intermediary constraint that defines the swing-by maneuver, which appears naturally from the integration of the equations of motion. Due to this absence of an intermediary constraint on the PCR5BP and due to the dynamic difference of the models, the swing-by maneuver can be changed by the Newton-Raphson method in order to converge. In other words, since there is no intermediary constraint prescribing the lunar swing-by maneuver, the Newton-Raphson method does not take into consideration what happens during the trajectory as long as the final constraints are satisfied, so the occurrence of the lunar swing-by maneuver on the PCR5BP essentially depends on the initial guess that defines the departure at the LEO.

This fact is better visualized on the Earth-Venus mission, Figure 23e, where the space vehicle performs a lunar swing-by maneuver in the context of the PCR5BP with a periselenium altitude smaller than the one of the patched-conic approximation. On the other hand, for the Earth-Mars mission, the initial guess for solving Problem 8 is so accurate that the periselenium altitude of the lunar swing-by maneuver based on the PCR5BP practically coincides with the prescribed altitude of the patched-conic approximation (Figure 24e); however, an overview of the complete trajectory (Figure 23a and Figure 23b), departure geometry (Figure 23c), and arrival geometry (Figure 23d) reveal that the shapes of the tra-

TABLE 9

SOLUTION FOR INTERPLANETARY MISSIONS*

Parameters	Earth-Mars	Earth-Venus
Δv_{LEO} (km/s)	3.469766	3.426035
Δv_{LMtO} or Δv_{LVO} (km/s)	2.101053	3.464753
Δv_{Total} (km/s)	5.570819	6.890788
Time of flight (days)	257.443	142.697
$\theta_E(0)$ (degrees)	0.0	0.0
Rendezvous angles (degrees)	41.605566	-42.836
$\theta_{M_t}(T)$ or $\theta_V(T)$ (degrees)	176.544391	185.939
$\theta_{EP}(0)$ (degrees)	-88.194	76.505
$\theta_M(0)$ (degrees)	43.940	209.472

*With lunar swing-by maneuver in the context of the PCR5BP.

jectories are different. A disagreement between the trajectories of different models is also observed for the Earth-Venus mission (Figure 24). Indeed, these differences are already expected, as explained before by Tables 8 and 9. For both missions, the visualization of trajectories in the inertial reference frame centered at the Sun of both models must be done in distinct figures since the x-axis of the inertial reference frame is not the same: the x-axis of the inertial reference frame used in context of the PCR5BP (Figure 23b and Figure 24b) is the Sun-Earth direction at $t = t_0$; on the other hand, the x-axis of the inertial reference frame used for the patched-conic approximation with lunar swing-by (Figure 23a and Figure 24a) is parallel to the direction Earth-Moon at $t = t_0$. Therefore, the comparison of the trajectories is performed by considering the relative positions of the bodies and rotating reference frames. In order to help this comparison, Figures 23a, 23b, 24a, and 24b highlight the rendezvous angles and the angles that define the arc of the complete trajectory. In Figures 23e and 24e, the comparison of trajectories is straightforward since both are shown in the Moon rotating reference frame. This reference frame is centered on Earth with the X-axis pointing towards the Moon at all time, so that it rotates following the orbital motion of the Moon around Earth; and the Y-axis is orthogonal to the X-axis in the plane of motion of the bodies. In these last figures, the changing from the inertial reference frame centered on the Sun (Figures 23a, 24a) to the Moon rotating reference frame centered on the Earth (Figures 23e, 24e) amplifies the characterization of the phases of the patched-conic approximation, in a way that sharper corners are observed.

3.2.2. *Optimal Solutions: The Three-Degree of Freedom Optimization Problem*

In order to obtain better conclusions about the fuel consumption and the time of flight for the Earth-Mars and Earth-Venus missions with an intermediary lunar swing-by maneuver, the three-degree of freedom optimization problem (Problem 9) is solved in the context of the PCR5BP, in which the parameters $\theta_{EP}(0)$, $\theta_{M_t}(0)$, and $\theta_M(0)$ are set as unknown to solve the problem.

As mentioned, all the optimization problems in this work are solved by means of the Sequential-Gradient Restoration Algorithm (SGRA) (Miele et al. 1969) for constrained functions. In this section, this algorithm is initialized using a solution of the TPBVP defined by Problem 8; the results are presented in Table 9. The first step of the SGRA is the gradient phase, i.e, an perturbation is induced in the initial point, given by the initial guess, in the direction opposite to the gradient of the function to be minimized, i.e., in the direction to decrease the fuel consumption to obtain a new point. After, this first gradient phase, a restoration phase is performed in order to restore this new point to satisfy the constraints. The gradient and restoration are applied sequentially until the tolerance of the function to be minimized is achieved. Therefore, after each restoration phase there is a solution of the TPBVP with decreasing fuel consumption. Figures 25 and 27 show the solution after each restoration phase for Earth-Mars and Earth-Venus, respectively.

Since there is no constraint that specifies the periselenium altitude, the SGRA eventually can determine trajectory solutions in which the space vehicle collides with the Moon. Thus, the solutions with decreasing fuel consumption in Figures 25 and 27 are classified as trajectories that collide and trajectories that do not collide with the Moon. For the Earth-Mars mission, the first solutions of the SGRA do not collide with the Moon (Figure 25). As the fuel consumption decreases, the solutions collide until they reach the minimum fuel consumption at 5.352415 km/s, a decrease of 218.404 m/s. The initial phase angle of the Moon decreases by about 46.008° (Figure 25a), the rendezvous angle increases about 4.515° (Figure 25c), and the initial phase angle of the space vehicle decreases about 48.743° (Figure 25d). The time of flight, however, almost does not change during the optimization algorithm, staying at 257.443 days (Figure 25b). In a practical way, the interesting solution is the one that does not collide with the Moon, which is indicated by the red arrow in Figure 25; results are highlighted in Ta-

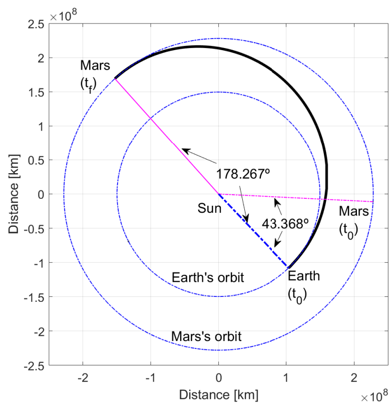

(a) Inertial reference frame. Patched-conic approximation.

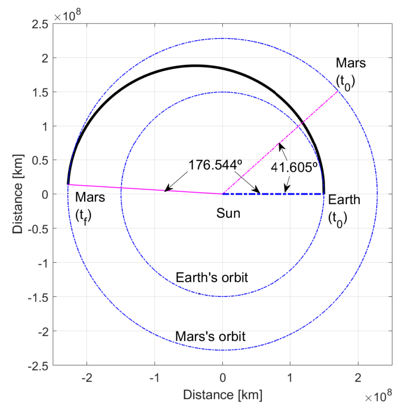

(b) Inertial reference frame. PCR5BP.

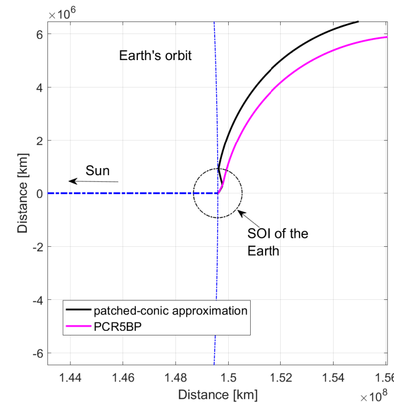

(c) Earth rotating reference frame centered at Sun.

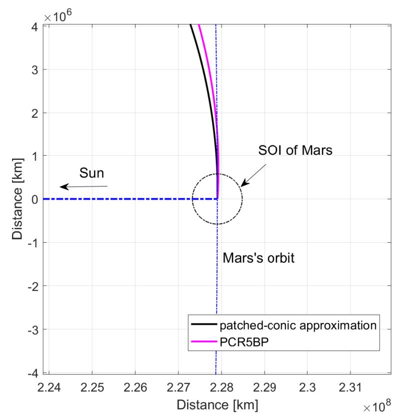

(d) Mars rotating reference frame centered at Sun.

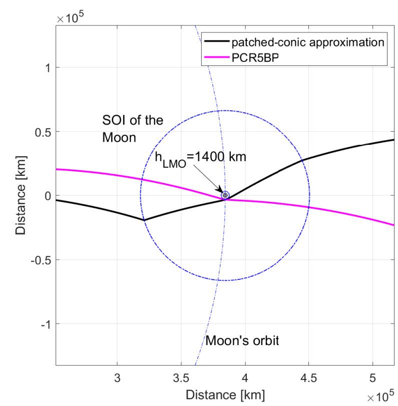

(e) Moon rotating reference frame centered at Earth. h_{LMO} is the periselenium altitude of the swing-by maneuver.

Fig. 23. Earth-Mars mission with a lunar swing-by maneuver. The color figure can be viewed online.

TABLE 10

MAIN PARAMETERS FOR THE SMALLEST FUEL CONSUMPTION TRAJECTORIES FOR EARTH-MARS MISSION WITH AND WITHOUT A LUNAR SWING-BY MANEUVER

Model	Δv_{LEO} (km/s)	Δv_{LM_tO} (km/s)	Δv_{Total} (km/s)	Time of Flight (days)	$\theta_{M_t}(T)$ (degrees)	$\theta_{EP}(0)$ (degrees)	$\theta_{M_t}(0)$ (degrees)
PCR4BP[1]	3.551905	2.100124	5.652029	257.861	179.075	298.382	43.918
PCR5BP[2]	3.404922	2.098633	5.503555	257.443	180.425	270.881	45.486

[1]Results from the two degree-of-freedom optimization problem based on the PCR4BP.

[2]Results from the two degree-of-freedom optimization problem based on the PCR5BP without a collision with the Moon.

ble 10 in comparison to the solution based on the PCR4BP. Therefore, the design of a lunar swing-by maneuver for the Earth-Mars mission saves up to 148.174 m/s of fuel consumption without changes on the time of flight, which stays at 257 days, and without many changes in the rendezvous angle, which increases only 1.568° (Table 10). The result of the trajectory without a collision with the Moon is, actu-

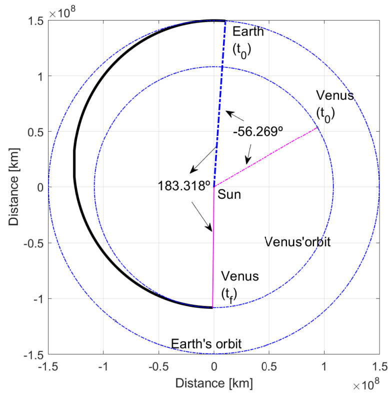

(a) Inertial reference frame. Patched-conic approximation.

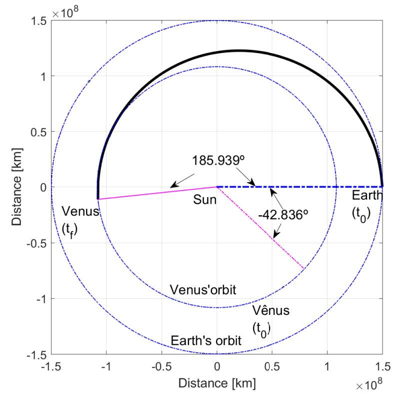

(b) Inertial reference frame. PCR5BP.

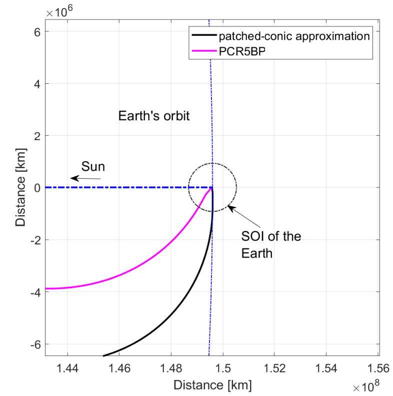

(c) Earth rotating reference frame centered at Sun.

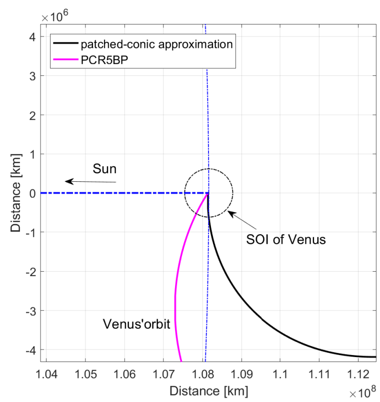

(d) Mars rotating reference frame centered at Sun.

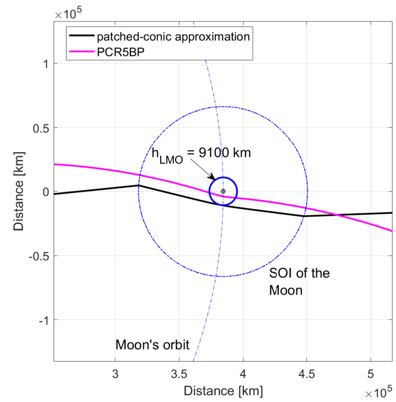

(e) Moon rotating reference frame centered at Earth. h_{LMO} is the periselenium altitude of the swing-by maneuver.

Fig. 24. Earth-Venus mission with a lunar swing-by maneuver. The color figure can be viewed online.

ally, a sub-optimal result extracted from the convergence of the optimization algorithm; thus, the same optimization problem applied to a different initial trajectory can lead to another sub-optimal trajectory. By observing Figures 25a, 25d, and Figure 25c the departure geometry must be accurate; otherwise, the space vehicle will collide to the Moon. By considering a window for the rendezvous angle of only 3.881° where the solutions without collision belong, Figure 25c, a maximum penalty on the fuel consumption of 67.264 m/s is observed.

Figure 26 plots three Earth-Mars trajectories with lunar swing-by maneuver: the first one is used as the initial guess to initialize the SGRA (magenta color); the second one is the optimal solution determined by the SGRA (black color); and, the third one is the trajectory determined by the SGRA with the smaller fuel consumption without a collision with the Moon (green color). The changing of the trajectory shape at departure from the Earth's SOI (Figure 26a) is well visualized and it is due to the convergence of the SGRA. The smaller fuel consumption trajectory without a collision with the Moon (green trajectory) is closer to the optimal trajectory (magenta) than the initial guess trajectory (magenta). In fact, the trajectory without collision and the optimal trajectory perform an intense swing-by maneuver, which is better visualized in Figure 26b. Note that, as trajectories with smaller fuel consumption are obtained by SGRA, the distance of the periselenium is smaller on the swing-by maneuver, which has great influence on the deflection of the trajectory. Thus, the greater the deflection the smaller is the fuel consumption. For the trajectory without collision with the Moon, the altitude of the periselenium is just 78.313 km. On the other hand, the shape of the optimal trajectory and the shape of the non-collision trajectory with the Moon at the arrival

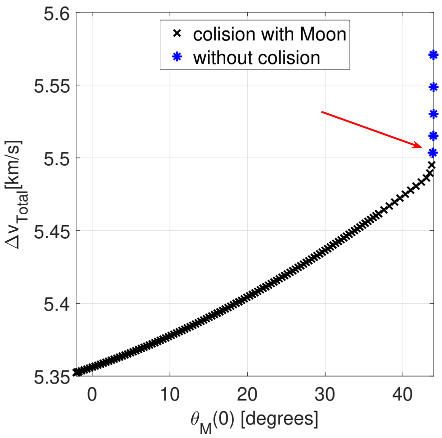

(a) $\Delta v_{total} \times \theta_M(0)$.

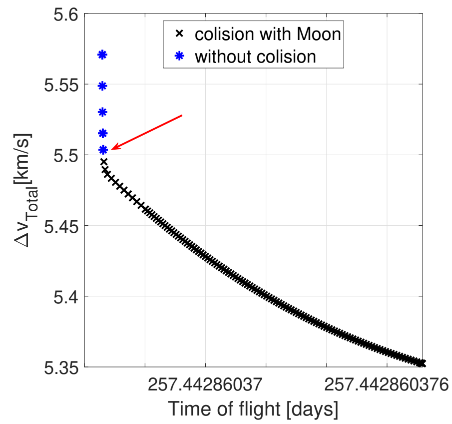

(b) $\Delta v_{total} \times$ Time of flight.

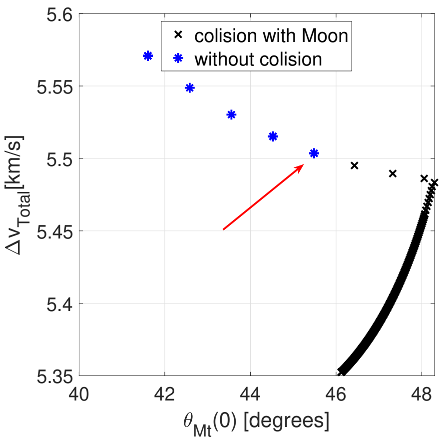

(c) $\Delta v_{total} \times \theta_{M_t}(0)$.

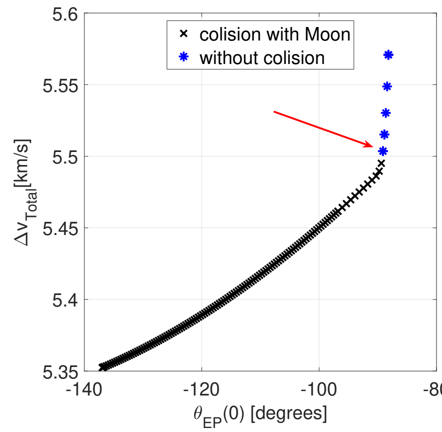

(d) $\Delta v_{total} \times \theta_{EP}(0)$.

Fig. 25. Earth-Mars mission with a lunar swing-by maneuver. The color figure can be viewed online.

to the Mars's SOI (Figure 26b) are practically the same, and both are close to the initial guess trajectory, which arrives closer to the tangent of the orbital motion of Mars. The complete view of the trajectories (Figure 26d) reveals that the local effect of the lunar swing-by maneuver does not have much influence on the complete trajectory, so, the time of flight of the three trajectories is basically the same.

For the Earth-Venus mission, the initial guess for the SGRA also does not collide with the Moon (Figure 27). The minimum fuel consumption solution is reached at 6.583586 km/s, i.e., a decrease of 307.201 m/s. The initial phase angle of the Moon decreases 13.016° (Figure 27a), the rendezvous angle increases 11.438° (Figure 27c), and the initial phase angle of the space vehicle decreases by about 15.191° (Figure 27d). The time of flight, similar to that of the Earth-Mars mission, almost does not change during the optimization algorithm, staying at 142.697 days (Figure 25b). Also, as trajectories with smaller fuel consumption are obtained by SGRA, the distance of the periselenium for the swing-by maneuver is smaller, so that the optimal solution collides with the Moon. For a practical purpose, the interesting solution is the one that does not collide with the Moon, which is indicated by the red arrow in Figure 27; results are highlighted in Table 11 in comparison to the solution based on the PCR4BP. Therefore, the design of a lunar swing-by maneuver for the Earth-Mars mission saves up to 170.913 m/s of fuel consumption without many changes in the time of flight, which increases by only 3.069 days, and without many changes in the rendezvous angle, which increases only 0.68° (Table 11). By observing Figures 27a, 27d, and Figure 27c the departure geometry must be accurate; otherwise, the space vehicle collides with the Moon. By considering a window for the rendezvous angle, Figure 27c, of only 11.464° in which there are trajectory solutions with a lunar swing-by maneuver without collision, a maxi-

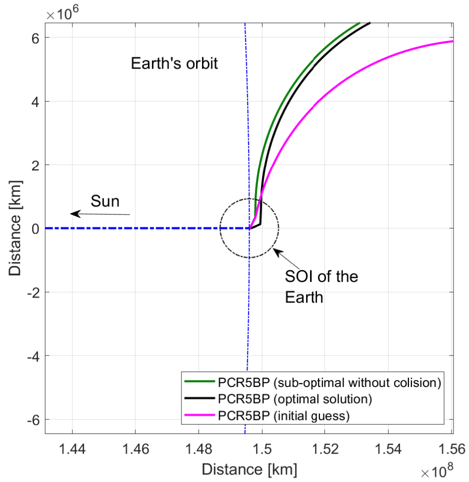

(a) Earth rotating reference frame centered at Sun.

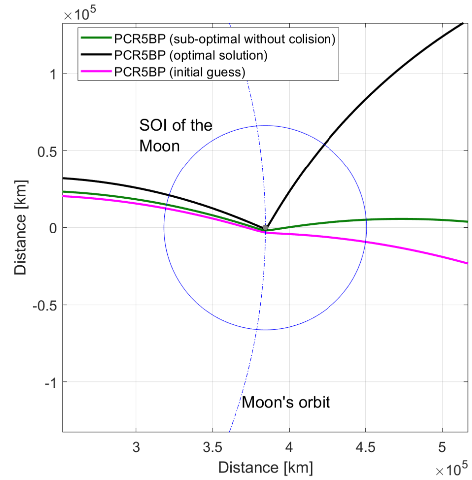

(b) Moon rotating reference frame centered at Earth.

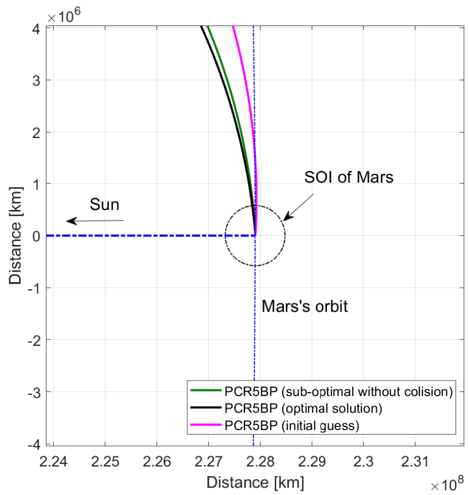

(c) Mars rotating reference frame centered at Sun.

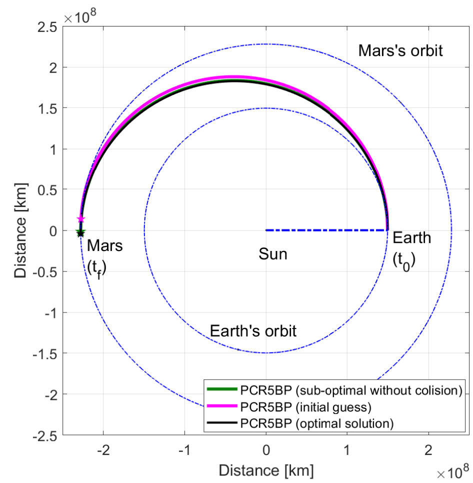

(d) Complete trajectory in the inertial reference frame centered at Sun.

Fig. 26. Optimal Earth-Mars trajectory with a lunar swing-by maneuver. The color figure can be viewed online.

mum penalty on the fuel consumption of 275.285 m/s is observed. Similar to the Earth-Mars mission, the results of the trajectory without collision with the Moon for the Earth-Venus mission is, actually, a sub-optimal result extracted from the convergence of the optimization algorithm, so, it depends on the trajectory that initializes this algorithm.

Figure 28 plots three Earth-Venus trajectories with lunar swing-by maneuver: the first one is used as the initial solution to initialize the SGRA (magenta color); the second one is the optimal solution determined by the SGRA (black color), the third one is the smaller fuel consumption trajectory without collision with the Moon, also determined by the SGRA (green color). Note in Figures 28a and 28b the huge deflection of the black trajectory. As the SGRA computes smaller fuel consumption trajectories, the distance of the periselenium on the swing-by maneuver decreases until the optimal trajectory is reached (black color). For the smaller fuel consumption trajectory without collision with the Moon, the altitude of the periselenium is just 44.468 km. In order to prescribe the periselenium altitude, one can add an intermediary constraint for the altitude of the swing-by maneuver; however, this problem becomes harder to solve since it becomes more restrictive. An interesting comparison between the Earth-Mars and the Earth-Venus mission is observed in Figures 26a and 28a: for the Earth-Mars mission, the lunar swing-by maneuver occurs when the Moon is ahead the Earth and farther from the Sun than Earth (Figure 26a); on the other hand,

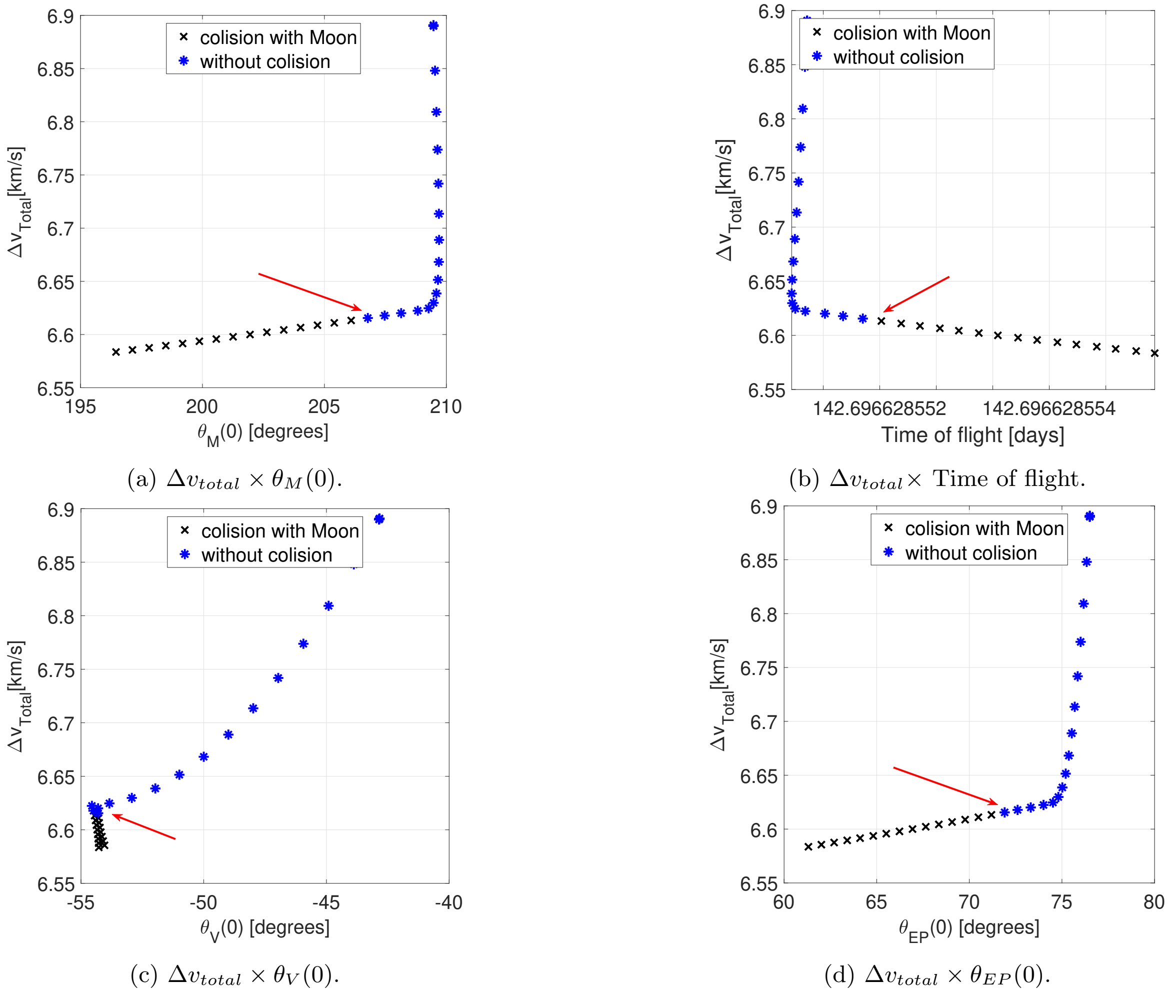

(a) $\Delta v_{total} \times \theta_M(0)$.

(b) $\Delta v_{total} \times$ Time of flight.

(c) $\Delta v_{total} \times \theta_V(0)$.

(d) $\Delta v_{total} \times \theta_{EP}(0)$.

Fig. 27. Earth-Venus mission with a lunar swing-by maneuver. The color figure can be viewed online.

TABLE 11

MAIN PARAMETERS FOR THE SMALLEST FUEL CONSUMPTION TRAJECTORIES FOR EARTH-VENUS MISSION WITH AND WITHOUT A LUNAR SWING-BY MANEUVER

Model	Δv_{LEO} [km/s]	Δv_{LM_tO} [km/s]	Δv_{Total} [km/s]	Time of Flight [days]	$\theta_V(T)$ [degrees]	$\theta_{EP}(0)$ [degrees]	$\theta_V(0)$ [degrees]
PCR4BP[1]	3.449138	3.337284	6.786422	139.628	173.795	105.084	-50.060
PCR5BP[2]	3.275623	3.339886	6.615509	142.697	174.475	71.907	-54.300

[1]Results from the two degree-of-freedom optimization problem based on the PCR4BP.

[2]Results from the two degree-of-freedom optimization problem based on the PCR5BP without a collision with the Moon.

for the Earth-Venus mission, the lunar swing-by maneuver occurs when the Moon is behind the Earth and closer to the Sun than Earth. In both cases, however, the swing-by maneuver occurs in a counterclockwise sense, since the space vehicle must accelerate during the swing-by maneuver. These differences in the position of the Moon are related to the type of transfer: inner transfer or outer transfer. For the outer transfer (Earth-Mars mission), the space vehicle must leave the SOI of Earth from ahead according to the Hohmann transfer; and, for the inner transfer (Earth-Venus mission), the space vehicle must leave

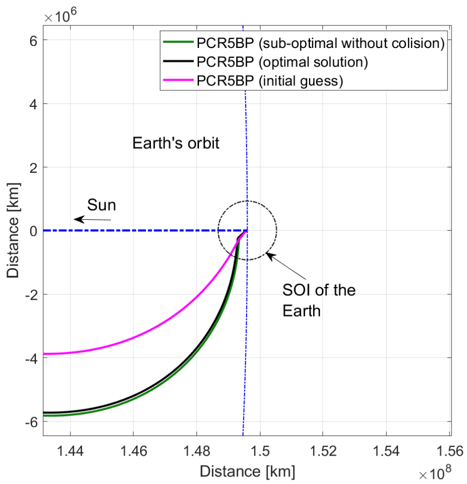

(a) Earth rotating reference frame.

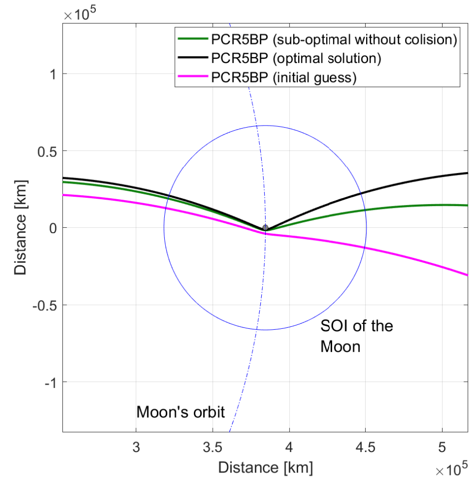

(b) Moon rotating reference frame.

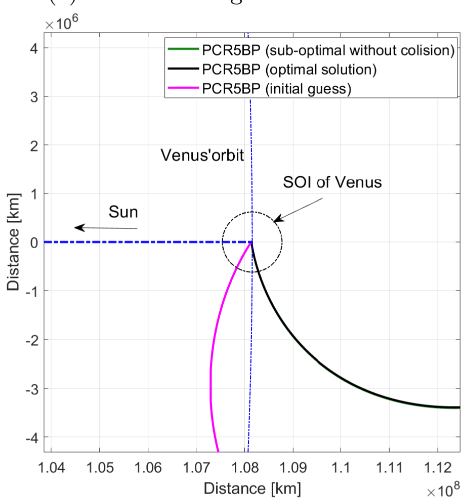

(c) Venus rotating reference frame.

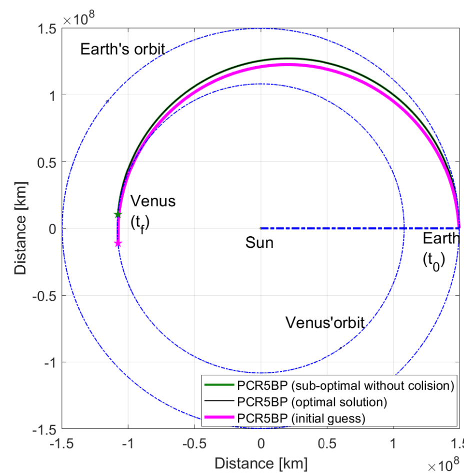

(d) Complete trajectory in the inertial reference frame centered at Sun.

Fig. 28. Optimal Earth-Venus trajectory with a lunar swing-by maneuver. The color figure can be viewed online.

the SOI of Earth from behind. Therefore, the lunar swing-by maneuver aids the space vehicle to achieve the hyperbolic excess velocity, which corresponds to an accelerative velocity increment of the Hohmann transfer for an outer mission, or it corresponds to a decelerating velocity increment of the Hohmann transfer for an inner mission.

Tables 12 and 13 compile the results already seen with the best transfer with and without lunar swing-by maneuver. The results determined by Miele and Wang (1999b) for the Earth-Mars mission are also repeated in order to highlight the similarity of the results determined by Miele and Wang (1999b) and the ones calculated in this work, specifically in the context of the PCR4BP. A detailed discussion about this result was already done in § 3.1 and § 3.2. As a final remark, Prado (2003) calculates the saving of fuel consumption due to a lunar swing-by maneuver for interplanetary trajectories based on the Hohmann transfer. In this way, for an altitude of the lunar swing-by maneuver of 102 km, Prado (2003) determines a saving of 124 m/s for the Earth-Mars mission, and a saving of 137 m/s for the Earth-Venus mission. For an altitude of the lunar swing-by maneuver of 12 km, Prado (2003) determines a saving of 129 m/s for the Earth-Mars mission, and a saving of 142 m/s for the Earth-Venus mission. The savings of fuel consumption for a more high fidelity model as the PCR5BP determined by the present work are practically the same as those determined by Prado (2003) or even a little larger: for the Earth-Mars mission the saving reaches 148

TABLE 12

MAIN PARAMETERS FOR THE SMALLEST FUEL CONSUMPTION TRAJECTORIES FOR EARTH-MARS MISSION

Model	Δv_{LEO} (km/s)	Δv_{LM_tO} (km/s)	Δv_{Total} (km/s)	Time of Flight (days)
PCR4BP[1]	3.551905	2.100124	5.652029	257.861
Miele[2]	3.552000	2.100000	5.652000	257.880
Patched-conic based on Hohmann	3.555746	2.101260	5.657006	264.430
Patched-conic based on Gauss	3.555572	2.101454	5.657026	263.579
Patched-conic detailed geometry[3]	3.514668	2.087434	5.602101	257.965
Patched-conic lunar swing-by	3.362211	2.086891	5.449101	257.443
PCR5BP[4] Lunar swing-by	3.404922	2.098633	5.503555	257.443

[1]Results from a two degree-of-freedom optimization problem.

[2]Results based on the PR4CP calculated by Miele and Wang (1999b).

[3]Smallest fuel consumption trajectory found for $\lambda_{Mt} = 89°$ (arrival ahead the SOI).

[4]Results from the two degree-of-freedom optimization problem based on the PCR5BP without a collision with the Moon.

TABLE 13

MAIN PARAMETERS FOR THE SMALLEST FUEL CONSUMPTION TRAJECTORIES FOR EARTH-VENUS MISSION

Model	Δv_{LEO} (km/s)	Δv_{LVO} (km/s)	Δv_{Total} (km/s)	Time of Flight (days)
PCR4BP[1]	3.449138	3.337284	6.786422	139.628
Patched-conic based on Hohmann	3.447245	3.339810	6.787055	151.822
Patched-conic based on Gauss	3.447417	3.339550	6.786967	151.771
Patched-conic detailed geometry [2]	3.406312	3.294024	6.700336	147.976
Patched-conic lunar swing-by	3.376566	3.289849	6.666415	149.440
PCR5BP[3] Lunar swing-by	3.275623	3.339886	6.615509	142.697

[1]Results from a two degree-of-freedom optimization problem.

[2]Smallest fuel consumption trajectory found for $\lambda_V = -87°$ (arrival behind the SOI).

[3]Results from the two degree-of-freedom optimization problem based on the PCR5BP without a collision with the Moon.

m/s (compare Δv_{Total} between the PCR4BP and the PCR5BP in Table 12). In this case, the altitude of the lunar swing-by maneuver is 78.313 km, which is larger than the 12 km altitude specified by Prado (2003). For the Earth-Venus mission the saving reaches 137 m/s (compare Δv_{Total} between the PCR4BP and the PCR5BP in Table 13). In this case, the altitude of the lunar swing-by maneuver, 44.468 km, is also larger than the 12 km altitude specified by Prado (2003). Therefore, despite the calculated savings being similar in the present work to the ones of Prado (2003), the higher fidelity model, based on the PCR5BP, provides trajectories with a larger lunar swing-by altitude for both missions, which increase the operational feasibility of the mission.

4. CONCLUSION

This work describes two-point boundary value problems to determine interplanetary trajectories with and without lunar swing-by maneuvers considering several models: patched-conic approximation based on Hohmann transfer, patched-conic approximation based on the Gauss problem; patched-approximation associated with a boundary problem; patched-conic approximation associated with a boundary problem and with an intermediary constraint that defines a lunar swing-by maneuver; a model based on the four-body problem; and a model based on the five-body problem. The comparison of the models illustrates that the patched-conic approximations provide good initial guesses for more complex models such as the PCR4BP and the PCR5BP models, making the convergence of the optimization problems easier.

The first part of the present work analyses interplanetary missions without a lunar swing-by maneuver. The interplanetary patched-conic with detailed geometry shows that the direction of the target orbit does not change the velocity increments, the time of flight, the rendezvous angle, and the initial phase angles of the space vehicle. The only difference due to the direction of the target orbit is the phase angle of the space vehicle at the arrival at the target orbit. Optimal interplanetary trajectories are computed in the context of the PCR4BP by a two-degree optimization problem. An analysis around the solutions of this two-degree optimization problem is performed by an one-degree optimization problem, which reveals that the penalty on the fuel consumption due to the delayed or early departures is more severe for the Earth-Venus mission than for the Earth-Mars mission. Future work can be accomplished to generalize and classify the results of the fuel consumption between interior and exterior planet missions.

The second part analyses interplanetary missions with a lunar swing-by maneuver. A first comparison is made between the results of a patched-conic approximation and the results of a model based on the PCR5BP, and it shows the possibility to save fuel consumption without changing the time of flight. These first solutions are utilized to initialize a three-degree of freedom optimization problem in which the position of the Moon, the rendezvous angle, the velocity increments, the time of flight, and the initial phase angle of the space vehicle are set as unknowns to minimize the fuel consumption. The results show that the optimal trajectory for the Earth-Mars and Earth-Venus mission collides with the Moon during the swing-by maneuver. However, sub optimal solutions that do not collide with the Moon are practical presenting a significant saving of fuel consumption without many changes on the time of flight when they are compared to the solutions without a lunar swing-by maneuver.

This research is supported by grant 2012/25308-5, São Paulo Research Foundation (FAPESP), and by CNPq under contract 301875/2017-0.

REFERENCES

Abdelkhalik, O. & Mortari, D. 2007, JSpRo, 44, 456, https://doi.org/10.2514/1.24701

Addis, B., Cassioli, A., Locatelli, M., & Schoen, F. 2011, Computational Optimization and Applications, 48, 635, https://doi.org/10.1007/s10589-009-9261-6

Batte, R. R., Mueller, D. D., & White, J. E. 1971, Fundamentals of astrodynamics (New York, NY: Dover Publications)

Battin, R. H. & Vaughan, R. M. 1984, JGCD, 7, 662, https://doi.org/10.2514/3.19910

Battin, R. H., Fill, T. J., & Shepperd, S. W. 1978, JGCD, 1, 50, https://doi.org/10.2514/3.21004

Bayer, T., Buffington, B., Castet, J.-F., et al. 2017, Europa mission update: Beyond payload selection, IEEE Aerospace Conference Proceedings, https://doi.org/10.1109/AERO.2017.7943832

Broucke, R. A. 1988, The celestial mechanics of gravity assist, AIAA/AAS Astrodynamics Conference (Washington, DC: AIAA), 69

Cichan, T., Bailey, S. A., Norris, S. D., et al. 2017, Mars Base Camp: An Architecture for Sending Human to Mars, IEEE Aerospace Conference

Daukantas, P. 2017, OptPN, 28, 26, https://doi.org/10.1364/OPN.28.5.000026

Dei Tos, D. A. & Topputo, F. 2019, JGCD, 42, 1343, https://doi.org/10.2514/1.g003838

Ellison, D. H., Conway, B. A., Englander, J. A., & Ozimek, M. T. 2018, JGCD, 41, 1149, https://doi.org/10.2514/1.g003077

Faria Venditti, F. C., Marconi Rocco, E., Bertachini De Almeida Prado, A. F., & Suhkanov, A. 2010, AcAau, 67, 1255, https://doi.org/10.1016/j.actaastro.2010.06.022

Foust, J. 2019, Gateway or bust: NASA's plan for a 2024 lunar landing depends on a much-criticized orbital outpost, IEEE Spectrum, 56, 32, https://doi.org/10.1109/mspec.2019.8747310

Gagg Filho, L. A. & da Silva Fernandes, S. 2016, Computational and Applied Mathematics, 35, 753, https://doi.org/10.1007/s40314-015-0247-y

_________. 2018, Computational and Applied Mathematics, 37, 27, https://doi.org/10.1007/s40314-017-0529-7

Genta, G. & Maffione, F. 2019, Choice of the Optimal Launch Date for Interplanetary Missions in Springer Optimization and Its Applications, ed. G. Fasano & J. Pintér, 111, https://doi.org/10.1007/s40314-017-0529-7

Gooding, R. H. 1990, CEMDA, 48, 145, https://doi.org/10.1007/BF00049511

Izzo, D., Sprague, Ch. I., & Tailor, D. V. 2019, Machine Learning and Evolutionary Techniques in Interplanetary Trajectory Design in Springer Optimization and Its Applications, ed. G. Fasanu & D. Pintér, 191, https://doi.org/10.1007/978-3-030-10501-3_8

Lavagna, M., Povoleri, A., & Finzi, A. E. 2005, AcAau, 57, 498, https://doi.org/10.1016/j.actaastro.2005.03.052

Lorenz, R. D., Turtle, E. P., Barnes, J. W., et al. 2018, JHATD, 34, 374

Marec, J. P. 1979, Optimal space trajectories (Amsterdam, Netherlands: Elsevier Scientific Publishing)

Meiss, J. H., Jaeger, M., Gronowski, M., Kachler, T., & Dickens, K. 2016, Evolution and Status of the Orion-ESM Propulsion Subsystem, AIAA, https://doi.org/10.2514/6.2016-5622

Miele, A. & Wang, T. 1997, JOTA, 95, 467, https://doi.org/10.1023/A:1022661519758

_________. 1999a, AcAau, 45, 655, https://doi.org/10.1016/s0094-5765(99)00117-4

_________. 1999b, AcAau, 45, 119, https://doi.org/10.1016/S0094-5765(99)00109-5

Miele, A., Huang, H. Y., & Heideman, J. C. 1969, JOTA, 4, 213, https://doi.org/10.1007/BF00927947

Miele, A., Wang, T., & Mancuso, S. 2004a, AcAau, 55, 79, https://doi.org/10.1016/j.actaastro.2003.12.018

Miele, A., Wang, T., & Williams, P. N. 2004b, AcAau, 55, 95, https://doi.org/10.1016/j.actaastro.2004.01.053

O'Dell, S. & Cichan, T. 2018, Crewed Missions to the Martian Surface via Mars Base Camp, AIAA 2018 SPACE and Astronautics Forum and Exposition, https://doi.org/10.2514/6.2018-5142

Petrescu, R. V., Aversa, R. A., Akash, B., et al. 2017, Lockheed Martin-A Short Review in Journal of Aircraft and Spacecraft Technology, 1, 50, https://doi.org/10.3844/jastsp.2017.50.68

Prado, A. F. B. A. 2003, J. Braz. Soc. Mech. Sci. & Eng., 25, https://doi.org/10.1590/S1678-58782003000200003

Press, W. H., Teukolsky, S. A., Vetterling, W. T., & Flannery, B. P. 1997, Numerical Recipes in Fortran 77. The Art of Scientific Computing

Prussing, J. E. 1979, JGCD, 2, 442, https://doi.org/10.2514/3.55905

Prussing, J. E. & Chiu, J. H. 1986, JGCD, 9, 17, https://doi.org/10.2514/3.20060

Prussing, J. E. & Conway, A. 1993, Orbital Mechanics, OUP, 1993

Shepard, M. K., Richardson, J., Taylor, P. A., et al. 2016, Icar, 281, 388, https://doi.org/10.1016/j.icarus.2016.08.011

Tsuda, Y., Yoshikawa, M., Saiki, T., Nakazawa, S., & Watanabe, S. 2018, AcAau, 156, 387, https://doi.org/10.1016/j.actaastro.2018.01.030

Weinzierl, M. 2018, Journal of Economic Perspectives, 32, 173, https://doi.org/10.1257/jep.32.2.173

Yang, B., Yang, H., & Li, S. 2019, AcAau, 165, 139, https://doi.org/10.1016/j.actaastro.2019.09.006

Sandro da Silva Fernandes: Mathematics Department, Instituto Tecnológico de Aeronáutica, Praça Marechal Eduardo Gomes 50, Vila das Acácias, 12228-900, São José dos Campos, SP, Brazil (sandro@ita.br).

Luiz Arthur Gagg Filho: Flight Mechanics Department, Instituto Tecnológico de Aeronáutica, Praça Marechal Eduardo Gomes 50, Vila das Acácias, 12228-900, São José dos Campos, SP, Brazil (arthurga@ita.br).

Revista Mexicana de Astronomía y Astrofísica, **59**, 45–65 (2023)

https://doi.org/10.22201/ia.01851101p.2023.59.01.03

PHYSICAL PROPERTIES AND MEMBERSHIP DETERMINATION OF THE OPEN CLUSTERS IC 4665, NGC 6871 AND DZIM 5 THROUGH $uvby-\beta$ PHOTOELECTRIC PHOTOMETRY[1]

J. H. Peña[2,3,4], A. Rentería[2,3], J. D. Paredes[2,5], and D. S. Piña[2,4]

Received December 4 2017; accepted September 13 2022

ABSTRACT

$uvby-\beta$ photoelectric photometry of stars in the direction of the open clusters IC 4665, NGC 6871 and Dzim 5 is presented. From this $uvby-\beta$ photometry we classified the spectral types which allowed us to determine the reddening and, hence, the distance. Membership of the stars to the cluster was determined. Our results are compared with those obtained by GAIA DR2.

RESUMEN

Se presenta fotometría $uvby-\beta$ de estrellas en la dirección de los cúmulos abiertos IC 4665, NGC 6871 y Dzim 5. A partir de la fotometría fotoeléctrica $uvby-\beta$ de las estrellas en la dirección de estos cúmulos clasificamos los tipos espectrales de cada estrella lo que nos permitió la determinación de su enrojecimiento y de sus distancias y, por ende, la pertenencia de las estrellas al cúmulo. Nuestros resultados se comparan con GAIA DR2.

Key Words: galaxies: photometry — open clusters and associations: general — parallaxes

1. MOTIVATION

Open clusters are a gold mine for the development of many astrophysical topics. They offer a unique opportunity, for example, to compare theoretical studies with observations; they provide opportunities to develop models of chemical enrichment with respect to the center of the galaxy, and serious studies on stability can be tested only through an analysis of open clusters. However, despite the importance of these topics, research in these fields begins with the determination of the cluster member stars.

Membership determination in open clusters is done, canonically, with proper motion studies; but in practice, main-sequence fitting is used since it is easier, although less accurate and cannot be used on a star-by-star basis. However, for distant or faint clusters membership determination is not an easy task. $uvby-\beta$ photometry of open clusters provides an accurate method for determining distances to each star and, through the global behavior, throws light on the distance to the cluster and, hence, the membership of each star to the cluster.

In this paper we present our results on three clusters: two, IC 4665 and NGC 6871, are relatively well-studied and the other, Dzim 5, has very little published information.

The open cluster IC 4665 has been a subject of many studies. The membership in the cluster has been determined in many different ways. The classical proper motions studies were done by Vasilevskis (1955) and the spectral classification of its members was done through classical spectroscopy.

With respect to the photometric studies, there are some classical works like that of Johnson (1954). With intermediate photometric bands there is the work of Crawford & Barnes (1972) who, with $uvby-\beta$ photometry, found an average cluster reddening $E(b-y)$ of 0.14, and a cluster distance modulus of 7.5, corresponding to a distance of 316 pc. They obtained the same values from an analysis of the B-type stars and the A- and F- type stars.

[1]Based on observations collected at the San Pedro Mártir Observatory, México.

[2]Instituto de Astronomía, Universidad Nacional Autónoma de México, México.

[3]Observatorio Astrónomico Nacional de Tonantzintla, Universidad Nacional Autónoma de México, México.

[4]Facultad de Ciencias, Universidad Nacional Autónoma de México, México.

[5]Facultad de Ciencias, Universidad Central de Venezuela, Venezuela.

Finding variables in the cluster has been a subject of some research. Barannikov (1994) confirmed that the star HD 161573 in the IC 4665 cluster has periodic ($P = 19$ d) variability.

With respect to NGC 6871 much research has been carried out. A good summary of its characteristics can be found in Southworth et al. (2004). They stated that the open cluster NGC 6871 was a concentration of bright OB stars which form the nucleus of the Cyg OB3 association. For this reason it is an important object in the study of the evolution of high-mass stars. The cluster itself has been studied photometrically several times, but the scarce data on its nature mean that determination of its physical parameters is difficult. They further note that: "UBV photometry of the 30 brightest stars was published by Hoag et al. (1961). Crawford, Barnes & Warren (1974) observed 11 stars in the Strömgren *uvby* system and 24 stars in the Crawford β system, finding significantly variable reddening and a distance modulus of 11.5 mag. This $uvby - \beta$ photometry was extended to 40 stars by Reimann (1989), who found reddening $E(b-y)$ with a mean value of 0.348 mag and an intercluster variation of about 0.1 mag. His derived distance modulus of 11.94 $\pm$ 0.08 and age of 12 Myr are both greater than previous literature values".

Southworth et al. (2004) carried out a study of the eclipsing binary V453 Cyg (W31) which, they claimed, is a member of NGC 6871. As we will see later, this is not the case.

The other cluster, Dzim 5 was reported by Dolidze & Jimsheleishvili (1966) but after this, there is only one reference to one of its members. WEBDA does not list distance, reddening age, metallicity or any other quantity except its coordinates. They refer only to the study of Kazlauskas et al., (2013) related to a new spectroscopic binary with which they establish that Dol–Dzim 5 is not a real open cluster.

Table 1 presents a summary of the most relevant findings of several papers for these clusters.

2. OBSERVATIONS

This article is a sequel to a paper on NGC 6633 that has already been published (Peña et al., 2017, Paper I). The observations were carried out over a long season by two different observers, one from June 22th to 30th and the other from July 1st to 8th, 2016 (ARL and CVR, respectively) with different objects in each one although some were taken continuously (NGC 6633, Peña et al., 2017, and V 2455 Cyg, Peña et al., 2019). The open cluster IC 4665 was observed for four nights from June 22nd to June 25th. NGC 6871 was observed for two nights, July 2nd and 3rd and Dzim 5 from July 5th to the 8th. The observing and reduction procedures were described in detail in Paper I. The reduction was done considering both seasons together as one long season to increase the accuracy of the standard stars.

The observations were all taken at the Observatorio Astronómico Nacional de San Pedro Mártir, México. The 0.84 m telescope, to which a spectrophotometer was attached, was utilized at all times. The stars to be observed were selected randomly by drawing concentric circles on the ID charts provided by WEBDA and observing all the bright stars in each circle.

The limit was the faintness of the stars, since to reach the desired accuracy faint stars would require an exceedingly long time of observation. Hence, no astrophysical considerations, nor previous knowledge of the selected stars, was considered. For IC 4665 we measured thirty stars, sixteen for NGC 6871 and fourteen for Dzim 5. Although some of the stars had already been observed, a comparison between the sets gave us confidence in the data as shown from the standard deviations of the values for the same star from several studies, in some cases from three or four different measurements. In the case of Dzim 5 averaging the large discrepancy in the color indexes m_1 and c_1 could have led to possible misinterpretations of the physical characteristics of the stars and, hence, of the cluster.

2.1. *Data Acquisition and Reduction*

During all the observed nights the following procedure was utilized: at least five ten-second integrations of each star and one ten-second integration of the sky for the *uvby* filters and the narrow and wide filters that define Hβ were done for each measurement. The reduction procedure was done with the numerical package NABAPHOT (Arellano-Ferro & Parrao, 1988). A series of standard stars was also observed on each night to transform the data into the standard system. The chosen standard system was that defined by the standard values of Olsen (1983), although some of the standard bright stars were also taken from the Astronomical Almanac (1996). The transformation equations are those defined by Crawford & Barnes (1970) and by Crawford & Mander (1966). See Paper I for details.

In these transformation equations the coefficients D, F, H and L are the slope coefficients for $(b-y)$, m_1, c_1 and β, respectively. The coefficients B, J and I are the color terms of V, m_1, and c_1. The averaged transformation coefficients of each night were listed

TABLE 1: Compilation of the determined data of the clusters

Author	$E(B-V)$	$E(b-y)$	DM	Dst	[Fe/H]	Age	Technique
				pc		log (age)	members/total
IC 4665							
Vasilevskies (1955)							proper motion
Alcaino (1965)	0.152						UBV
Becker & Fenkart (1971)	0.17		8.11	330			UBV
Crawford & Barnes (1972)		0.14	7.5	316			$uvby-\beta$
Sanders & Van Altena (1972)						8.556	proper motion
Patenaude (1978)						7.6	theory and UBV
Nicolete (1981)			7.9 ± 0.022	379 ± 46			Geneva photometric boxes
Morrel & Abt (1991)					0.04		spectroscopy
Stetson (1991)		0.112		335	0.04	8.703	compiled
Cargile & James (2010)				357 ± 12		7.623	
PP		0.143 ± 0.046	7.5 ± 0.3	323 ± 49	-0.20 ± 0.09	8.160	$uvby-\beta$
NGC 6871							
Cohen (1969)		0.38	11.4				β
Crawford et al. (1974)			11.5				$uvby-\beta$
Schild & Ramashin (1976)			11.1				Be
Babu (1983)				1600			Spectroscopy
Nicolet (1981)			11.19 ± 0.52	1730 ± 450			Geneva
PP		0.307 ± 0.044	10.9 ± 0.04			7.088	$uvby-\beta$
DZIM 5							
Kazlauskas et al. (2013)	0.02			400	-0.09 ± 0.17		Strömvil phot and rv
PP		0.1 ± 0.1	6.62 ± 0.46	215 ± 45	-0.14 ± 0.30		$uvby-\beta$

TABLE 2

SEASONAL STANDARD DEVIATIONS OF THE STANDARD STARS

ID	σV	$\sigma(b-y)$	σm_1	σc_1	$\sigma\beta$
Mean	0.029	0.013	0.008	0.020	0.017
Stand. Dev.	0.012	0.011	0.007	0.018	0.004

in Table 2 of Paper I along with their standard deviations. Season errors, Table 2, were evaluated by means of the nineteen standard stars observed for a total of 133 observed points. These uncertainties were calculated through the differences in magnitude and colors for all nights, for (V, $b-y$, m_1, c_1 and β) as (0.024, 0.010, 0.011, 0.015, 0.015), respectively, which provide a numerical evaluation of our uncertainties of the season. Emphasis is made on the large range of the standard stars in the magnitude and the color indexes: V:(5.2, 8.8); $(b-y)$:(0.00, 0.80); m_1:(0.09, 0.68); c_1:(0.08, 1.05) and β:(2.50, 2.90).

The numerical results obtained are presented in Table 3 of Paper I. In Column 1 we present the ID; in Columns two to six, the mean photometric values V, $(b-y)$, m_1, c_1 and β for each star. The corresponding unreddened indexes are presented in the subsequent columns. The mean values of the individual standard deviations are presented at the bottom of the last two rows of Table 2 of Paper I, as well as the standard deviation of the individual standard deviations. These values are a few hundredths or thousandths of magnitude for each color index and provide the accuracy of our photometry.

Tables 3, 4 and 5 report the observed $uvby-\beta$ photoelectric photometry for IC 4665, NGC 6871 and Dzim 5, respectively. In Tables 3 and 4 we list the following: in Column 1 the ID in WEBDA, subsequent columns report the magnitude V and the color indexes $(b-y)$, m_1, c_1, and β. Since each star was observed over several nights, mean values and their standard deviations were calculated. They are also presented in the tables, as well as the number of entries in the mean. This is number N presented in the last column of each table. For the open cluster Dzim 5 we present our $uvby-\beta$ photoelectric photometry with the ID numbers shown as in Kalauskas et al. (2013).

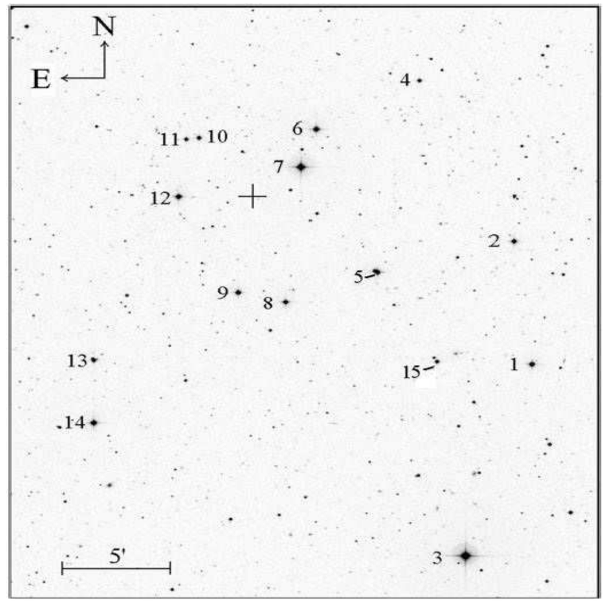

Fig. 1. ID chart of the observed stars in the direction of Dzim 5. The ID number follows that of Kalauskas et al. (2013)

3. COMPARISON WITH OTHER PHOTOMETRIES

A comparison with previous $uvby-\beta$ photoelectric photometry had to be done in order to test the goodness of our results and to enhance the sample by considering the previously measured stars in the direction of each cluster. A search, mostly from WEBDA, was done for references on $uvby-\beta$ photometry. These are presented in Table 6, in which the references and the number of the reported stars are listed. However, in our comparison, we only take into account those studies with a significant number of observed stars devoted to each cluster. Those stars with few points taken randomly in studies not devoted to the cluster were not included in the mean. Later, as we will see, a compilation of the stars in the direction of each cluster was done increasing the number of stars in the direction of the cluster, with the proven quality of their values.

Instead of considering the averaged values reported by WEBDA, we opted to include the original sources, because the mean value combined with our photometry would be biased; this saved us from cases like those presented for the open cluster IC 4665. The star W108, which we did not observe, but appears in the compilation of WEBDA, had two radically different values in magnitude reported: 7.508 and 9.820. Equally discrepant are the color indexes. To check which magnitude value was correct, we compared both with those reported in UBV in WEBDA which lists 7.460 and 7.490 mag in V. These systematic differences suggest a variable star. Nevertheless, the value corresponding to 9.820 was not further considered in our analysis.

TABLE 3

OBSERVED $uvby-\beta$ PHOTOELECTRIC PHOTOMETRY OF THE OPEN CLUSTER IC 4665

ID	V	$(b-y)$	m_1	c_1	$H\beta$	σV	$\sigma(b-y)$	σm_1	σc_1	$\sigma H\beta$	N
01	6.857	0.079	0.030	0.321	2.702	0.057	0.015	0.006	0.017	0.012	3
02	7.353	0.078	0.032	0.455	2.715	0.060	0.010	0.002	0.009	0.011	3
03	7.603	0.063	0.039	0.413	2.721	0.050	0.012	0.006	0.010	0.015	3
04	7.705	0.071	0.048	0.459	2.744	0.087	0.010	0.003	0.008	0.006	2
05	9.090	0.140	0.103	0.920	2.883	0.042	0.010	0.003	0.015	0.009	3
06	10.092	0.097	0.130	0.946	2.895	0.039	0.018	0.009	0.008	0.033	3
07	9.364	0.205	0.155	0.914	2.888	0.035	0.011	0.003	0.013	0.006	3
08	10.673	0.376	0.101	0.473	2.691	0.029	0.010	0.016	0.010	0.037	3
09	10.896	0.739	0.423	0.113	2.588	0.038	0.040	0.126	0.001	0.007	3
10	9.080	0.197	0.109	0.916	2.895	0.037	0.014	0.004	0.008	0.012	3
11	7.928	0.314	0.131	0.460	2.694	0.037	0.015	0.004	0.012	0.011	3
12	10.262	0.812	0.378	0.203	2.582	0.012	0.011	0.042	0.041	0.037	3
13	8.870	0.137	0.029	0.627	2.709	0.046	0.021	0.001	0.003	0.004	2
14	8.375	0.780	0.385	0.301	2.581	0.031	0.015	0.016	0.014	0.007	3
15	9.792	0.473	0.136	0.467	2.655	0.033	0.015	0.002	0.008	0.014	3
16	10.549	0.806	0.502	0.160	2.581	0.049	0.015	0.009	0.045	0.017	3
17	8.217	0.128	0.054	0.541	2.750	0.042	0.014	0.002	0.006	0.005	3
18	10.869	0.278	0.142	0.695	2.751	0.040	0.011	0.017	0.028	0.03	3
19	8.300	1.095	0.804	0.012	2.595	0.045	0.016	0.011	0.046	0.025	3
20	9.852	0.169	0.129	0.983	2.872	0.036	0.016	0.011	0.036	0.018	3
21	10.880	0.976	0.676	-0.049	2.602	0.023	0.008	0.015	0.089	0.002	2
22	7.771	0.063	0.038	0.345	2.703	0.027	0.019	0.009	0.017	0.015	3
23	7.995	0.102	0.034	0.442	2.725	0.026	0.020	0.010	0.013	0.010	3
24	7.123	0.084	0.026	0.431	2.687	0.038	0.013	0.003	0.009	0.009	3
25	8.807	0.164	0.131	0.995	2.904	0.037	0.011	0.003	0.008	0.025	3
26	10.395	0.210	0.159	0.864	2.843	0.025	0.018	0.008	0.019	0.026	3
27	10.942	0.433	0.070	0.409	2.609	0.030	0.020	0.012	0.039	0.033	3
28	7.480	0.077	0.159	0.979	2.899	0.029	0.009	0.003	0.001	0.003	2
29	9.745	0.373	0.123	0.277	2.597	0.033	0.007	0.004	0.011	0.008	2
30	10.188	0.800	0.550	0.254	2.595	0.032	0.016	0.042	0.094	0.021	3

All the analysis of the data of the three clusters is calculated in a linear fit in which the oldest source data are considered on the X axis and the newest, on the Y axis. A linear relation was calculated in a formula $Y_{new} = A + BX_{old}$. The goodness of the fit is demonstrated by both the correlation coefficient R and the standard deviation of the points. For a good fit, A should be small and B close to 1. The correlation coefficient, R, has to be near unity and the standard deviation, small. All the values obtained for each cluster are presented in Table 7. The final column in the table presents N, the number of entries. Figures 2, 3 and 4 present the comparisons among the principal data sets for IC 4665 (Crawford and Barnes (1972) vs present paper; for NGC 6871 Crawford et al. (1974) vs. Reimann (1989) and Kazlauskas (2013) vs. present paper, respectively.

For the cluster IC 4665 we considered the original sources of Crawford & Barnes (1972) with forty-five entries; of Stetson (1991) with only six measured stars; and our photometry (58 stars), to calculate the mean values of the stars. Of all the sets only star W32 showed anomalies. Its reported V magnitude in Crawford & Barnes (1972) is 10.188, whereas the V magnitude in Stetson (1991), is 8.330. The large difference could be due to either intrinsic variability or eclipses. We ended up with a sample of fifty-six stars of which ten are presented for the first time, four measured in the three sets and thirteen in the intersection of Crawford & Barnes (1972) and the

TABLE 4

OBSERVED $uvby-\beta$ PHOTOELECTRIC PHOTOMETRY OF THE OPEN CLUSTER NGC 6871

ID	V	$(b-y)$	m_1	c_1	$H\beta$	σV	$\sigma(b-y)$	σm_1	σc_1	$\sigma H\beta$	N
01	6.782	0.088	0.167	-0.240	2.473	0.017	0.010	0.000	0.015	0.001	2
03	7.339	0.252	-0.053	-0.055	2.541	0.016	0.003	0.008	0.016	0.006	2
05	7.889	0.262	-0.047	-0.076	2.553	0.035	0.003	0.001	0.007	0.005	2
08	8.700	0.225	-0.050	0.049	2.611	0.076	0.008	0.003	0.040	0.005	2
25	11.662	0.276	-0.039	0.275	2.718	0.029	0.010	0.013	0.020	0.018	2
24	11.721	0.233	0.026	0.279	2.699	0.029	0.011	0.007	0.039	0.018	2
153	8.474	0.884	0.532	0.332	2.558	0.006	0.004	0.020	0.006	0.006	2
07	8.779	0.225	-0.056	0.006	2.596	0.025	0.016	0.021	0.016	0.006	2
04	7.746	0.200	-0.022	-0.148	2.564	0.006	0.000	0.001	0.004		2
09	9.473	0.384	0.175	0.275	2.575	0.003	0.001	0.009	0.008	0.012	2
02	7.270	0.252	-0.055	-0.038	2.547	0.003	0.001	0.001	0.005	0.008	2
13	10.368	0.217	-0.024	0.126	2.690	0.021	0.000	0.013	0.011	0.011	2
31	8.423	0.222	-0.037	-0.021	2.575	0.234	0.001	0.004	0.008	0.008	2
12	10.347	0.343	0.157	0.321	2.628	0.007	0.008	0.012	0.012	0.018	2
15	10.791	0.246	-0.006	0.075	2.639	0.006	0.009	0.006	0.002	0.066	2
10	10.404	0.259	0.145	0.797	2.727	0.408	0.011	0.012	0.017	0.003	2

TABLE 5

OBSERVED $uvby-\beta$ PHOTOELECTRIC PHOTOMETRY OF THE OPEN CLUSTER DZIM 5

ID	V	$(b-y)$	m_1	c_1	Hβ	σV	σ $(b-y)$	σm_1	σc_1	σ Hβ	N
K07	9.254	0.815	0.780	0.194	2.570	0.003	0.000	0.008	0.021	0.013	3
K06	10.179	0.393	0.247	0.292	2.619	0.009	0.008	0.016	0.011	0.037	3
K10	11.444	0.331	0.130	0.324	2.605	0.014	0.010	0.014	0.014	0.031	3
K11	11.920	0.385	0.181	0.327	2.598	0.009	0.020	0.031	0.009	0.037	3
K12	10.357	0.538	0.375	0.323	2.560	0.006	0.001	0.009	0.012	0.007	3
K13	11.293	0.405	0.228	0.285	2.597	0.082	0.016	0.024	0.021	0.017	3
K14	10.001	0.315	0.145	0.397	2.655	0.043	0.003	0.008	0.010	0.028	3
K09	10.556	0.316	0.154	0.385	2.658	0.052	0.017	0.017	0.008	0.016	3
K08	10.608	0.646	0.523	0.323	2.562	0.012	0.008	0.011	0.011	0.029	3
K05	10.752	0.486	0.192	0.382	2.632	0.078	0.012	0.006	0.013	0.014	2
K15	11.828	0.406	0.237	0.382	2.674	0.104	0.030	0.040	0.045	0.044	3
K01	10.378	0.305	0.169	0.424	2.668	0.009	0.006	0.014	0.013	0.003	3
K02	11.178	0.820	0.726	0.245	2.571	0.017	0.020	0.048	0.059	0.036	3
K04	11.943	0.298	0.167	0.305	2.653	0.027	0.027	0.038	0.029	0.048	3

present paper's photometry. Only two were measured in both data sets of the literature, Crawford & Barnes (1972) and Stetson (1991). The mean value for each star is presented in Table 8 along with the standard deviation of each color index.

The column of photometric sources lists the authors whose values we consider in the mean; these are listed at the bottom of the table. The last column presents the spectral type determined from the $uvby-\beta$ photoelectric photometry in a procedure described below.

These coefficients are adequate despite the fact that the span of the color index limits is rather low, particularly in $(b-y)$ from 0 to 0.4; m_1 from 0 to 0.2. On the other hand, the magnitude V limits go from 7 to 11 mag. The linear fit in β was done without W88 which showed a relatively large difference (0.064).

The final list of compiled $uvby-\beta$ photoelectric photometry of IC 4665 is presented in Table 8. Col-

TABLE 6

REFERENCES WITH $uvby-\beta$ PHOTOMETRY FOR THE THREE CLUSTERS

Source	Number of reported stars
IC 4665	
Crawford & Barnes (1972)	47
Perry & Johnston (1982)	2
Schmidt (1982)	1
Olsen (1983)	2
Schuster & Nissen (1988)	2
Sinachopoulos (1990)	2
Stetson (1991)	6
Olsen (1993)	1
Present Paper (2022)	29
Total Number	57
NGC 6871	
Cohen (1969)	8
Crawford et al. (1974)	8
Crawford (1975)	1
Reimann (1989)	18
Present Paper (2022)	16
Total Number	23
DZIM 5	
Kazlauskas, (2013)	14
Present Paper (2022)	14
Total Number	15

umn 1 lists the ID of WEBDA, subsequent columns present the mean magnitudes V and color indexes $(b-y)$, m_1, c_1, and β. The standard deviations are also presented, as well as the references utilized in the mean. The references are presented at the bottom of the table.

For NGC 6871 Crawford et al. (1974) observed 8 stars in the complete $uvby-\beta$ system and 12 only in β; Reimann (1989) presented the majority of the observed stars, a sample of 18 stars in the $uvby-\beta$ system and 22 stars in $uvby$ only. His star 101 is considered to be W31. One more source, Cohen (1969) observed eight stars of the cluster but only in β. The same procedure as in IC 4665 was done, and the coefficients of the cross fits are presented in Table 7. The mean values of the three sources are listed in Table 9, along with the standard deviation and the number of sources involved in the mean. The whole sample is constituted of 23 stars.

In this table all but three stars have standard deviations on the order of hundredths of magnitude. These three stars are W08, W10 and W25. W08 and W25 which were observed by us and are listed in

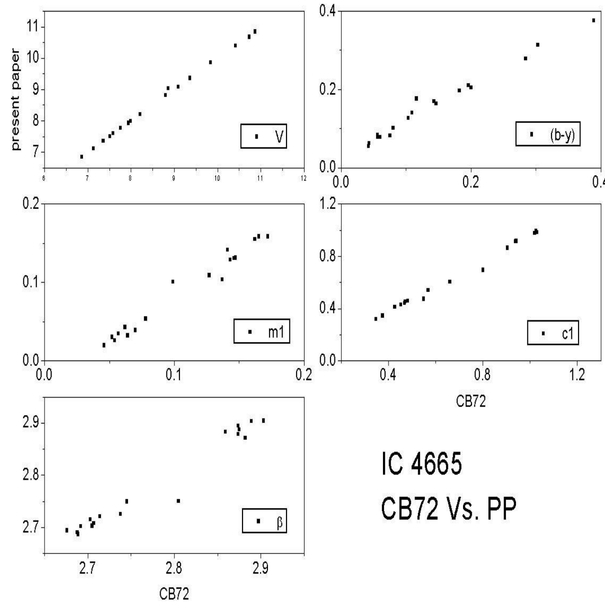

Fig. 2. Comparison of Crawford and Barnes (1972) vs. present paper's photometry for IC 4665.

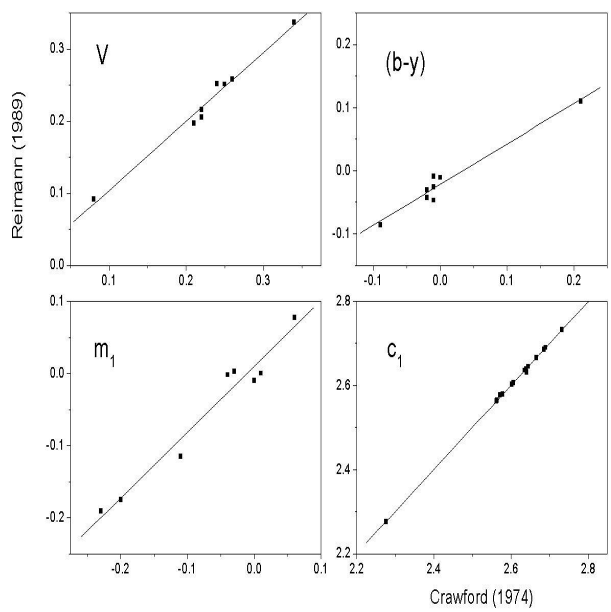

Fig. 3. Comparison of Crawford et al. (1974) vs. Reimann's photometry for NGC 6871.

the table, presented dispersions on the order of hundredths of magnitude, so the high dispersion found in Table 9 is due to either the photometry among the different sources Crawford et al. (1974), Reimann (1989) and Cohen (1969) and ours for star W08 or Crawford et al. (1974), Reimann (1989) and ours for star W25. For W10 we found a dispersion of 0.408,

TABLE 7

LINEAR REGRESSION OF THE $uvby-\beta$ COLOR INDEXES: PRESENT PAPER'S DATA VS. THE LITERATURE

	IC 4665				
Index	A	B	R	Std Dev	N
Crawford & Barnes (1972)	vs.	Stetson (1991)			
V	-0.1437	1.0020	0.9999	0.0411	6
$(b-y)$	-0.0011	0.9647	0.9995	0.0029	6
m_1	-0.0076	1.0369	0.9974	0.0036	6
c_1	-0.0170	1.0396	0.9996	0.0088	6
β	-0.4740	1.1725	0.9999	0.0011	6
Crawford & Barnes (1972)	vs.	Present Paper			
V	0.0460	0.9950	0.9990	0.0454	18
$(b-y)$	0.0308	0.9075	0.9903	0.0131	18
m_1	-0.0322	1.1326	0.9863	0.0090	18
c_1	-0.0230	0.9812	0.9959	0.0234	18
β	-0.0217	1.0089	0.9812	0.0179	17
	NGC 6871				
Crawford et al. (1974)	vs.	Reimann (1989)			
$(b-y)$	0.0087	0.9554	0.9908	0.0102	8
m_1	-0.0219	0.6423	0.9784	0.0128	8
c_1	0.0101	0.9139	0.9796	0.0209	8
β	0.0087	0.9966	0.9996	0.0030	15
Reimann (1989)	vs.	Present Paper			
V	-0.0305	1.0017	0.9979	0.1143	14
$(b-y)$	0.0131	0.9664	0.9797	0.0141	14
m_1	-0.0086	1.3661	0.9578	0.0279	14
c_1	-0.0247	1.3017	0.9872	0.0433	14
β	-1.0105	1.3866	0.9797	0.0143	10
Cohen (1969)	vs.	Present Paper			
β	-1.2661	1.4849	0.9746	0.0071	6
	DZIM 5				
Kazkalauskas et al (2013)	vs.	Present Paper			
V	-0.0921	1.0068	0.9998	0.0181	12
$(b-y)$	0.0078	0.9695	0.9987	0.0103	12
m_1	0.0959	0.5963	0.1167	0.2419	12
c_1	0.3938	-0.2354	-0.7397	0.0451	12

the highest of all the sample. This value was compared with that of Reimann (1989). There is always the possibility that this might show a variable nature of the star.

For the open cluster Dzim 5 there are only two sources with Strömgren photometry, that of Kazlauskas et al., (2013) with only 13 measured stars and ours, with 14 stars. In both sets, basically the same stars were measured. Only two, one in each set, were observed separately. Star 5 was identified but no $uvby-\beta$ measurements are presented. The whole sample therefore contains fifteen stars. Studying the results of the coefficients derived from the linear regression of the $uvby-\beta$ color indexes (newest data vs. older data in the literature) for the three clusters, we observe that R, the correlation coefficient, is always larger than 0.9, and that the standard deviation is less than few hundredths of magnitude implying that all data sets are consistent, except for those in DZIM 5. In DZIM 5 the correlation coefficient

TABLE 8

COMPILED $uvby-\beta$ PHOTOELECTRIC PHOTOMETRY OF IC 4665

ID	V	$(b-y)$	m_1	c_1	Hβ	σV	$\sigma\ (b-y)$	σm_1	σc_1	σ Hβ	Photom. Source	SpTyp
7	9.310	0.315	0.163	0.744	2.774						1	A9Vp
22	8.780	0.089	0.077	0.798	2.771							A0V1
23	8.060	0.070	0.093	0.825	2.826						1	A0V
27	10.320	0.172	0.160	0.978	2.899						1	A4V
28	7.432	0.240	0.105	0.978	2.775	0.003	0.005	0.000	0.008	0.004	1,2	A2V
32	8.330	0.067	0.066	0.964	2.733						1	A8I
34	11.000	0.457	0.091	0.474	2.712						1	F2V
37	11.360	0.384	0.114	0.574	2.698						1	F0V
38	10.702	0.382	0.100	0.512	2.690	0.040	0.009	0.001	0.054	0.002	1,3	F0V
39	9.377	0.199	0.159	0.943	2.887	0.026	0.006	0.004	0.030	0.011	1,2,3	A3V
42	10.896	0.739	0.423	0.056	2.588						3	LATE
43	9.090	0.125	0.120	0.931	2.871	0.000	0.022	0.024	0.015	0.017	1	A2V
44	10.092	0.097	0.130	0.946	2.895						3	A2V
47	9.764	0.380	0.118	0.287	2.623						3	F7V
48	11.580	0.392	0.088	0.510	2.669						1	F0V
49	7.691	0.057	0.072	0.471	2.735	0.006	0.001	0.007	0.001	0.002	1,3	A V
50	9.085	0.190	0.118	0.927	2.885	0.007	0.011	0.013	0.015	0.015	1,3	A2V
51	9.850	0.270	0.100	0.962	2.889						1	A2V
53	11.410	0.366	0.113	0.527	2.702						1	F0V
56	7.504	0.079	0.162	0.999	2.904	0.008	0.005	0.004	0.030	0.001	1,3	A2V
57	11.130	0.327	0.137	0.602	2.698						1	
58	7.599	0.049	0.058	0.424	2.714	0.008	0.012	0.016	0.010	0.007	1,2,3	B V
59	11.030	0.907	0.466	0.485	2.582						1	LATE
62	6.857	0.065	0.043	0.337	2.692	0.003	0.012	0.011	0.014	0.010	1,2,3	B V
63	10.560	0.222	0.167	0.837	2.834						1	A4V
64	7.357	0.067	0.048	0.462	2.709	0.005	0.016	0.022	0.011	0.009	1,3	B V
65	10.600	0.278	0.165	0.716	2.760						1	A8Vp
66	10.403	0.203	0.165	0.884	2.877	0.011	0.010	0.009	0.029	0.004	1,3	A5V
67	8.803	0.155	0.139	1.010	2.897	0.005	0.013	0.011	0.021	0.011	1,3	A3V
68	7.936	0.309	0.139	0.471	2.685	0.010	0.008	0.011	0.015	0.013	1,3	F0V
70	10.262	0.812	0.378	0.203	2.582						3	LATE
71	10.942	0.433	0.070	0.409	2.656						3	
72	7.765	0.048	0.053	0.360	2.704	0.008	0.009	0.013	0.021	0.001	1,3	B V
73	7.126	0.070	0.040	0.442	2.688	0.005	0.020	0.020	0.015	0.001	1,3	B V
74	10.549	0.806	0.502	0.160	2.581						3	LATE
76	8.213	0.115	0.066	0.554	2.747	0.005	0.017	0.017	0.019	0.003	1,3	B V
81	8.924	0.136	0.036	0.644	2.705	0.092	0.035	0.014	0.033	0.004	1,2,3	A0V
82	7.993	0.091	0.046	0.455	2.732	0.004	0.015	0.016	0.018	0.009	1,3	B V
83	10.210	0.191	0.137	0.996	2.888						1	A3V
84	9.792	0.473	0.136	0.467	2.655						3	G0V
86	10.390	0.412	0.102	0.574	2.663						1	F0V
88	10.858	0.281	0.141	0.747	2.778	0.017	0.004	0.000	0.074	0.038	1,3	A6V
89	9.846	0.156	0.136	1.006	2.877	0.009	0.018	0.010	0.032	0.007	1,3	A0V
90	8.300	1.095	0.804	0.012	2.595						3	LATE
92	10.845	0.974	0.676	0.281	2.562						3	LATE
95	9.880	1.256	0.470	0.591	0.000						1	LATE
96	8.907	0.490	0.335	0.284	2.555						1	LATE
98	8.375	0.780	0.385	0.301	2.581						3	LATE
99	7.530	1.259	0.232	0.904	0.000						1	LATE
102	9.290	0.111	0.136	1.092	2.908						1	A2V
105	7.490	0.040	0.084	0.535	2.732						1	B V
111	10.000	0.282	0.168	0.727	2.765						1	A9Vp
115	9.150	0.275	0.182	0.705	2.788						1	A8Vp
118	10.320	0.235	0.120	0.986	2.910						1	A3V
121	8.610	0.245	0.166	1.056	2.838						1	A4V
125	9.700	0.142	0.130	1.156	2.882						1	F2Ib
178	7.705	0.071	0.048	0.459	2.744						3	B V

Note: 1 Crawford, 1971; 2 Stetson, 1991; 3 PP.

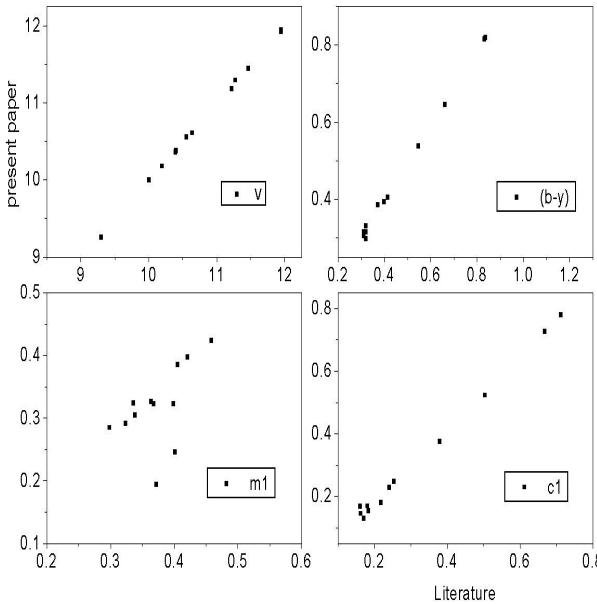

Fig. 4. Comparison of Kazlauskas (2013) vs. present paper photometry for Dzim 5.

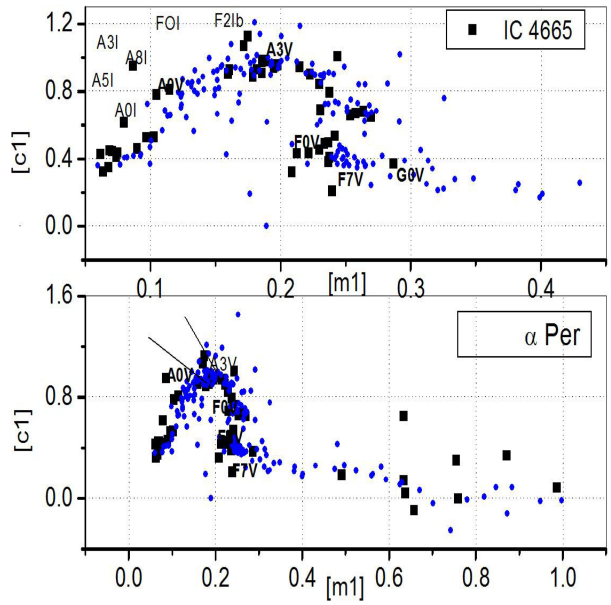

Fig. 5. Position of the stars of IC 4665 in the $[m_1]-[c_1]$ (filled squares) diagram of α Per (Peña & Sareyan, 2006), dots. The color figure can be viewed online.

R gave anomalous values in m_1 and c_1 implying, of course, no correlation between both sets. In view of this, we averaged only V and $(b-y)$ in the sets of Dzim 5 between Kazlauskas et al. (2013) vs. present paper. Their photometry did not include Hβ. The averaged values are presented in Table 10, following Kazlauskas et al., (2013) ID numbers: In Figure 1, star 15 was added because it was not observed by Kazlauskas et al., (2013). Because of the poor linear regression in m_1 and c_1 the average was done only for V and $(b-y)$. Table 10 presents the mean of the $uvby-\beta$ photometry and the standard deviation of the sources.

4. DETERMINATION OF CLUSTER PARAMETERS

In order to determine the physical characteristics of the stars in the three clusters, IC 4665, NGC 6871 and Dzim 5, the same procedure as in Paper I for NGC 6633 was carried out. This procedure briefly, consists of the following steps:

To evaluate the reddening we first established to which spectral class the stars belong: early (B and early A) or late (late A and F stars) types; the later class stars (G or later) were not considered in the analysis since there is no reddening calibration for MS stars.

To determine the spectral type of each star we utilized the compiled $uvby-\beta$ photoelectric photometry of each open cluster calculating the unreddened indexes $[m1]$, $[c1]$ and compared their position with the stars of the open cluster Alpha Per (Peña & Sareyan, 2006) for which the stars have well-defined spectral class. The results are presented schematically in Figures 5, 6 and 7 for IC 4665, NGC 6871 and Dzim 5, respectively. The last column of each compiled $uvby-\beta$ photoelectric photometry presents the assigned spectral type.

The photoelectrically classified spectral types of the stars are in very good agreement with those obtained by spectroscopy and reported by WEBDA. It can be seen that the observed stars, which are the brightest in the field, are of all spectral types in the case of NGC 6871 but all late type stars for Dzim 5.

The reddening was determined through Strömgren photometry once the spectral types were classified. The application of the calibrations for each spectral type, of Balona & Shobbrook (1984) and Shobbrook (1984) for O and early A type and of Nissen (1988) for late A and F stars, respectively, allowed us to determine their reddening and hence, their unreddened color indexes. As has been said, no determination of reddening was calculated for G or later spectral types. The procedure has been extensively described in Peña & Martínez (2014). Once the reddening is calculated, the distances can be determined for each star.

The output for the three clusters is presented in Tables 11, 12, and 13 for IC 4665, NGC 6871 and

TABLE 9

COMPILED $uvby-\beta$ PHOTOELECTRIC PHOTOMETRY OF NGC 6871

ID	V	$(b-y)$	m_1	c_1	Hβ	σV	σ $(b-y)$	σm_1	σc_1	σ Hβ	Photom. Source	SpTyp
1	6.788	0.087	0.162	-0.220	2.473	0.008	0.006	0.050	0.026		1,2,3,4	
2	7.288	0.251	-0.035	-0.016	2.558	0.025	0.001	0.018	0.019	0.010	1,2,3,4	B V
3	7.353	0.248	-0.037	-0.027	2.556	0.021	0.007	0.023	0.029	0.011	1,2,3,4	B V
4	7.767	0.202	-0.011	-0.124	2.571	0.029	0.007	0.011	0.020	0.006	1,2,3,4	B V
5	7.902	0.260	-0.037	-0.039	2.570	0.018	0.002	0.014	0.037	0.013	1,2,4	B V
6	8.187	0.339	-0.088	-0.188	2.276		0.002	0.003	0.018	0.175	1,2,4	B V
7	8.792	0.217	-0.025	0.005	2.600	0.019	0.010	0.027	0.005	0.162	1,2,3,4	B V
8	8.790	0.220	-0.029	0.062	2.608	0.127	0.004	0.020	0.014	0.003	1,2,3,4	B V
9	9.452	0.383	0.159	0.256	2.575	0.030	0.001	0.022	0.028		2,3	F9V
10	10.263	0.262	0.122	0.822	2.727	0.199	0.005	0.032	0.035		2,3	A2V
11	10.332	0.205	-0.005	0.075	2.636						2	B V
12	10.335	0.345	0.133	0.314	2.628	0.017	0.003	0.034	0.009		1,2	F9V
13	10.372	0.210	-0.002	0.116	2.660	0.006	0.011	0.031	0.014	0.026	1,2	B V
14	10.796	0.210	-0.004	0.244	2.637					0.006	1,2	B V
15	10.776	0.254	-0.020	0.118	2.639	0.021	0.012	0.020	0.061	0.000	1,2,3	B V
16	10.980	0.203	0.009	0.255	2.550					0.141	1,2	B V
17	11.251	0.320	-0.019	0.238							2	B V
18	11.319	0.171	0.094	1.225							2	F2Ib
19	11.542	0.194	0.024	0.298							2	B V
20	11.558	0.256	0.015	0.612	2.571						2	B V
21	11.661	0.244	-0.040	0.380	2.666					0.000	1,2	B V
22	11.646	0.214	0.110	0.896							2	A2V
23	11.638	0.172	0.084	0.177							2	
24	11.732	0.229	0.032	0.253	2.690	0.017	0.005	0.008	0.036	0.008	1,2,3	B V
25	11.761	0.256	-0.017	0.293	2.699	0.140	0.029	0.031	0.025	0.016	1,2,3	B V
26	11.830	0.230	0.102	0.832							2	A2V
27	11.874	0.286	-0.016	0.335	2.732					0.000	1,2	B V
28					2.77						1	
29					2.782						1	
30					2.788						1	
31=R101	8.402	0.218	-0.025	-0.010	2.583	0.029	0.006	0.018	0.014	0.011	2,3	B V
R102	9.780	1.094	0.431	0.274							2	LATE
R103	12.117	0.220	0.024	0.481							2	B V
R104	11.259	0.260	0.012	0.479							2	B V
R105	11.756	0.388	0.056	0.431							2	A0V
R106	11.718	0.261	-0.002	0.227							2	
R107	10.775	0.239	0.077	0.857							2	B V

Note: 1 Crawford, 1974; 2 Reimann, 1989; 3 PP, 4 Cohen.

Dzim 5, respectively. In each table Column 1 lists the ID of the star, Column 2 the reddening $E(b-y)$; Columns 3 to 5 the unreddened indexes $(b-y)$, m_1, c_1; Column six lists $H\beta$, the remaining columns list the V_0 and the absolute magnitude M_V. The next two columns present the distance modulus, in magnitudes, and the distance in parsecs. In the case of F type stars we present [Fe/H]. The last column provides the assigned membership, either M for the member stars or N for the non-members. Member stars within one sigma from the mean are considered members, the others, non-members. Figures 8, 10 and 11 present the histograms of the distance modulus for the stars.

TABLE 10

COMPILED $uvby-\beta$ PHOTOELECTRIC PHOTOMETRY OF DZIM 5

ID	V	$(b-y)$	m_1	c_1	$H\beta$	σV	$\sigma(b-y)$	Photom. Source	
1	10.390	0.308	0.169	0.424	2.668	0.018	0.004	1,2	F9V
2	11.198	0.828	0.726	0.245	2.571	0.027	0.012	1,2	LATE
3	08.763	1.115	0.719	0.528				1	
4	11.944	0.309	0.167	0.305	2.653	0.000	0.016	1,2	G0
5	10.752	0.486	0.192	0.382	2.632			2	LATE
6	10.188	0.397	0.247	0.292	2.619	0.013	0.005	1,2	LATE
7	09.275	0.823	0.780	0.194	2.570	0.031	0.011	1,2	LATE
8	10.622	0.654	0.523	0.323	2.562	0.021	0.012	1,2	LATE
9	10.557	0.313	0.154	0.385	2.658	0.001	0.003	1,2	F9V
10	11.456	0.326	0.130	0.324	2.605	0.016	0.008	1,2	F8
11	11.932	0.378	0.181	0.327	2.598	0.018	0.010	1,2	G1V
12	10.374	0.542	0.375	0.323	2.560	0.024	0.006	1,2	LATE
13	11.284	0.410	0.228	0.285	2.597	0.012	0.007	1,2	LATE
14	10.002	0.317	0.145	0.397	2.655	0.001	0.003	1,2	F8V
15	11.828	0.406	0.237	0.382	2.674			2	LATE

Note: 1 Kazlauskas (2013, V and $(b-y)$ only; 2 PP.

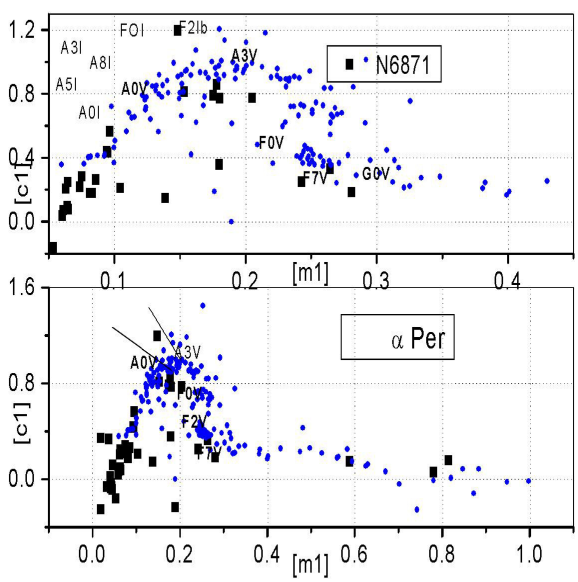

Fig. 6. Position of the stars of NGC 6871 in the $[m_1]-[c_1]$ (filled squares) diagram of α Per (Peña & Sareyan, 2006), dots. The color figure can be viewed online.

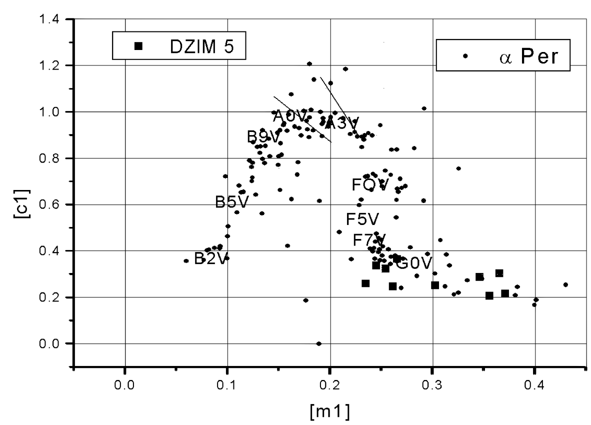

Fig. 7. Position of the stars of Dzim 5 in the $[m_1]-[c_1]$ (filled squares) diagram of Alpha Per (Peña & Sareyan, 2006).

As can be seen in Figure 8, in the case of IC 4665, the Gaussian peak is at 7.5 ± 0.6. Those stars within these limits are considered to be member stars and are denoted by M in Table 11. Those outside these limits are considered to be non-members and are denoted by NM in the same table. The last column of Table 11 lists the membership probabilities reported by WEBDA. For IC 4665 out of forty-four compiled stars within the spectral class limits, twenty five can be considered members of the cluster. Of these, eleven stars have high membership probability reported by WEBDA, larger than 0.7 and only four have very low membership probability. Of the nineteen stars that we considered out of the cluster limits, only three have been assigned a high membership probability in the literature. So, overall, the agreement is not bad and, hence, the membership that we assigned for those eight stars that did not have previously assigned probability is a new and important result. Among the F type stars that are within the distance limits there are five stars with determined [Fe/H]. The mean value gives -0.221 ± 0.230 if the large value of -0.597 of W71 is considered; without

TABLE 11

REDDENING AND UNRREDDENED PARAMETERS OF IC 4665

ID	$E(b-y)$	$(b-y)_0$	m_0	c_0	Hβ	V_0	M_V	DM	Distance	[Fe/H]	Membership	Probab
											PP	Webda
49	0.000	0.228	0.072	0.471	2.735	7.69	4.54	3.15	43		NM	0.85
68	0.052	0.257	0.155	0.461	2.685	7.71	3.53	4.19	69	-0.09	NM	
47	0.053	0.327	0.134	0.276	2.623	9.53	4.99	4.54	81	-0.50	NM	
115	0.112	0.163	0.216	0.683	2.788	8.67	3.26	5.41	121		NM	
56	0.096	-0.017	0.191	0.981	2.904	7.09	1.31	5.78	143		NM	
34	0.227	0.230	0.159	0.429	2.712	10.02	4.06	5.97	156	-0.11	M	
07	0.145	0.170	0.206	0.715	2.774	8.69	2.69	5.99	158		M	
84	0.171	0.302	0.187	0.433	2.655	9.06	3.02	6.04	161	0.26	M	0
28	0.266	-0.026	0.185	0.927	2.775	6.29	-0.19	6.48	197		M	
71	0.153	0.280	0.116	0.378	2.656	10.28	3.75	6.54	203	-0.60	M	
67	0.173	-0.018	0.191	0.977	2.897	8.06	1.25	6.81	231		M	0.74
111	0.103	0.179	0.199	0.706	2.765	9.56	2.71	6.85	234		M	
38	0.135	0.247	0.141	0.485	2.690	10.12	3.20	6.92	242	-0.30	M	0.04
50	0.221	-0.031	0.184	0.885	2.885	8.13	1.17	6.96	247		M	0.84
23	0.107	-0.037	0.125	0.805	2.826	7.60	0.61	6.99	250		M	
66	0.130	0.073	0.204	0.858	2.877	9.84	2.69	7.15	270		M	0.86
121	0.158	0.087	0.213	1.024	2.838	7.93	0.77	7.17	271		M	
39	0.229	-0.03	0.228	0.900	2.887	8.39	1.18	7.21	277		M	0.86
51	0.299	-0.029	0.190	0.905	2.889	8.56	1.20	7.36	297		M	
62	0.147	-0.082	0.087	0.309	2.692	6.23	-1.15	7.38	299		M	0.02
43	0.154	-0.029	0.166	0.902	2.871	8.43	1.03	7.39	301		M	0.83
63	0.110	0.112	0.200	0.815	2.834	10.09	2.69	7.39	301		M	
178	0.137	-0.066	0.089	0.433	2.744	7.11	-0.34	7.45	309		M	0
65	0.094	0.184	0.193	0.697	2.760	10.20	2.74	7.46	311		M	0.87
53	0.130	0.236	0.152	0.501	2.702	10.85	3.36	7.49	314	-0.17	M	0.23
102	0.101	0.010	0.166	1.073	2.908	8.86	1.30	7.56	325		M	0
105	0.097	-0.057	0.113	0.516	2.732	7.07	-0.49	7.56	325		M	0
64	0.133	-0.066	0.088	0.437	2.709	6.79	-0.84	7.62	335		M	0.83
88	0.114	0.167	0.175	0.724	2.778	10.37	2.73	7.64	337		M	0.84
73	0.138	-0.068	0.082	0.416	2.688	6.53	-1.20	7.73	352		M	0.47
76	0.172	-0.057	0.118	0.521	2.747	7.47	-0.28	7.75	355		M	0.78
82	0.158	-0.067	0.093	0.425	2.732	7.31	-0.50	7.81	365		M	0.8
118	0.260	-0.025	0.198	0.937	2.910	9.20	1.38	7.83	368		M	
58	0.119	-0.070	0.094	0.401	2.714	7.09	-0.76	7.85	372		M	0.88
86	0.139	0.273	0.144	0.546	2.663	9.79	1.90	7.89	379	-0.25	M	
37	0.145	0.239	0.158	0.545	2.698	10.73	2.79	7.94	388	-0.08	M	0.1
89	0.175	-0.019	0.188	0.973	2.877	9.09	1.06	8.04	405		M	0.22
83	0.213	-0.022	0.201	0.956	2.888	9.29	1.17	8.12	421		M	0.8
72	0.126	-0.078	0.091	0.336	2.704	7.22	-0.95	8.17	430		M	0.46
27	0.196	-0.024	0.219	0.941	2.899	9.48	1.28	8.20	436		M	
57	0.089	0.238	0.164	0.584	2.698	10.75	2.51	8.24	444	0.00	M	0.67
48	0.127	0.265	0.126	0.485	2.669	11.03	2.78	8.26	448	-0.45	M	
32	0.000	0.18	0.066	0.964	2.733	8.33	0.06	8.27	451		M	0.58
22	0.128	-0.039	0.115	0.774	2.771	8.23	-0.07	8.30	457		M	
44	0.124	-0.027	0.167	0.922	2.895	9.56	1.25	8.31	459		NM	
81	0.185	-0.049	0.092	0.609	2.705	8.13	-1.03	9.15	677		NM	0.86
Mean	0.152							7.43	319	-0.19		
Std dev	0.056							0.64	85	0.25		

this value the mean value of [Fe/H] is -0.127 ± 0.107. At any rate, for our analysis we considered a solar value. WEBDA does not assign a metallicity value for IC 4665. Figure 9 presents the distance modulus histograms for each spectral type. In Figure 9 it can be seen the peaks for each spectral group, F, A, B and combined; they are all centered at the same distance modulus.

For NGC 6871 most of the observed stars could not be analyzed with the prescriptions to determine the reddening because many of them did not have Hβ measurements. With the compiled sample of

TABLE 12

REDDENING AND UNREDDENED PARAMETERS OF NGC 6871

ID	$E(b-y)$	$(b-y)_0$	m_0	c_0	$H\beta$	V_0	M_V	DM	Distance (pc)	Membership (pp)
12	0.012	0.328	0.134	0.308	2.620	10.3	4.6	5.6	134	NM
25	0.022	0.228	-0.003	0.286	2.690	11.7	5.5	6.1	168	NM
37	0.484	-0.034	0.135	0.848	2.950	10.4	1.7	8.7	541	NM
10	0.057	0.203	0.137	0.809	2.720	10.0	1.1	9.0	621	NM
8	0.335	-0.115	0.080	-0.004	2.600	7.4	-3.6	11.0	1574	close
27	0.368	-0.088	0.100	0.260	2.730	10.3	-0.7	11.0	1581	close
13	0.320	-0.110	0.096	0.049	2.660	9.0	-2.2	11.2	1734	close
7	0.329	-0.119	0.079	-0.063	2.600	7.4	-3.9	11.3	1806	close
5	0.383	-0.123	0.085	-0.103	2.570	6.3	-5.1	11.4	1886	close
31	0.338	-0.120	0.076	-0.074	2.583	6.95	-4.47	11.42	1924	close
24	0.316	-0.096	0.125	0.190	2.690	10.4	-1.4	11.7	2208	far
11	0.314	-0.114	0.094	0.010	2.630	9.0	-2.9	11.9	2354	far
14	0.307	-0.097	0.092	0.182	2.630	9.5	-2.5	12.0	2459	far
15	0.361	-0.111	0.088	0.041	2.630	9.2	-2.8	12.0	2483	far
21	0.320	-0.080	0.056	0.319	2.660	10.3	-1.8	12.0	2549	far
4	0.330	-0.130	0.089	-0.183	2.570	6.3	-5.8	12.2	2711	far
Mean (close)								11.2	1751	close
Std dev								0.2	149	
Mean (far)								12.0	2461	far
Std dev								0.2	171	

TABLE 13

REDDENING AND UNREDDENED PARAMETERS OF DZIM 5

ID	$E(b-y)$	$(b-y)_0$	m_0	c_0	Hβ	V_0	M_V	DM	Distance	[Fe/H]
12	0.020	0.285	0.175	0.420	2.668	10.29	3.76	6.53	203	0.164
8	0.022	0.294	0.161	0.381	2.658	10.46	4.07	6.39	190	-0.051
7	0.021	0.294	0.151	0.393	2.655	9.91	3.88	6.03	161	-0.174
14	0.000	0.306	0.167	0.305	2.653	11.94	4.98	6.96	247	0.004
3	0.000	0.340	0.130	0.324	2.605	11.44	4.26	7.19	274	-0.627
Mean	0.01							6.62	215	-0.14
Std dev	0.01							0.46	45	0.30

Table 9, represented schematically in Figure 3, we realized that most of the stars lie in the early type stars branch. The applicable prescription for early type stars gives the results presented in Table 12. In this table we have separated the stars in three categories depending on their distance; the first group labelled as non-members, and for the second and third group, those below and above distance modulus of 11.5, were labelled as “close” and “far”, respectively. Mean values and standard deviation were calculated for the second and third groups. As can be seen, no overlap is possible, even considering the limits of the standard deviation, assuring us of a separate existence. The histogram of the distance is presented in Figure 10 in which the two groups are clearly discernible.

In this figure the stars are grouped in two peaks. A Gaussian fit determined one at a distance of 1750 ± 80 pc and the other at $2430\pm$ 194 pc. Given the uncertainties one cannot group all the stars in just one cluster because the spread would be too large. We encountered this situation before when we studied the cluster of NGC 6882/5 (Peña et al., 2008) where we found two clusters at distances of

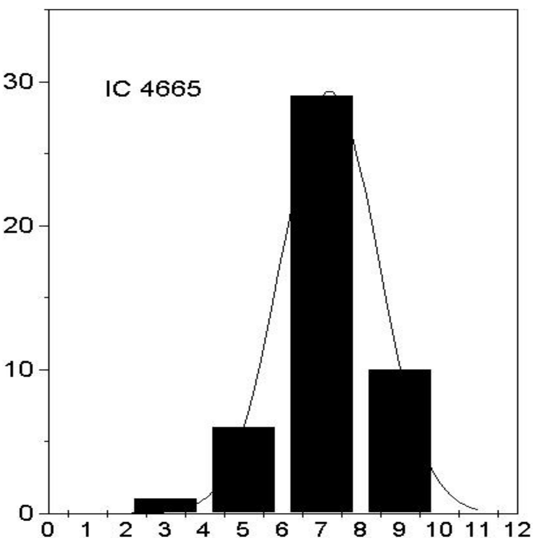

Fig. 8. Histogram of the distance modulus (X axis) of the stars in the direction of IC 4665.

289 ± 92 pc and 1019 ± 134 pc. At the bottom of each group in Table 12 we present the mean values and the standard deviation of reddening $E(b-y)$, distance modulus and distance for the stars that we consider to be members of each cluster. Unfortunately, the membership probability reported in the literature is for only five stars, none of which was measured in this paper.

In the case of the open cluster Dzim 5 it has been suggested in the literature that there is no clear evidence of the existence of the cluster. We have measured, as did Kazlauskas (2013), the fourteen brightest stars in the field. Given the limitation imposed by the telescope-spectrophotometer system, no fainter stars could be observed. In the $[m_1]$ - $[c_1]$ diagram we can see that all the stars are of spectral types F and later, and there is no evidence of earlier stars. Hence, the analysis with the prescription of Nissen (1988) has to be considered and yields the results presented in Table 13 for the five F type stars shown schematically in Figure 11. They are all located at nearly the same distance, 215 ± 45 pc, and have a [Fe/H] value of -0.14 ± 0.30. This value is close to that determined from the values reported in Column nine of Table 2 of Kazlauskas (2013). The mean values and the standard deviation of reddening $E(b-y)$, distance modulus, and distance for the stars that we consider to be members are presented at the bottom of Table 13. However, the question of the real existence of a cluster constituted by only four or five late type stars still remains.

To determine age one must first determine the temperature of the hottest main sequence stars. The

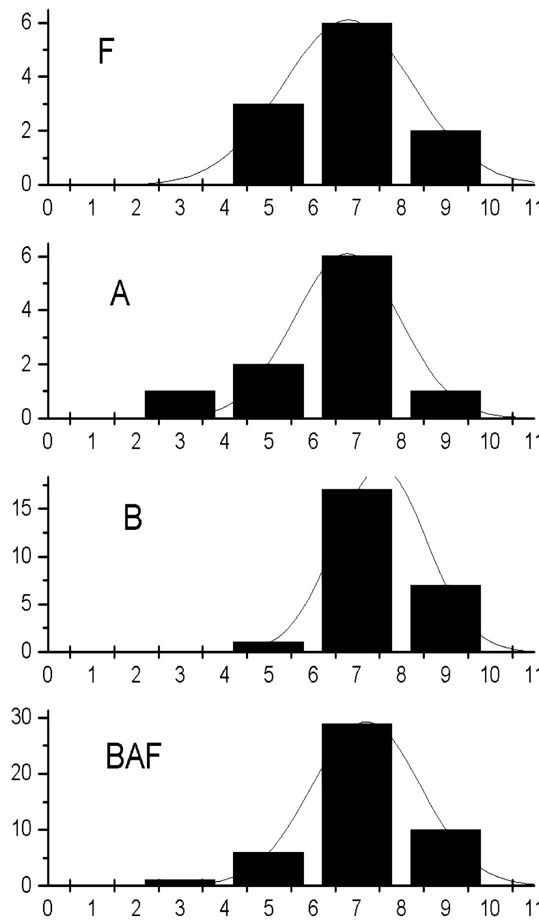

Fig. 9. Histogram of the distance modulus (X axis) of the stars in the direction of IC 4665 for each spectral type.

effective temperature of these hottest stars was calculated by plotting the location of all stars on the theoretical grids of Lester, Gray and Kurucz (1986, hereinafter LGK86), after we calculated the unreddened colors (Figures 15, 16 and 17) for the correct chemical composition of the considered model.

For IC 4665 we have utilized the c_0 vs. Hβ diagram of LGK86 which allows the determination of the temperatures of the hottest star with an accuracy of a few hundreds of degrees (Figure 15). This star is W62 at 16900 K.

For NGC 6871 we had to consider the existence of the two overlapped clusters. For the closest, the two hottest stars over the MS are stars W11 and W15 of 25000K and 23000K, whereas for the other cluster, the hottest star on the MS is star W13 at 35000K (Figure 16). For Dzim 5, Figure 17 represents the unreddened points in the $(b-y)$ vs. c_0 diagram. The hottest star, W15 has a temperature of 6,200 K.

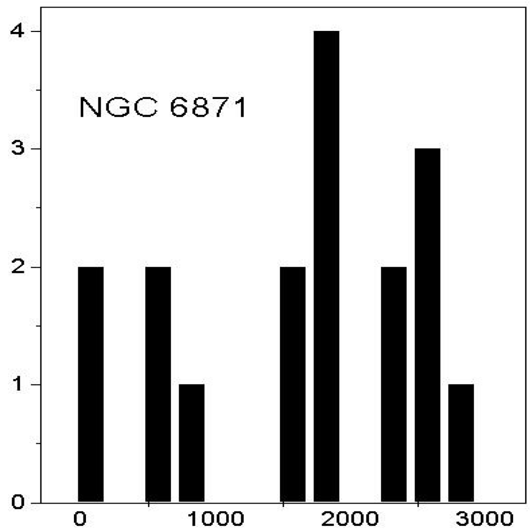

Fig. 10. Histogram of the distance (pc) (X axis) of the stars in the direction of NGC 6871.

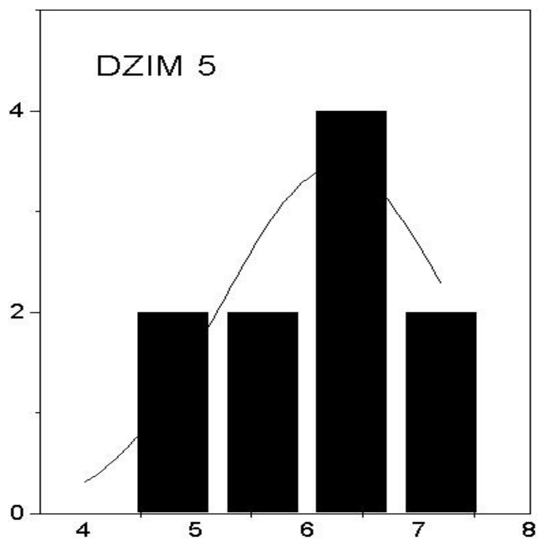

Fig. 11. Histogram of the distance modulus (X axis) of the stars in the direction of Dzim 5.

Once the membership and effective temperature have been established, age is determined through the calibrations of Meynet, Mermilliod & Maeder (1993) as a function of the temperature:

- if the $\log T_e$ is in the range [4.25, 4.56],

$$\log_{10}(\text{age}) = -.3499 \times \log T_e + 22.476, \quad (1)$$

- if the $\log T_e$ is in the range [3.98, 4.25],

$$\log_{10}(\text{age}) = -3.611 \times \log T_e + 22.956, \quad (2)$$

- if the $\log T_e$ is in the range [3.79, 3.98],

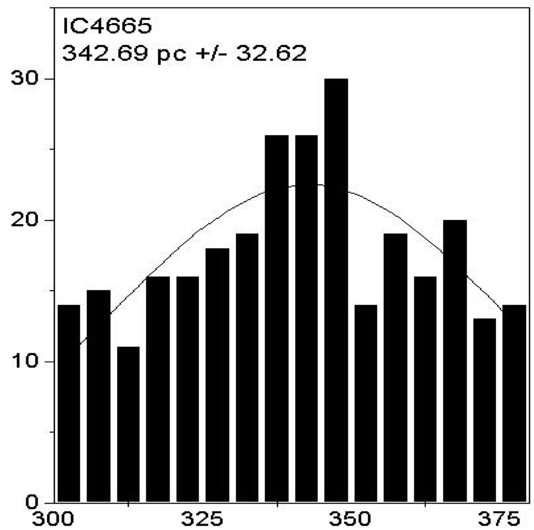

Fig. 12. Histogram of the distances (pc) to the cluster IC 4665 determined through the GAIA Data Release 2 (GAIA DR2).

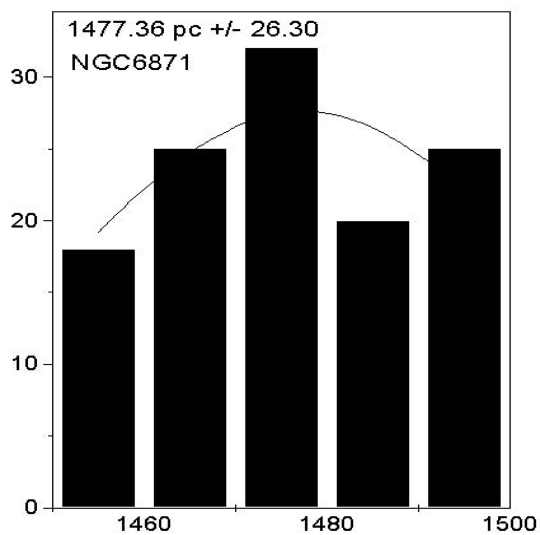

Fig. 13. Histogram of the distances (pc) to the cluster NGC 6871 determined through the GAIA Data Release 2 (GAIA DR2).

$$\log_{10}(\text{age}) = 15.142\,[\log_{10}(T_e)]^2 - 122.810\log_{10}(T_e) + 257.518\ . \quad (3)$$

The location of the member stars in the isochrones provided by WEBDA has also been done. Since this figure is presented in the customary HR diagram $(B - V)$ vs. V those stars that were determined to be members have been identified in the data set of Hogg & Kron (1955). The chemical composition that best fits the data is 0.019. This model correctly describes the evolutive path. The other impor-

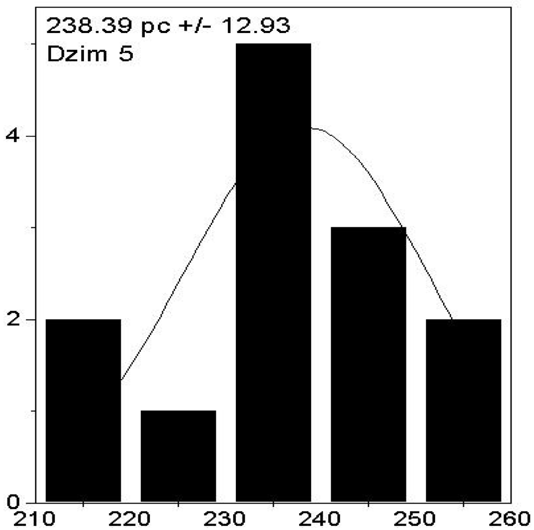

Fig. 14. Histogram of the distances (pc) to the cluster Dzim 5 determined through the GAIA Data Release 2 (GAIA DR2).

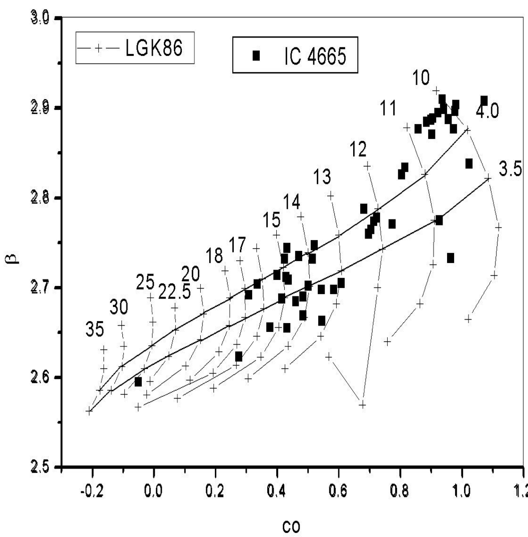

Fig. 15. Location of the unreddened points of IC 4665 (filled squares) in the LGK86 grids. The values of the effective temperature, indicated in thousands Kelvins as a vertical dashed line and surface gravity, indicated as a horizontal straight line, can be measured.

tant parameters from the isochrone plot of Webda (Geneva) are a distance modulus of 7.73, $E(B-V)$ of 0.174, Av of 0.158 and a log age of 7.65.

In the case of NGC 6871, WEBDA does not report metallicity values and all the stars measured turned out to be early type stars. There was one star of spectral type A which does not belong to the cluster and two more of spectral type G or later for which there is no calibration. In view of this we

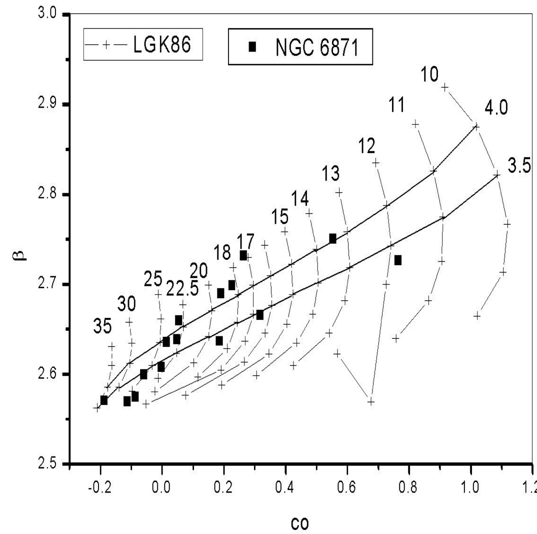

Fig. 16. As in Figure 15 but for NGC 6871. Location of the unreddened points of the open cluster NGC 6871 (filled squares) in the LGK86 grids. As in Figure 15 the values of effective temperature indicated in thousands Kelvins as a vertical dashed line and surface gravity, indicated as a horizontal straight line, can be measured.

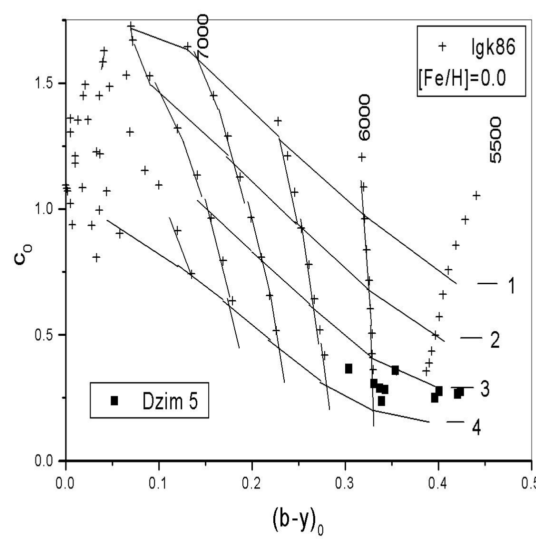

Fig. 17. Location of the unreddened points of Dzim 5 (filled squares) in the LGK86 grids. Values of effective temperature, in Kelvins, and surface gravity are indicated.

considered a solar composition. The location of the stars in the LGK86 grids for this cluster is presented in Figure 16. The value of log age is presented in Table 14.

TABLE 14

DISTANCE AND AGE DETERMINATION FOR EACH CLUSTER

Cluster	Distance	Star	T_e	$\log T_e$	log age
	pc		K		
IC 4665	343 ± 71	62	16000	4.204	7.775
NGC 6781-I	1713 ± 123	5,7	25000	4.398	7.088
NGC 6781-II	2464 ± 156	4	35000	4.544	6.576
Dzim 5	152 ± 32	15	6200	3.792	9.550

5. DISTANCES TO THE CLUSTERS DETERMINED THROUGH THE GAIA DATA RELEASE 2 (GAIA DR2)

The above mentioned membership determined through the distance distribution on a histogram has been tested on the open cluster Alpha Per (Peña & Sareyan, 2006). However, this determination can be verified using more modern and advanced techniques such as GAIA Data Release 2 for 2018, providing astrometric data from more than a billion sources. The distances cannot be determined merely by inverting the parallax since going from parallax to distance is not trivial. The way to obtain the pure geometric distance is by considering a Bayesian statistical analysis (Luri et al. 2018). Once the parallax has been obtained, the parallax data can be used to infer geocentric distance taking this correction to account for the non-linearity of the transformations and the asymmetry of the resulting probability distribution as mentioned by Bailer-Jones (2018). In their paper they present a set of data of 1.3 billion stars with corrected pure geometric distances from the GAIA DR2 sources.

The data of the 1.3 billion sources are now accessible in the GAIA archive (`http://gea.esac.esa.int/archive/`) and were used in the present paper to look for the existence of the studied clusters, IC 4665, NGC 6871 and Dzim 5. To do so, we performed a cone search centered on the coordinates (RA/Dec) of the cluster with a radius greater than that assumed by Webda for the cluster, using the whole sample and taking 20 as a magnitude limit.

In the case of NGC 6871 the radius was chosen through visual inspection. In Table 15, Column 1 lists the ID, Column 2, the coordinates from Webda, Column 3, the assumed cluster diameter in arcmin, Column 4, the considered radius which contains the whole cluster, Column 5 the number of stars contained in the cone and Column 6 the distance in parsecs in the histograms (Figures 12, 13 and 14). The uncertainties are the RMS error of the fit. These results are also presented in Table 15 for IC 4665, NGC 6871 and Dzim 5, respectively.

The comparison of our determined distance measures with those in the Gaia catalog DR2 were also done on a star-by-star basis. These are presented in Tables 16, 17 and 18 for IC 4665, NGC 6871 and Dzim 5, respectively; Column 1 lists the ID of Webda, Column 2, the ID of GAIA DR2 ordered by the distance obtained in the present paper (Column 3). Column 4 presents GAIA's distance and the final column lists the assumed membership in the present paper.

6. DISCUSSION AND CONCLUSIONS

Our study of the three clusters through $uvby-\beta$ photoelectric photometry has been done and led us to derive interesting results. The first cluster, IC 4665, is a well-known cluster which has served as a prototype for classical works. This allowed us to do two things with our photometry. First, to corroborate the goodness of our photometric values; and second, with an extended basis, to corroborate the previous findings.

Although the observational data of NGC 6871 are scarce, with the GAIA DR2 results we were able to confirm the existence of two accumulations of stars, which, as in the case of NGC 6882/5 (Peña et al. 2008), show up as two distinct clusters in the line of sight. However, there are some differences in interpretation between the GAIA DR2 results and those we obtained through Strömgren photometry: W11, W15, W21, W24, and W31 are placed in the nearest cluster, while we put them in the farthest one; W7 appears in the farthest cluster with the GAIA DR2 results, but in the nearest with ours. There is also the case of W25. We discarded it as a member of either cluster, but GAIA places it in the nearest cluster. As was mentioned in § 3, in our analysis this star presents a high dispersion, as can be seen in Table 9, and this dispersion could have caused the differences in interpretation. There is one star, W101, which we did not observe. We listed it in Table 9 but different sources assigned very discordant values to its magnitude. In view of these discrepancies we did not consider it in the analysis. At any rate, there are two clusters in the same direction regardless of the distance determination technique.

The final cluster, Dzim 5, as here stated and according to previous works, might not be a cluster despite the claim of its existence by Dolidze & Jimsheleishvili (1966). Our findings are puzzling. We found that there is a small group of five or six stars, basically at the same distance, and all are of

TABLE 15

DISTANCES TO THE CLUSTERS DETERMINED THROUGH GAIA DATA RELEASE 2

ID	RA/Dec	Assumed cluster diameter	Used radius	No. Stars in Cone	GAIA distance
	hh:mim:sec deg:min:sec	arcmin	arcmin		pc
IC 4665	17:46:18 +05:43:00	45	30	33101	342 ± 32
NGC 6871	20:05:59 +35:46:36	18	11	19032	1477 ± 26
DZIM 5	16:27:24 +38:04:00	27	15	1113	238 ± 13

TABLE 16

IC 4665, STAR BY STAR DISTANCE COMPARISON BETWEEN GAIA AND THE PRESENT PAPER

ID WBDA	ID GAIA	Dst PP (pc)	Dst GAIA (pc)	Membership PP
68	4473856639546336640	69	119	N
47	4474127634803192448	81	110	N
56	4474079015773324928	143	155	N
67	4474058984045718400	231	313	N
50	4473670783424690816	247	326	M
66	4474073518215093632	270	340	M
62	4474048263807307776	289	272	M
43	4474064447244215168	301	357	M
65	4474102036798006912	311	343	M
49	4474066504530306688	333	339	M
64	4474059087124940672	335	352	M
76	4474053727005666816	339	307	M
73	4474061835904011776	352	362	M
58	4474071147393145344	364	347	M
82	4474057437857436032	373	322	M
89	4474081588455448320	398	336	M
72	4474106297406021632	430	336	M
44	4474062523098811904	459	616	N
81	4473855501377642368	619	455	N
Mean		334	334	
Std dev		51	24	

late spectral type. There is no indication of early type stars, present or past. The comparison with GAIA DR2 confirms the validity of our results since of the five distances determined, four are of the same order of magnitude.

We have compared our findings with those of GAIA DR2. For IC 4665 the results are amazingly coincident, corroborating the goodness of the $uvby-\beta$ photometric calibration. For NGC 6871 we found two clusters in the same direction, such as for NGC 6882/5 (Peña at al. 2008). Our comparison with GAIA DR2 is in accordance with the existence of two clusters. Star W25 gives very different results: we determined a distance of 168 pc whereas GAIA fixed its distance at 1682 pc. Stars W4, W5, W7 and W101 do not have distances reported by GAIA. Finally, for Dzim 5 there is an accumulation of a few stars at the same distance determined by GAIA DR2, within the uncertainties. These results, particularly IC 4665, prove, as we did for the open cluster Alpha Per, that the results inferred from $uvby-\beta$ photoelectric photometry are trustworthy.

Unveiling the truth of open clusters is not a simple task. The nitty gritty obviously rests on determining the membership of the stars to the cluster. $uvby-\beta$ photoelectric photometry is a well-known canonical method. Results like those of the open cluster Alpha Per (Peña & Sareyan, 2006) ensure the credibility of the results. One of these open clusters presented here, IC 4665, which has been well studied, corroborates the goodness of our results since it gives the same results as those previously determined through different methods. There are other clusters

TABLE 17

NGC 6871, STAR BY STAR DISTANCE COMPARISON BETWEEN GAIA AND THE PRESENT PAPER

ID Webda	ID GAIA (DR2)	Dst PP (pc)	Dst GAIA (pc)	Membership (GAIA)
12	2059099444490880000	134	167	NM
25	2059076041181621888	168	1819	close
37	2059070681062443904	541	409	NM
10	2059101604826977152	621	557	NM
8	2059075839349023104	1574	1754	close
27	2059112913509204352	1581	1626	close
13	2059071887978880512	1734	1870	close
7	2059073159271061632	1806	2439	far
5	2059075873709364864	1886	1754	close
31	2059095424401407232	1924	1459	close
24	2059076041181622144	2208	1570	close
11	2059075255233453824	2354	1777	close
14	2059076389104969856	2459	2158	far
15	2059099856807768960	2483	1748	close
21	2059075804989882496	2549	1711	close
4	2059070135632404992	2711	1936	far
Mean (close)			1709	close
Std dev			123	
Mean (far)			2178	far
Std dev			252	

TABLE 18

DZIM 5, STAR BY STAR DISTANCE COMPARISON BETWEEN GAIA AND THE PRESENT PAPER

ID Webda	ID GAIA	Dst PP (pc)	Dst GAIA (pc)	Membership PP
7	1331325688646042624	161	247	N
8	1331330292850992256	190	246	N
12	1331988758581273600	203	316	M
14	1332086683834797312	247	360	M
3	1332082427523975168	274	790	M
Mean		241	489	
Std dev		36	262	

which apparently are well-observed, like NGC 6871 but that, when carefully analyzed, reveal that there are few observations (only twenty-three stars with full $uvby-\beta$ photoelectric photometry). What was unexpected was the presence of not one, but of another cluster in the same line of sight; the clusters are at distance modulus of 11.2 ± 0.1 and 12.0 ± 0.1. The histogram of the distances to the cluster determined through the GAIA Data Release 2 (GAIA DR2) suggests the presence of another peak. Finally, with respect to Dzim 5 we only add little to the puzzle beyond the categorical statement of its existence by Dolidze & Jimsheleishvili (1966) to the denial of its existence by Kazlauskas et al., (2013), we could not add much. The results of this study showed that the m_1 and c_1 indexes of provided by Kazlauskas et al. had serious errors that could have led the authors to erroneous conclusions. Our findings suggest the presence of a small group of only late type stars at the same distance, a cluster by definition, but we could not find any vestiges of early type stars either in the present or in the past. The GAIA DR2 results also show an accumulation of stars at 238 ± 13 pc, close to the value determined in the present work (152 ± 32 pc).

We would like to thank the staff of the OAN for their assistance in securing the observations. This work was partially supported by Papiit IN104917, IG100620 and PAPIME 113016. ARL & CVR thank the IA-UNAM for the opportunity to carry out the observations. Proofreading was done by J. Miller. C. Guzmán, F. Salas, B. Juarez, C. Villarreal, J. Calderón, J. Guillen and J. Díaz assisted us at different stages. Comments and suggestions of an anonymous referee improved the paper. This research has made use of the Simbad databases operated at CDS, Strasbourg, France and the NASA ADS Astronomy Query Form.

REFERENCES

Alcaino, G. 1965, Bulletin / Lowell Observatory, 126, 7

Arellano-Ferro, A. & Parrao, L. 1988, Reporte Técnico 57, IA-UNAM

Babu, G. S. D. 1983, JApA, 4, 235, https://doi.org/10.1007/BF02714918

Balona, L. A. & Shobbrook, R. R. 1984, MNRAS, 211, 375, https://doi.org/10.1093/mnras/211.2.375

Barannikov, A. A. 1994, AstL, 20, 442

Becker, W. & Fenkart, R. 1971, A&AS, 4, 241

Cargile, D. A. & James, D. J. 2010, AJ, 140, 677, https://doi.org/10.1088/0004-6256/140/3/677

Cohen, H. L. 1969, AJ, 74, 1168, https://doi.org/10.1086/110918

Crawford, D. L. & Barnes, J. V. 1970, AJ, 75, 978, https://doi.org/10.1086/111051

__________. 1972, AJ, 77, 862, https://doi.org/10.1086/111359

Crawford, D. L., Barnes, J. V., & Warren, W. H. Jr. 1974, AJ, 79, 623, https://doi.org/10.1086/111584

Crawford D. L. & Mander, J. 1966, AJ, 71, 114, https://doi.org/10.1086/109865

Dolidze, M. V. & Jimsheleishvili, G. N. 1966, ATsir, 382, 7

Gaia Collaboration, Brown, A. G. A., Vallenari, A., et al. 2018, A&A, 616, 1, https://doi.org/10.1051/0004-6361/201833051

Hoag, A. A., Johnson, H. L., Iriarte, B., et al. 1961, PUSNO, 17, 343

Hogg, A. R. & Kron, G. E. 1955, AJ, 60, 100, https://doi.org/10.1086/107121

Johnson, H. L. 1954, ApJ, 119, 181, https://doi.org/10.1086/145807

Kazlauskas, A., Sperauskas, J., & Boyle, R.P. 2013 NewA, 19, 34, https://doi.org/10.1016/j.newast.2012.07.003

Lester, J. B., Gray, R. O., & Kurucz, R. L. 1986, ApJ, 61, 509, https://doi.org/10.1086/191122

Luri, X., Brown, A. G. A., Sarro, L. M., et al. 2018, A&A, 616, 9, https://doi.org/10.1051/0004-6361/201832964

Meynet, G., Mermilliod, J.-C., & Maeder, A. 1993, A&AS, 98, 477

Morrel, N. & Abt, H. A. 1991, ApJ, 378, 157, https://doi.org/10.1086/170415

Nicolete, B. 1981, A&A, 104, 185

Nissen, P. E. 1988, A&A, 199, 146

Olsen, E. H. 1983, A&AS, 54, 55

__________. 1993, A&AS, 102, 89

Patenaude, M. 1978, A&A, 66, 225

Paunzen, E. & Mermilliod, J. C. 2007, Webda, A Site Devoted to Stellar Open Clusters

Perry, C. L. & Johnston, L. 1982, ApJS, 50, 451, https://doi.org/10.1086/190833

Peña, J. H. & Sareyan, J. P. 2006, RMxAA, 42, 179

Peña, J. H., Peniche, R. Garrido, R., et al. 2008 RMxAA, 44, 111

Peña, J. H. & Martinez, A. 2014, RMxAA, 50, 119

Peña, J. H, Robleto-Orús, A., Piña, D. S., et al. 2017, RMxAA, 53, 309

Peña, J. H, Rentería, A., Villareal, C., & Piña, D. S. 2019, RMxAA, 55, 193, https://doi.org/10.22201/ia.01851101p.2019.55.02.07

Reimann, H.-G. 1989, AN, 310, 273

Sanders, W. L. & Van Altena, W. F. 1972, A&A 17, 193

Schild, R. & Romanishin, W. 1976, ApJ, 204, 493, https://doi.org/10.1086/154194

Schmidt, E. G. 1982, AJ, 87, 1197, https://doi.org/10.1086/113201

Schuster, W. J. & Nissen, P. E. 1988, A&AS, 73, 225

Sinachopoulos, D. 1990, A&AS, 86, 75

Southworth, J., Maxted, P. F. L., & Smalley, B. 2004, MNRAS, 351, 1277, https://doi.org/10.1111/j.1365-2966.2004.07871.x

Stetson, P. B. 1991, AJ, 102, 589, https://doi.org/10.1086/115895

Shobbrook, R. R. 1984, MNRAS, 211, 659, https://doi.org/10.1093/mnras/211.3.659

Vasilevskis, S. 1955, AJ, 60, 384

J. D. Paredes: Facultad de Ciencias, Universidad Central de Venezuela, Venezuela.

J. D. Paredes, J. H. Peña, D. S. Piña, and A. Rentería: Instituto de Astronomía, UNAM, Apdo. Postal 70-264, Ciudad de México, México (jhpena@astroscu.unam.mx).

J. H. Peña and A. Rentería: Observatorio Astrónomico Nacional de Tonantzintla, Universidad Nacional Autónoma de México, México.

J. H. Peña and D. S. Piña: Facultad de Ciencias, Universidad Nacional Autónoma de México, México.

Revista Mexicana de Astronomía y Astrofísica, **59**, 67–82 (2023)

https://doi.org/10.22201/ia.01851101p.2023.59.01.04

PHOTOMETRIC OBSERVATIONS OF MINOR PLANETS WITH THE TONANTZINTLA SCHMIDT CAMERA I. LIGHT CURVE ANALYSIS OF MAIN-BELT AND NEAR-EARTH ASTEROIDS

J. R. Valdés[1], R. Mújica[1], J. Guichard[1,2], S. Camacho[1,2], G. Cerdán[1], J. Michimani[1], and R. Vega[1]

Received April 28 2022; accepted September 15 2022

ABSTRACT

We report photometric observations of nine main-belt asteroids (MBAs), four near-Earth asteroids (NEAs), and one Mars-crossing asteroid (MCA) carried out with the historical Tonantzintla Schmidt Camera between 2015 and 2018, as part of a process of reactivation of this telescope for astrometric and photometric follow-up observations of MBAs and NEAs. This observational program is part of the commitment made by INAOE when requesting its inclusion in the International Asteroid Warning Network (IAWN). We present the light curves of these 14 asteroids and their corresponding Fourier analyses to determine the rotation period of the asteroids and the brightness amplitude of their light curves.

RESUMEN

Reportamos las observaciones fotométricas de nueve asteroides del cinturón principal (MBAs), un asteroide que cruza la órbita de Marte (MCA) y cuatro asteroides cercanos a la Tierra (NEAs), realizadas con la histórica Cámara Schmidt de Tonantzintla, entre 2015 y 2018, como parte de un proceso de reactivación de este telescopio para dedicarlo a observaciones astrométricas y fotométricas de MBAs y NEAs. Este programa observacional forma parte de las tareas que el Instituto Nacional de Astrofísica, Óptica y Electrónica (INAOE) debe llevar a cabo luego de solicitar su inclusión en la Red Internacional de Alerta de Asteroides (IAWN). Presentamos las curvas de luz de estos 14 asteroides y el análisis de Fourier que permitió determinar el periodo de rotación y la amplitud de la variación de la curva de luz.

Key Words: minor planets, asteroids: general — techniques: photometric

1. INTRODUCTION

Photometric observations of asteroids are very useful due to rapid variations of the observed geometry, even during one opposition. A good average of these geometries can produce a robust physical model of the asteroid that describes its state of rotation and global shape (Kaasalainen et al. 2002). Physical properties such as the rotation period, the amplitude of the light curve (the ratio between two asteroid axes, one side-on and one point-on), the absolute magnitude, H, and the slope parameter, G, are obtained from the photometric observations. To calculate the last two parameters, we need to know, in addition, the distance of the asteroid from the Earth and the Sun at the time of the observations. The first two parameters are obtained from the analysis of the light curve. Applying the inversion method to the light curves observed at different phase angles, and from at least two different oppositions (Kaasalainen & Torppa 2001; Kaasalainen et al. 2001, 2004) allows us to obtain physical parameters, such as the inclination of the rotation axis, the size and the shape of the asteroids, in a reliable manner.

In the last decades, the introduction of CCD detectors made possible a remarkable increase in the number of asteroids for which their state of rotation is known. The large amount of accumulated data has established clear patterns in the rotation of small bodies of the Solar System, and in particular,

[1]Instituto Nacional de Astrofísica, Óptica y Electrónica (INAOE), Puebla, México.

[2]Centro Regional de Enseñanza de Ciencia y Tecnología del Espacio para América Latina y el Caribe (CRECTEALC), México.

the fact that the small asteroids have short periods of rotation (Pravec & Harris 2000). The large population of NEAs discovered in recent years has also made possible the study of small asteroids that are very fast rotators.

The observations reported here are part of an extended program that we started in 2015 with two main goals. First, to contribute to the determination of physical parameters of MBAs and NEAs within the framework of the participation of the Mexico Campus of the Regional Centre for Space Science and Technology Education for Latin America and the Caribbean (CRECTEALC) and the INAOE Astrophysical Department in the activities of the International Asteroid Warning Network (IAWN); and secondly, to reactivate the Tonantzintla Schmidt Camera (CST) as a full-time telescope for astrometric and photometric observations of minor bodies of the Solar System.

The paper is organised as follows: in § 2 we describe the CST status, in § 3 we discuss the observational strategy and data reduction procedure. How we obtained the composite light curve of the observed asteroids and the results of the Fourier analysis for each object are presented in § 4 and § 5, respectively. At the end, we present our perspectives and conclusions.

2. REACTIVATION OF THE TONANTZINTLA SCHMIDT CAMERA

The fundamental aim of the most recent upgrade of the CST is to use it on a dedicated basis to observe MBAs, NEOs, Potentially Hazardous Asteroids (PHAs, asteroids with a minimum orbit intersection distance to Earth's orbit equal or less than 0.05 AU and an absolute magnitude (H) equal to or less than 22.0), and asteroids that could be targets of future space missions. Astrometric and photometric observations were carried out to determine precise orbital parameters of asteroids belonging to the aforementioned groups that permitted us to determine other parameters such as rotation periods, shapes, sizes and inclination of the axes of rotation.

The CST introduced Mexico into modern astrophysics. In the 1940s, the CST was one of the most important telescopes of its class in the world, due to the size of its mirror (D = 77.4 cm), as well as its location, at a latitude of 19° N, in the National Astrophysical Observatory of Tonantzintla (OANTon), in Puebla, Mexico. The CST made it possible to observe the entire plane of the Galaxy, something that was not possible from other observatories in the northern hemisphere. The optical system was built in the Harvard Observatory workshops. The telescope started operation in 1944, but its main scientific observations were carried out between 1948 and 1994. During this period, the CST telescope produced a vast collection of direct (10,446 photographic plates) and spectroscopic images (4,236 photographic plates); the latter were acquired through a 3.96° and 69.85 cm diameter objective prism. The spectroscopic plates had a primary astrophysical value, covering a 10° strip of the entire galactic disk, the galactic center, the galactic poles, and the regions of the M31 and M33 galaxies (Díaz-Hernández et al. 2011). This plate collection is now part of the UNESCO Memory of the World-Mexico.

Since 1948, under the guidance of Guillermo Haro, the CST was dedicated to the development of a series of strategic research lines, among which we can mention the observation of planetary nebulae, Herbig-Haro objects, T-Tauri stars, flare stars, young stars in the direction of the galactic poles, blue emission line galaxies, quasars and the spectral classification of stars, mainly in the southern region of the celestial sphere. Most of the scientific results derived from these investigations were published in the Bulletin of the Tonantzintla and Tacubaya Observatories (1952-1973).

Due to the light pollution caused by the growth of the cities around the OANTon and the low quantum efficiency of the astronomical plates, as of the mid-1990s these detectors were no longer used in astronomical observations with the CST. A new image acquisition system was installed, using a cooled CCD detector, a field flattening lens, and a new telescope control system (Jáuregui-García et al. 2014). In 2015, a new telescope upgrade was done. This included recoating of the reflecting surface of the mirror, cleaning of the corrector lens, maintenance of the mechanical system of the telescope and renewal of the electronic data acquisition system (Valdés et al. 2015a,b). As mentioned, the current CST optical system has an additional component, a field flattening lens. Using direct images taken with the CST in its current configuration, we empirically calculated the image scale of the optical system and obtained a value of 96.6 arcsec/mm, which coincides with the results reported by Cardona et al. (2011).

It is known that in 1945 the CST mirror was returned to the Harvard Observatory to be rectified; however, the results of this correction were never published. Because of this, one of the objectives of the 2015 upgrade was to determine the true focal length (F) of the mirror using a Ronchi interferometric test, which gave a result of $F = 2158.8 \pm 1.4$ mm.

We also used a high precision ION laser tracker to produce a 3D model of the mirror topography using more than 50 contact points on its surface. The high-precision, 3D model obtained made it possible to determine the radius of curvature ($Rc = 4314.8 \pm 0.22$ mm) and the focal length ($F = 2157.4 \pm 0.7$ mm) of the mirror. This value of F produces a plate scale of 95.6 arcsec/mm. Our results contrast with those reported by Wolfschmidt (2009), $F = 2170$ mm and plate scale, $s = 95.05$ arcsec/mm.

In order to verify the results obtained from the optical tests performed on the telescope mirror, a 60.3×59.3 arcmin section of an astronomical plate taken with the Schmidt Camera, with central coordinates AR = 07h 18m 42.3s and DEC = $+35^\circ\, 42'\, 10''\!.7$, was digitized at a resolution of 1,600 pixels/inch, which produced a pixel of 15.8 microns. The astrometric measurements on the digitized image yielded a plate scale of 1.51 arcsec/pixel. Considering that one pixel equaled 15.8 microns, the plate scale in the digitized image was 95.56 arcsec/mm, which is in good agreement with the plate scale values (95.6 arcsec/mm) calculated from the optical tests. Previously, Díaz-Hernández et al. (2011) had reported a plate scale of 1.51 arcsec/pix in a study performed on the CST spectroscopic plates, providing a dispersion of 1.533 mm between Hβ and Hγ, 0.954 mm between Hγ and Hδ, and 0.626 mm between Hδ and Hϵ.

3. OBSERVATIONAL STRATEGY

3.1. *The Sample*

This observation program was designed in the framework of the commitments acquired by INAOE when requesting its inclusion in the IAWN, an international asteroid warning network under the auspices of the United Nations (UN) and the leadership of the NASA's Planetary Defense Coordination Office (PDCO). IAWN was established in 2014 as a result of recommendations made by the UN General Assembly in 2013 to create an international network of organizations involved in detecting, tracking, and characterizing NEOs, as an international response to a potential NEO impact threat. At the time of writing of this article, IAWN had a membership of 40 observatories. The IAWN is tasked with developing a strategy using well-defined communication plans and protocols to assist governments in the analysis of asteroid impact consequences and in the planning of mitigation responses.

The observed asteroids presented here were selected using the Ephemeris Generator of the Collaborative Asteroid Light Curve Link[3]. From the list of observable asteroids from the CST location, we selected those whose periods are known as they are necessary for shape determination. In addition, we wanted to verify the accuracy of periods as observed by the CST. We chose asteroids with rotational periods between two and three hours that can be covered at least twice per night. Nevertheless, we made some exceptions. We also observed objects with periods that could not be observed completely in one night to see if we could construct the phase plot light curve by observing the object during 2–3 nights. Other selection criteria were the possibility of covering a phase angle variation greater than 20 degrees during the observed opposition and that the orbital velocities should be less than 4.45 arcsec/min in order to keep the asteroid in the same field throughout the night, avoiding the need to change the reference stars used to construct the light curve.

On the other hand, in order to apply the light curve inversion method to determine the asteroid shape, it is necessary that the selected asteroids have publicly available light curves on the Asteroid Light curve Photometry Database (ALCDEF). According to the minor planet Light curve Database (LCDB) file description (Warner et al. 2009), the U code provides an assessment of the quality of the period solution, not necessarily of the data per se. The rating goes from 3, for a completely unambiguous light curve, in terms of the calculated period, to 0 for a result that later was proven to be incorrect. It is therefore desirable that the parameter defining the LCDB Status has values U=3 or 3-, which means that the quality of the light curves is optimal.

The observed set of objects consisted of 14 asteroids: nine main-belt asteroids (MBAs), four Near-Earth Asteroids (NEAs), and one Mars-crossing asteroid (MCAs), as listed in Table 1.

3.2. *Observations and Data Reduction*

Photometric observations were carried out with the 77.4 cm Tonantzintla Schmidt Camera of INAOE between October and December 2015 and between March and May 2018. The telescope's current optical system has a field-flattening lens that provides a focal distance of 2135.2 mm and an image scale of 96.6 arcsec mm^{-1}. During the 2015 observing runs we used a 1530×1020 pixel (9.0×9.0 μm^2) SBIG ST-8 CCD camera, that produced an image scale of 0.86 arcsec pix^{-1}, and a field-of-view (FOV) of 22.2×14.8 arcmin.

[3]`https://minplanobs.org/MPInfo/php/callopplcdbquery.php`

At the beginning of 2018 we upgraded the image acquisition system with the installation of a SBIG STF-8300 color CCD Camera, equipped with a 3326 × 2540 pixel ($5.4 \times 5.4\mu m^2$) high resolution Kodak KAF-8300C full frame sensor with microlens technology and antiblooming for improved quantum efficiency. This new system provides an image scale of 0.52 arcsec pix^{-1}, and a FOV of 28.8×22.0 arcmin.

Selected physical parameters of the observed asteroids, such as semi-major axis (a), eccentricity (e), taxonomic class, absolute magnitude (H), diameter, and albedo, are listed in Table 1, while their observational circumstances, including geocentric (r) and heliocentric (Δ) distances, and phase angle (α), are shown in Table 2. Where there were different albedo values reported for the same asteroid, we gave preference to the Wide-field Infrared Survey Explorer *WISE* measurements (Mainzer et al. 2011).

When the absolute magnitude and the albedo of observed asteroids were known, their diameters were calculated using equation (1), where p_ν is the reported albedo. Otherwise, when there were no reports on the asteroid albedos, we used equation (2), assuming that the average albedo of asteroids is 14% and that an asteroid whose absolute magnitude is 17.75, corresponds to an asteroid of 1 km in size.

$$D = 10^{[6.259 - log_{10} p_\nu - 0.4 \times H]}, \tag{1}$$

$$D = (1\text{km}) \times 10^{(17.75 - H)/5}. \tag{2}$$

Depending on the brightness of the observed objects and weather conditions, the integration times varied between 30 and 120 s. For each observing run, master bias, dark and flat-field images were produced. Scientific images were corrected for bias, dark and flat-field effects using Image Reduction and Analysis Facility (IRAF) packages.

Differential photometry and period analysis were done using the *MPO Canopus* analysis tool (Warner 2014). In each case, we used four solar analogs nonvariable comparison stars, in the same FOV, to generate light curves. Comparison stars were selected near the path covered by the asteroids during the night.

4. LIGHT CURVE ANALYSIS

The obtained light curves for the observed asteroids are presented in Figures 1 to 14, and the results of the corresponding Fourier analysis (Harris et al. 1989) in Table 3. Assuming that the light curve of an asteroid is produced by a given geometry in rotation, the brightness of an object is proportional to the projected area, and the ratio of minimum to maximum cross sections (CS_{min}, and CS_{max}, respectively) is determined by the peak-to-peak amplitude (A) of the light curve through a very simple formula (Harris et al. 2014):

$$A = -2.5 \log(CS_{min}/CS_{max}). \tag{3}$$

This ratio, the values of the rotation period, and the amplitude of the light curve, are reported in Table 3. In order to resolve the possible ambiguities in deriving the correct rotation periods of observed asteroids, we used the constraints on amplitude variation *versus* harmonic order of the Fourier function proposed by Harris et al. (2014). The Fourier fit order used in the composite light curve is shown in the fifth column of Table 3.

The light curves show the relative instrumental magnitude *versus* the rotational phase, calculated with the rotation periods given in Table 3. The caption of the figures indicates, for each night, the plot symbol used, the UT time of observations, the JD for zero rotational phase, and the corresponding phase angle. The zero phase is corrected for the light travel-time effect. Uncertainty bars are plotted for each individual data point. The *MPO Canopus* Fourier analysis tool provides the period solution and the Fourier coefficients defining the shape of the composite light curve for each data set. The solution also provides the instrumental magnitude offset between each asteroid and its comparison stars, for each individual light curve that we used to calculate the peak-to-peak amplitude of the composite light curves.

5. RESULTS

5.1. *(711) Marmulla*

(711) Marmulla (1911 LN, 1927 AB) is an Inner Main-Belt asteroid, that belongs to the Flora family (a = 2.2369 AU., i = 6.0991°). It was discovered on March 1, 1911 by J. Palisa at Vienna. (711) Marmulla has albedo values that correspond to a S-class asteroid; $p_V = 0.22 \pm 0.09$ (Nugent et al. 2016), and $p_V = 0.224 \pm 0.030$ (Usui et al. 2011).

We observed this asteroid at four different values of phase angle, $\alpha = 7.68°$, 9.52° (grouped in a single light curve), 12.95°, and 22.11°. We obtained 37 images on March 12, 2018, 187 images on March 16, 2018, 109 images on March 24, and 88 images on April 9, 2018; exposure times ranged from 50 to 90 s.

The best values for the periods obtained from the Fourier analysis of our three light curves

TABLE 1

SELECTED PHYSICAL PARAMETERS OF THE OBSERVED ASTEROIDS

Asteroid	a (AU)	e	Taxonomic class	H (mag)	Diameter (km)	Albedo	Comments
(711) Marmulla	2.2369	0.1955	S, Sr	11.84	12.31	0.22±0.09[a]	MB-Inner Asteroid Flora family
(1036) Ganymed	2.6629	0.5335	S,Sr	9.25	40.76	0.218±0.048[b]	NEA, Amor group
(1117) Reginita	2.2475	0.1983	S	11.81	9.77	0.3585±0.0785[b]	MB-Inner Asteroid
(1318) Nerina	2.3073	0.2039	M	12.37	10.90	0.1721±0.0208[b]	MB-Inner Asteroid Phocaea family
(1346) Gotha	2.6269	0.1782	S	11.44	13.13	0.2794±0.0411[b]	MB-Middle Asteroid Eunomia family
(1363) Herberta	2.9036	0.0682	S	11.36	12.4	0.337±0.157[c,d]	MB-Outer Asteroid Koronis family
(1492) Oppolzer	2.1729	0.1165	S	13.0	11.34	0.089±0.026[e]	MB-Inner Asteroid
(1627) Ivar	1.8630	0.3965	S,Sr	12.68	10.71	0.134±0.025[b]	NEA, Amor group
(1831) Nicholson	2.2390	0.1279	S	12.57	7.58	0.296±0.053[c,d]	MB-Inner Asteroid
(1847) Stobbe	2.6114	0.0214	Xc,M	11.13	16.64	0.2315±0.0162[b]	MB-Middle Asteroid
(1866) Sisyphus	1.8933	0.5384	S,Sw	12.44	8.67	0.255±0.0162[b]	NEA, Apollo group
(3800) Karayusuf	1.5779	0.0757	S	15.09	1.59	0.657±0.123[d,f]	Mars-crosser
(5692) Shirao	2.6554	0.1819	S	12.55	8.84	0.2218±0.0290[b]	MB-Middle Asteroid
(25916) 2001 CP44	2.5613	0.4979	Sw	13.68	4.83	0.262±0.047[b]	NEA, Amor group

[a]Nugent et al. (2016). [b]Mainzer et al. (2011). [c]Masiero et al. (2012). [d]Mainzer et al. (2016). [e]Tedesco et al. (2004). [f]Nugent et al. (2015).

(2.804±0.001 h, 2.876±0.074 h, and 2.627±0.041 h) are very similar to the values on the LCDB database reported by different authors.

5.2. *(1036) Ganymed*

Asteroid (1036) Ganymed is the largest NEA that we observed. It belongs to the Amor group, and is classified as S type with an albedo of 0.218±0.048 (Mainzer et al. 2011) and a corresponding diameter of 40.76 km. It was discovered by W. Baade at the Bergedorf Observatory in Hamburg on 23 October, 1924.

We observed this asteroid at three different values of phase angle, $\alpha = 6.18°$, 6.26° and 6.35°. Observations are grouped in a single light curve. We obtained 382 images on March 19, 2018, with an exposure time of 40 seconds, and 653 images on March 20, 2018, and 276 images on March 21, 2018, with exposure times of 30 s.

From the Fourier analysis of the light curve we show here, we obtained a value of the period equal to 10.318±0.013 h, very similar to the 35 values compiled on LCDB.

5.3. *(1117) Reginita*

(1117) Reginita (1927 KA) is an Inner Main-Belt asteroid. It was discovered on May 24, 1927 by J. Comas Solú at the Fabra Observatory in Barcelona (Schmadel 2012). (1117) Reginita has a very high albedo among the taxonomic class S. Pravec et al. (2012) reported a value of $p_V = 0.3516$ from *WISE* thermal observations while Nugent et al. (2016) obtained an albedo of 0.36±0.13, and a diameter D=9.82±2.35 km from *NEOWISE* Reactivation Mission observations. Mainzer et al. (2011) derived $p_V = 0.3585 \pm 0.0785$, and D=10.193±0.250 km applying thermal models to the *NEOWISE* data at 3.4, 4.6, 12, and 22 μm.

On October 4, 2015, at a phase angle of 16.73°, we obtained 221 images with a 30 s exposure time. Fourier analysis of the light curve produced the best fit at 2.942±0.012 h, similar to the values reported by Wisniewski, Michalowski & Harris (1995), Kryszczyńska et al. (2012), Chang et al. (2015), Waszczak et al. (2015), and another seven authors included on LCDB. The obtained peak-to-peak amplitude, 0.16 magnitude, is in the range of values reported by the previously mentioned authors for this asteroid. We observed again Reginita in 2018, obtaining almost the same result 2.945±0.002 h, by using 81 images of 60 s exposure time at a phase angle of 22.70°, obtained on April 8, and 74 images

TABLE 2

OBSERVATIONAL CIRCUMSTANCES FOR THE OBSERVED ASTEROIDS

Asteroid	Date (UT)	RA (J2000.0)	DEC (J2000.0)	Δ (AU)	r (AU)	α (degrees)	V (mag)	Filter[a]
(711) Marmulla	2018 Mar. 12.67	10h 19m 48.2s	+13° 36′ 59.″5	1.5590	2.5180	7.68	15.2	C
	2018 Mar. 16.66	10h 15m 53.5s	+13° 47′ 24.″7	1.5727	2.5112	9.52	15.3	C
	2018 Mar. 24.69	10h 09m 00.9s	+14° 01′ 28.″8	1.6102	2.4985	12.95	15.5	R
	2018 Apr. 09.63	10h 00m 32.1s	+14° 00′ 05.″9	1.4824	2.2052	22.11	16.0	R
(1036) Ganymed	2018 Mar. 19.10	10h 43m 02.0s	−18° 54′ 38.″0	3.1662	4.0832	6.21	15.4	C
	2018 Mar. 20.10	10h 42m 18.7s	−18° 46′ 40.″0	3.1682	4.0834	6.22	15.4	C
	2018 Mar. 21.20	10h 41m 31.5s	−18° 37′ 42.″0	3.1701	4.0835	6.23	15.4	C
(1117) Reginita	2015 Oct. 04.10	23h 04m 02.6s	−10° 28′ 14.″0	1.013	1.956	13.73	14.0	C
	2018 Apr. 08.85	16h 34m 57.2s	−14° 58′ 38.″2	1.2511	2.0314	22.70	14.8	R
	2018 Apr. 09.63	10h 00m 32.1s	−14° 00′ 05.″9	1.2435	2.0298	22.51	14.8	R
(1318) Nerina	2018 Mar. 17.59	11h 19m 14.5s	+11° 38′ 33.″6	0.0879	1.8634	6.52	13.7	R
	2018 Mar. 27.56	11h 02m 43.1s	+09° 13′ 53.″3	0.0895	1.8547	12.27	14.0	R
(1346) Gotha	2018 Mar. 29.58	07h 12m 43.1s	+12° 59′ 32.″2	2.0593	2.4323	23.88	15.9	R
(1363) Herberta	2015 Dec. 15.01	04h 08m 52.7s	+20° 01′ 38.″0	1.996	2.945	6.18	15.6	C
	2015 Dec. 16.07	04h 08m 05.0s	+19° 59′ 23.″0	2.001	2.945	6.54	15.6	C
	2015 Dec. 17.08	04h 07m 18.7s	+19° 57′ 11.″0	2.007	2.946	6.94	15.7	R
(1492) Oppolzer	2018 Mar. 18.60	11h 26m 34.2s	+11° 06′ 23.″4	0.9991	1.9840	5.85	14.8	R
	2018 Mar. 26.59	11h 19m 46.2s	+12° 14′ 25.″1	1.0114	1.9763	10.27	15.0	R
(1627) Ivar	2018 Mar. 17.26	15h 08m 07.2s	−02° 07′ 19.″0	0.8931	1.7084	26.71	14.8	C
	2018 Mar. 27.23	15h 15m 17.8s	−00° 19′ 43.″0	0.7784	1.6543	24.37	14.4	R
(1831) Nicholson	2018 Mar. 10.79	10h 11m 31.8s	+21° 32′ 15.″5	1.3065	2.2495	10.42	15.4	C
	2018 Mar. 11.62	10h 10m 44.6s	+21° 35′ 12.″3	1.3095	2.2481	10.89	15.4	C
	2018 Mar. 14.67	10h 11m 31.8s	+21° 32′ 15.″5	1.3065	2.2495	10.42	15.4	C
	2018 Mar. 25.59	10h 00m 07.4s	+21° 58′ 48.″7	1.3748	2.2275	17.00	15.7	R
	2018 Apr. 14.58	09h 55m 39.8s	+21° 15′ 25.″6	1.5245	2.1978	23.43	16.1	R
	2018 Apr. 20.61	09h 56m 55.2s	+20° 47′ 35.″0	1.5781	2.1889	24.78	16.2	R
	2018 Apr. 21.60	09h 57m 14.3s	+20° 42′ 24.″9	1.5872	2.1874	24.98	16.2	R
(1847) Stobbe	2018 Abr. 18.71	15h 20m 07.8s	−01° 26′ 49.″7	1.6289	2.5612	9.77	14.9	R
(1866) Sisyphus	2018 Mar. 25.32	13h 26m 02.8s	+53° 01′ 21.″0	2.2221	2.8935	16.72	17.3	C
(3800) Karayusuf	2018 Mar. 28.79	15h 59m 16.6s	+14° 15′ 06.″1	0.6393	1.4596	34.23	16.3	R
(5692) Shirao	2018 Mar. 18.80	12h 44m 30.8s	−03° 20′ 21.″6	1.2770	2.2558	6.22	15.1	R
	2018 Mar. 26.79	12h 39m 24.5s	−01° 46′ 18.″8	1.2505	2.2459	2.21	14.8	R
	2015 Apr. 07.74	124h 31m 10.7s	+00° 37′ 20.″9	1.2411	2.2321	4.86	14.9	R
(25916) 2001 CP44	2018 Apr. 14.36	16h 41m 45.5s	+03° 31′ 27.″0	0.8411	1.6754	27.21	15.6	R
	2018 Apr. 16.33	16h 43m 19.0s	+03° 39′ 11.″0	0.8193	1.6632	26.92	15.5	R

[a]C = Clear filter (no filter), R = R-band filter.

of 90 s exposure time, at a phase angle of 22.43°, obtained on April 9.

5.4. *(1318) Nerina*

(1318) Nerina is an inner Main-Belt asteroid, belonging to the Phocaea family. It was discovered on March 24, 1934 by C. Jackson at Johannesburg (Schmadel 2012). Mainzer et al. (2011) derived a value of $p_V = 0.1721 \pm 0.208$ that is in correspondence with an M-type asteroid.

We observed (1318) Nerina at two values of phase angle, $\alpha = 6.52°$, and 12.27°. We obtained 377 images with 30 s exposure time on March 17, 2018, and 84 images on March 27, 2018, with a 60 s exposure time.

The Fourier analysis of the two light curve data we obtained gave us the period values 2.586±0.013 h and 2.463±0.033 h, both with a difference of less than one percent with respect to the 11 values found on the LCDB database.

TABLE 3

ROTATION PERIOD AND BRIGHTNESS AMPLITUDE OF THE OBSERVED ASTEROIDS

Asteroid	Period* (h)	Period** (h)	Amplitude (mag)	Fourier fit order	CS_{min}/CS_{max}
(711) Marmulla	2.804±0.001	2.721	0.13	8th	0.89
	2.876±0.074		0.09	6th	0.92
	2.627±0.041		0.17	6th	0.86
(1036) Ganymed	10.318±0.013	10.297	0.15	6th	0.87
(1117) Reginita	2.944±0.012	2.946	0.16	4th	0.86
	2.945±0.002		0.28	6th	0.77
(1318) Nerina	2.586±0.013	2.528	0.07	6th	0.94
	2.463±0.033		0.10	8th	0.91
(1346) Gotha	2.563±0.057	2.64067	0.21	6th	0.82
(1363) Herberta	3.018±0.002	3.015	0.16	8th	0.86
(1492) Oppolzer	3.770±0.020	3.76945	0.11	8th	0.90
	3.566±0.076		0.11	8th	0.90
(1627) Ivar	4.795±0.001	4.795	0.90	2nd	0.44
(1831) Nicholson	3.216±0.001	3.228	0.29	8th	0.77
	3.220±0.022		0.31	6th	0.75
	3.217±0.001		0.41	8th	0.69
(1847) Stobbe	5.621±0.012	5.617	0.41	6th	0.61
(1866) Sisyphus	2.391±0.028	2.400	0.12	6th	0.91
(3800) Karayusuf	2.270±0.084	2.2319	0.32	4th	0.74
(5692) Shirao	2.957±0.032	2.8878	0.13	6th	0.89
	2.900±0.055		0.13	4th	0.89
	2.866±0.085		0.14	6th	0.88
(25916) 2001 CP44	4.2020±0.0024	4.6021	0.22	6th	0.82

*The value derived in this work.

**The value in the LCDB summary table.

5.5. *(1346) Gotha*

(1346) Gotha is a Main-Belt asteroid that belongs to the Eunomia family. It was discovered in 1929, on February 5, by K. Reinmuth at Heidelberg (Schmadel 2012). Mainzer et al. (2011) derived a value of $p_V = 0.2794 \pm 0.0411$, in agreement with a S-type taxonomic classification established by Tholen (1984).

From the light curve generated with 62 images of 120 s exposure time obtained on March 29, 2018, at a phase angle α equal to 23.88°, the best fit value obtained for the period, from the Fourier analysis, is 2.563±0.057 h, consistent with five out the six values reported on the LCDB database.

5.6. *(1363) Herberta*

(1363) Herberta (1935 RA) is an Outer Main-Belt asteroid, belonging to the Konoris family ($2.83 < a < 2.91$, $i < 3.5$). It was discovered on August 30, 1935 by E. Delporte at the Royal Belgium Observatory in Uccle (Schmadel 2012). Based on MOVIS NIR colors, Popescu et al. (2018) proposed a S-type taxonomic classification. The value of albedo $p_V = 0.337 \pm 0.157$, determined by Masiero et al. (2012), is close to the upper limit for S-complex asteroids.

A total of 427 images of Herberta were taken over three nights, from December 15 to 17, 2015 with 60 s of exposure time. The phase angle values for the observation nights were 6.18°, 6.56° and 6.94°, respectively. All the observations were grouped in a single light curve.

The best value we obtained for the period, from the Fourier analysis, is equal to 3.018±0.002 h; meanwhile, the only value reported on LCDB is equal to 3.015±0.005 h.

5.7. *(1492) Oppolzer*

(1492) Oppolzer was discovered in 1938 by Y. Väisälä (Schmadel 2012). (1492) Oppolzer is a S-type (Vereš et al. 2015) Inner Main-Belt asteroid. The taxonomy for this asteroid was determined from

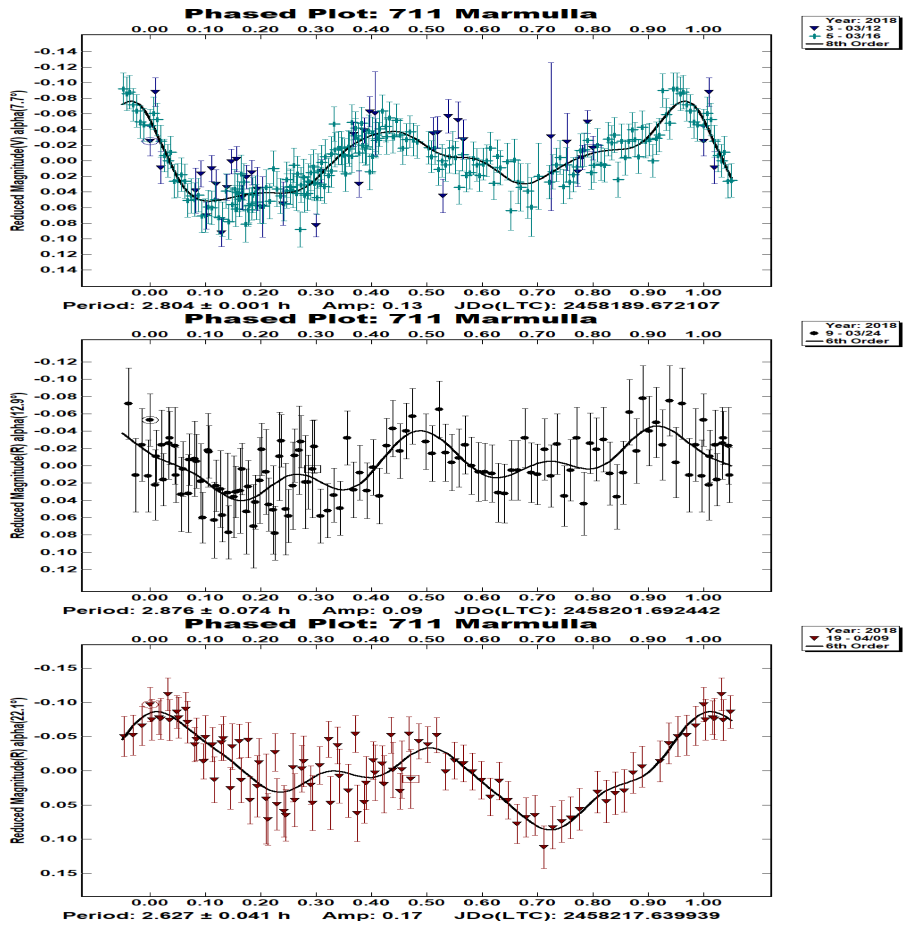

Fig. 1. Light curves of (711) Marmulla observed on March 12, 16 and 24, and April 9, 2018. The color figure can be viewed online.

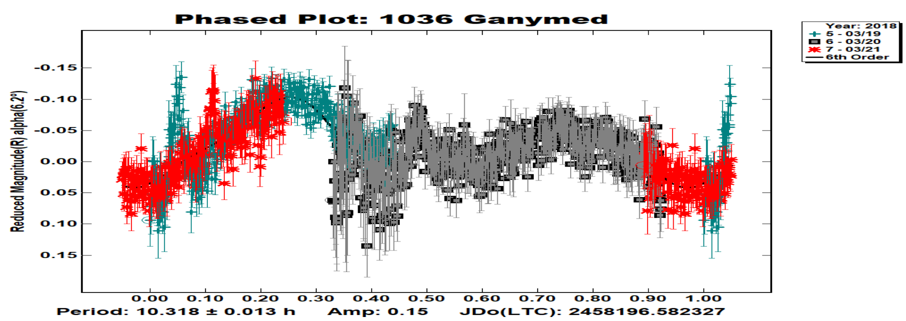

Fig. 2. Composite light curve of (1036) Ganymed observed on March 19, 20 and 21, 2018. The color figure can be viewed online.

photometry obtained at the Pan-STARRS PS1 telescope; however, the albedo ($p_V = 0.089 \pm 0.026$) reported by Tedesco et al. (2004), using the observations of the *IRAS* mission, is very low and corresponds more closely to a C-class asteroid.

We observed this asteroid at two values of phase angle, $\alpha = 5.85°$ and $\alpha = 10.27°$. We obtained 375 images of 40 s exposure time on March 18, 2018, and 129 images on March 26, 2018, of 60 s exposure time. One of the values we obtained for the period, 3.77±0.02 h, is in complete agreement with the seven values on LCDB, with a difference of less than 0.1 percent. For the second value, 3.566±0.076 h, the difference is larger.

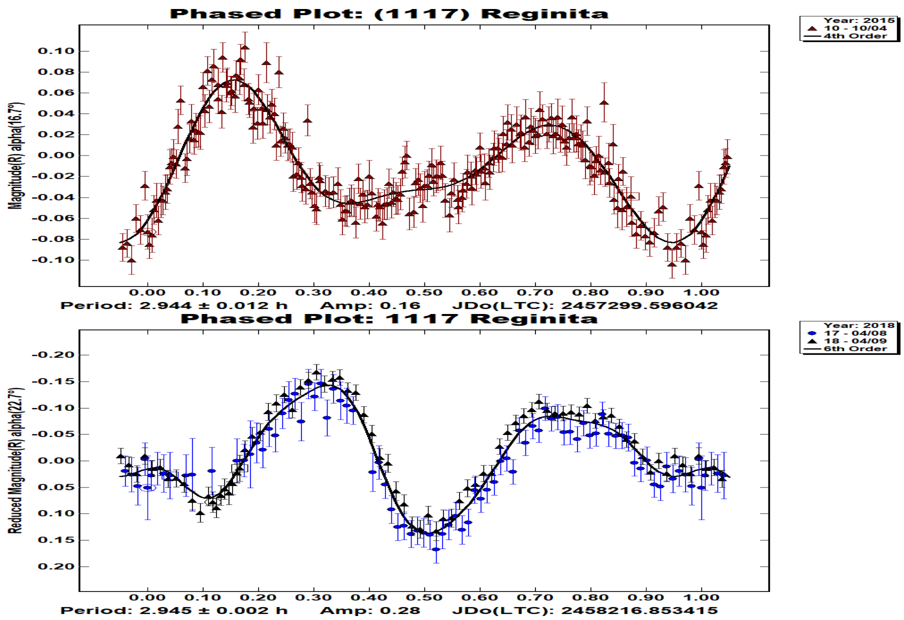

Fig. 3. Top panel: Light curve of (1117) Reginita observed on October 4, 2015. Bottom panel: Light curve of (1117) Reginita observed on April 8 and 9, 2018. The color figure can be viewed online.

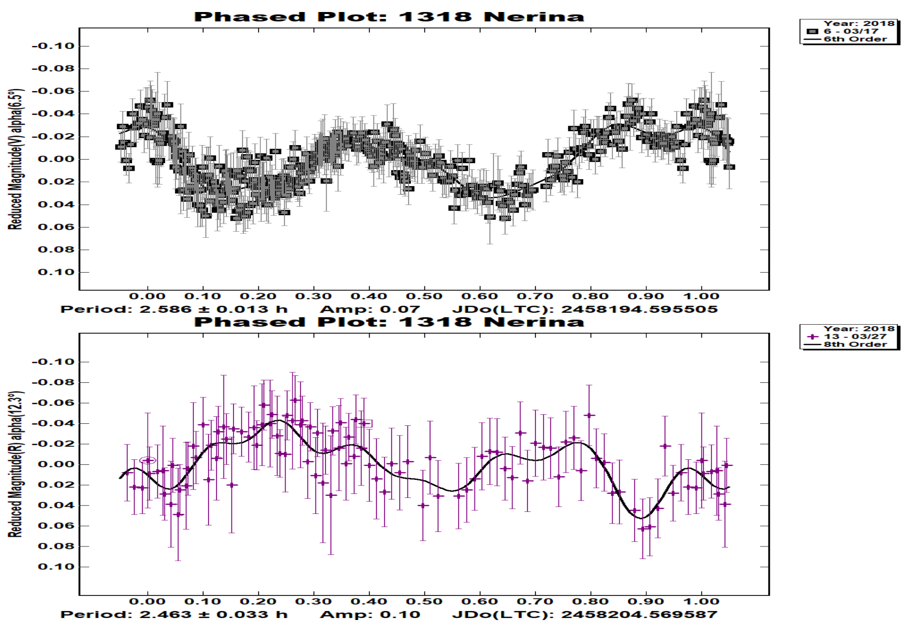

Fig. 4. Top panel: Light curve of (1318) Nerina observed on March 17, 2018. Bottom panel: Light curve observed on March 27. The color figure can be viewed online.

5.8. *(1627) Ivar*

(1627) Ivar was discovered on September 25, 1929 by E. Hertzsprung at Johannesburg (Schmadel 2012).

We obtained 600 images of 30 s exposure time for this asteroid on March 17, 2018, at phase angle $\alpha = 26.71°$, and 68 images of 60 s exposure time on March 27, 2018, at phase angle, 24.33°. As the

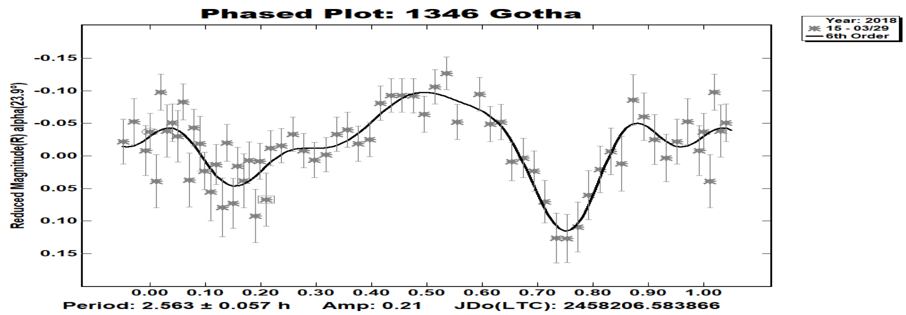

Fig. 5. Light curve of (1346) Gotha observed on March 29, 2018. The color figure can be viewed online.

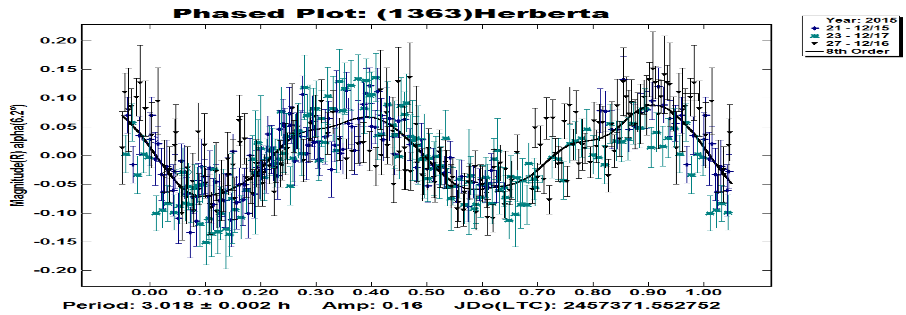

Fig. 6. Composite light curve of (1363) Herberta observed on December 15, 16, 17, 2015. The color figure can be viewed online.

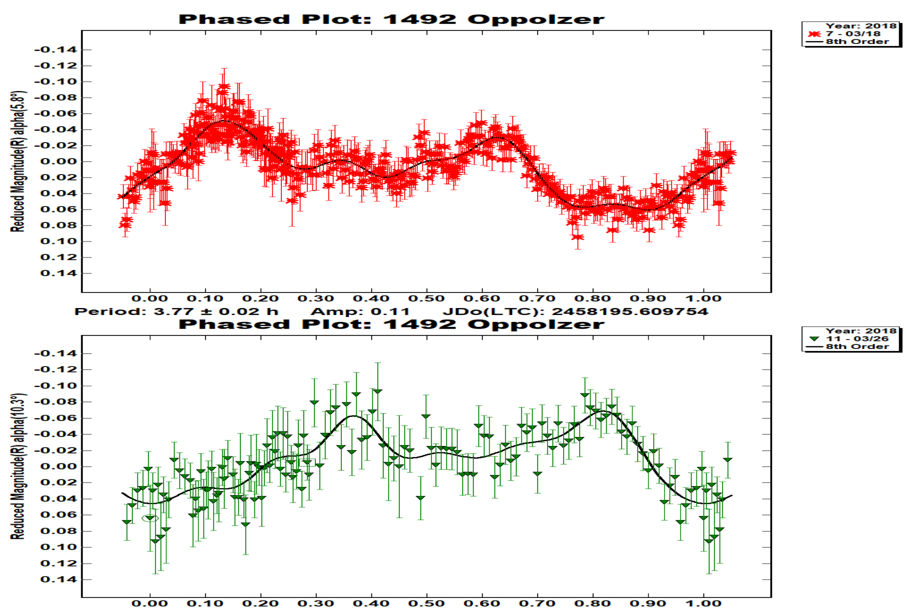

Fig. 7. Top panel: Light curve of (1492) Oppolzer observed on March 18, 2018. Bottom panel: Light curve of (1492) Oppolzer observed on March 26, 2018. The color figure can be viewed online.

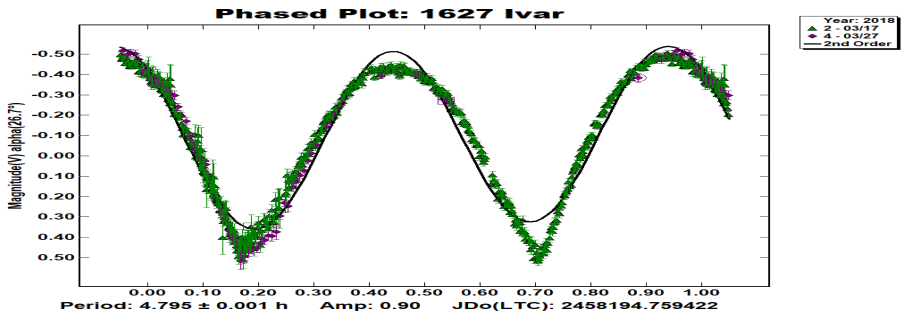

Fig. 8. Composite light curve of (1627) Ivar observed on March 17, 27. 2018. The color figure can be viewed online.

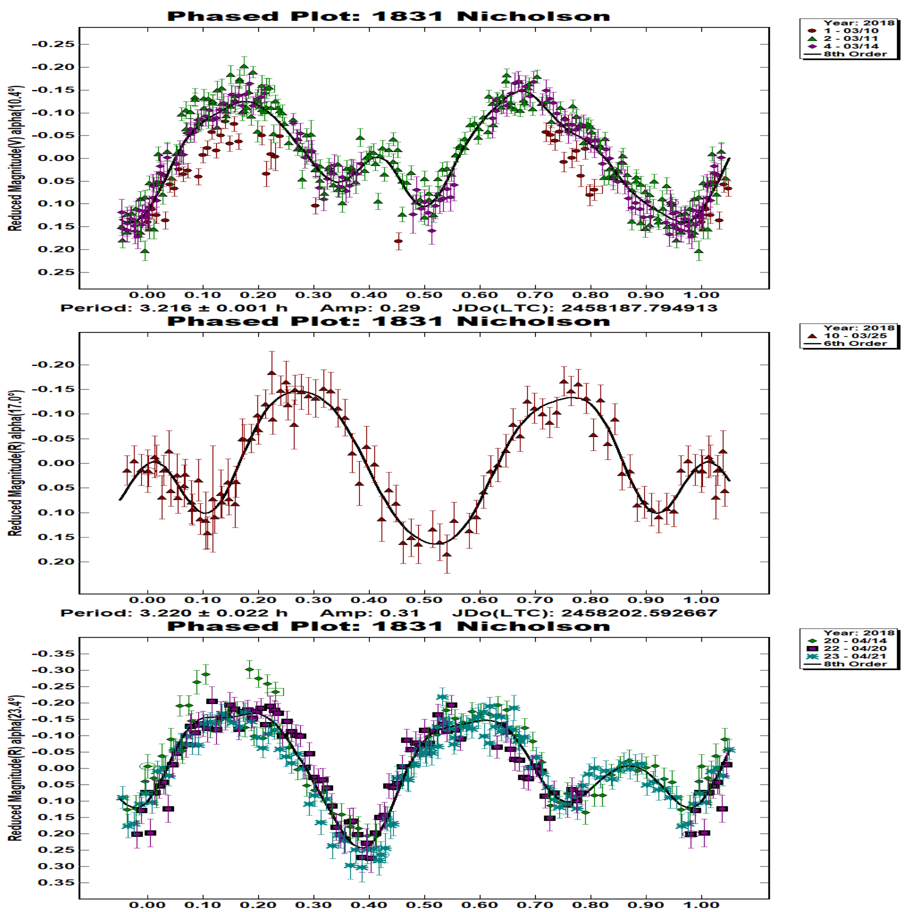

Fig. 9. Top panel: Composite light curve of (1831) Nicholson observed on March 10, 11, 14, 2018. Middle panel: Light curve of (1831) Nicholson observed on March 25, 2018. Bottom panel: Composite light curve of (1831) Nicholson observed on April 14, 20, 21, 2018. The color figure can be viewed online.

phase angles have very similar values, we grouped the observations in a single light curve.

The value we obtained for the period, 4.795±0.001 h is exactly the same as the best value reported on LCDB. This asteroid has been well observed; there are 16 values reported on this database.

5.9. *(1831) Nicholson*

(1831) Nicholson was discovered on April 17, 1968, by P. Wild at Zimmerwald, Switzerland

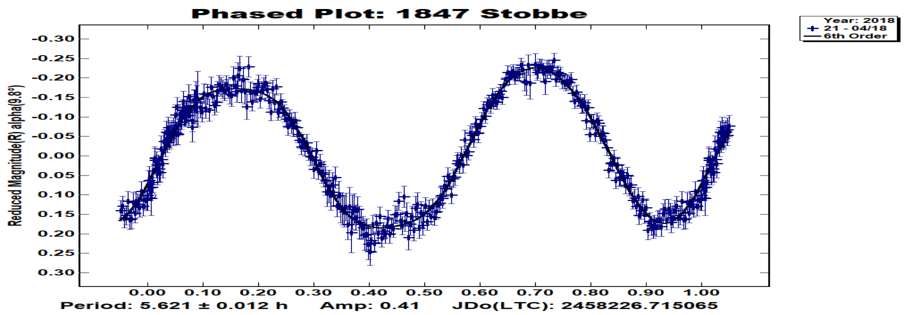

Fig. 10. Light curve of (1847) Stobbe observed on April 18, 2018. The color figure can be viewed online.

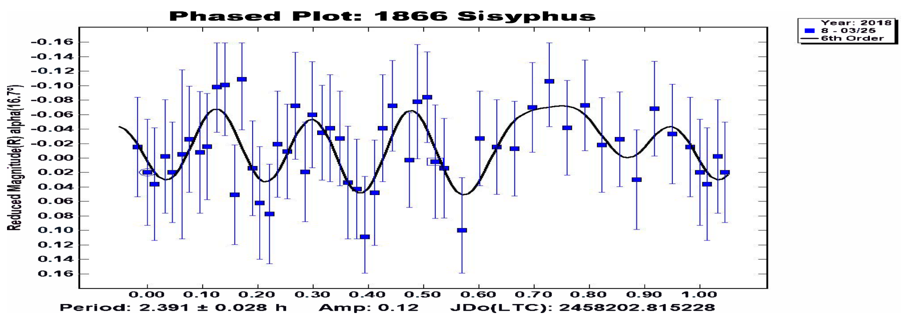

Fig. 11. Light curve of (1866) Sisyphus observed on March 25, 2018. The color figure can be viewed online.

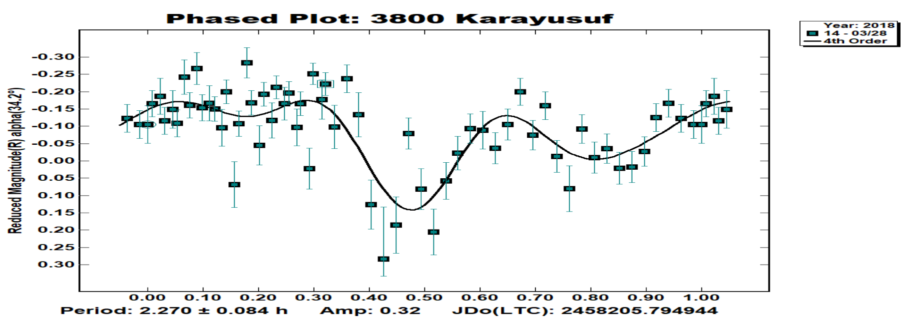

Fig. 12. Light curve of (3800) Karayusuf observed on March 28, 2018. The color figure can be viewed online.

(Schmadel 2012). It is an S-type asteroid (Bus & Binzel 2002) from the inner region of the Main-Belt. Masiero et al. (2012) has estimated an albedo value of $p_V = 0.296 \pm 0.053$ which is in good agreement with the values for S-complex asteroids.

We observed this asteroid in 2018. We grouped the March 10, 11 and 14 observations in a single light curve, the March 25 observations in another, and in a third light curve we grouped observations carried out on April 14, 20 and 21. We obtained 756 images with exposure times ranging from 30 s to 120 s. The phase angles covered were $\alpha = 10.40°$ to $24.98°$.

The best period values obtained from the Fourier analysis for our three light curves, 3.216±0.001 h, 3.220±0.022 h, and 3.217±0.001 h, are completely consistent with the four values on LCDB.

5.10. *(1847) Stobbe*

(1847) Stobbe was discovered on 1916 February 1, by H. Thiele at Bergedorf, Germany (Schmadel 2012). This is a middle Main-Belt asteroid that was originally classified as a Xc asteroid by Bus & Binzel (2002) during the Phase II of the Small Main-Belt Asteroid Spectroscopic Survey. More recently, Mainzer et al. (2011), using NEOWISE photome-

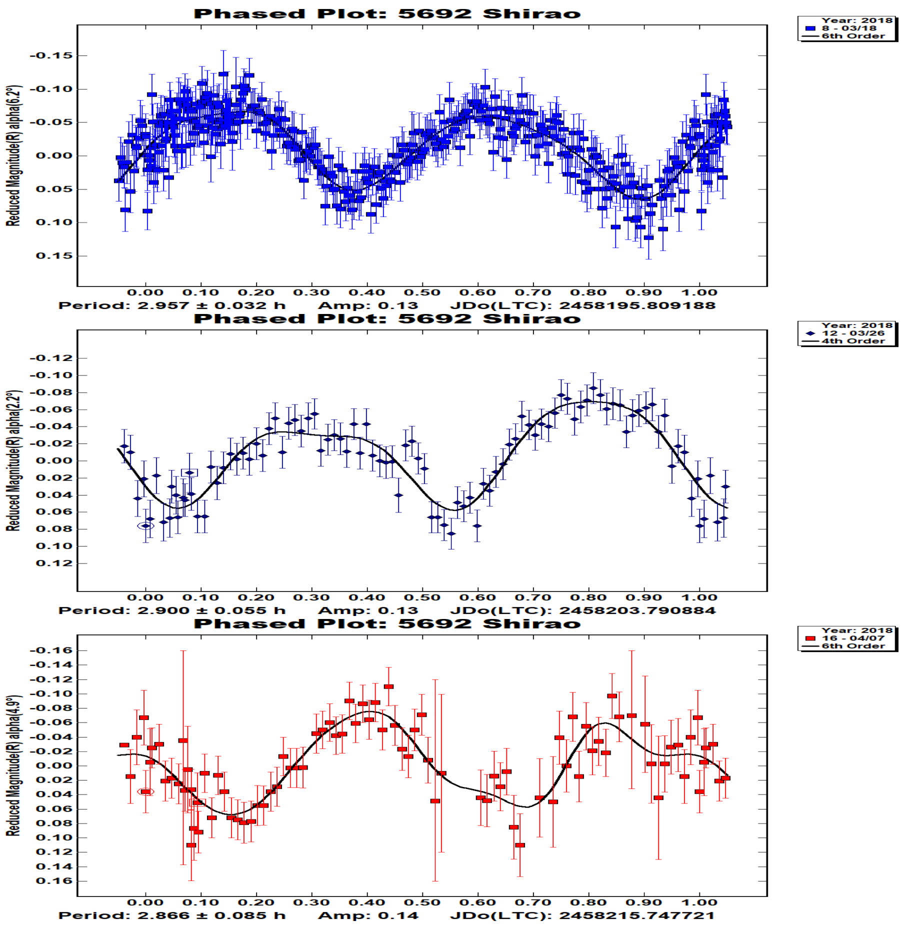

Fig. 13. Top panel: Light curve of (5692) Shirao observed on March 18, 2018. Middle panel: Light curve of (5692) Shirao observed on March 26, 2018. Bottom panel: Light curve of (5692) Shirao observed on April 7, 2018. The color figure can be viewed online.

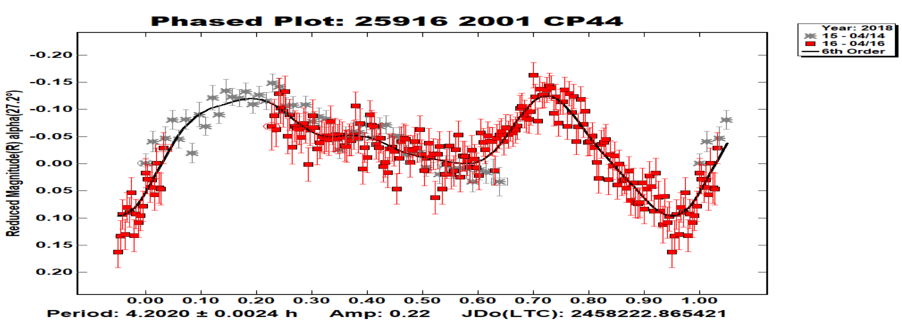

Fig. 14. Composite light curve of (25916) 2001 CP44 observed on April 14, 16, 2018. The color figure can be viewed online.

try, suggested an M-type taxonomy for this asteroid. P-type, M-type and E-type asteroids are included in the larger X-type group and are differentiated by optical albedo values (Tholen & Barucci 1989).

The typical optical albedo for M-type asteroids is between 0.1 and 0.3, so the albedo of $p_V = 0.2315 \pm 0.0162$ reported by Mainzer et al. (2011) corresponds to this type.

We observed this asteroid on April 18, 2018. We obtained 52 images with 60 s exposure time at a phase angle $\alpha = 9.77°$. The period we obtained from the light curve Fourier analysis is equal to

5.621±0.012 h, very similar to three out of the four values on LCDB. The largest difference with our result corresponds to the value 6.37±0.02 (Malcolm 2002), that is also the least recent value obtained.

5.11. *(1866) Sisyphus*

(1866) Sisyphus was discovered on December 5, 1972 by P. Wild at Zimmerwald, Switzerland (Schmadel 2012). It is a NEA that belongs to the Apollo group. Mainzer et al. (2011) reported a value of $p_V = 0.255 \pm 0.049$, which is in correspondence with the taxonomic classifications S-type and Sw-type provided by Bus & Binzel (2002) and Binzel et al. (2019), respectively, both observing this asteroid as part of optical spectroscopic surveys.

This asteroid was observed on March 25, 2018. We obtained 48 images with a 210 s exposure time at a phase angle $\alpha = 16.74°$. Even though the amplitude of this light curve is of a similar order as the photometric uncertainties on the individual points, the best fit we obtained for the period, 2.391±0.028 h, is in agreement with the thirteen values reported on LCDB, most of them around 2.4 h.

5.12. *(3800) Karayusuf*

(3800) Karayusuf is an S-type (Bus & Binzel 2002; Binzel et al. 2019) Mars-crosser (MC) asteroid discovered on January 4, 1984, by E. F. Helin at Palomar in California, USA (Schmadel 2012). A very high value of its albedo, $p_V = 0.66 \pm 0.12$, not corresponding to an S-type asteroid, was reported by Nugent et al. (2015). With an absolute magnitude H=15.09, this albedo value gives a size of 1.59 km, one of the smallest asteroids in our sample. However, Alí-Lagoa & Delbo' (2017), using the NEA thermal model to provide diameters and albedos of MCs with available WISE/NEOWISE data, proposed an albedo $p_V = 0.281 \pm 0.056$ for this asteroid. With this correction, the size of (3800) Karayusuf can increase to 2.43 km.

With an exposure time of 120 s, we obtained 60 images of this asteroid on March 28, 2018. Its phase angle on that night was 34.23° and the derived period was 2.270±0.084 hours. There are 11 values reported on LCDB, all of them quite similar to the one derived from our data.

5.13. *(5692) Shirao*

(5692) Shirao was discovered on March 23, 1992 by K. Endate and K. Watanabe at Kitami (Schmadel 2012). It is an S-type (Vereš et al. 2015) middle Main-Belt asteroid. Mainzer et al. (2011) reported a typical S-type albedo $p_V = 0.2218 \pm 0.0290$.

We observed this asteroid in 2018, on March 18 and 26, and April 7. A total of 235 images were obtained. Exposure time for March 18 images was 30 s and 60 s for the other two nights. The phase angle for March 18 was 6.22°, for March 26 was 2.21° and 4.86° for April 7, so we decided to construct three different light curves. The corresponding periods derived from Fourier analysis are 2.957±0.032 h, 2.900±0.055 h, and 2.866±0.085 h, very similar to the best value reported on the LCDB summary table (2.8878 h).

5.14. *(25916) 2001 CP44*

(25916) 2001 CP44 is the only Amor-type NEA in our sample. It has a diameter of 5.7 km and was discovered by LINEAR at Socorro, New Mexico. This is clearly an S-complex asteroid, classified as an Sq-type (Thomas et al. 2014; Popescu et al. 2019), S-type (Lin et al. 2018), and Sw-type (Binzel et al. 2019). Mainzer et al. (2011) reported a typical S-type albedo $p_V = 0.262 \pm 0.047$.

We obtained a total of 250 images of this asteroid in 2018. On April 14 (53 images, exposure time 120 s, phase angle 27.17°) and April 16 (197 images, exposure time 60 s, and phase angle 26.86°).

From our light curve we derived a period equal to 4.2020±0.0024 h, while, on LCDB there are two clear sets of values, one around 4.2 h, reported during 2012-2014, and another around 4.6 h, reported during 2018. The difference can be due to observations being made during different apparitions.

6. CONCLUSIONS

The results of the analyses of the photometric observations of the 14 asteroids reported in the present work validate the success of the process of reactivation of the Tonatzintla Schmidt Camera. From the light curve analyses, we noticed that even those with larger errors reproduce with very good agreement the periods previously determined by other authors. For each of the objects in our sample, we compared the best fit value of the period with those values on the summary line on LCDB, considered the most likely to be correct, and we found that the difference between them and ours was always less than 3%, and very often less than 1%.

There is one exception, (25916) 2001 CP44, which has two clearly distinct sets of values for its reported periods, one of them is equal, within the error bars, to the best value we found from our data; however, for the second one the difference is larger. As we mentioned, the difference can be due to observations being made during different apparitions.

In subsequent papers we will discuss these results as part of a larger sample of asteroids that we have already observed. We will present the analyses of the observations, including other results such as the determination of their morphological properties.

In concluding, we want to remark that the Tonantzintla Schmidt Camera is now dedicated to astrometric and photometric follow-up observations of Main Belt and Near-Earth Asteroids. It is a fundamental part of the asteroid observation program to fulfill the commitments made by INAOE and CRECTEALC regarding their contributions to the International Asteroid Warning Network (IAWN).

The authors would like to acknowledge the telescope technicians A. Marquez and C. Escamilla for their help during the observations and during the whole reactivation process of the CST, as well as J. Alva†, the INAOE engineer expert on the CST; without his historical knowledge it would have been very difficult to reactivate the telescope. We also want to thank L. Altamirano and D. Sánchez de la Llave, former INAOE General Director and former INAOE Research Director, respectively, and J. Moctezuma, A. Tuxpan, J. Escobar and P. García-Flores, members of the INAOE Computer Vision Lab.

REFERENCES

Alí-Lagoa, V. & Delbo', M. 2017, A&A, 603, 55, https://doi.org/10.1051/0004-6361/201629917

Binzel, R. P., DeMeo, F. E., Turtelboom, E. V., et al. 2019, Icar, 324, 41, https://doi.org/10.1016/j.icarus.2018.12.035

Bus, S. J. & Binzel, R. P. 2002, Icar, 158, 146, https://doi.org/10.1006/icar.2002.6856

Cardona, O., Carramiñana, A., Carrasco, E., & Escamilla, C. 2011, Nuevo Sistema de Adquisición de Imágenes Astronómicas de la Cámara Schmidt utilizando un CCD Enfriado. Reporte Técnico de la Coordinación de Astrofíisica, INAOE. http://inaoe.repositorioinstitucional.mx/jspui/handle/1009/911

Chang, C.-K., Ip, W.-H., Lin, H.-W., et al. 2015, ApJS, 219, 27, https://doi.org/10.1088/0067-0049/219/2/27

Díaz-Hernández, R., González, J. J., Costero, R., & Guichard, J. 2011, Proc. SPIE8011, 2nd Congress of the International Commission for Optics: Light for the Development of the World, https://doi.org/10.1117/12.903386

Harris, A. W., Pravec, P., Galád, A., et al. 2014, Icar, 235, 55, https://doi.org/10.1016/j.icarus.2014.03.004

Harris, A. W., Young, J. W., Bowell, E., et al. 1989, Icar, 77, 171, https://doi.org/10.1016/0019-1035(89)90015-8

Jáuregui, J. M., Cardona, O., Escamilla, C., Castillo-Domínguez, E., & López-Cruz, O. 2014, Sistema de Control para la Cámara Schmidt de Tonantzintla. Reporte Técnico No. RT0612. Coordinación de Astrofísica, INAOE. http://inaoe.repositorioinstitucional.mx/jspui/handle/1009/1158

Kaasalainen, M., Pravec, P., Krugly, Y. N., et al. 2004, Icar, 167, 178, https://doi.org/10.1016/j.icarus.2003.09.012

Kaasalainen, M., Mottola, S., & Fulchignoni, M. 2002, Asteroids III, ed. W. F. Bottke Jr., A. Cellino, P. Paolicchi, and R. P. Binzel (Tuczon, AZ: UAP), 139

Kaasalainen, M. & Torppa, J. 2001, Icar, 153, 24, https://doi.org/10.1006/icar.2001.6673

Kaasalainen, M., Torppa, J., & Muinonen, K. 2001, Icar, 153, 37, https://doi.org/10.1006/icar.2001.6674

Kryszczyńska, A., Colas, F., Polińska, M., et al. 2012, A&A, 546, 72, https://doi.org/10.1051/0004-6361/201219199

Lin, C.-H., Ip, W.-H., Lin, Z.-Y., et al. 2018, Planet. Space Sci., 152, 116, https://doi.org/10.1016/j.pss.2017.12.019

Mainzer, A., Grav, T., Masiero, J., et al. 2011, ApJ, 741, 90, https://doi.org/10.1088/0004-637X/741/2/90

Mainzer, A. K., Bauer, J. M., Cutri, R. M., et al. 2016, NASA Planetary Data System, EAR-A-COMPIL-5-NEOWISEDIAM-V1.0

Malcolm, G. 2002, Minor Planet Bulletin, 29, 28

Masiero, J. R., Mainzer, A. K., Grav, T., et al. 2012, ApJ, 759, 8, https://doi.org/10.1088/2041-8205/759/1/L8

Minor Planet Circular 6210. 1981 Aug. 1

Nesvorny, D. 2015, NASA Planetary Data System, EAR-A-VARGBDET-5-NESVORNYFAM-V.3.0

Nesvorný, D., Brož, M., & Carruba, V. 2015, Asteroids IV, 297, https://doi.org/10.48550/arXiv.1502.01628

Nugent, C. R., Mainzer, A., Masiero, J., et al. 2015, ApJ, 814, 117, https://doi.org/10.1088/0004-637X/814/2/117

Nugent, C. R., Mainzer, A., Bauer, J., et al. 2016, AJ, 152, 63, https://doi.org/10.3847/0004-6256/152/3/63

Popescu, M., Licandro, J., Carvano, J. M., et al. 2018, A&A, 617, 12, https://doi.org/10.1051/0004-6361/201833023

Popescu, M., Vaduvescu, O., de León, J., et al. 2019, A&A, 627, 124, https://doi.org/10.1051/0004-6361/201935006

Pravec, P., Harris, A. W., Kušnirák, P., Galád, A., & Hornoch, K. 2012, Icar, 221, 365, https://doi.org/10.1016/j.icarus.2012.07.026

Pravec, P. & Harris, A. W. 2000, Icar, 148, 12, https://doi.org/10.1006/icar.2000.6482

Schmadel, L. 2012, Dictionary of Minor Planet Names (Berlin: Springer Berlin Heidelberg), https://doi.org/10.1007/978-3-642-29718-2

Tedesco, E. F., Noah, P. V., Noah, M., et al. 2004, NASA Planetary Data System, IRAS-A-FPA-3-RDR-IMPS-V6.0

Tholen, D. J. 1984, Asteroid Taxonomy from Cluster Analysis of Photometry, Ph.D. Thesis, The University of Arizona

Tholen, D. J. & Barucci, M. A. 1989, in Asteroids II (Tuczon, AZ: UAP), 298

Thomas, C. A., Emery, J. P., Trilling, D. E., et al. 2014, Icar, 228, 217, https://doi.org/10.1016/j.icarus.2013.10.004

Usui, F., Kuroda, D., Müller, T. G., et al. 2011, PASJ, 63, 1117, https://doi.org/10.1093/pasj/63.5.1117

Valdés, J. R., Márquez, A., Guichard, J., et al. 2015a, Procedimiento para retirar la celda y el espejo de la Cámara Schmidt de Tonantzintla. Reporte Técnico. Coordinación de Astrofísica. INAOE

Valdés, J. R, Márquez, A., Guichard, J., et al. 2015b, Procedimiento para la limpieza de la Lente Correctora de la Cámara Schmidt de Tonantzintla. Reporte Técnico. Coordinación de Astrofísica. INAOE

Vereš, P., Jedicke, R., Fitzsimmons, A., et al. 2015, Icar, 261, 34, https://doi.org/10.1016/j.icarus.2015.08.007

Warner, B. D., Harris, A. W., & Pravec, P. 2009, Icar, 202, 134, https://doi.org/10.1016/j.icarus.2009.02.003

Warner, B. D. 2014, MPO Software, MPO Canopus version 10.4.3.17. Bdw Publishing. http://www.minorplanetobserver.com/

Waszczak, A., Chang, C.-K., Ofek, E. O., et al. 2015, AJ, 150, 75, https://doi.org/10.1088/0004-6256/150/3/75

Wisniewski, W. Z., Michalowski, T. M., Harris, A. W., & McMillan, R. S. 1995, Abstracts of the Lunar and Planetary Science Conference, 26, 1511

Wolfschmidt, G. 2009, AN, 330, 555, https://doi.org/10.1002/asna.200911216

S. Camacho and J. Guichard: Centro Regional de Enseñanza de Ciencia y Tecnología del Espacio para América Latina y el Caribe (CRECTEALC), (jguich, sergio.camacho@inaoep.mx).

S. Camacho, G. Cerdán, J. Guichard, J. Michimani, R. Mújica, J. R. Valdés, and R. Vega: Instituto Nacional de Astrofísica, Óptica y Electrónica (INAOE). Luis Enrique Erro # 1, Tonantzintla, Puebla, México C.P. 72840, (sergio.camacho@inaoep.mx, guillermocerdanher@gmail.com, jguich, michimani, rmujica, jvaldes, rvega@inaoep.mx)

Revista Mexicana de Astronomía y Astrofísica, **59**, 83–97 (2023)

https://doi.org/10.22201/ia.01851101p.2023.59.01.05

NUMERICAL INVESTIGATIONS OF THE ORBITAL DYNAMICS AROUND A SYNCHRONOUS BINARY SYSTEM OF ASTEROIDS

L. B. T. Santos[1], Allan Kardec de Almeida Jr[1,2], P. A. Sousa-Silva[3], M. O. Terra[4], D. M. Sanchez[5], S. Aljbaae[1], A. F. B. A. Prado[6,7], and F. Monteiro[8]

Received May 15 2022; accepted October 5 2022

ABSTRACT

In this article, equilibrium points and families of periodic orbits in the vicinity of the collinear equilibrium points of a binary asteroid system are investigated with respect to the angular velocity of the secondary body, the mass ratio of the system and the size of the secondary. We assume that the gravitational fields of the bodies are modeled considering the primary as a mass point and the secondary as a rotating mass dipole. This model allows to compute families of planar and halo periodic orbits that emanate from the equilibrium points L_1 and L_2. The stability and bifurcations of these families are analyzed and the results are compared with the results obtained with the restricted three-body problem (RTBP). The results provide an overview of the dynamical behavior in the vicinity of a binary asteroid system.

RESUMEN

En este artículo, se investigan los puntos de equilibrio y las familias de órbitas periódicas en la vecindad de los puntos de equilibrio colineal de un sistema binario de asteroides con respecto a la velocidad angular del cuerpo secundario, la relación de masa del sistema y el tamaño del secundario. Suponemos que los campos gravitatorios de los cuerpos se modelan asumiendo el primario como punto masa y el secundario como dipolo de masa giratorio. Este modelo permite calcular familias de órbitas planas y periódicas de halo que emanan de los puntos de equilibrio L_1 y L_2. Se analiza la estabilidad y bifurcaciones de estas familias y se comparan los resultados con los obtenidos con el problema de los tres cuerpos restringido (RTBP). Los resultados brindan una descripción general del comportamiento dinámico en la vecindad de un sistema binario de asteroides.

Key Words: celestial mechanics — minor planets, asteroids: general

1. INTRODUCTION

In recent years, the investigation and analysis of small celestial bodies have become fundamental to deep space exploration. Thus, understanding the dynamical behavior in the vicinity of small bodies is of great interest for the design of exploration missions and also for planetary science.

However, describing how a particle behaves around these objects is a challenging subject in astrodynamics, mainly due to the combination of the rapid rotation of the asteroids around their axis together with the non-spherical shapes.

In particular, an increasing number of binary asteroid systems has been observed throughout the Solar System and, in particular, among the near-Earth asteroids (NEAs). It is estimated that about 15% of NEAs larger than 0.3 km are binary systems (Pravec et al. 2006; Margot et al. 2015). Most of these binaries are formed by a more massive primary component, usually with a nearly spherical shape, and a small secondary component, generally referred to as

[1]Division of Space Mechanics and Control. National Institute for Space Research, INPE. São José dos Campos, Brazil.
[2]Instituto de Telecomunicações, Portugal.
[3]São Paulo State University, UNESP, Brazil.
[4]Technological Institute of Aeronautics, ITA. São Paulo dos Campos, Brazil.
[5]The University of Oklahoma, Norman OK, USA.
[6]Postgraduate Division - National Institute for Space Research (INPE), São Paulo, Brazil.
[7]Professor, Academy of Engineering, RUDN University, Moscow, Russia.
[8]National Observatory, ON. Rio de Janeiro, Brazil.

satellite (Pravec et al. 2006; Pravec & Harris 2007; Walsh et al. 2008; Zhang et al. 2020).

There are several types of binary asteroid systems, which have been grouped according to their physical properties (e.g. size, rotation, mass ratio, diameter; Pravec & Harris 2007). The characteristics of these groups also suggest different formation mechanisms. As shown by Pravec & Harris (2007), the Type A binary asteroids are composed of small NEAs, Mars crossers (MC), and Main-Belt Asteroids (MBA), with primary components less than 10 km in diameter and with a component size ratio (D_s/D_p) less than 0.6. The Type B, in turn, consists of small asteroids with nearly equal size components ($D_s/D_p > 0.7$) and with primary diameters smaller than 20 km. The Types L and W are, respectively, composed of large asteroids ($D > 20$ km) with relatively very small component size ratio ($D_s/D_p < 0.2$) and of small asteroids ($D < 20$ km) with relatively small satellites ($D_s/D_p < 0.7$) in wide mutual orbits.

Most Type A binary asteroids are synchronous systems, that is, the rotation period of the secondary component is equal to the orbital period around the center of mass of the system (Pravec et al. 2006, 2016). Numerical simulations revealed that binary systems are likely to undergo a chaotic process of energy dissipation involving tidal forces that allows the system to evolve to a fully synchronous end state (Jacobson & Scheeres 2011). According to Jacobson & Scheeres (2011), the higher the mass ratio of the binary system, the faster the synchronization can be achieved. This happens because each member of the system exerts tidal forces with the same proportion over each other. Thus, as most systems have mass ratios less than 0.5, we find in the literature a larger number of systems with only the secondary component coupled with the orbital movement (Pravec et al. 2016).

Performing semi-analytical and/or numerical investigations of the orbits and equilibrium solutions around asteroid systems using simplified models can be useful to provide some preliminary understanding of such systems (Werner 1994; Liu et al. 2011). Simplified models can be used to approximate the gravitational field of irregularly shaped bodies, requiring less computational effort and generating considerable results in a short period of time. Another advantage of using a simplified model is that we can easily investigate the effects of a given parameter on the dynamics of a spacecraft around asteroids, such as, the distribution of stable periodic orbits (Lan et al. 2017), the stability of the equilibrium points (Zeng et al. 2015; Barbosa Torres dos Santos et al. 2017), as well as the permissible parking regions (Yang et al. 2015; Zeng et al. 2016). In addition, simplified models can be used to support the orbit design (Wang et al. 2017) and feedback control (Yang et al. 2017).

Due to their advantage and considerable results, several simplified models have been proposed to study the orbital dynamics of a particle in the vicinity of irregular bodies. For example, Riaguas et al. (1999, 2001) analyzed the dynamics of a particle under the gravitational force of an asteroid modeled as a straight segment. Zeng et al. (2016) analyzed the influence of the parameters k (angular velocity) and μ (mass ratio) on the equilibrium solutions using the rotating mass dipole model and observed that there are always 5 equilibrium points when considering the primary bodies as points of mass. Other works have investigated the dynamics around small irregular bodies using a simplified model given by an homogeneous cube (Liu et al. 2011), a simple flat plate (Blesa. 2006), a rotating mass dipole (Zeng et al. 2015; Barbosa Torres dos Santos et al. 2017; dos Santos et al. 2017), the dipole segment model (Zeng et al. 2018), a rotating mass tripole (Lan et al. 2017; dos Santos et al. 2020; Santos et al. 2021), and many others.

In particular, aiming to understand the dynamical environment in the vicinity of irregular bodies, Aljbaae et al. (2020) investigated the dynamics of a spacecraft around the asynchronous equal-mass binary asteroid (90) Antiope; the authors applied the Mascon gravity framework using the shaped polyhedral source (Chanut et al. 2015; Aljbaae et al. 2017) to consider the perturbation due to the polyhedral shape of the components. The perturbations of the solar radiation pressure at the perihelion and aphelion distances of the asteroid from the Sun were also considered in that study. In order to investigate the stability of periodic orbits, (Chappaz & Howell 2015) considered the asynchronous binary asteroid system using the triaxial ellipsoid model and observed that the non-spherical shape of the secondary body significantly influences the behavior of the halo orbit around L_1 and L_2 .

As said before, simplified models are useful to provide some preliminary understanding of the motion around binary systems, and the circular restricted three-body problem is suitable and often used to investigate the dynamics around small bodies (de Almeida Junior & Prado 2022). Furthermore, even landing trajectories have been evaluated using a spherical shape for the gravitational field of the primaries in the circular restricted three-body problem

(Tardivel & Scheeres 2013; Celik & Sanchez 2017; Ferrari et al. 2016). Although the orbit-attitude coupled equations of motion for a binary asteroid can be obtained using a more sophisticated model, which takes into consideration a potential for a non-spherical distribution of mass (Scheeres et al. 2021; Wen & Zeng 2022), they are only essential for very close encounters, such as for landing approaches. In this study, the dynamics is investigated for orbits around the binary system of asteroids. Thus, in this contribution, a more simplified model is used, whose results capture the essential parts of the physics of the problem, although its accuracy depends on the parameters of the specific mission. Therefore, we carry out a numerical investigation using the simplified model called a Restricted Synchronous Three-Body Problem, as introduced by Barbosa Torres dos Santos (2017). The practical advantage of using this model is that we can, in a relatively simple way, analyze the influence of the dimension of the secondary body on the dynamics of a spacecraft in the neighborhood of M_2.

We focus on the behavior of a particle of negligible mass in the vicinity of a binary system of Type A (NEAs and MBAs). The reason for choosing this class of asteroids is that the NEAs, in particular, are asteroids that pass near the Earth and most of the systems that are part of this class are synchronous systems. Our aim is to understand how the parameters of the dipole, the dimension (d) and the mass ratio (μ^*) of the system, influence the stability, period and bifurcation of the periodic orbits around the equilibrium points. In § 2 we provide the equation of motion of the three-body synchronous restricted problem. In § 3, we investigate the influence of the force ratio (k) on the appearance of the equilibrium points, keeping the values of μ^* and d fixed. Then, in § 4, we investigate the influence of μ^* and d on periodic orbits (planar and halo) around the equilibrium points L_1 and L_2, considering k fixed ($k = 1$). Finally, in § 5, we provide the final considerations that were obtained in this article.

2. EQUATIONS OF MOTION

Consider that the motion of a particle with negligible mass, $P(x,\ y,\ z)$, is dominated by the gravitational forces of the primary bodies M_1 and M_2. As already mentioned, the distance between M_1 and M_2 is assumed to be $D = 12$ km, which will be the normalization factor in the rest of this work. The larger primary is considered to be a point mass with mass m_1 and the secondary is modeled as a rotating mass dipole formed by m_{21} and m_{22}, as shown in Figure 1.

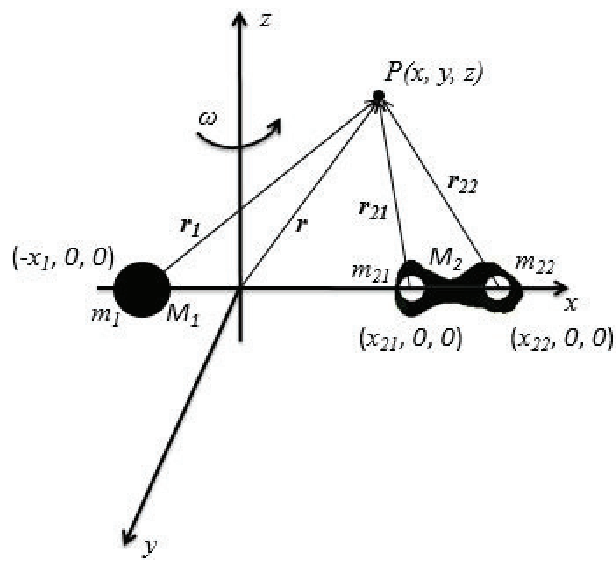

Fig. 1. Representative image of the geometric shape of the system considered (not in scale).

In canonical units, the sum of the masses of the bodies M_1 and M_2 is unitary. In this work, for all numerical simulations, we assume that $m_1 > m_{21} = m_{22}$ and that the mass ratio is defined by $\mu^* = m_{21}/(m_1 + m_{21} + m_{22})$. By analogy, $\mu^* = \mu/2$, with μ being the usual mass ratio used in the classical restricted three-body problem.

The angular velocity, given by $\boldsymbol{\omega} = \omega\mathbf{z}$, is aligned with the z-axis of the system. Here, the unit of time is defined such that the orbital period of the primary bodies around the center of mass of the system is equal to ω^{-1}. Because the system is synchronous, the orbital period of M_2 around the center of mass is the same as its orbital period around the axis of the dipole.

With respect to the barycentric rotating frame, the masses m_1, m_{21} and m_{22} are fixed along the x-axis with coordinates $x_1 = -2\mu^*$, $x_{21} = -2\mu^* - \frac{d}{2} + 1$ and $x_{22} = -2\mu^* + \frac{d}{2} + 1$, respectively, where d, given in canonical units, is the distance between m_{21} and m_{22}.

Using the generalized potential

$$\Omega = \frac{x^2 + y^2}{2} + k\left(\frac{1 - 2\mu^*}{r_1} + \frac{\mu^*}{r_{21}} + \frac{\mu^*}{r_{22}}\right), \qquad (1)$$

we can write the equations of motion of P in a rotating frame centered on the barycenter of the system (M_1-M_2) as follows:

$$\begin{bmatrix} \dot{x} \\ \dot{y} \\ \dot{z} \\ \ddot{x} \\ \ddot{y} \\ \ddot{z} \end{bmatrix} = \begin{bmatrix} \dot{x} \\ \dot{y} \\ \dot{z} \\ 2\dot{y} + D_x\Omega \\ -2\dot{x} + D_y\Omega \\ D_z\Omega \end{bmatrix}, \tag{2}$$

with

$$r_1 = \sqrt{(x - x_1)^2 + y^2 + z^2},$$
$$r_{21} = \sqrt{(x - x_{21})^2 + y^2 + z^2},$$
$$r_{22} = \sqrt{(x - x_{22})^2 + y^2 + z^2},$$

where $D_x\Omega$ denotes the partial derivative of Ω with respect to x and the same notation is used for y and z. The dimensionless parameter k represents the ratio between gravitational and centrifugal accelerations, $k = G(M)/(\omega^{*2}D^3)$, where M is the total mass of the system in kg, ω^* is the angular velocity of the M_2 in rad/s, D is the distance, in meters, between M_1 and the center of mass of M_2 and, finally, $G = 6.67408 \times 10^{-11}\mathrm{m}^3\mathrm{kg}^{-1}\mathrm{s}^{-2}$ (Zeng et al. 2015; Feng et al. 2016).

The free parameters of the system are d, μ^* and k, which correspond, respectively, to the size of M_2, the mass ratio and a parameter accounting for the rotation of the asteroid. When k is equal to 1, the bodies orbit the center of mass of the system without any internal forces in the dipole. On the other hand, when $k < 1$, the dipole is stretching, while it is compressing when $k > 1$. Therefore, depending on the class of the binary system being analyzed, we need to consider the force ratio value (k). A particular case occurs when d (distance from the mass dipole) is equal to zero, causing the bodies of mass m_{21} and m_{22} to overlap, becoming a point of mass, with mass ratio $2\mu^*$. The classical Restricted Three-Body Problem corresponds to the particular case $d = 0$ and $k = 1$ (McCuskey 1963; Szebehely 1967). Also, when $d \neq 0$ and $k = 1$, we have the Restricted Synchronous Three-Body Problem (Barbosa Torres dos Santos et al. 2017).

2.1. *Equilibrium Point and Stability Analysis*

Let $\mathbf{x} = (x,\ y,\ z,\ \dot{x},\ \dot{y},\ \dot{z}) \in \mathbb{R}^6$ be the state vector of a massless particle and $f : \mathbb{R}^6 \to \mathbb{R}^6$ be

$$f(\mathbf{x}) = \begin{bmatrix} f_1 \\ f_2 \\ f_3 \\ f_4 \\ f_5 \\ f_6 \end{bmatrix} = \begin{bmatrix} \dot{x} \\ \dot{y} \\ \dot{z} \\ 2\dot{y} + D_x\Omega \\ -2\dot{x} + D_y\Omega \\ D_z\Omega \end{bmatrix}. \tag{3}$$

The equilibrium points L_i, $i = 1, 2, 3, 4, 5$, are defined as the zeros of $f(\mathbf{x})$. To determine the linear stability of each equilibrium, one needs to translate the origin to the position of this equilibrium point and linearize the equations of motions around this point. Thus, the linearization over any of these equilibrium points is

$$\dot{\mathbf{x}} = D_{L_i}\mathbf{x}, \tag{4}$$

where D_{L_i} is the derivative of $f(\mathbf{x})$ computed at the equilibrium point L_i.

To determine the linear stability of the equilibrium points (L_i, $i = 1, 2, 3, 4$ and 5), it is necessary to transfer the origin of the coordinate system to the position of the equilibrium points (x_0, y_0, z_0) and then to linearize the equations of motion around these points, obtaining the results shown below.

$$\begin{split}\ddot{\xi} - 2\dot{\eta} =& \Omega_{xx}(x_0, y_0, z_0)\xi + \Omega_{xy}(x_0, y_0, z_0)\eta + \\ & \Omega_{xz}(x_0, y_0, z_0)\zeta\ ,\end{split} \tag{5}$$

$$\begin{split}\ddot{\eta} + 2\dot{\xi} =& \Omega_{yx}(x_0, y_0, z_0)\xi + \Omega_{yy}(x_0, y_0, z_0)\eta + \\ & \Omega_{yz}(x_0, y_0, z_0)\zeta\ ,\end{split} \tag{6}$$

$$\begin{split}\ddot{\zeta} =& \Omega_{zx}(x_0, y_0, z_0)\xi + \Omega_{zy}(x_0, y_0, z_0)\eta + \\ & \Omega_{zz}(x_0, y_0, z_0)\zeta\ ,\end{split} \tag{7}$$

where the partial derivatives in (x_0, y_0, z_0) mean that the value is calculated at the equilibrium point being analyzed. Partial derivatives are shown in equations 8 - 13.

$$\begin{split}\Omega_{xx} =& 1 + k\Bigg[\frac{3(1-2\mu^*)(x-x_1)^2}{((x-x_1)^2+y^2+z^2)^{5/2}} - \\ & \frac{1-2\mu^*}{((x-x_1)^2+y^2+z^2)^{3/2})} + \\ & \frac{3\mu^*(x-x_{21})^2}{((x-x_{21})^2+y^2+z^2)^{5/2}} - \\ & \frac{\mu^*}{((x-x_{21})^2+y^2+z^2)^{3/2}} - \\ & \frac{3\mu^*(x-x_{22})^2}{((x-x_{22})^2+y^2+z^2)^{5/2}} + \\ & \frac{\mu^*}{((x-x_{22})^2+y^2+z^2)^{3/2}}\Bigg],\end{split} \tag{8}$$

$$\begin{aligned}\Omega_{yy} =& 1 + k\Bigg[\frac{3(1-2\mu^*)y^2}{((x-x_1)^2+y^2+z^2)^{5/2}} - \\ & \frac{1-2\mu^*}{((x-x_1)^2+y^2+z^2)^{3/2}} + \\ & \frac{3\mu^* y^2}{((x-x_{21})^2+y^2+z^2)^{5/2}} - \\ & \frac{\mu^*}{((x-x_{21})^2+y^2+z^2)^{3/2}} + \\ & \frac{3\mu^* y^2}{((x-x_{22})^2+y^2+z^2)^{5/2}} - \\ & \frac{\mu^*}{((x-x_{22})^2+y^2+z^2)^{3/2}}\Bigg],\end{aligned} \tag{9}$$

$$\begin{aligned}\Omega_{zz} =& k\Bigg[\frac{3(1-2\mu^*)z^2}{((x-x_1)^2+y^2+z^2)^{5/2}} - \\ & \frac{1-2\mu^*}{((x-x_1)^2+y^2+z^2)^{3/2}} + \\ & \frac{3\mu^* z^2}{((x-x_{21})^2+y^2+z^2)^{5/2}} - \\ & \frac{\mu^*}{((x-x_{21})^2+y^2+z^2)^{3/2}} + \\ & \frac{3\mu^* z^2}{((x-x_{22})^2+y^2+z^2)^{5/2}} - \\ & \frac{\mu^*}{((x-x_{22})^2+y^2+z^2)^{3/2}}\Bigg],\end{aligned} \tag{10}$$

$$\begin{aligned}\Omega_{xy} = \Omega_{yx} =& k\Bigg[\frac{3(1-2\mu^*)(x-x_1)^2 y}{((x-x_1)^2+y^2)^{5/2}} + \\ & \frac{3\mu^*(x-x_{21})^2)y}{((x-x_{21})^2+y^2)^{5/2}} + \\ & \frac{3\mu^*(x-x_{22})y}{((x-x_{22})^2+y^2)^{5/2}}\Bigg],\end{aligned} \tag{11}$$

$$\begin{aligned}\Omega_{xz} = \Omega_{zx} =& k\Bigg[\frac{3(1-2\mu^*)(x-x_1)z}{((x-x_1)^2+y^2+z^2)^{5/2}} + \\ & \frac{3\mu^*(x-x_{21})z}{((x-x_{21})^2+y^2+z^2)^{5/2}} + \\ & \frac{3\mu^*(x-x_{22})z}{((x-x_{22})^2+y^2+z^2)^{5/2}}\Bigg],\end{aligned} \tag{12}$$

$$\begin{aligned}\Omega_{yz} = \Omega_{zy} =& k\Bigg[\frac{3(1-2\mu^*)yz}{((x-x_1)^2+y^2+z^2)^{5/2}} + \\ & \frac{3\mu^* yz}{((x-x_{21})^2+y^2+z^2)^{5/2}} + \\ & \frac{3\mu^* yz}{((x-x_{22})^2+y^2+z^2)^{5/2}}\Bigg].\end{aligned} \tag{13}$$

In equations 5 - 7, ξ, η and ζ represent the position of the particle with respect to the equilibrium point. Through numerical analysis, we observed that the equilibrium points exist only in the xy plane, regardless of the values assigned to d, μ^* and k. Due to the fact that the equilibrium points for the rotating mass dipole model are in the xy plane, the equation 7 is decoupled (it does not depend on ξ and η); therefore, the equation of motion 7 becomes

$$\ddot{\zeta} = -\vartheta\zeta, \tag{14}$$

where ϑ is constant and depends on the values assigned to d, μ^* and k. Equation 14 shows that the motion perpendicular to the xy plane is periodic with frequency $\omega = \sqrt{\vartheta}$. Motion in the z direction is therefore limited with

$$\zeta = c_3\cos(\sqrt{\vartheta}t) + c_4\sin(\sqrt{\vartheta})t, \tag{15}$$

where c_3 and c_4 are integration constants.

When the motion is in the xy plane, the nontrivial characteristic roots of the equations 5, 6 were obtained in Barbosa Torres dos Santos et al. (2017) (considering $k = 1.$). The linearization around L_1 and L_2 provides a pair of real eigenvalues (*saddle*), corresponding to one-dimensional stable and unstable manifolds, and one pair of imaginary eigenvalues, suggesting a two-dimensional central subspace in the plane xy, which accounts for an oscillatory behavior around the equilibrium point of the linear system (Howell 1982; Haapala et al. 2015). Hence, in general, for L_1 and L_2, the stability type is *saddle*$\times$*center*$\times$*center* for the problem studied here and also for the CRTPB considering $0 < \mu \leq 0.5$. The Lyapunov Center Theorem guarantees, for the planar case, the existence of a one-parameter family of periodic orbits emanating from each of the collinear equilibrium points. Thus, for the spatial case, two one-parameter families of periodic orbits around L_1 and L_2 are expected. It was observed that the nature of the eigenvalues of the collinear equilibrium points is not altered when we vary d, μ^* and k.

Consider the linearized dynamics around the L_1 equilibrium point. We will adopt the coordinates $\mathbf{x'} = (\xi; \eta; u; v)$, where u and v are the velocities in the x and y direction, respectively, for the physical variables in the linearized planar system. To differentiate, we will use the coordinates $\mathbf{x_0} = (x; y; \dot{x}; \dot{y})$ for the physical variables in the nonlinear system and, finally, $\mathbf{y} = (y_1;\ y_2;\ y_3;\ y_4)$ for the variables in the diagonalized system. We know that if we choose an initial condition anywhere near the equilibrium point the real components of the eigenvalues (stable and unstable) will dominate the particle's behavior. But instead of specifying any initial condition for the system, we want to find an orbit around the equilibrium point L_1, for example, with some desired behavior, such as a periodic orbit. This becomes easy if we use the diagonalized system ($\mathbf{y_0}$) to determine the initial conditions. As we want to minimize the component in the unstable direction of the non-linear path, we must choose the initial conditions that correspond to the harmonic motion of the linear system. Thus, we choose the initial condition in the diagonalized system as $\mathbf{y_0} = (0; 0; y_3; y_4)$, where the non-zero initial values can be complex numbers and are intended to amplify the oscillatory terms. Null terms have the function of nullifying exponential (unstable) terms. In fact, if we want to get real solutions at the $\mathbf{x}'$ coordinates, we must consider y_3 and y_4 as complex conjugates. Transforming these conditions back to the original coordinates of the linear system, from the transformation $\mathbf{x_0} = T\mathbf{y_0}$, we find the initial conditions in the linearized system $\mathbf{x_0'} = (x', y', u, v)$, where T is the matrix of the eigenvectors of the state transition matrix A. The Jacobian matrix A contains the Hessian pseudo potential derived from the truncated Taylor series expansion over the reference solution.

Due to the fact that these initial conditions were chosen to nullify the unstable and stable eigenvectors, they provide a harmonic movement in the linear system.

Now that we have the initial conditions for the linear system, we want to find a periodic planar orbit in the nonlinear system.

We note that the potential function for the system studied here depends only on the distances that a spacecraft are from the primary bodies, that is, it has symmetry with respect to the x-axis. Taking advantage of the fact that the planar orbits are symmetrical with respect to the x-axis, the initial state vector takes the form $\mathbf{x_0}= [x_0 \; 0, \; 0, \; \dot{y}_0]^T$. These symmetries were used to find symmetric periodic orbits. This was done by determining the initial conditions, on the x-axis, where the initial velocity is perpendicular to this axis ($\dot{y}$) and then the integration is done until the path returns by crossing the x-axis with the speed orientation $\dot{y}_f$ opposite to the initial condition. This orbit can be used as an initial guess to use Newton's method, where the target state is quoted above; that is, that the orbit returns to x-axis with normal velocity. The equations of motion and the state transition matrix are incorporated numerically until the trajectory crosses the x-axis again. The final desired condition has the following form: $\mathbf{x_f}= [x_f \; 0, \; 0, \; \dot{y}_f]^T$.

3. COLLINEAR EQUILIBRIUM POINTS AS A FUNCTION OF THE RATIO BETWEEN GRAVITATIONAL AND CENTRIFUGAL ACCELERATIONS

In this section, we analyze the influence of the parameter k on the position of the collinear equilibrium points, since the influence of d and μ^* on the collinear points has already been performed in the work of Barbosa Torres dos Santos et al. (2017).

To determine how k affects the positions of the collinear equilibrium points, we consider $\mu^* = 1 \times 10^{-3}$ and $d = 1/12$ canonical units.

Figure 2 shows the x coordinates of L_1, L_2 and L_3 as a function of k. Because they are at both ends of the x axis, the positions of L_2 (right curve) and L_3 (left curve) are more affected than the position of L_1. Consider that there are three forces acting on the system: (i) the gravitational force of M_1; (ii) the gravitational attraction of M_2; and (iii) the centrifugal force, which is directly proportional to the angular velocity of the system around the center of mass and the distance between the equilibrium point and the center of mass of the system. Thus, by decreasing the angular velocity of the asteroid system around the center of mass, as k becomes larger, it is necessary to increase the distance between P and the center of mass, such that the centrifugal force remains at the same value and it counterbalances the gravitational forces from M_1 and M_2, which remain unchanged. Thus, L_2 and L_3 move away from the center of mass of the system. Although L_1 also moves away from the center of mass of the system, it does so in a more subtle way. This is because, when moving away from the center of mass of the system, L_1 approaches M_2. Regarding the gravitational force increases, a balancing force is needed to prevent L_1 from going too close to M_2.

As shown in Figure 2, the x coordinates of L_2 and L_3 tend to $\pm\infty$, respectively, when $k \to \infty$, that is, when the asteroid system ceases to rotate. This implies that L_2 and L_3 cease to exist when the asteroids are static. On the other hand, the equilibrium point L_1 continues to exist when $k \to \infty$, due to the balance between the gravitational forces between M_1 and M_2.

4. PERIODIC ORBITS AROUND THE FIRST AND SECOND COLLINEAR EQUILIBRIUM POINTS AS A FUNCTION OF THE MASS PARAMETER AND THE SIZE OF THE DIPOLE

Based on previous knowledge about Type A asteroids, we consider that the most massive primary

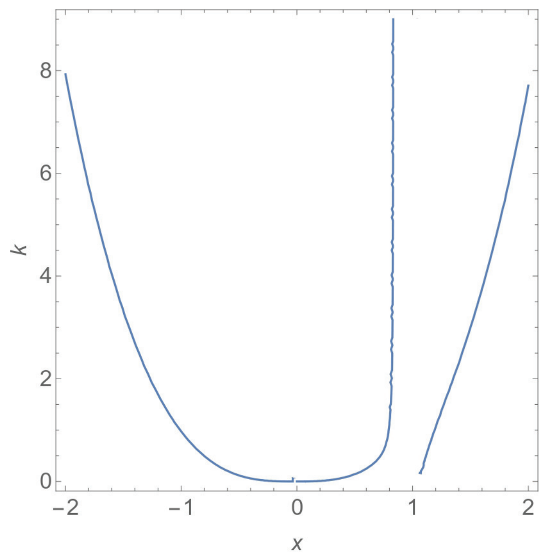

Fig. 2. x-coordinates of the equilibrium points L_1, L_2 and L_3 for different values of k. The color figure can be viewed online.

is spherical in shape and with a diameter of 5 km (Pravec & Harris 2007; Walsh & Jacobson 2015). Also, knowing that, on average, the mutual orbit of type A binary asteroids has a semi-major axis of about 4.8 primary component radii (Walsh & Jacobson 2015), we consider that the distance between the bodies is 12 km, which is the normalization factor for the distances. Finally, type A asteroids are known to have moderately sized secondaries, ranging from 4% to 58% of the size of the primary; the mass ratios $[m_2/(m_1+m_2)]$ vary from 6.4×10^{-5} to 2.0×10^{-1}. Based on this evidence, we will consider in this analysis the dimension of the secondary from 0 to 2 km, where we vary it in steps of 500 meters, and a range of the mass ratios from 1×10^{-5} to 1×10^{-1}, where we vary them in steps of 10^{-1}.

Periodic orbits are of special interest to explore the dynamical behavior of a massless particle in the vicinity of two primary bodies.

The results below were obtained by calculating approximately 3500 orbits from each family, starting from an initial condition with very low amplitude, and continuing the families until the orbits obtained came near the surface of the asteroids. To find symmetric periodic orbits, we consider $k = 1$, that is, the bodies orbit the center of mass of the system without any internal forces.

Each family was calculated for different values of μ^* and d to highlight the effect of the mass ratio of the system and of the elongated shape of the secondary body on the dynamical behavior of a space vehicle in the vicinity of the binary system. To analyze the influence of the elongation of the secondary body on the periodic orbits, we determined the periodic orbits considering the values $d = 0$; 0.5; 1; 1.5 and 2 km. Also, aiming to understand the influence of μ^* on the periodic orbits, we determined the periodic orbits considering the values $\mu^* = 10^{-5}$; 10^{-4}; 10^{-3}; 10^{-2} and 10^{-1}.

We are interested in the stability of the periodic solutions, which can be determined by analyzing the eigenvalues of the monodromy matrix. Given the sympletic nature of the dynamical system, if λ is a characteristic multiplier, then $1/\lambda$ also is, as well as $\overline{\lambda}$ and $1/\overline{\lambda}$. Thus, the periodic solutions investigated have six characteristic multipliers that appear in reciprocal pairs, with two of them being unitary (Meyer & Hall 1992; Bosanac 2016). The other four may be associated with the central subspace or with the stable/unstable subspace. In general, a particular orbit has six characteristic multipliers of the form 1, 1, λ_1, $1/\lambda_1$, λ_2 and $1/\lambda_2$.

The stability indices offer a useful measure of orbital stability. Following Broucke (1969), the stability index is defined as $s_i = |\lambda_i + 1/\lambda_i|$, $i = 1, 2$. A periodic orbit is unstable and there is a natural flow out and into the orbit if any stability index is greater than 2, that is, if $s_i > 2$. On the other hand, a periodic orbit is stable and has no unstable subspace if $s_i < 2$ (Zimovan-Spreen et al. 2020). The magnitude of the stability index is directly related to the arrival/departure flow rate. The higher the value of s_i, the more unstable is the periodic orbit and bifurcations can occur when $s_i = 2$.

Given that the periodic orbits growing from the collinear points inherit the stability properties of L_1, L_2, and L_3, the eigenvalues of the monodromy matrix of these orbits and corresponding stability indices appear as: (i) a trivial pair of unitary values, resulting in $s_0 = 2$; (ii) a real pair of reciprocals , resulting in $s_1 > 2$; and (iii) a pair of complex conjugate eigenvalues with unitary absolute value, implying $s_2 < 2$. Thus, for the subsets of the periodic orbit (PO) families near the equilibria, s_1 is related to the stable/unstable subspace ($\lambda^{W_s}/\ \lambda^{W_u}$), while s_2 is the stability index corresponding to the pair accounting for the central subspace.

4.1. *Planar Orbits*

Figure 3 shows a family of planar orbits around L_1 with $\mu^* = 10^{-5}$ and $d = 0$. The orbits obtained do not intersect the asteroid although, as seen in Figure 3, as the amplitude increases along the family, the orbits expand from the vicinity of the equi-

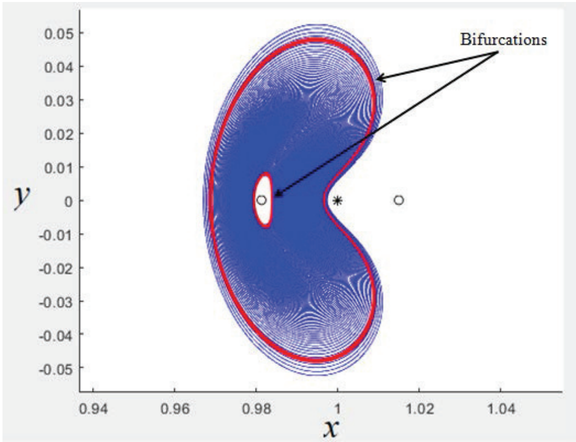

Fig. 3. Planar orbits around of the equilibrium point L_1 considering $\mu^* = 10^{-5}$ and $d = 0$. The color figure can be viewed online.

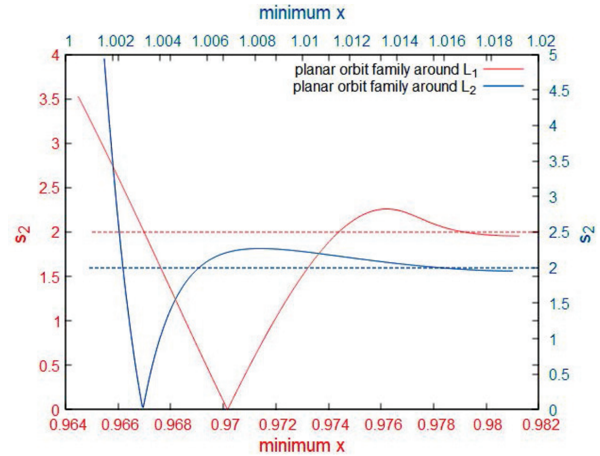

Fig. 4. Stability index (s_2) around L_1 (red) and L_2 (green) considering $d = 0$ and $\mu^* = 10^{-5}$. The color figure can be viewed online.

librium point towards the surface of the secondary body (black asterisk).

In Figure 3, the red orbits indicate where bifurcations occur, that is, when one of the stability indices s_1 or s_2 reaches the critical value 2. Note in Figure 3 that the maximum position reached by the infinitesimal mass body in the x component, when the second bifurcation occurs, is greater than the position of the secondary body.

Although many bifurcations exist in dynamical systems, only two types of bifurcation are of particular interest for the focus of this work; the pitchfork and period-multiplying bifurcations.

A family of periodic orbits undergoes a pitchfork bifurcation when the stability of the periodic orbit changes as a parameter evolves, which in our case is the energy constant. During this type of local bifurcation, a pair of eigenvalues (non-trivial) of the monodromy matrix pass through the critical values $\lambda_1 = 1/\lambda_1$ (or $\lambda_2 = 1/\lambda_2$) $= +\,1$ of the unit circle. Consequently, the stability index passes through s_1 (or s_2) $= 2$ (Bosanac 2016). In addition, the stability of the periodic orbits changes along a family, and an additional family of a similar period is formed. This new family of orbits has the same stability as the members of the original family before the bifurcation arose. On the other hand, a period-doubling bifurcation is identified when a pair of non-trivial eigenvalues ($\lambda_{1,2}$ and $1/\lambda_{1,2}$, where $\lambda_{1,2}$ means λ_1 or λ_2), passes through $\lambda_{1,2} = 1/\lambda_{1,2} = -1$ of the unit circle. Therefore, it represents a critical value of the stability index, such that $s_{1,2} = -2$ (Bosanac 2016).

When building the families of planar orbits, with $d = 0$ and $\mu^* = 10^{-5}$, we observe that the stability index (s_2) reaches the critical value three times for planar orbits around L_1 and L_2, as seen in Figures 4. In both figures, the horizontal axis displays the minimum x value along the orbits. The stability index s_1 does not reach the critical value for this μ^* and d.

For $\mu^* = 10^{-5}$, the equilibrium point L_1 is located at $x = 0.981278$, $y = 0$ and $z = 0$, while L_2 is at position $x = 1.01892$, $y = 0$ and $z = 0$. The orbits with smaller amplitudes are close to the equilibrium point (right side of Figures 4) and the first bifurcation occurs for a small amplitude orbit ($x \approx 0.97583$ for L_1 and $x \approx 1.01577$ for L_2). As we continue the planar family, the stability index s_2 shown in Figure 4 continues to increase, reaches a maximum, decreases and reaches the value 2 again, where another bifurcation occurs, with $x \approx 0.99408$ for L_1 and $x \approx 1.0056$ for L_2. As we continue the families of planar orbits around L_1 and L_2, the stability index decreases, reache a minimum, increases and again and reaches the critical value 2, where another bifurcation occurs. After the third bifurcation, the stability index further increases and we did not detect additional bifurcations given that, as the orbits are very close to the center of mass of the secondary body, our Newton method looses track of planar orbits, converging to a completely different family of orbits.

Figures 5 (a), (b) and (c) provide information about the types of the bifurcations that occur along the family of planar orbits. For $\mu^* = 10^{-5}$ and $d = 0$, analyzing the path of the characteristic multipliers in Figures 5 (a) and (b), we find that the first bifurcation is a supercritical pitchfork bifurcation, while the second one corresponds to a subcritical pitch-

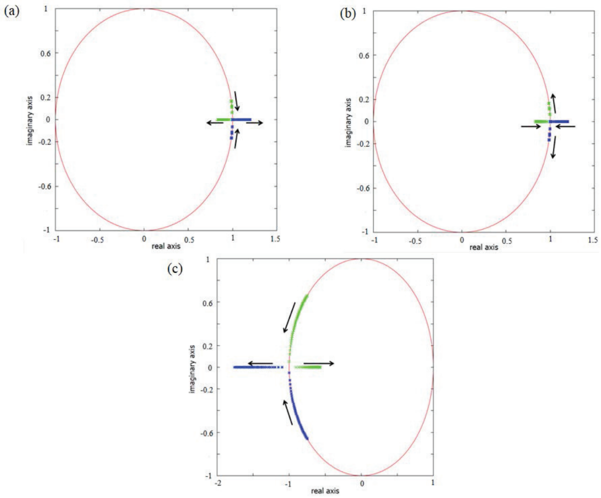

Fig. 5. (a) Behavior of the characteristic multipliers at the first pithckfork bifurcation around L_1 and L_2. (b) Behavior of the characteristic multipliers at the second pithckfork bifurcation around L_1 and L_2. (c) Behavior of the characteristic multipliers that leads to the period-doubling bifurcation around L_1 and L_2. In these cases we consider $d = 0$ and $\mu^* = 10^{-5}$. The color figure can be viewed online.

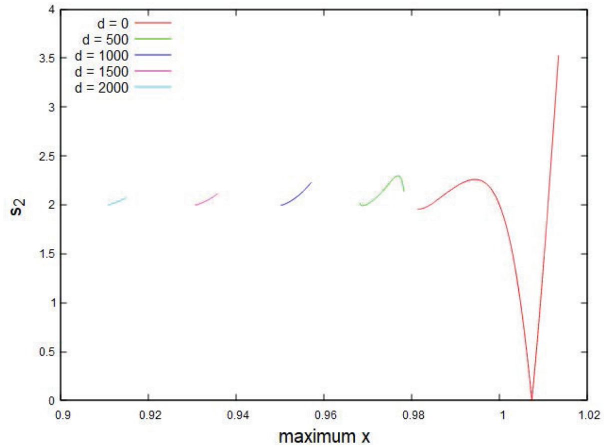

Fig. 6. Planar orbit stability index around L_1 for different values of d. The color figure can be viewed online.

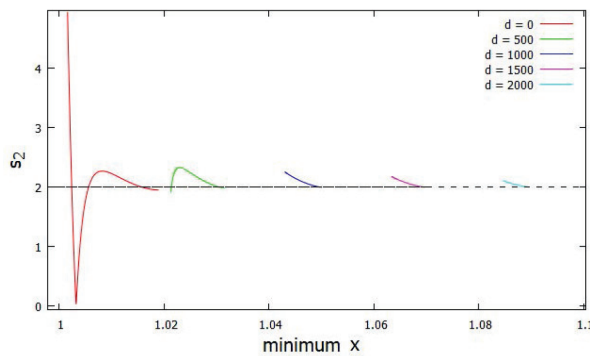

Fig. 7. Planar orbit stability index around L_2 for different values of d. The color figure can be viewed online.

fork case. This suggests that new families of periodic orbits appear in those regions when the bifurcation occurs (Feng et al. 2016). In fact, after the first bifurcation (low amplitude periodic orbit), it is possible to detect halo orbits, while after the second bifurcation the family of axial orbits appears (Grebow 2006). Unlike the planar Lyapunov orbits, halo and axial orbits are three-dimensional.

Figure 5 (c) shows the behavior of the eigenvalues at the third bifurcation. The characteristic multipliers start in the imaginary plane and move until they collide on the negative real axis and start to reach only real values on the negative axis. Thus, the eigenvalues indicate a period-doubling bifurcation.

Figure 6 and 7 provides information about the stability index (considering the values of s_2), around L_1 and L_2, respectively, when we increase the dipole dimension from 0 meters, that is, the body is modeled as a mass point, up to the dimension of 2000 meters. In this analysis we consider the constant mass ratio in the value of $\mu^* = 10^{-5}$. When we consider the dipole as a point mass body ($d = 0$), it is possible to observe three bifurcations (the red curve passes through the critical value three times). We can observe that as we increase the dimension of the secondary, the second bifurcation points in the planar orbits around L_1 and L_2 cease to exist because the trajectories collide with the secondary body. This is because, as the dimension of the dipole varies and the planar orbits approach the secondary body, our Newton method looses track of the planar orbits, converging to a completely different family of the orbits. Note that, the larger the dipole size, the smaller the planar orbit family found.

4.2. *Influence of the Mass Parameter and the Size of the Dipole on the Planar Orbits*

Now, we investigate how the planar orbits evolve as a function of the dipole size and mass ratio in canonical units. With the normalization factor being $D = 12000$ meters, the dipole sizes used in our study were $d = 0$, 500, 1000, 1500 and 2000 meters.

Figures 8 provide information about the stability index s_1 of the planar orbits around L_1, respectively, as a function of d and μ^*. In both figures, the color code accounts for the size of the dipole (d).

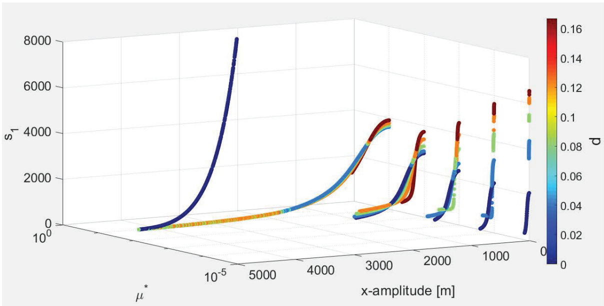

Fig. 8. Stability index (s_1) of the planar orbits around L_1 for different values of d and μ^*. The color figure can be viewed online.

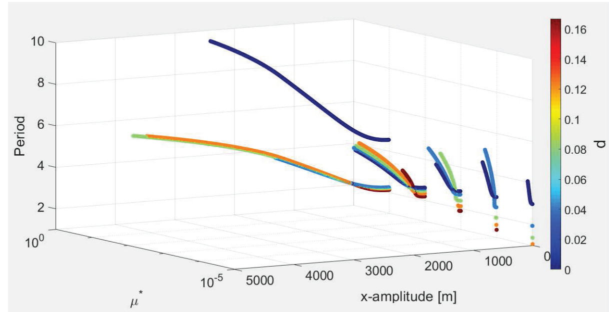

Fig. 9. Period of planar orbits around L_1 for different values of d and μ^*. The color figure can be viewed online.

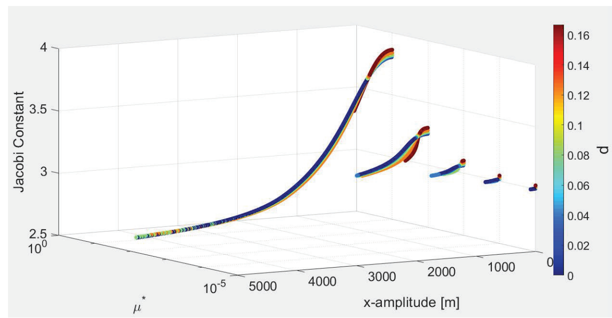

Fig. 10. Jacobi constant of planar orbits around L_1 for different values of d and μ^*. The color figure can be viewed online.

First, we investigate the solutions as d varies and μ^* is kept constant. Note that, in Figures 8, in general, when the size of the dipole increases, the planar orbits become more unstable. This means that the larger the secondary body, the more unstable the planar orbits are.

If we consider $d = 0$, which corresponds to the CRTBP, we observe that as μ^* increases, the orbits become increasingly unstable. On the other hand, when the elongated form of the secondary body is taken into account, s_1 becomes smaller as μ^* increases, and it only increases again after $\mu^* = 10^{-1}$. This information is important for space missions, since a high value in the stability index (s_i) indicates a divergent mode that moves the spacecraft away from the vicinity of the orbit quickly. In general, the stability index is directly related to the space vehicle's orbital maintenance costs and inversely related to the transfer costs. This same analysis was performed around the L_2 equilibrium point, where we found similar results.

Next, we analyze the period of the planar orbits in terms of d and μ^* around L_1. As shown in Figures 9, for low amplitude, as d increases, with μ^* kept constant, the period of the planar orbits decreases. This is because the mass distribution of the secondary body allows part of the mass of the asteroid to be closer to the negligible mass particle, causing the gravitational attraction to become larger, thus increasing the acceleration in the vicinity of the secondary body and decreasing the orbital period. On the other hand, when the x-amplitude is large, the results can be inverted, as shown in Figure 9. In general, when the amplitude of the orbit increases, the orbital period becomes longer. Similar results were found in the vicinity of L_2.

Considering the family with $d = 0$, when μ^* increases the period of the orbits remains similar, except when $\mu^* = 10^{-1}$. Conversely, when the elongation of the secondary body is considered, in general, for a given value of d the larger the mass ratio, the longer the orbital period.

Finally, we analyze the energy of the system in terms of d and μ^*, as shown in Figure 10.

We find that when d or μ^* increase, the energy required to orbit a given equilibrium point decreases. That is, the more elongated the secondary body and the larger the value of μ^*, the less energy is needed to orbit a given equilibrium point. This also means that, as the size of the dipole increases or as the mass ratio of the system increases, the bifurcations occur at lower energies. The same analysis performed for L_1 can be done for L_2.

4.3. *Computing Halo Orbits*

Halo orbits are a three-dimensional branch of planar orbits that appear when the planar orbit stability index reaches the critical value $s_2 = 2$. Figure 11 shows a family of halo orbits around L_1 with $\mu^* = 10^{-5}$ and $d = 0$. The orbits are in three-dimensional space and as the amplitude increases along the family, the halo orbits expand from the

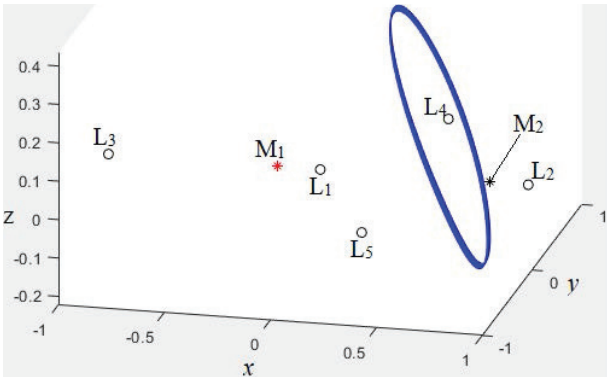

Fig. 11. Halo orbits around the L_1 equilibrium point considering $\mu^* = 10^{-5}$ and $d = 0$. The color figure can be viewed online.

vicinity of the equilibrium point towards the surface of the secondary (black asterisk).

To find the initial conditions of the halo orbit, we keep the coordinate x_0 fixed and search for z_0^*, $\dot{y}_0^*$ and $T/2^*$ such that $\dot{x}^*(T/2^*)$, $\dot{z}^*(T/2^*)$ and $y^*(T/2^*)$ are all null. Then, to find the halo orbit, we use as initial guess the position x_0, velocity ($\dot{y}$) and period (T) of the planar orbit when the stability index $s_2 = 2$. Knowing these initial conditions, all that remains is to determine the initial guess of the position on the z axis, such that we can find the halo orbit. Because the halo and planar orbit are similar (when $s_2 = 2$), the position on the z axis of the halo orbit must have a very small value (almost planar orbit). Thus, in this work, the value of $z_0 = 0.0001$ canonical units was used as the initial guess for the position on the axis z. A Newton method for this problem is

$$\mathbf{x}_{n+1} = \mathbf{x}_n - [Df(\mathbf{x}_n)]^{-1} f(\mathbf{x}_n), \tag{16}$$

with $\mathbf{x} = (z, \dot{y}, T/2)$ and $\mathbf{x}_0 = (z_0, \dot{y}_0, T_0/2)$. Here $(z_0, \dot{y}_0, T_0/2)$ is the initial guess of the halo orbit.

The differential is

$$Df(\mathbf{x}) = \begin{bmatrix} \phi_{4,3} & \phi_{4,5} & g_4(x_0, 0, z(T/2), 0, \dot{y}(T/2), 0) \\ \phi_{6,3} & \phi_{6,5} & g_6(x_0, 0, z(T/2), 0, \dot{y}(T/2), 0) \\ \phi_{2,3} & \phi_{2,5} & g_2(x_0, 0, z(T/2), 0, \dot{y}(T/2), 0) \end{bmatrix}, \tag{17}$$

where $\phi_{i,j}$ are elements of the monodromy matrix, $g : U \subset \mathbb{R}^6 \to \mathbb{R}^6$ is the vector field of the restricted synchronous three-body problem, $z(T/2) = \phi_3(x_0, 0, z, 0, y, 0, T/2)$ and $\dot{y}(T/2) = \phi_5(x_0, 0, z, 0, y, 0, T/)$. With this information, we expect that if $\mathbf{x}_0$ is close enough to the halo orbit, then $\mathbf{x}_n \to \mathbf{x}^*$ as $n \to \infty$. g is given by equation 18.

$$g(x, y, z, \dot{x}, \dot{y}, \dot{z}) = \begin{bmatrix} g_1(x, y, z, \dot{x}, \dot{y}, \dot{z}) \\ g_2(x, y, z, \dot{x}, \dot{y}, \dot{z}) \\ g_3(x, y, z, \dot{x}, \dot{y}, \dot{z}) \\ g_4(x, y, z, \dot{x}, \dot{y}, \dot{z}) \\ g_5(x, y, z, \dot{x}, \dot{y}, \dot{z}) \\ g_6(x, y, z, \dot{x}, \dot{y}, \dot{z}) \end{bmatrix} = \begin{bmatrix} \dot{x} \\ \dot{y} \\ \dot{z} \\ 2\dot{y} + D_x\Omega \\ -2\dot{x} + D_y\Omega \\ D_z\Omega \end{bmatrix}. \tag{18}$$

All the information we need to start Newton's method is shown above.

From the cylinder theorem, it was possible to find a halo orbit family. Thus, having found a halo orbit and noticing that it has exactly two unit eigenvalues, we can use that as a starting point to move along the cylinder. We use the initial conditions from the previous halo orbit as a starting point to find the next halo orbit at a slightly larger value of x (x coordinate closer to the secondary asteroid). If we find another halo orbit here, we iterate through the process. In this way it was possible to calculate a halo orbit family. The x coordinate step to determine each halo orbit was $x = 0.00002$.

4.4. *Halo Orbits*

Figures 12 and 13 illustrate how the halo orbits appear at the tangent bifurcations of the planar orbits around L_1 and L_2 when $\mu^* = 10^{-5}$ and $d = 0$. As we built the family of halo orbits, we observed that the amplitude of the orbits increases as the halo orbits move towards the secondary.

For the conditions considered here, the halo orbit appears at $x \approx 0.98418$ for L_1 and at $x \approx 1.01575$ for L_2. Figure 14 shows the path of the characteristic multipliers over the unit circle to the halo orbit around L_1 and L_2. Initially, the characteristic multipliers move in the direction shown by the purple arrows until they collide with the negative real axis, configuring a periodic doubling bifurcation. After moving subtly along the real negative axis, the characteristic multipliers return, moving in the direction of the red arrows, colliding again at -1 and then assuming imaginary values, configuring another periodic doubling bifurcation.

Figures 15 and 16 provide information about the s_1 stability index as a function of d and μ^*. Note

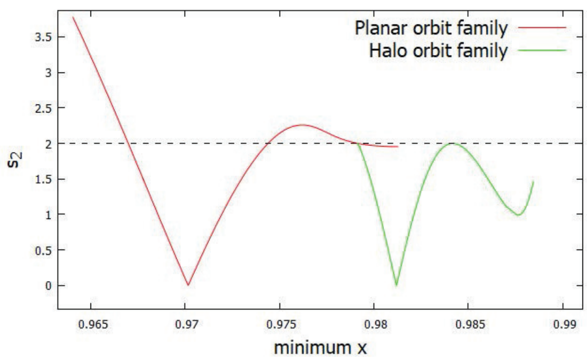

Fig. 12. Stability index (s_2) of the planar and halo orbit families around L_1 considering $d = 0$ and $\mu^* = 10^{-5}$. The color figure can be viewed online.

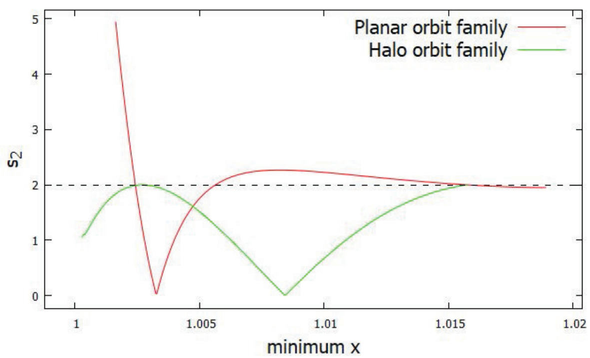

Fig. 13. Stability index (s_2) of the planar and halo orbit families around L_2 considering $d = 0$ and $\mu^* = 10^{-5}$. The color figure can be viewed online.

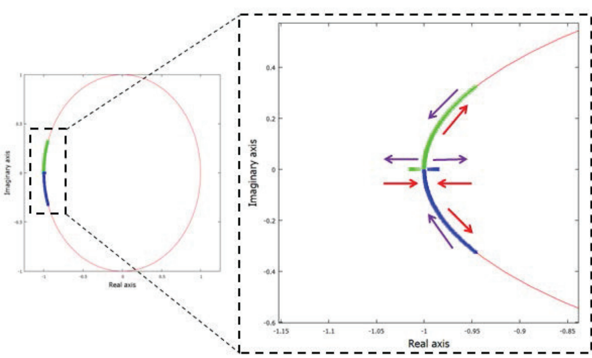

Fig. 14. Behavior of the of characteristic multipliers at the period doubling bifurcation. The color figure can be viewed online.

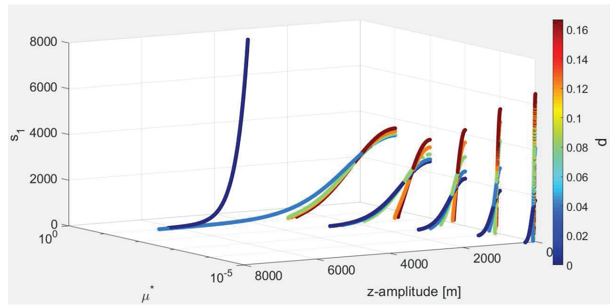

Fig. 15. Stability index (s_1) of halo orbits around L_1 as a function of d and μ^*. The color figure can be viewed online.

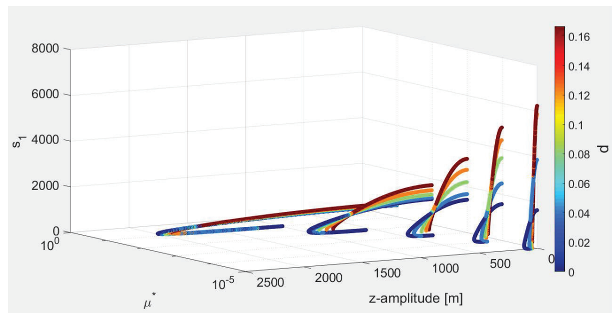

Fig. 16. Stability index (s_1) of halo orbits around L_2 as a function of d and μ^*. The color figure can be viewed online.

that the smaller the amplitudes of the halo orbits, the larger the value of the stability index s_1, when considering fixed d and μ^*. As the amplitude of the halo orbit increases, the stability index decreases. If we set $d = 0$, we still detect stable halo orbits for small values of μ^*. These orbits were also found by several authors using the restricted three-body problem and are called near rectilinear halo orbits (NRHO) (Howell 1982; Zimovan-Spreen et al. 2020). NRHOs are defined as the subset of the halo orbit family with stability indexes around $s_i \pm 2$ and with no stability index considerably greater in magnitude than the others.

Figures 17 and 18 provide information about the stability index s_1 as the size of the dipole increases from 0 to 2000 meters and the mass ratio is kept constant at $\mu^* = 10^{-5}$. The influence of the dimension of the secondary body on the stability of the halo orbits is clear in the plots. Note that, as the size of the secondary increases, the values of s_1 become larger in the vicinity of the equilibrium point L_1 and L_2.

Note that it is unlikely to detect NRHOs around L_1 when we take into account the elongated shape of the secondary body and assume small values of μ^*. On the other hand, there are several NRHOs around L_2. In this work, we found NRHOs up to $d = 1500$ meters, as shown in Figure 18.

However, as shown in Howell (1982), the stability index also depends on the mass ratio of the system. Considering $d = 0$ and increasing μ^*, the stability

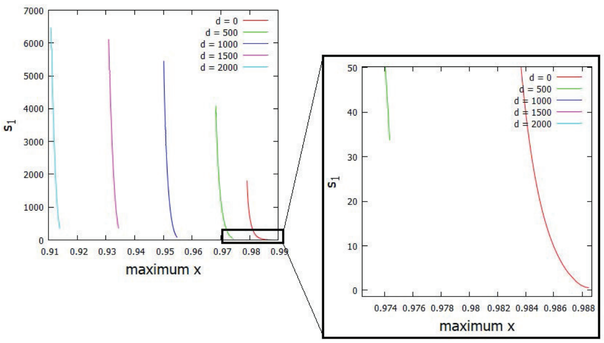

Fig. 17. Halo orbit stability index around L_1 for different values of d. The color figure can be viewed online.

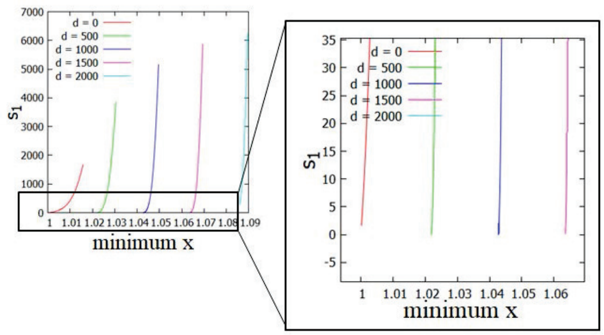

Fig. 18. Halo orbit stability index around L_2 for different values of d. The color figure can be viewed online.

index s_1 increases. We did not detect any NRHO for values of $\mu^* \geq 10^{-1}$ and $d = 0$. However, we find NRHO for $\mu^* \geq 10^{-1}$ and $d = 0$ around L_2. These results are similar to those obtained by Howell (1982). However, taking into account the elongation of the secondary and assuming large values of μ^* ($\mu^* \geq 10^{-1}$), it is possible to find family members of stable halo orbits around L_1 and L_2. Thus, in the model used in this article, stable periodic orbits in the vicinity of irregular bodies exist, even when the secondary has a non-spherical shape. This agrees with the results obtained by Chappaz & Howell (2015), who found stable orbits around L_1 and L_2 taking into account the elongated shape of the secondary body and considering $\mu = 0.4$ with the triaxial ellipsoid model.

Now we analyze how the period of the halo orbits around L_1 and L_2 is affected by d and μ^*. As d increases and μ^* is kept constant, the periods of the halo orbits decrease, as shown in Figures 19 and 20.

This is because the gravitational attraction is stronger near the particle, due to the mass distribution of the secondary body, causing the acceleration to increase and the orbital period to decrease. As the amplitude of the halo orbit increases, its orbital period becomes shorter.

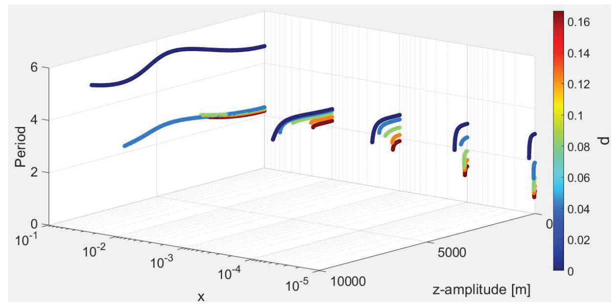

Fig. 19. Period of the halo orbits around L_1 as a function of d and μ^*. The color figure can be viewed online.

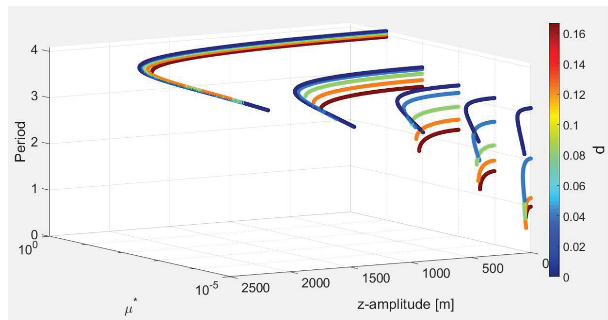

Fig. 20. Period of the halo orbits around L_2 as a function of d and μ^*. The color figure can be viewed online.

Considering the elongated shape of the asteroid, but keeping d constant and increasing μ^*, we notice that the period of the halo orbits become longer. This is because, as μ^* increases, the equilibrium point move away from the secondary body, thus the halo orbits are further away from the secondary body, which causes the gravitational acceleration to decrease, and thus the orbital period of the particle along the orbit to increase.

Figures 21 and 22 provide information on the behavior of the Jacobi constant of the halo orbits as a function of d and μ^*. Note that when d or μ^* increase, the range of value of the Jacobi constant also increases. This is important information in terms of the application to space missions. Note that the larger the mass ratio of the system, or the longer the secondary body, the less energy is needed for the halo orbits to branch from the planar orbits.

5. CONCLUSION

In this paper, the general dynamical environment in the vicinity of binary asteroid systems is explored. Based on the physical and orbital parameters of type A asteroids, the positions of the collinear balance

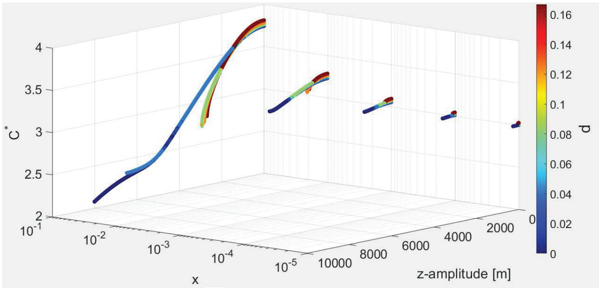

Fig. 21. Jacobi constant of the halo orbits around L_1 with respect to d and μ^*. The color figure can be viewed online.

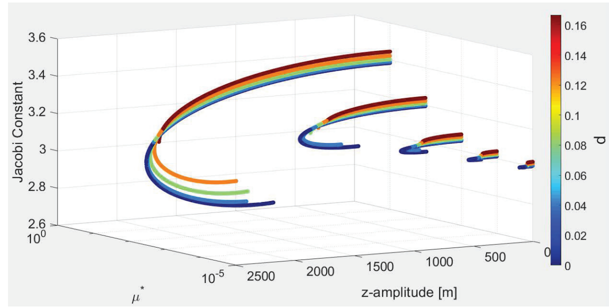

Fig. 22. Jacobi constant of the halo orbits around L_2 with respect to d and μ^*. The color figure can be viewed online.

points as a function of angular velocity were computed. We found that the locations of the collinear equilibrium points L_3 and L_2 are more sensitive to changes in the rotation rate, compared to L_1.

Families of planar and halo orbits were computed around these equilibrium points and we found that the closer the periodic orbits are to the equilibrium point, the more unstable they are.

Numerical evidence shows that the stability of the periodic orbits around the equilibrium points depends on the size of the secondary body and on the mass ratio of the system. We observed that, the more elongated the secondary body, the more unstable the planar orbits are. Additionally, we detected unstable and stable halo orbits when $d = 0$ and when $d \neq 0$.

Finally, we observed that, keeping the mass ratio constant, the more elongated the secondary body, the lower the orbital periods of planar and halo orbits around the equilibrium points.

Thus, if a spacecraft were to be placed in the vicinity of an equilibrium point, fuel consumption required for orbital maintenance would be higher around more elongated secondary bodies.

The authors wish to express their appreciation for the support provided by: Grants 140501/2017-7, 150678/2019-3, 422282/2018-9 and 301338/2016-7 from the National Council for Scientific and Technological Development (CNPq); Grants 2016/24561-0, 2016/18418-0, 2018/06966-8 and 2018/07377-6 from São Paulo Research Foundation (FAPESP); Grant 88887.374148/2019-00 from the National Council for the Improvement of Higher Education (CAPES); Grant E-26/201.877/2020, from Rio de Janeiro Research Foundation (FAPERJ) and to the National Institute for Space Research (INPE). This publication has been supported by the RUDN University Scientific Projects Grant System, Project No 202235-2-000

REFERENCES

Aljbaae, S., Chanut, T. G. G., Carruba, V., et al. 2017, MNRAS, 464, 3552, https://doi.org/10.1093/mnras/stw2619

Aljbaae, S., Prado, A. F. B. A., Sanchez, D. M., & Hussman, H. 2020, MNRAS, 496, 1645, https://doi.org/10.1093/mnras/staa1634

Barbosa Torres dos Santos, L., Bertachini de Almeida Prado, A. F., & Merguizo Sanchez, D. 2017, Ap&SS, 362, 61, https://doi.org/10.1007/s10509-017-3030-2

Blesa, F. 2006, Monografías del Seminario Matemático García de Galdeano, 33, 67

Bosanac, N. 2016, Leveraging natural dynamical structures to explore multi-body systems, Ph-D Thesis, Purdue Universitaty

Broucke, R. 1969, AIAA Journal, 7, 1003, https://doi.org/10.2514/3.5267

Celik, O. & Sanchez, J. P. 2017, JGCD, 40, 1390, https://doi.org/10.2514/1.G002181

Chanut, T. G. G., Aljbaae, S., & Carruba, V. 2015, MNRAS, 450, 3742, https://doi.org/10.1093/mnras/stv845

Chappaz, L. & Howell, K. C. 2015, CeMDA, 123, 123, https://doi.org/10.1007/s10569-015-9632-5

de Almeida Junior, A. K. & Prado, A. F. B. A. 2022, NatSR, 12, 4148, https://doi.org/10.1038/s41598-022-08046-x

dos Santos, L. B. T., de Almeida Prado, A. F. B., & Sanchez, D. M. 2017, Ap&SS, 362, 202, https://doi.org/10.1007/s10509-017-3177-x

dos Santos, L. B. T., Marchi, L., Sousa-Silva, P. A., et al. 2020, RMxAA, 56, 269, https://doi.org/10.22201/ia.01851101p.2020.56.02.09

Feng, J., Noomen, R., Visser, P., & Yuan, J. 2016, AdSpR, 58, 387, https://doi.org/10.1016/j.asr.2016.04.032

Ferrari, F., Lavagna, M., & Howell, K. 2016, CeMDA, 125, 413, https://doi.org/10.1007/s10569-016-9688-x

Grebow, D. J. 2009, Master of Science in Aeronautics, Thesis, Purdue University

Haapala, A. F., Howell, K. C., & Folta, D. C. 2015, AcAau, 112, 1, https://doi.org/10.1016/j.actaastro.2015.02.024

Howell, K. C. 1982, AsDyn, 1981, 528

Jacobson, S. A. & Scheeres, D. J. 2011, Icar, 214, 161, https://doi.org/10.1016/j.icarus.2011.04.009

Lan, L., Yang, H., Baoyin, H., & Li, F. 2017, Ap&SS, 362, 169, https://doi.org/10.1007/s10509-017-3148-2

Liu, X., Baoyin, H., & Ma, X. 2011, Ap&SS, 333, 409, https://doi.org/10.1007/s10509-011-0669-y

Margot, J.-L., Pravec, P., Taylor, P., Carry, B., & Jacubson, S. 2015, Asteroids IV, ed. P. Michael, F. E. De Meu, & W. F. Bottke (Tuczon, AZ: UAP), 355, https://doi.org/10.48550/arXiv.1504.00034

McCuskey, S. W. 1963, Introduction to celestial mechanics (Reading, MA: Addison-Wesley Pub. Co)

Meyer, K. R. & Hall, G. R. 1992, Sci, 255, 1756

Pravec, P., Scheirich, P., Kušnirák, P., et al. 2006, Icar, 181, 63, https://doi.org/10.1016/j.icarus.2005.10.014

Pravec, P. & Harris, A. W. 2007, Icar, 190, 250, https://doi.org/10.1016/j.icarus.2007.02.023

Pravec, P., Scheirich, P., Kušnirák, P., et al. 2016, Icar, 267, 267, https://doi.org/10.1016/j.icarus.2015.12.019

Riaguas, A., Elipe, A., & Lara, M. 1999, Impact of Modern Dynamics in Astronomy, Colloquium 172 of the International Astronomical Union, 169

Riaguas, A., Elipe, A., & López-Moratalla, T. 2001, CeMDA, 81, 235

Santos, L. B. T., Marchi, L. O., Aljbaae, S., et al. 2021, MNRAS, 502, 4277, https://doi.org/10.1093/mnras/stab198

Scheeres, D. J., Van wal, S., Olikara, Z., & Baresi, N. 2019, AdSpR, 63, 476, https://doi.org/doi:10.1016/j.asr.2018.10.016

Szebehely, V. 1967, Theory of orbits. The restricted problem of three bodies (New York, NY: Academic Press)

Tardivel, S. & Scheeres, D. J. 2013, JGCD, 36, 700, https://doi.org/10.2514/1.59106

Walsh, K. J., Richardson, D. C., & Michel, P. 2008, Natur, 454, 188, https://doi.org/10.1038/nature07078

Walsh, K. J. & Jacobson, S. A. 2015, Asteroids IV, ed. P. Michel, F. E. DeMeo, & W. F. Bottke, University of Arizona Press, 375, https://doi.org/10.48550/arXiv.1506.06689

Wang, W., Yang, H., Zhang, W., & Ma. G. 2017, Ap&SS, 362, 229, https://doi.org/10.1007/s10509-017-3206-9

Wen, T. & Zeng, X. 2022, AdSpR, 69, 2223, https://doi.org/10.1016/j.asr.2021.12.021

Werner, R. A. 1994, CeMDA, 59, 253, https://doi.org/10.1007/BF00692875

Yang, H.-W., Zeng, X.-Y., & Baoyin, H. 2015, RAA, 15, 1571, https://doi.org/10.1088/1674-4527/15/9/013

Yang, H.-W, Baoyin, H., Bai, X., & Li, J. 2017, Ap&SS, 362, 27, https://doi.org/10.1007/s10509-017-3007-1

Zeng, X., Jiang, F., Li, J., & Baoyin, H. 2015, Ap&SS, 356, 29, https://doi.org/10.1007/s10509-014-2187-1

Zeng, X., Gong, S., Li, J., & Alfriend, K. T. 2016, JGCD, 39, 1223, https://doi.org/10.2514/1.G001061

Zeng, X., Baoyin, H., & Li, J. 2016, Ap&SS, 361, 14, https://doi.org/10.1007/s10509-015-2598-7

Zeng, X., Zhang, Y., Yu, Y., & Liu, X. 2018, AJ, 155, 85, https://doi.org/10.3847/1538-3881/aaa483

Zhang, R., Wang, Y., Shi, Y., & Xu, S. 2020, AcAau, 177, 15, https://doi.org/10.1016/j.actaastro.2020.07.006

Zimovan-Spreen, E. M., Howell, K. C., & Davis, D. C. 2020, CeMDA, 132, 28, https://doi.org/10.1007/s10569-020-09968-2

S. Aljbaae, Allan Kardec de Almeida Jr, & L. B. T. dos Santos: Division of Space Mechanics and Control. National Institute for Space Research, INPE. São José dos Campos, Brazil.

Allan Kardec de Almeida Jr: Instituto de Telecomunicações, 3810-193 Aveiro, Portugal (allan.junior@inpe.br).

P. A. Sousa-Silva: São Paulo State University, UNESP. São João da Boa Vista, Brazil (priscilla.silva@unesp.br).

M. O. Terra: Technological Institute of Aeronautics, ITA. São Paulo dos Campos, Brazil (maisa@ita.br).

D. M. Sanchez: The University of Oklahoma, Norman OK, USA.

A. F. B. A. Prado: Postgraduate Division - National Institute for Space Research (INPE), São Paulo, Brazil (antonio.prado@inpe.br).

A. F. B. A. Prado: Professor, Academy of Engineering, RUDN University, Miklukho-Maklaya street 6, Moscow, Russia, 117198 (antonio.prado@inpe.br).

F. Monteiro: National Observatory, ON. Rio de Janeiro, Brazil (filipeastro@on.br).

Revista Mexicana de Astronomía y Astrofísica, **59**, 99–104 (2023)

https://doi.org/10.22201/ia.01851101p.2023.59.01.06

SOME PREDICTIONS OF SCALING RELATIONS: THE CASE OF THE BLACK HOLE IN M87

A. L. Iannella and A. Feoli

Department of Engineering, University of Sannio, Benevento, Italy.

Received April 4 2022; accepted October 21 2022

ABSTRACT

In the context of supermassive black holes and their host galaxies, we consider two scaling relations: $M_\bullet - R_e\sigma^3$ and $M_\bullet - M_G\sigma^2$, to derive three fundamental parameters for the supermassive black hole at the center of M87. In this paper we will get predictions for the efficiency and mass of the black hole, and the temperature of its accretion disk, by comparing them with the respective experimental values.

RESUMEN

En el contexto de los hoyos negros supermasivos y sus galaxias anfitrionas consideramos dos relaciones de escala: $M_\bullet - R_e\sigma^3$ y $M_\bullet - M_G\sigma^2$, para obtener tres parámetros fundamentales del hoyo negro supermasivo en el centro de M87. En este trabajo, al compararlas con los valores experimentales respectivos, obtenemos predicciones para la eficiencia y la masa del hoyo negro, así como para la temperatura del disco de acreción.

Key Words: accretion, accretion discs — black hole physics — galaxies: individual: M87 — quasars: supermassive black holes

1. INTRODUCTION

Today, it is increasingly evident that local galaxies of different morphological types host a supermassive black hole (SMBH) at their center (Kormendy and Richstone 1995; Richstone et al. 1998; Ferrarese and Ford 2005). In the literature, it is possible to find many correlations to understand the link between the mass of a supermassive black hole with the properties of the galaxy, such as the brightness or mass of the bulge, the scattering speed, the effective radius, the Sérsic index, etc. (Magorrian et al. 1998; Tremaine et al. 2002; Marconi and Hunt 2003; Haring and Rix 2004; Aller and Richstone 2007; Graham 2008; Hu 2008; Kisaka et al. 2008; Beifiori et al. 2009; Gültekin et al. 2009a), but also the correlations between the process of accretion of SMBHs and the formation and evolution of their galaxies (Silk and Rees 1998; Burkert and Silk 2001; Cavaliere and Vittorini 2002; King 2003; Wyithe and Loeb 2003; Granato et al. 2004; Haiman et al. 2004; Begelman and Nath, 2005; Murray et al. 2005; Sazonov et al. 2005; Croton et al. 2006; Hopkins et al. 2007a; Sijacki et al. 2007; Pipino et al. 2009a, b). There are numerous scaling relations found between the mass of the supermassive black hole and the different properties of the host spheroidal component, such as the bulge luminosity, mass, effective radius, central potential, dynamical mass, concentration, Sérsic index, binding energy, X-ray luminosity, momentum parameter, etc. (Ferrarese and Merritt 2000; Gebhardt et al. 2000; Laor 2001; Merritt and Ferrarese 2001; Wandel 2002; Graham and Driver 2005; Hopkins et al. 2007b; Gultekin et al. 2009b; Soker and Meiron 2011).

Among the various scaling relations, we consider $M_\bullet - R_e\sigma^3$ (Feoli and Mancini, 2011) and $M_\bullet - M_G\sigma^2$ (Feoli and Mele, 2005), where R_e, M_G and σ are the effective radius of the host spheroidal component, the mass and the velocity dispersion of the host galaxy, respectively.

The aim of this paper is, using these two scaling relations, to predict three particularly interesting parameters concerning the giant elliptical galaxy M87, which has been well studied in detail by Event Horizon Collaboration: the mass of the black hole, its efficiency and the temperature of the black hole accretion disk.

2. EFFICIENCY OF THE BLACK HOLE

The first parameter that we propose to derive is the efficiency ϵ of the black hole in the conversion of the matter captured into emitted radiation. This parameter has been obtained using Feoli and Mancini's model (2011).

The core of the model is the transformation of the angular momentum of the matter falling into the black hole, into the angular momentum of the radiation emitted during the process. Further details can be found in Feoli and Mancini (2011), Feoli (2014a) and Beltramonte et al. (2019). This model works better for the early-type galaxies, as can be observed in Feoli and Iannella (2019) and in Beltramonte et al. (2019).

Feoli and Mancini's model (2011) allows an estimate of ϵ for each single black hole, through the following relation:

$$\epsilon = \frac{R_e \sigma^3}{2 M_\bullet c G}, \tag{1}$$

where G is the gravitational constant and c the speed of light.

From this relation, by entering the parameters of the galaxy M87, we obtain $\epsilon = 0.007 \pm 0.003$. The effective radius $R_e = 0.82 \pm 0.07$ in Log(kpc) and the velocity dispersion $\sigma = 2.42 \pm 0.02$ in Log(km s^{-1}) have been taken from van den Bosch (2016) and the black hole mass $M_\bullet = 9.813 \pm 0.047$ in $Log(M_\odot)$ from the EHT Collaboration (VI, 2019). The value of the obtained efficiency is in good agreement with the value found in the EHT Collaboration (VIII, 2021), i.e. $\epsilon \lesssim 1\%$.

Of course, the model based on the conservation of angular momentum can also be used in a different way, i.e. if we know the efficiency of the black hole we can calculate the angular momentum of the matter orbiting around the hole, but not the spin of the black hole itself. The argument of angular momentum has been faced in a series of papers cited in Feoli (2014a), Feoli and Mancini (2011), and Beltramonte et al. (2019).
An interesting and more recent discussion of the angular momentum problem in an accretion disc can be found in Blandford and Globus (2022).

3. PREDICTION OF THE BLACK HOLE MASS

Feoli and Mele (2005) proposed a correlation between the mass of a supermassive black hole and the kinetic energy of the host galaxy. This correlation was tested with many different samples and fitting methods (Feoli and Mele, 2007; Feoli and Mancini, 2009; Mancini and Feoli, 2012; Benedetto et al. 2013; Iannella and Feoli, 2020) and a theoretical background was proposed in Feoli (2014b). Furthermore, in Iannella et al. (2021), the predictive power of the relation has been analysed and the statistical elaboration done previously has been enhanced. Finally, this relation proved to be very competitive with its very low intrinsic scatter (Saglia et al. 2016).

The relation can be very useful to understand the evolution of galaxies, just like the HR diagram is for the evolution of stars (Feoli and Mancini 2009), and allows good predictions of the masses of some black holes, so we decided to use it to predict the mass of the galaxy M87.

We have used the relation of Feoli and Mele (2005) to infer the mass of the black hole of M87:

$$Log M_\bullet = (m \pm se(m)) \left(Log \frac{M_G \sigma^2}{c^2} \pm se\left(Log \frac{M_G \sigma^2}{c^2} \right) \right) + (b \pm se(b)), \tag{2}$$

where m and b are respectively the slope and the intercept of the linear relation with the corresponding uncertainties.

We have considered the regression coefficients, which are the slope m and the intercept b for the $M_\bullet - M_G \sigma^2$ and $M_\bullet - \sigma$ relations, of the five samples taken from Iannella and Feoli (2020).

The predictions are reported in Table 1, and they are compared with those inferred by the correlation $M_\bullet - \sigma$ in Table 2 and with the experimental value of the EHT Collaboration (VI, 2019), that we indicate in logarithmic scale $Log\, M_\bullet = 9.813 \pm 0.047$ and in units of $M_\odot$.

It is evident that the $M_\bullet - M_G \sigma^2$ relation deduces in almost all cases a mass value closer to the experimental one than the one predicted by $M_\bullet - \sigma$, also having a narrower range of values. The only case in which this does not happen is in van den Bosch_174's sample, for which the intrinsic scatter of the linear relation is the highest (Iannella and Feoli, 2020).

We also want to compare our results with Nokhrina et al. (2019). They propose a method of estimating BH mass for core-jet AGN, following the theoretical model by Beskin et al. (2017) and obtaining the different values of BH mass for different magnetizations, reported in Table 3b. It is possible to observe that, within the errors, the black hole masses of Nokhrina et al. (2019) for different magnetizations are comparable with the results of this paper, reported in Table 3a.

TABLE 1

PREDICTIONS OF BLACK HOLE MASS WITH $M_\bullet - M_G\sigma^2$

Sample (1)	m (2)	b (3)	*Log* $M_\bullet$ (4)	*Log* $M_{\bullet,low}$ (5)	*Log* $M_{\bullet,high}$ (6)
1st Sample: Cappellari	0.99 ±0.09	3.76 ±0.42	9.32	8.30	10.37
2nd Sample: van den Bosch_174	1.02 ±0.05	3.21 ±0.26	8.93	8.25	9.64
3rd Sample: van den Bosch_108	0.92 ±0.05	3.93 ±0.24	9.09	8.44	9.76
4th Sample: de Nicola-Saglia	0.72 ±0.04	5.19 ±0.17	9.46	8.97	9.97
5th Sample: Saglia	0.73 ±0.04	5.16 ±0.17	9.49	9.00	10.00

Columns: (1) Sample. (2)-(3) The regression coefficients taken from Iannella and Feoli (2020). (4) M87 predicted black hole mass. (5) Black hole mass predicted minimal value. (6) Black hole mass predicted maximal value.

TABLE 2

PREDICTIONS OF BLACK HOLE MASS WITH $M_\bullet - \sigma$

Sample (1)	m (2)	b (3)	*Log* $M_\bullet$ (4)	*Log* $M_{\bullet,low}$ (5)	*Log* $M_{\bullet,high}$ (6)
1st Sample: Cappellari	5.20 ±0.46	-3.44 ±1.05	9.15	6.89	11.44
2nd Sample: van den Bosch_174	5.10 ±0.25	-3.39 ±0.56	8.95	7.69	10.22
3rd Sample: van den Bosch_108	4.94 ±0.26	-2.92 ±0.60	9.03	7.71	10.37
4th Sample: de Nicola-Saglia	4.99 ±0.26	-3.11 ±0.61	9.41	8.01	10.84
5th Sample: Saglia	5.05 ±0.27	-3.24 ±0.62	9.44	8.01	10.88

Columns: (1) Sample. (2)-(3) The regression coefficients taken from Iannella and Feoli (2020). (4) M87 predicted black hole mass. (5) Black hole mass predicted minimal value. (6) Black hole mass predicted maximal value.

3.1. *Temperature of the Black Hole Accretion Disk*

To better explain the experimental relation proposed in Feoli and Mele (2005), a simple model that links the mass of a supermassive black hole and the kinetic energy of the corresponding galactic bulge has been presented in Feoli (2014b). Feoli's approach starts by considering that the accretion process of the SMBH involves a thermodynamic transformation of the gas falling inside the radius of influence of the hole, describing the process with a simple model. Starting from considering an ideal and relativistic gas that flows from the outer parts of the spheroidal component (bulge) of a galaxy, with volume V_G and radius R_G, to the sphere of influence of a central SMBH, having volume $V_\bullet$ and radius R_{inf}, we can write the following conservation equation, which connects two equilibrium states:

$$T_\bullet V_\bullet^{\gamma-1} = T_{GAS} V_G^{\gamma-1}, \tag{3}$$

where $T_\bullet$ is the temperature inside the region of influence of the black hole, and T_{GAS} is the temperature of the gas in the galaxy. We can write the previous equation in this way

$$T_\bullet = T_{GAS} \left(\frac{R_G}{R_{inf}}\right)^{3(\gamma-1)}, \tag{4}$$

and we assume:

$$R_{inf} \simeq \frac{GM_\bullet}{\sigma^2}, \tag{5}$$

$$R_G = \frac{GM_G}{\sigma^2}, \tag{6}$$

$$T_{GAS} = \frac{m_H \sigma^2}{k}, \tag{7}$$

and that $T_\bullet$ is of the order of the electron temperature T_e near the black hole:

$$T_\bullet = \delta\, T_e = \delta \frac{m_e c^2}{k} = \delta(5.9 \times 10^9)K, \tag{8}$$

where m_H is the mass of the hydrogen atom, k the Boltzmann constant, m_e is the electron mass and δ a parameter. Considering that the adiabatic index

TABLE 3

BLACK HOLE MASSES OF M87 IN COMPARISON

TABLE 3a. Data from this paper

Sample (1)	*Log* $M_\bullet$ (2)
1st Sample: Cappellari	9.32 ±1.04
2nd Sample: van den Bosch_174	8.93 ±0.70
3rd Sample: van den Bosch_108	9.09 ±0.66
4th Sample: de Nicola-Saglia	9.46 ±0.50
5th Sample: Saglia	9.49 ±0.50

Columns: (1) Sample. (2) The predicted black hole mass.

TABLE 3b. Data from Nokhira et al. (2019)

σ_M (1)	*Log* $M_\bullet$ (2)
5	9.89 ±0.15
10	9.82 ±0.14
20	9.72 ±0.13

Columns: (1) Michel's magnetization parameter. (2) Estimated black hole mass.

for an ideal relativistic gas is $\gamma = 4/3$, we obtain (for more details see Feoli, 2014b):

$$M_\bullet = \frac{m_H}{\delta m_e}\left(\frac{M_G \sigma^2}{c^2}\right), \tag{9}$$

where M_G is the bulge mass. Taking the logarithm of the previous equation and measuring the black hole masses and galaxy masses in solar units, we find:

$$Log\, M_\bullet = Log\left(\frac{m_H}{m_e}\right) - Log\,\delta + Log\left(\frac{M_G \sigma^2}{c^2}\right), \tag{10}$$

that is,

$$Log\, M_\bullet = 3.264 - Log\,\delta + Log\left(\frac{M_G \sigma^2}{c^2}\right). \tag{11}$$

We obtain the scaling relation proposed by Feoli and Mele (2005):

$$Log\, M_\bullet = b + m\, Log\left(\frac{M_G \sigma^2}{c^2}\right), \tag{12}$$

where $b = 3.264 - Log\,\delta$ is a normalization and $m = 1$ is the slope.

The model is able to recover the right order of magnitude for the temperature near the SMBH. We apply the relation found in Feoli (2014b) to the experimental data of M87 contained in Saglia's sample and we find the temperature of the black hole accretion disk $T = (1.44 \pm 0.57) \times 10^9 K$, which is of the same order of magnitude given by the EHT Collaboration (V, 2019), i.e. $T \approx 6 \times 10^9 K$ for the peak brightness of the ring. Our prediction can also be compared with the values estimated by Kim et al. (2018) ($T = (1-3) \times 10^{10} K$) and by Akiyama et al. (2015) ($T = 1 \times 10^{10} K$). Many determinations of temperature exist. In particular, the problem of the X-ray flux of M87 has been well studied by different researchers (Di Matteo et al. 2003; Imazawa et al. 2021) but the derived temperatures are, of course, lower than the one measured at the peak brightness of the ring.

4. CONCLUSIONS

In this paper we have proposed to derive three important parameters for the supermassive black hole of the elliptical galaxy M87: the efficiency of the black hole, its mass and the temperature of the accretion disk. These three parameters were obtained by applying two models that we have proposed in Feoli and Mancini (2011), Feoli and Mele (2005) and Feoli (2014b), managing to make correct predictions. The results we have obtained are very interesting and promising; therefore, by improving the experimental data with increasingly precise tools and testing our relationships accordingly, it will be possible to make increasingly reliable predictions.

We thank Elisabetta Liuzzo for private communications.

REFERENCES

Akiyama, K., Lu, R.-S., Fish, V. L., et al. 2015, ApJ, 807, 150, https://doi.org/10.1088/0004-637X/807/2/150

Aller, M. C. & Richstone, D. O. 2007, ApJ, 665, 120, https://doi.org/10.1086/519298

Beifiori, A., Sarzi M., Corsini, E. M., et al. 2009, ApJ, 692, 856, https://doi.org/10.1088/0004-637X/692/1/856

Begelman, M. C. & Nath, B. B. 2005, MNRAS, 361, 1387, https://doi.org/10.1111/j.1365-2966.2005.09249.x

Beltramonte, T., Benedetto, E., Feoli, A., & Iannella, A. L. 2019, Ap&SS, 364, 212, https://doi.org/10.1007/s10509-019-3705-y

Benedetto, E., Fallarino, M. T., & Feoli, A. 2013, A&A, 558, 108, https://doi.org/10.1051/0004-6361/201322189

Beskin, V., Chernoglazov, A., Kiselev, A., Nokhrina, E. E. 2017, MNRAS, 472, 3971, https://doi.org/10.1093/mnras/stx2204

Blandford, R. & Globus, N. 2022, MNRAS, 514, 5141, https://doi.org/10.1093/mnras/stac1682
Burkert, A. & Silk, J. 2001, ApJ, 554, 151, https://doi.org/10.1086/321698
Cavaliere, A. & Vittorini, V. 2002, ApJ, 570, 114, https://doi.org/10.1086/339494
Croton, D. J., Springel, V., White, S. D. M., et al. 2006, MNRAS, 365, 11, https://doi.org/10.1111/j.1365-2966.2005.09675.x
Di Matteo, T., Allen, S. W., Fabian, A. C., Wilson, A. S., & Young, A. J. 2003, ApJ, 582, 133, https://doi.org/10.1086/344504
Event Horizon Telescope Collaboration, V. 2019, ApJ, 875, 5, https://doi.org/10.3847/2041-8213/ab0f43
———, VI. 2019, ApJ, 875, 6, https://doi.org/10.3847/2041-8213/ab1141
———, VIII. 2019, ApJ, 910, 13, https://doi.org/10.3847/2041-8213/abe4de
Feoli, A. 2014a, AN, 335, 193, https://doi.org/10.1002/asna.201211910
———. 2014b, ApJ, 784, 34, https://doi.org/10.1088/0004-637X/784/1/34
Feoli, A. & Iannella, A. L. 2019, Proceeding of 2019 IEEE International Workshop on Metrology for Aerospace, 590, https://doi.org/10.1109/MetroAeroSpace.2019.8869588
Feoli, A. & Mele, D. 2005, IJMPD, 14, 1861, https://doi.org/10.1142/s0218271805007528
———. 2007, IJMPD, 16, 1261, https://doi.org/10.1142/s0218271807010729
Feoli, A.& Mancini, L. 2009, ApJ, 703, 1502, https://doi.org/10.1088/0004-637X/703/2/1502
———. 2011, IJMPD, 20, 2305, https://doi.org/10.1142/s0218271811020330
Ferrarese, L. & Ford, H. C. 2005, SSRv, 116, 523, https://doi.org/10.1007/s11214-005-3947-6
Ferrarese, L. & Merritt, D. 2000, ApJ, 539, 9, https://doi.org/10.1086/312838
Gebhardt, K., Bender, R., Bower, G., et al. 2000, ApJ, 539, 13, https://doi.org/10.1086/312840
Graham, A. 2008, ApJ, 680, 143, https://doi.org/10.1086/587473
Graham, A. W. & Driver S. P. 2005, PASA, 22, 118, https://doi.org/10.1071/AS05001
Granato, G. L., De Zotti, G., Silva, L., Bressan, A., & Danese, L. 2004, ApJ, 600, 580, https://doi.org/10.1086/379875
Gültekin, K., Richstone, D. O., Gebhardt, K., et al. 2009a, ApJ, 698, 198, https://doi.org/10.1088/0004-637X/698/1/198
Gültekin, K., Cackett, E. M., Miller, J. M., et al. 2009b, ApJ, 706, 404, https://doi.org/10.1088/0004-637X/706/1/404
Haiman, Z., Ciotti, L., & Ostriker J. P. 2004, ApJ, 606, 204, https://doi.org/10.1086/383022
Häring, N. & Rix, H.-W 2004, ApJ, 604, 89, https://doi.org/10.1086/383567
Hopkins, P. F., Hernquist, L., Cox, T. J., Robertson, B., & Krause, E. 2007a, ApJ, 669, 45, https://doi.org/10.1086/521590
———. 2007b, ApJ, 669, 67, https://doi.org/10.1086/521601
Hu, J. 2008, MNRAS, 386, 2242, https://doi.org/10.1111/j.1365-2966.2008.13195.x
Iannella, A. L. & Feoli, A. 2020, Ap&SS, 365, 162, https://doi.org/10.1007/s10509-020-03875-6
Iannella, A. L., Greco, L., & Feoli, A. 2021, Ap&SS, 366, 52, https://doi.org/10.1007/s10509-021-03958-y
Imazawa, R., Fukazawa, Y., & Takahashi, H. 2021, ApJ, 919, 110, https://doi.org/10.3847/1538-4357/ac0ae4
Kim, J.-Y., Krichbaum, T. P., Lu, R.-S., et al. 2018, A&A, 616, 188, https://doi.org/10.1051/0004-6361/201832921
King, A. R. 2003, ApJ, 596, 27, https://doi.org/10.1086/379143
Kisaka, S., Kojima, Y., & Otani, Y. 2008, MNRAS, 390, 814, https://doi.org/10.1111/j.1365-2966.2008.13797.x
Kormendy, J. & Richstone, D. 1995, ARA&A, 33, 581, https://doi.org/10.1146/annurev.aa.33.090195.003053
Laor, A. 2001, ApJ, 553, 677, https://doi.org/10.1086/320989
Magorrian, J., Tremaine, S., Richstone, D., et al. 1998, AJ, 115, 2285, https://doi.org/10.1086/300353
Mancini, L. & Feoli, A. 2012, A&A, 537, 48, https://doi.org/10.1051/0004-6361/201117168
Marconi, A. & Hunt, L. K. 2003, ApJ, 589, 21, https://doi.org/10.1086/375804
Merritt, D. & Ferrarese, L. 2001, ASPC 249, The Central Kiloparsec of Starbust an AGN: The La Palma Connection, ed. J. H. Knapen, J. E. Beckman, I. Shlosman, & T. J. Mahoney, (San Francisco, CA: ASP), 335
Murray, N., Quataert, E., & Thompson, T. A. 2005, ApJ, 618, 569, https://doi.org/10.1086/426067
Nokhrina, E. E., Gurvits, L. I., Beskin, V. S., et al. 2019, MNRAS, 489, 1197, https://doi.org/10.1093/mnras/stz2116
Pipino, A., Silk, J., & Matteucci, F. 2009a, MNRAS, 392, 475, https://doi.org/10.1111/j.1365-2966.2008.14077.x
Pipino, A., Kaviraj, S., Bildfell, C., et al. 2009b, MNRAS, 395, 462, https://doi.org/10.1111/j.1365-2966.2009.14534.x
Richstone, D., Ajhar, E. A., Bender, R., et al. 1998, Nature, 395, 14, https://doi.org/10.48550/arXiv.astro-ph/9810378
Saglia, R. P., Opitsch, M., Erwin, P., et al. 2016, ApJ, 818, 47, https://doi.org/10.3847/0004-637x/818/1/47
Sazonov, S. Y., Ostriker, J. P., Ciotti, L., & Sunyaev, R. A. 2005, MNRAS, 358, 168, https://doi.org/10.

1111/j.1365-2966.2005.08763.x
Sijacki, D., Springel, V., Di Matteo, T., & Hernquist, L. 2007, MNRAS, 380, 877, https://doi.org/10.1111/j.1365-2966.2007.12153.x
Silk, J. & Rees, M. J. 1998, A&A, 331, 1, https://doi.org/10.48550/arXiv.astro-ph/9801013
Soker, N. & Meiron, Y. 2011, MNRAS, 411, 1803, https://doi.org/10.1111/j.1365-2966.2010.17810.x
Tremaine, S., Gebhardt, K., Bender, R., et al. 2002, ApJ, 574, 740, https://doi.org/10.1086/341002
van den Bosch, R. C. E. 2016, ApJ, 831, 134, https://doi.org/10.3847/0004-637x/831/2/134
Wandel, A. 2002, ApJ, 565, 762, https://doi.org/10.1086/338134
Wyithe, J. S. B. & Loeb, A. 2003, ApJ, 595, 614, https://doi.org/10.1086/377475

Antonio Feoli and Antonella L. Iannella: Department of Engineering, University of Sannio, Piazza Roma 21, 82100 Benevento, Italy (feoli, aiannella@unisannio.it).

Revista Mexicana de Astronomía y Astrofísica, **59**, 105–112 (2023)

https://doi.org/10.22201/ia.01851101p.2023.59.01.07

REFRACTION OF A HERBIG-HARO JET TRAVELLING THROUGH A SHEAR LAYER

A. C. Raga[1], A. Castellanos-Ramírez[2], and J. Cantó[2]

Received June 27 2022; accepted October 21 2022

ABSTRACT

We study the problem of a radiative Herbig-Haro (HH) jet which travels through a slip surface into a region of side-streaming environment. The interaction with the streaming environment produces an oblique shock that deflects the jet beam. A simple, analytic model for this shock gives the jet deflection as a function of the incidence angle and the environment-to-jet ram pressure ratio. We find that in the case of higher environmental ram pressure, for a high enough incidence angle, the jet stalls and does not penetrate substantially into the streaming environment. We present 3D gas dynamic simulations illustrating the jet deflection and stalling regimes. Possible applications to HH jets showing sudden deflections in their propagation are discussed.

RESUMEN

Estudiamos el problema de un jet Herbig-Haro (HH) radiativo que pasa a través de una superficie de contacto a una región de medio ambiente en movimiento lateral. La interacción con el medio ambiente en movimiento produce un choque oblicuo que deflecta el haz del jet. Un modelo analítico sencillo para este choque da la deflección del jet en función del ángulo de incidencia y del cociente de presiones hidrodinámicas entre el medio ambiente y el jet. Encontramos que en el caso de medio ambiente con mayor presión hidrodinámica, para un ángulo de incidencia suficientemente alto el jet se estanca, y no penetra sustancialmente dentro del medio ambiente en movimiento. Presentamos simulaciones hidrodinámicas 3D que ilustran los regímenes de deflección y de estancamiento. Se discuten posibles aplicaciones a jets HH que muestran deflecciones repentinas en su propagación.

Key Words: ISM: jets and outflows — ISM: kinematics and dynamics — stars: pre-main-sequence — stars: winds, outflows

1. INTRODUCTION

Herbig-Haro (HH) jets sometimes show sudden changes of direction, which have been generally attributed to collisions with dense obstacles. The best studied example of this effect is the HH 110 outflow.

HH 110 was discovered by Reipurth & Olberg (1991). It was soon realized that this object corresponds to a jet which becomes brighter and less collimated after a sudden change in direction (Reipurth et al. 1996; Rodríguez et al. 1998). Proper motions (e.g., Kajdic et al. 2012) and spatially resolved spectroscopy (e.g., Riera et al. 2003; López et al. 2010) can be interpreted in this jet deflection context. This object has even been compared to laboratory experiments of jets deflected by collisions with an obstacle (Hartigan et al. 2009).

Though HH 110 is the most notable example, qualitatively similar situations are found in regions with high spatial concentrations of YSO outflows. For example, Walawander et al. (2005) found some notable deflected jets in the Perseus molecular cloud, and Hayashi & Pyo (2009) in the L1551 dark cloud. These objects mostly await more detailed studies.

Raga & Cantó (1995) modeled analytically and numerically (with 2D gas dynamics) the initial deflection of a jet by an oblique collision with a dense obstacle, and suggested that HH 110 might correspond to such a flow. However, at later times the jet penetrates the cloud, and has a curved trajectory before reemerging (Raga & Cantó 1996), not

[1]Instituto de Ciencias Nucleares, UNAM, México.
[2]Instituto de Astronomía, UNAM, México.

resembling HH 110. 3D simulations of this type of jet/cloud interaction were presented by de Gouveia Dal Pino (1999) and Raga et al. (2002).

In the present paper, we study the passage of a jet through a slip boundary, in which the environment is stationary (with respect to the jet source) on one side, and in supersonic sideways motion on the other side. This situation could represent a jet impacting on a supersonically travelling cloud (which would be a reasonable scenario in a region with supersonic turbulence), or on material disturbed by the previous passage of another YSO outflow.

We first present analytic considerations for evaluating the deflection of the jet as a function of the environment/jet ram pressure balance ratio p and the incidence angle ϕ of the interaction (§ 2). Finding that there are two regimes (a jet deflection and a stagnation case), we then compute two 3D simulations illustrating the very different resulting flows (§ 3). The results are summarized in § 4, and we discuss the possible application of these models to observed deflected HH jets in § 5.

2. ANALYTIC CONSIDERATIONS

Let us consider the problem of a steady jet flow emerging from a stationary environment into a region with a moving environment. For the sake of simplicity, we assume that the jet emerges at an angle ϕ with respect to the (infinitely narrow) environmental velocity shear surface, and that the plane containing the jet and the environmental velocities is perpendicular to this shear surface. This situation is shown schematically in Figure 1.

In a cut through the midplane of the flow, two oblique shocks are formed: one of them refracting the jet beam, and the other one deflecting the flowing environment. These shocks lie at angles β and α, respectively, with respect to the environmental shear layer (see Figure 1). The velocities behind these two shocks (v_{jr} and v_{ar}) are parallel, forming a deflected environment/jet flow. For the case of a 2D problem, the two shocks are straight, and we will assume that this is also a reasonable approximation for the mid-plane of a cylindrical jet/plane shear layer interaction.

The postshock flow velocities form angles α_1 and $\beta_1 >$ with the shock surfaces. The tangents of these angles are inversely proportional to the compression in each shock, so that for the highly radiative HH flow case (in which the compressions have typical values of ≈ 100) they will have values $\ll 1$. It is therefore a good approximation to set $\alpha \approx \beta$ (see Figure 1).

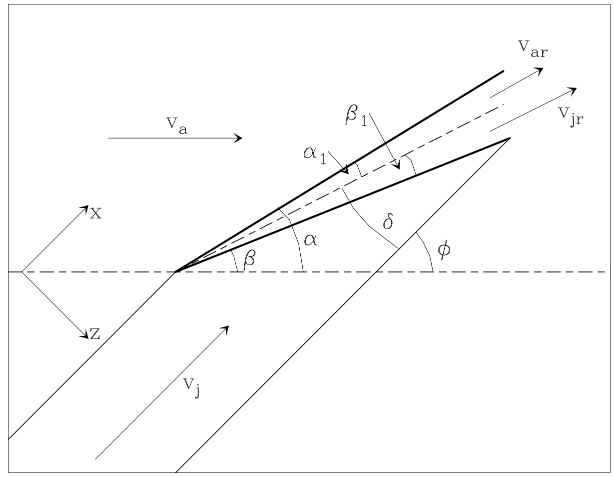

Fig. 1. Schematic diagram showing an interface (dashed horizontal line) between a stationary environment (below) and a streaming environment (above) of velocity v_a. A jet (of velocity v_j impacts on the interface at angle ϕ. Two shocks are formed: one that deflects the jet (at an angle β to the interface) and a second one that deflects the environment (at an angle α). The contact discontinuity separating the deflected jet and environmental gas lies in between these two shocks. The deflected environment has a velocity v_{ar} and the deflected jet a velocity v_{jr}, both parallel to the shocked environment/jet contact discontinuity. The jet beam goes through a deflection $\delta = \phi - \alpha$. The xz-reference system used in the numerical simulations (in which the jet travels along the x-axis) is shown with the arrows in the center left region of the schematic diagram.

With this condition, the balance between the two post (strong) shock pressures is:

$$\rho_j v_{jn}^2 = \rho_a v_{an}^2 \,, \tag{1}$$

$$\to \sin^2(\phi - \alpha) = p^2 \sin^2 \alpha \,, \tag{2}$$

with

$$p = \sqrt{\frac{\rho_a}{\rho_j}} \frac{v_a}{v_j} \,, \tag{3}$$

where ρ_j and ρ_a are the densities and v_j and v_a the velocities (with components normal to the shocks v_{an} and v_{jn}) of the jet and the environment, respectively. Clearly, p is the square root of the environment-to-jet ram pressure ratio. From equation (2) we then obtain the shock angle α as a function of the incidence angle ϕ:

$$\tan \alpha = \frac{\sin \phi}{p + \cos \phi} \,. \tag{4}$$

In the α_1, $\beta_1 \ll 1$ high compression approximation, the deflection angle between the impinging (v_j)

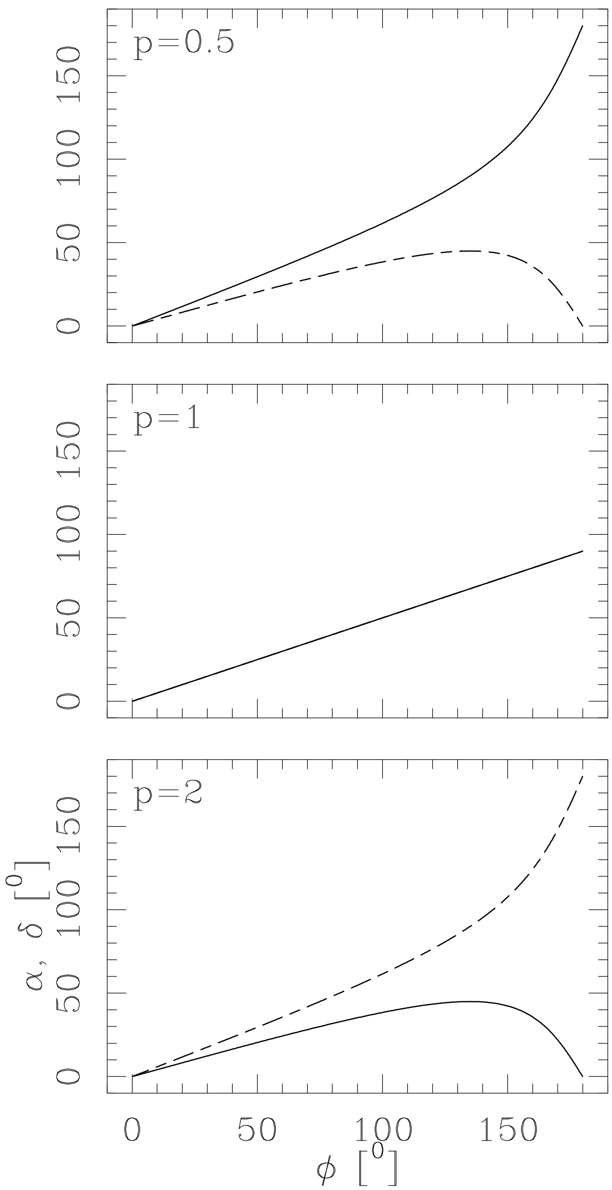

Fig. 2. The α (solid lines) and δ (dashed line) angles (i.e., the angle of the jet shock with respect to the environmental shear layer and the jet deflection angle, respectively, see Figure 1) as a function of the incidence angle ϕ. The results shown in the three frames correspond to $p = 0.5$, 1 and 2 (see equation 3). For $p = 1$, α and ϕ coincide.

and refracted (v_{jr}) jet velocities is $\delta = \phi - \alpha$ (see Figure 1). Using equation (2) we then obtain:

$$\tan\delta = \frac{\sin\phi}{1/p + \cos\phi} \,. \tag{5}$$

The shock angle α and the deflection angle δ (equations 2 and 5, respectively) are shown as a function of p and ϕ (see equation 3) in Figure 2. Using equation (5) we can now calculate the velocity of the deflected jet:

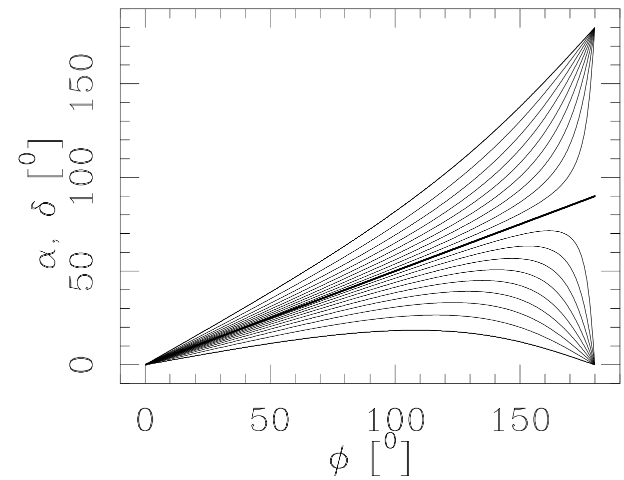

Fig. 3. The displayed curves correspond to α as a function of ϕ for $p = 0.1$, 0.2, ... 1, 1/0.9, 1/0.8, 1/0.7, ... 1/0.1 for (top to bottom curves) or to δ as a function of ϕ for $1/p = 0.1$, 0.2, ... 1, 1/0.9, 1/0.8, 1/0.7, ... 1/0.1 (top to bottom curves). The thick, central straight line is the $p = 1$ solution.

$$v_{jr} = v_j \cos\delta \,, \tag{6}$$

see Figure 1.

It is clear that α and δ switch their values under a $p \to 1/p$ transformation (see equations 4 and 5), as can be seen in Figure 2. This property is an expected result due to the symmetry of the jet/streaming environment interaction (see Figure 1).

Also, the $p = 1$ case (equal jet and environmental ram pressures, see equation 3) produces the straightforward result:

$$\delta = \alpha = \phi/2 \,, \tag{7}$$

deduced from equations (4-5).

In Figure 3, we show α (or δ) for a number of different p (or $1/p$) values. Two families of solutions (having values of either 1 or 0 for $\phi = 180°$) are separated by the linear, $p = 1$ solution (see equation 7).

It is clear that for $p < 1$ there is a maximum possible value δ_m for the jet deflection (see Figures 2 and 3). From equation (5) it is straightforward to show that this maximum occurs for an incidence angle

$$\cos\phi_m = -p \,, \tag{8}$$

and has a maximum deflection

$$\tan\delta_m = \frac{p}{\sqrt{1-p^2}} \,. \tag{9}$$

Figure 4 shows these two angles as a function of p.

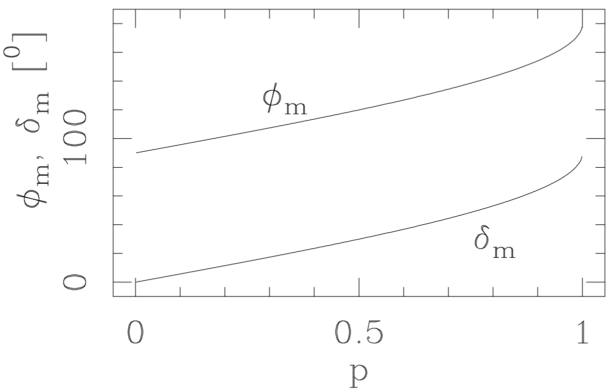

Fig. 4. Maximum jet deflection angle δ_m and incidence angle ϕ_m at which the maximum deflection occurs as a function of p.

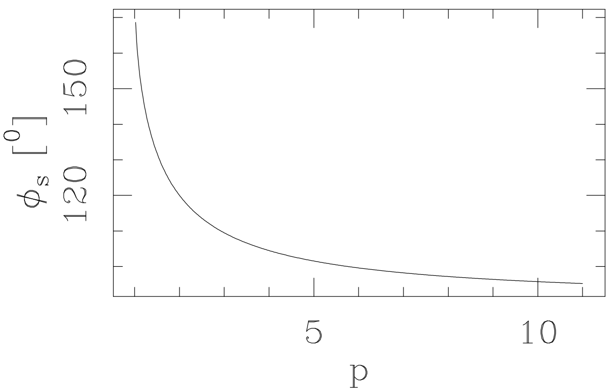

Fig. 5. Incidence angle for jet stagnation ϕ_s as a function of p.

Another interesting feature of the jet deflection is that for $p > 1$ one can have $\delta > 90°$. For

$$\cos\phi_s = -1/p\,, \tag{10}$$

the jet flow has a stagnation ($\delta = 90°$) at a shock perpendicular to the jet flow (this result being straightforwardly obtained from equation 5). Figure 5 shows ϕ_s as a function of p.

For $\phi > \phi_s$, we have deflections $\delta > 90°$. This corresponds to a regime in which the jet is deflected into a direction that goes against the streaming environment. Because this occurs only in the $p > 1$ regime of high environmental ram pressure, this deflected material will quickly slow down and remain close to the jet/streaming environment interaction region. This "stalled jet" regime is explored below with a gas dynamic simulation.

Finally, we note that the mixed jet/streaming environment flow emerging from the two-flow interaction region has an environment to jet mass ratio

$$r_{aj} = \frac{\rho_a v_{an}}{\rho_j v_{jn}} = \sqrt{\frac{\rho_a}{\rho_j}}\,, \tag{11}$$

the second equality being a direct result of the ram-pressure balance condition (see equation 1). As the flow travels away from the interaction region (shown in Figure 1), more environmental mass is incorporated into the beam of the curved flow.

3. NUMERICAL SIMULATIONS

3.1. *The Two Computed Models*

In order to illustrate the general characteristics of jet flows interacting with an environmental velocity shear, we have calculated two models:

- M1: a cylindrical jet with initial radius $r_j = 10^{16}$ cm, density $n_j = 10^3\text{cm}^{-3}$, temperature $T_j = 100$ K and velocity $v_j = 100$ km s^{-1} emerging from a stationary environment of density $n_b = 500$ cm^{-3} and temperature $T_b = 200$ K into a flowing medium of velocity $v_a = 30$ km s^{-1} (with a density $n_a = 10^3$ cm^{-3} and temperature $T_a = 100$ K) at an incidence angle $\phi = 60°$.
- M2: the same jet, but emerging from a stationary environment of density $n_b = 500$ cm^{-3} and temperature $T_b = 200$ K into a flowing medium of velocity $v_a = 50$ km s^{-1} with a density $n_a = 10^4$ cm^{-3} and temperature $T_a = 10$ K at an incidence angle $\phi = 150°$.

For model M1, the p parameter (the square root of the streaming environment to jet ram pressure ratio, see equation 3) is $p_1 = 0.3$. From Figure 3, we see that for this value of p and for the $\phi = 60°$ incidence angle of this model, we expect a jet deflection of $\approx 30°$.

For model M2, we have a p parameter $p_2 = 1.58$. From Figure 5, we see that for this value of p, the minimum incidence angle for jet stagnation has a $\phi_s \approx 129°$, so that the $\phi = 150°$ incidence angle of this model should lead to the formation of a stagnated jet flow.

3.2. *The Numerical Setup*

We have used a 3D version of the yguazú-a code (described in detail by Raga et al. 2000, and extensively used over the last two decades) with a 5-level binary adaptive grid of maximum resolution $= 3.9 \times 10^{14}$ cm along the three Cartesian axes. This results in a resolution of the jet diameter with ≈ 51 grid points.

In the two simulations, the jet is injected along the x-axis, and the environment has two regions, an upper one of density n_a, temperature T_a and velocity

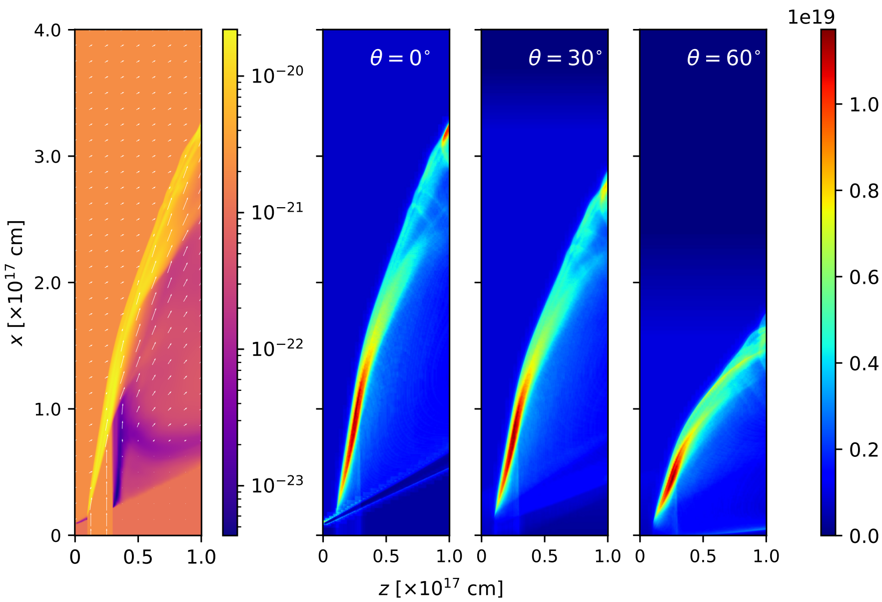

Fig. 6. Results obtained for model M1 (see the text) after a $t = 2000$ yr time-integration. The left panel shows the zx-midplane density map (given in g cm^{-3} by the bar at the right of the frame), and (white) arrows with lengths and directions corresponding to the local flow velocities. The three right panels show column density maps (given in 10^{19} cm^{-2} by the bar at the right) computed assuming $\theta = 0$, 30 and 60° angles between the x-axis and the plane of the sky (as shown on the top of the three panels). The z- and x-axes are given in units of 10^{17} cm. The color figure can be viewed online.

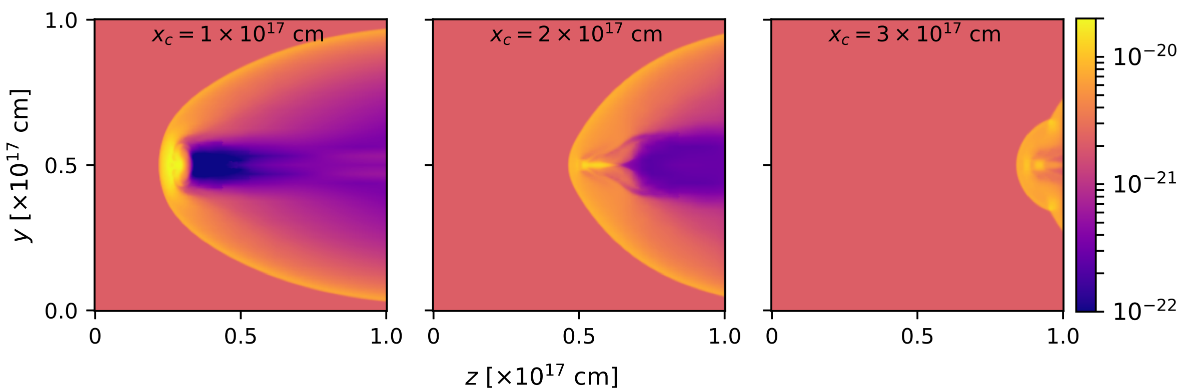

Fig. 7. Results obtained for model M1 (see the text) after a $t = 2000$ yr time-integration. The three panels show the density stratifications on yz-cuts (see Figure 6) at three different values of x (1, 2 and 3×10^{17} cm), as labeled on the top of each frame). The color figure can be viewed online.

v_a (in the xz-plane) directed obliquely at an angle of $90 - \phi$, anticlockwise with respect to the z-axis (where ϕ is the incidence angle of the jet with respect to the environmental velocity slip line). Therefore, the velocity shear region separating the lower (stationary) and upper (moving) regions of the environment is parallel to the y-axis and inclined on the xz-plane.

In the simulations, inflow boundaries are applied on the yz-plane within the $r_j = 10^{16}$ cm cylindrical jet beam and along the $z = 0$ plane, where the flowing environment is injected in the upper region of the domain. The remaining edges of the computational domain are treated as outflow boundaries.

The gas dynamic code integrates the continuity equation, the three momentum and the energy equa-

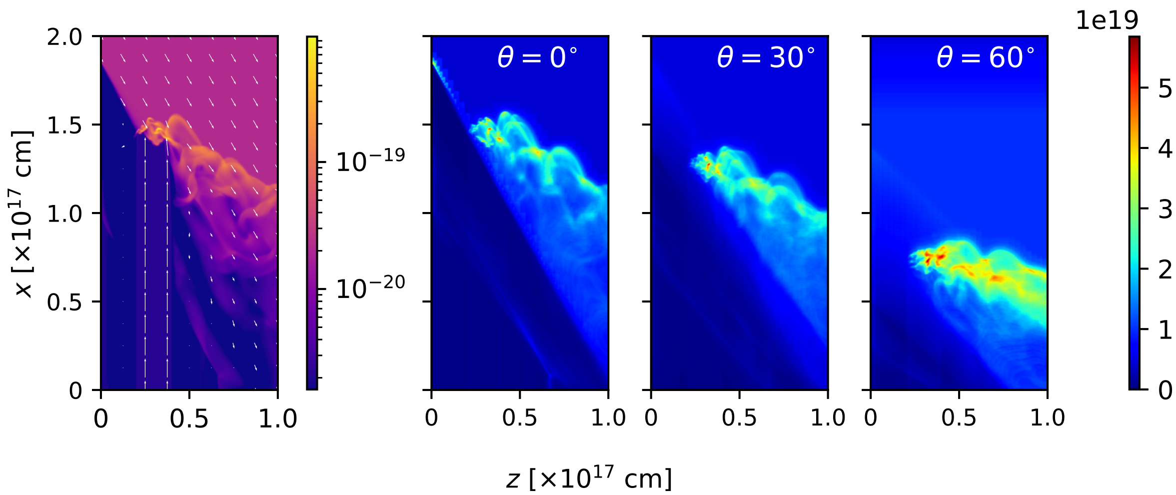

Fig. 8. The same as Figure 6 but for model M2. The color figure can be viewed online.

tions, together with a rate equation for neutral H (which includes collisional ionization and radiative recombination). The parametrized cooling rate of Raga et al. (2002) is included in the energy equation. The gas in all of the computational domain is initially neutral, with a seed electron density coming from singly ionized C, allowing the gas to become collisionally ionized in the hot, post-shock regions.

The simulations are started with the jet beam in contact with the slip boundary, and are integrated in time until an approximately stationary flow configuration is obtained. The resulting flows are presented in the following subsection.

3.3. *The Deflected Jet and the Stalled Jets*

Figure 6 shows the flow resulting from model M1 after a 2000 yr time-integration. The first panel shows an xz-cut through the middle of the jet beam, displaying the density stratification and the flow field. The other three panels show the column density calculated for three orientations ($\theta = 0$, 30 and 60°) between the z-axis and the plane of the sky.

We find that the jet shows the deflection shock of our analytic model, and that after the end of the deflection shock, the locus of the jet beam curves due to the ram pressure of the streaming environment, The column density maps (three right panels of Figure 6) show that the deflected flow has a curved, collimated jet morphology for all chosen orientation angles (including the more head-on, $\theta = 60°$ observational perspective).

The curved jet beyond the deflection shock is the jet/sidewind interaction regime that has been studied by Cantó & Raga (1995), in which the jet develops a "plasmon shaped" cross section. This plasmon cross section is seen in the yz-density cuts shown in Figure 7, corresponding to planes perpendicular to the initial direction of the jet flow.

Figure 8 shows the flow resulting from model M2 after a 2000 yr time-integration. The mid-plane density stratification shows that the jet terminates at a shock with a complex, time-dependent shape. The post-shock material forms a series of clumps or eddies that are advected by the impinging environment, forming a turbulent trail.

The column density maps show that this turbulent trail has a complex 3D structure, with considerably higher column densities when observed in more head-on directions (see the $\theta = 60°$ frame of Figure 8). The complexity of the structure is illustrated by the yz-density cut (taken at $x = 1.38 \times 10^{17}$ cm) shown in Figure 9.

4. SUMMARY

We developed an analytic model (§ 2) of a radiative jet going through an environmental shear surface. We obtain a full solution in the limiting case of high compression in the two radiative shocks produced in the interaction.

For given values of the dimensionless parameter p (equal to the square root of the streaming environment to jet ram-pressure ratio, see equation 3), we find expressions for the jet deflection angle δ (see equation 5) and the angle α between the interaction shocks and the environmental shear surface (see equation 4) as a function of the incidence angle ϕ (see Figures 1, 2 and 3).

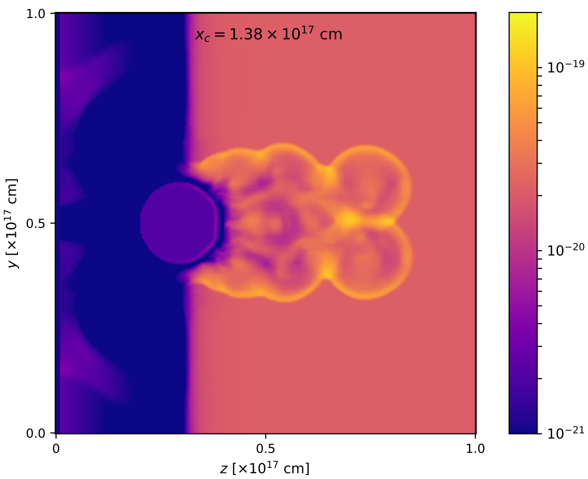

Fig. 9. Density yz-cut at $x = 1.38 \times 10^{17}$ cm obtained from model M2 (see the text) after a $t = 2000$ yr time-integration. The color figure can be viewed online.

Two interesting results are that:

- for $p < 1$ (higher jet ram-pressure), there is a maximum possible jet deflection angle δ_m (given as a function of p by equation 9, and shown in Figure 4);

- for $p > 1$ (higher environmental ram-pressure), one has deflections $\delta > 90°$ (i.e., the jet is deflected in a direction against the flowing environment) for incidence angles $\phi > \phi_s$ (with ϕ_s given by equation 10, and shown in Figure 5 as a function of p).

The interactions with $\phi > \phi_s$ correspond to stalled jets, in which the post-interaction shock jet is stopped and then entrained by the streaming environment.

In order to illustrate the "deflected" and "stalled" jet interaction regimes, we computed two 3D simulations with values of p (see equation 3) and incidence angle ϕ (see Figure 1) clearly placing the flows in each of these two regimes. These simulations are described in § 3, and the results are shown in Figures 6-9.

We find that:

- the deflected jet regime leads to a clean deflection of the jet beam (from a vertical, to an oblique direction in the panels of Figure 6), and at larger distances (beyond the end of the jet deflection shock) by a curved jet locus resulting from the continuing interaction of the deflected jet with the streaming environment;

- the stalled jet regime shows an abrupt end of the jet flow at the position of the environmental shear, followed by a turbulent structure in which the stalled jet material is incorporated into the environmental flow (see Figures 8 and 9).

We are not aware of an observed HH jet deflection that could be in this latter regime.

5. CONCLUSIONS

We have presented analytic and numerical models for a radiative jet that travels through an environmental shear surface, which divides an internal region around the jet source (which shares the motion of the jet source) and an external region with a non-zero velocity (with respect to the jet source).

This flow configuration could correspond to different situations. For example:

- the case of an internal region that is denser than the external region could correspond to a jet emerging from a dense core (containing the jet source) into a lower density, streaming environment;

- the case of a lower density internal region and a denser external region could correspond to a narrow jet meeting a broader outflow (e.g., a spatially extended molecular outflow), or a dense cloud in motion relative to the jet source.

These two cases are relevant for regions with many bipolar jet systems, such as the L1551 cloud (e.g., Hayashi & Pyo 2009), the Perseus molecular cloud (Walawander et al. 2005) and NGC 1333 (Raga et al, 2013), some of which show several jets with sudden changes in projected direction. Both jet-cloud and jet-molecular outflow collisions are possibly occurring.

Our present model is also relevant for the case of the remarkable HH 110 deflected jet system (e.g., Kajdic et al. 2012). This object has been modeled as an oblique collision of a jet with a dense cloud (e.g., de Gouveia Dal Pino 1999; Raga & Cantó 2005). Raga et al. (2002) carried out a more extended numerical exploration of the jet/cloud collision problem and obtained deflected jets that qualitatively resemble HH 110. They noted, however, that for reasonable jet/cloud density contrasts it was not possible to maintain the jet deflection at the cloud surface for a long enough timescale, as the jet starts boring through the cloud.

The addition of a relative motion between the jet source and the cloud directly solves this problem. The models of the present paper show that this relative motion results in an approximately stationary jet deflection, which will last until the collision region reaches the edge of the cloud. The relative jet source/cloud motion is probably the missing element in all of the models that have been previously calculated for the HH 110 flow.

This work was supported by the DGAPA (UNAM) grant IG100422. A. Castellanos-Ramírez acknowledges support from a CONACyT postdoctoral fellowship, and the resources on the Miztli supercomputer obtained through the project LANCAD-UNAM-DGTIC-408. We thank an anonymous referee for helpful comments that gave rise to figures 7 and 9, equation 11, and modifications throughout the paper.

REFERENCES

de Gouveia Dal Pino, E. M. 1999, ApJ, 526, 862, https://doi.org/10.1086/308037

Hartigan, P., Foster, J. M., Wilde, B. H., et al. 2009, ApJ, 705, 1073, https://doi.org/10.1088/0004-637X/705/1/1073

Hayashi, M. & Pyo, T.-S. 2009, AJ, 694, 582, https://doi.org/10.1088/0004-637X/694/1/582

Kajdiĉ, P., Reipurth, B., Raga, A. C., Bally, J., & Walawender, J. 2012, AJ, 143, 106, https://doi.org/10.1088/0004-6256/143/5/106

López, R., García-Lorenzo, B., Sánchez, S. F., et al. 2010, MNRAS, 406, 2193, https://doi.org/10.1111/j.1365-2966.2010.16831.x

Raga, A. C. & Cantó, J. 1995, RMxAA, 31, 51

________. 1996, MNRAS, 280, 567, https://doi.org/10.1093/mnras/280.2.567

Raga, A. C., Navarro-González, R., & Villagrán-Muniz, M. 2000, RMxAA, 36, 67

Raga, A. C., de Gouveia Dal Pino, E. M., Noriega-Crespo, A., Minini, P. D., & Velázquez, P. F. 2002, A&A, 392, 267, https://doi.org/10.1051/0004-6361:20020851

Raga, A. C., Noriega-Crespo, A., Carey, S. J., & Arce, H. G. 2013, ApJ, 145, 28, https://doi.org/10.1088/0004-6256/145/2/28

Reipurth, B. & Olberg, M. 1991, A&A, 246, 535

Riera, A., Raga, A. C., Reipurth, B., et al. 2003, AJ, 126, 327, https://doi.org/10.1086/375759

Rodríguez, L. F., Reipurth, B., Raga, A. C., & Cantó, J. 1998, RMxAA, 34, 69

Walawander, J., Bally, J., & Reipurth, B. 2005, AJ, 129, 2308, https://doi.org/10.1086/428955

J. Cantó & A. Castellanos-Ramírez: Instituto de Astronomía, Universidad Nacional Autónoma de México, Ap. 70-468, 04510 CDMX, México.

A. C. Raga: Instituto de Ciencias Nucleares, Universidad Nacional Autónoma de México, Ap. 70-543, 04510 CDMX, México (raga@nucleares.unam.mx).

Revista Mexicana de Astronomía y Astrofísica, **59**, 113–122 (2023)

https://doi.org/10.22201/ia.01851101p.2023.59.01.08

OPTIMIZED SPECTRAL ENERGY DISTRIBUTION FOR SEYFERT GALAXIES

Luc Binette[1,2], Yair Krongold[1], Sinhue A. R. Haro-Corzo[3], Andrew Humphrey[4,5], and Sandy G. Morais[4,6]

Received October 4 2022; accepted November 2 2022

ABSTRACT

The temperature predicted by photoionization models for the narrow line region of Seyfert 2 galaxies is lower than the value inferred from the observed [O III] λ4363Å/λ5007Å line ratio. We explore the possibility of considering a harder ionizing continuum than typically assumed. The spectral ionizing energy distribution, which can generate the observed λ4363Å/λ5007Å ratio, is characterized by a secondary continuum peak at 200 eV.

RESUMEN

La temperatura predicha por modelos de fotoionización de la región de líneas angostas (NLR) es inferior al valor deducido por el cociente de líneas [O III] λ4363Å/λ5007Å que se observa en galaxias Seyfert 2. Exploramos la posibilidad de un continuo ionizante mucho más duro que el que típicamente se usa. La distribución de energía espectral ionizante que logra reproducir el cociente de λ4363Å/λ5007Å observado se caracteriza por un segundo pico en el continuo a 200 eV.

Key Words: accretion, accretion discs — galaxies: Seyfert — plasmas — quasars: emission lines

1. INTRODUCTION

It has been proposed early on that photoionization is the excitation mechanism of the plasma associated to the narrow line region of active galactic nuclei (AGN) (Osterbrock 1978, and references therein). Prevailing photoionization models of the narrow-line region (NLR) of AGN consider a distribution of clouds that extends over a wide range of cloud densities and ionization parameter values, whether the targets are Type I (Baldwin et al. 1995; Korista et al. 1997) such as quasars, Seyfert 1's and broad-line radio galaxies (BLRG), or Type II objects (Ferguson et al. 1997; Richardson et al. 2014) which consist of Seyfert 2's, QSO 2's and narrow-line radio galaxies (NLRG). One difficulty reported by Storchi-Bergmann et al. (1996), Bennert et al. (2006b), Villar-Martín et al. (2008) and Dors et al. (2015, 2020) is that the temperature predicted by photoionization models is lower than the value inferred from the observed [O III] λ4363Å/λ5007Å line ratio (hereafter labeled $R_{\rm OIII}$). This discrepancy defines the so-called "temperature-problem", which is mentioned below and refers only to the *spatially unresolved* NLR. Our basic assumption is that photoionization is the dominant excitation mechanism. We cannot rule out the presence of shocks, but combining shocks and photoionization in order to fit a sample of objects that share a similar temperature would a require fine-tuning of both heating mechanism, which would not be a convincing procedure. We recognize that observations of the spatially outflowing plasma, which is labelled extended narrow line region (ENLR), indicate in some Seyferts the presence of a much hotter plasma. For instance, the IFU MUSE/VLT observations of the Seyfert 2 Circinus by Fonseca-Faria et al. (2021) reveal temperatures as high as 20 000 °K within the ENLR, which standard photoionisation models cannot reproduce. The current work addresses only the NLR where we will assume that the dominant heating mechanism

[1]Instituto de Astronomía, UNAM, México.
[2]Département de physique, de génie physique et d'optique, Université Laval, Québec.
[3]Escuela Nacional de Estudios Superiores (ENES) Unidad Morelia, UNAM, México.
[4]Instituto de Astrofísica e Ciências do Espaço, Universidade do Porto, Portugal.
[5]DTx – Digital Transformation CoLAB, University of Minho, Portugal.
[6]Departamento de Física e Astronomia, Faculdade de Ciências, Universidade do Porto, Portugal.

is photoionization, although we do not rule out that other factors might affect the $R_{\rm OIII}$ ratio, such as a non-Maxwellian electron energy distribution (Morais et al. 2021), or the contribution of matter-bounded clouds to the emission line spectrum (Binette et al. 1997).

The $R_{\rm OIII}$ ratio is a valid temperature diagnostic when the low density regime (LDR) applies (such as in H II regions), that is, for plasma of densities $\lesssim 10^4\,{\rm cm}^{-3}$; otherwise collisional deexcitation becomes important, which causes the $R_{\rm OIII}$ ratio to increase with density, independently of the temperature. The presence of significant collisional deexcitation appears to be the norm in Type I AGN, as shown by the work of Baskin & Laor (2005, hereafter BL05) who compared the $R_{\rm OIII}$ values observed in 30 quasars[7]. In Type II AGN, however, there is indirect evidence that collisional deexcitation is not dominant. For instance, the $R_{\rm OIII}$ ratios of Seyfert 2's are found to be similar to those observed within the spatially resolved component, the so-called extended narrow line region (ENLR), where LDR conditions are known to apply. More direct evidence of LDR conditions in Type II nuclei was recently presented by Binette et al. (2022, hereafter BVM) who used the measurements of the [Ar IV] λλ4711,40Å doublet ratio observed by Koski (1978, hereafter Kos78) in seven Seyfert 2's, and found that the densities were $\lesssim 10^4\,{\rm cm}^{-3}$. The average NLR temperature inferred was 13 500 °K, which standard single-zone photoionization models cannot reproduce, assuming standard input parameter values.

In the present work, we will investigate whether an optimization of the spectral energy distribution (SED) of the ionizing source might contribute to the resolution of the temperature problem. Since we do not directly observe the far-UV region of the ionizing continuum due to interstellar absorption, the current study is speculative in nature. Alternative interpretations of the temperature discrepancy will be the subject of future publications.

2. A DOUBLE BUMP IONIZING ENERGY DISTRIBUTION

2.1. *Standard Ionizing SEDs*

The ionizing radiation from the nucleus is expected to originate from thermal emission by gas accreting onto a supermassive black hole. Although thermal in nature, the energy distribution is broader than a blackbody since the continuum emission is considered to take place from an extended disk that

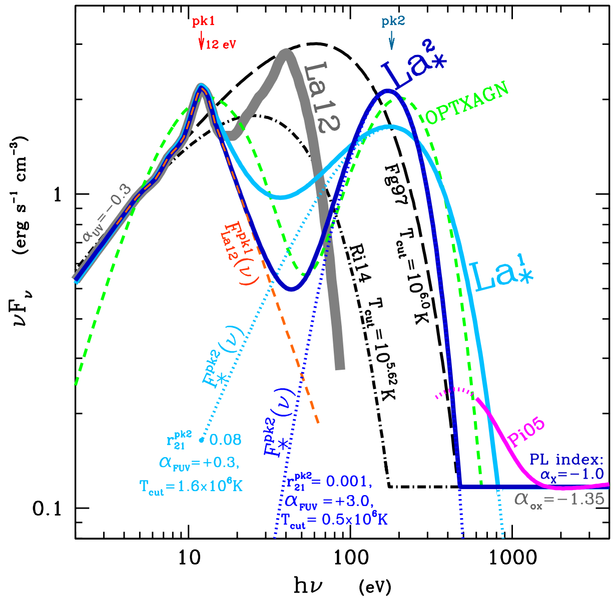

Fig. 1. Ionizing spectral energy distributions described in § 2, in νF_ν units: (1) the SED adopted by Fg97 for their LOC calculations with $T_{cut} = 10^{6.0}$ °K (long dashed line), (2) the optimized SED with $T_{cut} = 10^{5.62}$ °K of Ri14 (dot-short dash line), and (3) the double-bump reprocessed distribution of La12 (thick grey line), and (4) two modified versions $La^1_\star$ (cyan) and $La^2_\star$ (blue) of the La12 reprocessed distribution. The $La^1_\star$ (cyan) and $La^2_\star$ (blue) SEDs were obtained by summing up the truncated La12 SED, $F^{pk1}_{La12}(\nu)$ (red dashed line), to both cyan and blue *dotted lines* $F^{pk2}_*(\nu)$ distributions. The light-green dashed line corresponds to an accretion disk model including optically thick Compton emission by a warm plasma. It was calculated using the OPTXAGN model in XSPEC (Done et al. 2012, see § 5.3). The above SEDs were renormalized to νF_ν of unity at 5 eV (2480 Å). In the X-ray domain, a power-law of index −1.0 was assumed with an α_{OX} of −1.35. The magenta line represents the average of the soft X-ray excess measurements inferred by Pi05, assuming $\alpha_{OX} = -1.35$ with respect to the La12 distribution. The color figure can be viewed online.

covers a wide temperature range. In their photoionization models, Ferguson et al. (1997, hereafter Fg97) and Richardson et al. (2014, hereafter Ri14) assumed a SED where the dominant ionizing continuum corresponds to a thermal distribution of the form

$$F_\nu \propto \nu^{\alpha_{UV}} \exp(-h\nu/kT_{cut}), \qquad (1)$$

where T_{cut} is the UV temperature cut-off and α_{UV} the low-energy slope of the 'big bump', which is typically assumed to be $\alpha_{UV} = -0.3$. This thermal component dominates the ionizing continuum up to the X-ray domain where a power-law of index −1.0

[7]The term 'quasar' is used to refer to Type I AGN.

takes over. The values for T_{cut} adopted by Fg97 and Ri14 are $10^{6.0}$ and $10^{5.62}$ °K, respectively. Both distributions are shown in Figure 1. In both cases we have assumed a standard X-ray-to-optical spectral index[8] α_{OX} of -1.35.

2.2. *The Proposition of a Double-Peaked SED*

To address the temperature problem, Lawrence (2012, hereafter La12) explored the possibility that a population of internally cold very thick ($N_{\rm H} > 10^{24}\,{\rm cm}^{-2}$) dense clouds ($n \approx 10^{12}\,{\rm cm}^{-3}$) covers the accretion disk at a radius of $\approx 35\,R_s$ from the black-hole, where R_s is the Schwarzschild radius. The cloud's high velocity turbulent motions blur its line emission as well as reflect the disk emission, resulting in a double-peaked SED superposed to the reflected SED. The first peak at $\approx$ 1100Å represents the clouds reprocessed radiation while the second corresponds to the disk radiation reflected by the clouds. The resulting SED is represented by the thick light-gray continuous line in Figure 1. The main advantage of this distribution is its ability to account for the 'universal' knee observed at 12 eV in quasars. The assumed position of the second peak at 40 eV would however need to be shifted to much higher energies in order to significantly increase the photoheating efficiency and subsequently reproduce the observed $R_{\rm OIII}$ ratio. This possibility, which is explored in the current work, might imply adjustments of the 'reprocessing model' since the turbulent clouds, hypothesised by La12, would likely need to extend to much smaller radii than the assumed value of $35\,R_s$. Alternatively, the hotter inner component of the accretion disk might progressively become uncovered at smaller disk radii. We note that similar double-peaked SEDs would arise if the primary disk emission was further Compton up-scattered to higher energies owing to the presence of an optically thick warm plasma in addition to the hot thin corona responsible for the hard X-rays (Done et al. 2012). We will further discuss this possibility in § 5.

2.3. *Components of Our Modified Double-Peak La$^1_\star$ SED*

After experimenting with different shapes and positions for the second peak, it was found that the presence of a deep valley at $\simeq 35$ eV can result in an increase of the plasma temperature (*i.e.* higher $R_{\rm OIII}$ ratio). To explore double-peak SEDs, we proceeded as follows. First, we extracted a digitized version of the published La12 SED. To eliminate the 40 eV peak we extrapolated the declining segment of the first peak. The resulting distribution is represented by the red dashed line labelled $F^{pk1}_{La12}(\nu)$ in Figure 1. For the second peak, $F^{pk2}_{*}(\nu)$, we adopted the formula, $\nu^{\alpha_{UV}} \exp(-h\nu/k\,T_{cut})$ (i.e. equation 1). All the double-bump SEDs which we explored were obtained by simply summing both distributions:

$$F_\nu = F^{pk1}_{La12}(\nu) + R\ r^{pk2}_{21}\,\nu^{\alpha_{FUV}} \exp\left(-h\nu/k\,T_{cut}\right), \tag{2}$$

where $R = F^{pk1}_{La12}(\nu_{pk1})/F^{pk2}_{*}(\nu_{pk1})$ is the renormalization factor which we define at $h\nu_{pk1} = 12$ eV, the energy where the first peak reaches its maximum in νF_ν. The position and width of the second peak depends on both parameters α_{UV} and T_{cut} while its intensity is set by the parameter r^{pk2}_{21}. The main benefit of the second peak is to increase the local heating rate due to He$^+$ photoionization (c.f. § 5.1).

After comparing the plasma temperatures reached when different combinations of the parameters T_{cut}, α_{FUV} and r^{pk2}_{21} are considered, we concluded that the optimal position for the second peak is ≈ 200 eV. Moving it to higher values was not an option, as it generated an excessive flux in the soft X-rays that is not observed in Type II AGN.

Our first version for the optimal SED, labelled La$^1_\star$, is shown in Figure 1 (cyan solid line). It assumes an index $\alpha_{FUV} = +0.3$ as in Ri14 and Fg97, which corresponds essentially to the index of the standard Shakura-Sunyaev accretion disk model (Shakura & Sunyaev 1973; Pringle 1981; Cheng et al. 2019) of $\alpha_{FUV} = 1/3$. The value derived for the parameter T_{cut} is $1.6\,10^6$ °K and the optimal value for the scaling factor is $r^{pk2}_{21} = 0.08$. Increasing r^{pk2}_{21} further would require a reduction in T_{cut}, otherwise the resulting SED would extend too far into the soft X-rays.

2.4. *An Alternative Double-Peak SED: La$^2_\star$*

The La$^1_\star$ SED drops off around 800 eV (Figure 1). It is important to ensure that the predicted flux beyond 500 eV does not exceed the soft X-rays measurements. While some AGN show extreme emission in the so-called X-ray soft excess up to 1–2 keV, others do not. One solution would be to adopt larger values for the parameter α_{FUV}. To illustrate this, our second version of the double-bump SED, labelled La$^2_\star$, uses a much larger α_{FUV} of +3. In this case the optimal value for the parameter T_{cut} has to be as low as $0.5\,10^6$ °K so that the second peak occurs at essentially the same energy as in the La$^1_\star$ SED. Because the peak profile is much narrower (dotted

[8] The X-ray spectral index is defined as $\alpha_{OX} = 0.3838 \times \log(f_{2\rm kev}/f_{2500\rm A})$, where $f_{2\rm keV}$ and $f_{2500\rm A}$ are the fluxes at rest-frame 2 keV and 2500Å, respectively.

blue line), the scaling parameter r_{21}^{pk2} turns out to be much smaller, at 0.001.

Note that if we had assumed the Planck equation, as in La12, for the second peak instead of equation 1, the favored position of the second peak near 200 eV would correspond to a blackbody temperature of $T_{BB} \simeq 500\,000\,^{\circ}$K, that is, five times higher[9] than the $T_{BB} \simeq 100\,000\,^{\circ}$K temperature proposed by La12.

2.5. *The Unaccounted Soft X-Ray Excess Below 2 keV*

There are few competing processes that have been proposed to explain the physical mechanism responsible for the so called X-ray soft excess. The most popular ones include a dual-coronal system (e.g. Done et al. 2012) or relativistic blurred reflection (e.g. Ross & Fabian 2005). For illustrative purposes, we show in Figure 1 the "average soft excess" component observed with XMM-Newton (magenta line) by Piconcelli et al. (2005, hereafter Pi05). It corresponds to the best-fit average of 13 quasars with $z < 0.4$ using the parameters from Table 5 of Pi05, as described in Haro-Corzo et al. (2007). This component was re-scaled so as to reproduce an α_{OX} of -1.35 with respect to the La12 SED. The dotted section below 600 eV is speculative, as it is not reliably constrained by X-ray measurements.

The soft excess varies strongly among different individual objects and its nature might be completely different than the emission in the extreme UV postulated here. On the other hand, the Comptonization of disk photons by a warm plasma can explain the presence of the soft excess (Done et al. 2012) and at the same time produce double-peaked SEDs with the second peak near 200 eV (see § 2.2). The same might be true for blurred reflection/emission, as relativistic line emission has been used to (1) model the soft excess in a successful way (e.g. Ross & Fabian 2005), and (2) produce specific ionizing SEDs that result in two emission bumps in the extreme UV (La12, see § 2.2). While tantalizing, exploring these possibilities is beyond the scope of this paper. The important point is that the proposed SEDs in this paper are consistent with the soft excess observed in quasars.

3. OBSERVED $R_{\rm OIII}$ RATIOS AMONG AGN

3.1. *Seyfert 2 Samples*

In order to compare our calculations with observed ratios among Type II AGN, we adopt the three samples used by BVM, which are represented in Figure 2 by black open symbols. They correspond to the following dereddened[10] measurements:

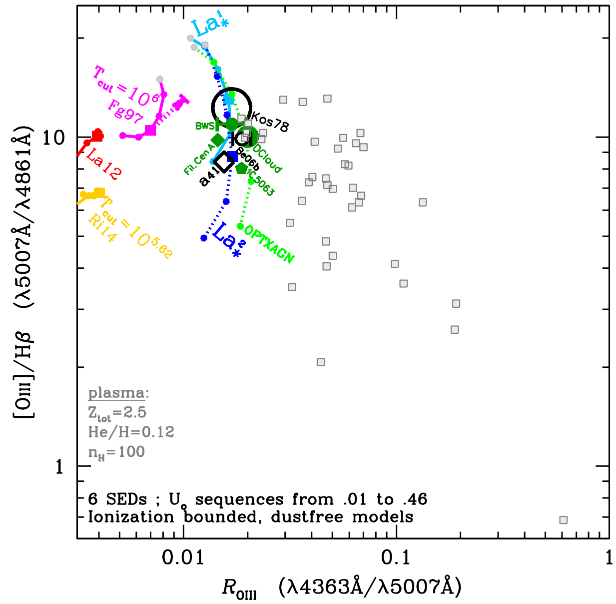

Fig. 2. Dereddened NLR ratios of [O III]/Hβ vs. $R_{\rm OIII}$. *Data set*: line ratios from three samples of Type II AGN, all represented by open *black* symbols and consisting of: (1) the average of seven Seyfert 2's from Kos78 (large circle); (2) the average of four Seyfert 2's from Be06b (small circle); (3) the high excitation Seyfert 2 subset a41 from Ri14 (diamond). ENLR measurements are all represented by dark-green filled symbols consisting of: (1) the average of two Seyfert 2's and two NLRGs (small dot) from BWS; (2) the Seyfert 2 IC 5063 long slit spectrum of Be06b (pentagon); (3) the average of seven spatially resolved optical filaments of the radio-galaxy Centaurus A (green square) from Mo91; (4) the 8 kpc *distant cloud* from radiogalaxy Pks 2152−699 by Ta87 (large green dot). Type I AGN ratios are overlaid consisting of 30 quasars studied by BL05 (open grey squares). *Models*: Five sequences of photoionization models are overlaid along which U$_\circ$ increases from 0.01 (grey dot) to 0.46 in steps of 0.33 dex, assuming a constant plasma density of $n_H^\circ = 10^2\,{\rm cm}^{-3}$. A square identifies models with U$_\circ$ = 0.1. The SEDs were borrowed from Ri14 (yellow), La12 (red) and Fg97 (magenta). The dotted magenta arrow shows the effect caused by adopting a reduced abundance of 1.4 $Z_\odot$. Calculations using the two double-peaked La$_\star^1$ and La$_\star^2$ SEDs are coded in cyan and blue colors, respectively, while those that assume Comptonization of the accretion disk photons are coded in light-green. The color figure can be viewed online.

[9]Corresponding to a peak shift from 40 eV to 200 eV.

[10]All reddening corrections were carried out by the referred authors.

1. The seven Seyfert 2's from Kos78. The average ratios is $R_{\rm OIII} = 0.0168$ (i.e. $10^{-1.77}$), which is represented by a large black disk whose radius of 0.088 dex corresponds to the RMS $R_{\rm OIII}$ dispersion. A unique characteristic of this sample is the availability of measurements from the weak [Ar IV] $\lambda\lambda$4711,40Å doublet ratio, which can be used as a direct density indicator of the plasma responsible for the high excitation lines.

2. The average of four Seyfert 2 measurements (IC 5063, NGC 7212, NGC 3281 and NGC 1386) observed by Bennert et al. (2006b, hereafter Be06b). It is represented by a small black circle corresponding to a mean $R_{\rm OIII}$ of 0.0188. The pseudo error bars represent an RMS dispersion of 0.042 dex.

3. The high excitation Seyfert 2 subset a41 from Ri14 (open diamond), with $R_{\rm OIII} = 0.0155$, representing the high ionization end of the sequence of reconstructed spectra of Ri14, which were extracted from a sample of 379 AGN.

3.2. *Spatially Resolved ENLR*

We superpose in Figure 2 the ratios observed from the *spatially resolved* emission component of AGN, the so-called ENLR, which consists of *off-nuclear* line emission from plasma with densities typically $< 10^3\,{\rm cm}^{-3}$ (e.g. Tadhunter et al. 1994; Bennert et al. 2006a,b). The selected measurements are represented by the filled dark-green symbols, which stand for the following four samples: (1) the average (small filled dot) of two Seyfert 2's and two NLRGs from (Binette et al. 1996, hereafter BWS); (2) the long-slit observations of the Seyfert 2 IC 5063 by Be06b (pentagon); (3) the average of seven spatially resolved optical filaments from the radio-galaxy Centaurus A (filled square) from Morganti et al. (1991, hereafter Mo91); and (4) the 8 kpc *distant cloud* from radio galaxy Pks 2152−699 observed by Tadhunter et al. (1987, hereafter Ta87) (large dot). Pseudo-error bars denote the RMS dispersion of the BWS sample.

3.3. *Quasar Sample*

For illustrative purposes, we overlay in Figure 2 the measurements of the NLR ratios (open grey squares) from 30 quasars of redshifts $z < 0.5$, which were studied by BL05. The $R_{\rm OIII}$ ratios are found to extend from 0.01 up to 0.2, providing clear evidence that collisional deexcitation takes place within the NLR of Type I objects.

3.4. *Data set Comparison*

The detailed study of BVM of the Seyfert 2 sample from Kos78 rely on the measured density sensitive [Ar IV] $\lambda\lambda$4711,40Å doublet. The authors found no evidence that significant collisional deexcitation was affecting the observed $R_{\rm OIII}$ ratios, even after considering a power-law distribution of the densities in their plasma calculations of $R_{\rm OIII}$ and [Ar IV] ratios. Furthermore, both Seyfert 2's and ENLR measurements occupy a similar position in Figure 2, which is likely a consequence of LDR, since detailed studies of ENLR spectra are consistent with plasma densities $\ll 10^4\,{\rm cm}^{-3}$. By contrast, quasar NLR measurements of BL05 span a wide range in $R_{\rm OIII}$, with the lowest ratios lying close to the values seen in Seyfert 2's and in the ENLR plasma. This dichotomy between Type I and II objects is likely the manifestation of the observer's perspective on the NLR as a consequence of the *unified AGN geometry*, whereby the densest NLR components become progressively obscured in Type II objects due to the observer's lateral perspective on the ionizing cone. A graphical description of such geometry is illustrated by Figure 2 of Bennert et al. (2006c).

4. PHOTOIONIZATION CALCULATIONS

Our photoionization calculations were carried using the version Ig of the code MAPPINGS I (Binette et al. 2012). Recent updates are described in Appendix A. We compare below our models with the observed $R_{\rm OIII}$ as well as the He II/Hβ λ4686Å/λ4861Å ratios, assuming different ionizing continua.

4.1. *Dust-Free Plasma with Abundances Above Solar*

In this paper, we will only consider the case of a dust-free plasma. Insofar as plasma metallicities, it is generally accepted that gas abundances of galactic nuclei are significantly above solar values. The metallicities we adopt below correspond to $2.5\,Z_\odot$, a value within the range expected for galactic nuclei of spiral galaxies, as suggested by the Dopita et al. (2014) landmark study of the Seyfert 2 NGC 5427 using the Wide Field Spectrograph (WiFeS: Dopita et al. 2010). The authors determined the ISM oxygen abundances from 38 H II regions spread between 2 and 13 kpc from the nucleus. Using their inferred metallicities, they subsequently modelled the line ratios of over 100 'composite' ENLR-H II region emission line spaxels as well as the line ratios from the central NLR. Their highest oxygen abundance reaches $3\,Z_\odot$ (i.e. $12 + \log({\rm O/H} = 9.16)$. Such a high value is shared by other observational and theoretical studies that confirm the high metallicities of Seyfert nuclei (Storchi-Bergmann & Pastoriza 1990; Nagao et al. 2002; Ballero et al. 2008). Our selected abundance set is twice the solar reference set of Asplund et al. (2006), i.e. with O/H $= 9.8 \times 10^{-4}$, except for C/H and N/H which reach four times the solar values owing to secondary enrichment.

We can expect the enriched metallicities of galactic nuclei to be accompanied by an increase in He abundance. We followed a suggestion from David Nicholls (private communication, ANU) of extrapolating to higher abundances the metallicity scaling formulas that Nicholls et al. (2017) derived from local B stars abundance determinations. At the adopted O/H ratio, the proposed scaling formula described by equation A1 in Appendix A implies a value of He/H = 0.12, which is higher than the solar ratio of 0.103 adopted by Ri14. The effect on the equilibrium temperature, however, is relatively small as the calculated $R_{\rm OIII}$ ratios are found to increase by only 0.06 dex whether one assumes the Fg97, Ri14 or La12 SED.

4.2. *Characterization of the Temperature Problem*

The difficulty in reproducing the observed $R_{\rm OIII}$ ratio is illustrated by the three ionization parameter sequences shown in Figure 2 that fall on the extreme left of the diagram. Two of the SEDs were borrowed from the standard NLR models of Ri14 (yellow) and Fg97 (magenta) while the third corresponds to the double-peaked SED from La12 (in red). Along each sequence, the ionization parameter[11], U$_{\rm o}$, increases in steps of 0.33 dex, from 0.01 (light gray dot) up to 0.46. These sequences do not reach the $R_{\rm OIII}$ domain occupied by our sample of Seyfert 2's, with some models falling outside the plot boundaries.

4.3. *Calculations with the La$^1_\star$ and La$^2_\star$ SEDs*

The procedure followed to define the double-peaked La$^1_\star$ and La$^2_\star$ energy distributions (Figure 2) has been described in § 2.3 and 2.4. Photoionization calculations using either SED are successful in reproducing the $R_{\rm OIII}$ ratios from the Seyfert 2 Kos78 sample (black circle), as shown by the solid cyan and dotted blue lines in Figure 2, which represent ionization parameter sequences with U$_{\rm o}$ increasing in steps of 0.33 dex, from 0.01 (the light-gray dot) up to 0.46, assuming a constant plasma density of $n_H^{\rm o} = 10^2\,{\rm cm}^{-3}$. A square identifies models with

[11] $U_{\rm o} = \frac{\phi_0}{c n_H^{\rm o}}$, where ϕ_0 is the ionizing photon flux impinging on the photoionized slab, $n_H^{\rm o}$ the hydrogen density at the *face* of the cloud and c the speed of light.

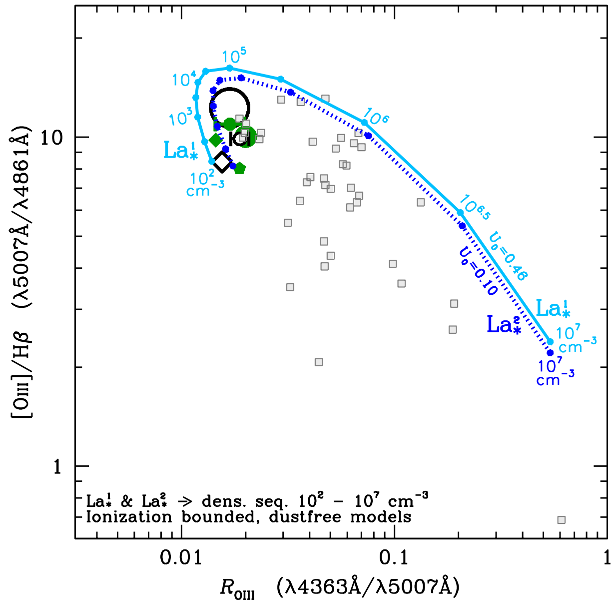

Fig. 3. Dereddened [O III]/Hβ (λ5007Å/λ4861Å) and He II/Hβ (λ4686Å/λ4861Å) line ratios. The observational data sets of § 3 are represented by the same symbols as in Figure 2. Overlaid are two sequences of models along which $n_H^{\rm o}$ increases from 10^2 to $10^7\,{\rm cm}^{-3}$ in steps of 0.5 dex. The ionization parameter is U$_{\rm o}$ = 0.46 for the La$^1_\star$ sequence (cyan) and U$_{\rm o}$ = 0.10 for the La$^2_\star$ sequence (blue). The color figure can be viewed online.

U$_{\rm o}$ = 0.1. Our models suggest that either of the double-bump SEDs has the potential of resolving the temperature discrepancy encountered with conventional ionizing distributions.

We would qualify the two La$^1_\star$ and La$^2_\star$ SEDs as representing two extreme cases with respect to the parameter α_{FUV}. Ionizing continua that assumed intermediate values, in the range $0.3 < \alpha_{FUV} < 3$, would be equally successful in reproducing the observed $R_{\rm OIII}$ ratios provided the parameters T_{cut} and r_{21}^{pk2} were properly adjusted to maintain the second peak centered at 200 eV and at an intermediate height between La$^1_\star$ and La$^2_\star$.

In order to compare our models with Type I AGN (open grey squares), we calculated density sequences along which the density increases in steps of 0.5 dex, from $n_H^{\rm o} = 100$ to $10^7\,{\rm cm}^{-3}$. These calculations are shown in Figure 3. For each sequence, we selected the U$_{\rm o}$ value that made the models cover the upper envelope of the quasar [O III]/Hβ ratios, which are U$_{\rm o}$ = 0.46 and 0.10 for the La$^1_\star$ and La$^2_\star$ SEDs, respectively. The vertical dispersion in the observed [O III]/Hβ ratios is noteworthy. The simplest interpretation might be the need of considering a distribution of cloud densities, as favored by the dual-density models of BL05. Alternatively, in the case of the Ri14 LOC models, the observed dispersion suggests that the density power-law index β might take different values.

4.4. *The He II/Hβ Diagnostic Ratio*

When comparing different ionizing distributions, an important ratio to consider is He II/Hβ λ4686Å/λ4861Å since, as pointed out by Ri14, the latter is sensitive to the hardness of the ionizing continuum. Figure 4 illustrates the behavior of the dereddened [O III]/Hβ vs. He II/Hβ ratios assuming either the $La^1_\star$ or the $La^2_\star$ ionizing continua. They reproduce reasonably well the He II/Hβ ratio observed among the Seyfert 2's of Kos78 and Be06b. Also overlaid is the γ sequence from the LOC calculations (yellow dashed line) of Ri14, assuming a density weighting parameter β of -1.4, the value favored by the authors when modeling their four AGN subsets[12].

If we compare the Type II samples (black open symbols) with the spatially resolved ENLR (dark-green symbols), we notice a wider dispersion among the He II/Hβ ratios than for the $R_{\rm OIII}$ ratios of Figure 3, which is surprising given the fact that the He II/Hβ ratio depends little on density or temperature. This could be an indication that the emitting plasma in some cases is not fully ionization-bounded, as proposed by BWS.

5. DISCUSSION

5.1. *Plasma Heating from He$^+$ Photoionization*

The presence of high excitation lines among NLR spectra such as He II, C III], C IV, [Ne III] indicates a hard ionizing continuum. As a consequence of the SED hardness, the heating rate as well as the resulting equilibrium temperatures are higher than in H II regions, due to the higher energies of the ejected photoelectrons and to the significant contribution of He$^+$ photoionization to the total heating rate, at least within the front layers of the exposed nebulae. The fraction of ionizing photons with energies above 54.4 eV is 24 % and 26 % for the $La^2_\star$ and $La^1_\star$ SEDs, respectively, and 23 % for the Fg97 distribution[13]. These values are quite similar, but when a dip takes place below 50 eV, as in the $La^2_\star$ and $La^1_\star$ SEDs (see Figure 1), the peak of the distribution in νF_ν shifts to higher energies ($\simeq$ 200 eV). Consequently, the plasma heating rate[14] rises above the rate obtained with the Fg97 SED, essentially as a result of the increase in the mean energy of the photoelectrons ejected from ionization of He$^+$.

[12]Each subset represents a composite emission line spectrum assembled from a sample of Seyfert 2 spectra of the SLOAN database. They form an ionisation sequence in a BPT diagram that covers the locus of AGN, as described by the authors. The high excitation a41 subset is best reproduced assuming a weighing parameter γ value of $\simeq -0.75$.

[13]The fraction is 19 % for the OPTXAGN SED.

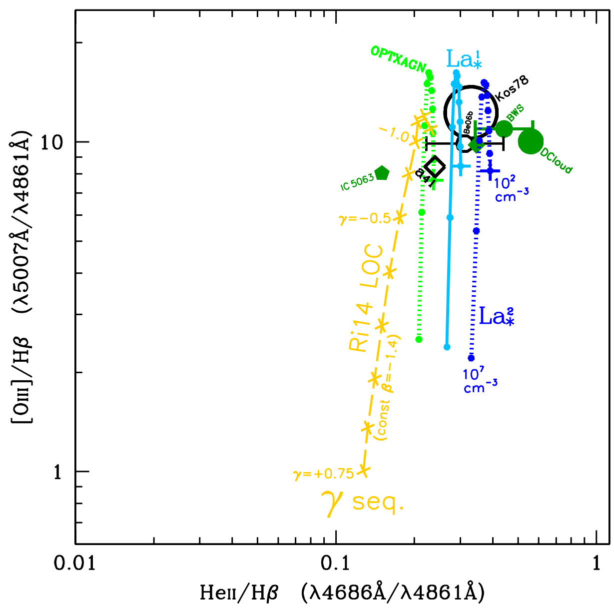

Fig. 4. Dereddened [O III]/Hβ (λ5007Å/λ4861Å) and He II/Hβ (λ4686Å/λ4861Å) line ratios. The observational data sets of § 3 are represented by the same symbols as in Figure 2. Both density sequences from previous Figure 3, using the $La^1_\star$ (cyan) and $La^2_\star$ (blue) SEDs, are overlaid. The light-green dotted line represents a density sequence assuming the accretion disk SED derived using the OPTXAGN routine. In each sequence, a cross identifies the lowest density model with $n^o_H = 100\,{\rm cm}^{-3}$. The yellow dashed line represents the dust free LOC model sequence from Ri14 with $\beta = -1.4$, along which the radial weighing parameter γ varies from $+0.75$ to -2.0 in steps of -0.25. The color figure can be viewed online.

5.2. *The Shape of the EUV Dip Near 40 eV*

Being able to reproduce the observed $R_{\rm OIII}$ measurements of Seyfert 2's by assuming the above double-peaked $La^1_\star$ and $La^2_\star$ SEDs does not prove it is the right solution to the temperature problem, but it is a possibility worth exploring further. One advantage of the proposed distributions is that, unlike the conventional thermal SEDs of Ri14 or Fg97, they incorporate the 'universal' knee observed near 12 eV in high redshift quasars, which Zheng et al. (1997) and Telfer et al. (2002) studied using the *Hubble Space*

[14]The heating rate is the result of the thermalization of the photoelectrons ejected from the H I, He$^+$ and, to a lesser extent, He^0 species.

Telescope archival database. Using the Far Ultraviolet Spectroscopic Explorer database, Scott et al. (2004) find an average index α_ν of -0.56 in AGN of redshifts < 0.33, which is significantly flatter than the average of $\simeq -1.76$ found at redshifts $z \gtrsim 2$ (Telfer et al. 2002). How steeply the flux declines beyond 12 eV is rather uncertain and could also depend on the AGN luminosity (Scott et al. 2004).

5.3. *Comptonized Accretion Disk Models*

The pertinence of a second peak to describe the harder UV component is provided by the work of Done et al. (2012), who built a self-consistent accretion model where the primary emission from the disc is partly Comptonized by an optically thick warm plasma, forming the EUV. This plasma that, according to Done et al. (2012), might itself be part of the disk would exist in addition to the optically thin hot corona above the disc responsible for producing the hard X-rays.

Using the OPTXAGN routine in XSPEC[15], we calculated an accretion disk model that allowed the second peak to occur at a similar position as that of the $\mathrm{La}^2_\star$ SED. It is represented in Figure 1 by the light green dashed curve. Different sets of parameters in the OPTXAGN model can match the double peaked $\mathrm{La}^1_\star$ and $\mathrm{La}^2_\star$ SEDs, provided extreme accretion rates are assumed ($\mathrm{L/L}_{Edd} \geq 1$). Such accretion rates are not proper of the Type II objects discussed here, but rather of extreme Narrow Line Seyfert 1 nuclei. Even though the OPTXAGN model was not developed to generate the double peak SEDs postulated in this work, we should note that a wide set of SEDs with different double peaks or even more extreme FUV peaks can be produced using different, less stringent, parameters. Our aim in presenting this SED, apart from matching our $\mathrm{La}^2_\star$ SED, was to exemplify how different physical processes at different accretion disk scales might result in an ionizing distribution capable of reproducing the observed R_{OIII} ratio. We plan to fully explore under which conditions (e.g. more conservative SEDs with moderate accretion rates), dual temperature Comptonization disk models can achieve this.

An additional drawback is that the OPTXAGN model does not reproduce the knee observed at 12 eV. Expanding the range of parameters in this model might circumvent this issue. Overall, we note the striking similarity of the OPTXAGN with that of $\mathrm{La}^2_\star$, considering that they were built independently and with completely different scientific motivations. Photoionization calculations with this SED indicate that, as expected, it can reproduce the observed R_{OIII} ratio, as shown by the light-green dotted line in Figure 2. The He II/Hβ ratio, however, is somewhat under-predicted, as shown in Figure 2. This appears to be caused by the first peak of the OPTXAGN SED being significantly thicker than in the $\mathrm{La}^2_\star$ SED.

[15] Using commands described in `http://heasarc.gsfc.nasa.gov/xanadu/xspec/manual/node132.html` (Done et al. 2012; Kubota & Done 2018).

AH acknowledges support from NVIDIA in the form of a GPU under the NVIDIA Academic Hardware Grant Program. SGM acknowledges support from the Fundação para a Ciência e a Tecnologia (FCT) through the Fellowships PD/BD/135228/2017 (PhD::SPACE Doctoral Network PD/00040/2012), POCH/FSE (EC) and COVID/BD/152181/2021. AH and SGM were also supported by Fundação para a Ciência e a Tecnologia (FCT) through the Research Grants UIDB/04434/2020 and UIDP/04434/2020, and an FCT-CAPES Transnational Cooperation Project "Parceria Estratégica em Astrofísica Portugal-Brasil".

APPENDIX

A. RECENT UPDATES TO THE CODE MAPPINGS Ig

We incorporated the following tools in the version Ig of MAPPINGS I.

a) We implemented the new routine OSALD which calculates various line ratio diagnostics that can be used to infer the temperature and/or density cut-off using observed line ratios. It assumes an isothermal plasma that covers a wide range of densities, up to a predefined cut-off density. The diagnostics can also be applied to line ratios not previously dereddened since OSALD offers the option of dereddening the line ratios from the observed Balmer lines. It is also possible to assume a dust extinction that correlates with the plasma density, a possibility relevant to the NLR of Type II AGN. The routine is described in § 5 (and Appendix C of BVM).

b) Based on the work of Pequignot et al. (1991), the recombination rates from N^{+2}, O^{+3} and O^{+2} to the corresponding metastable levels $^1S_0$ and $^1D_2$ of [N II] and [O III] and levels ^2P and ^2D of [O II], respectively, have been incorporated in the calculation of the corresponding emission line intensities. In the case of the $^1S_0$ level of [O III], we added the missing contribution from dielectronic recombination (Christophe Morisset, private communication). As for the S^{+2} and S^{+3} ions, we estimated their recombination rates to metastable levels by extrapolation from the O^{+2} and O^{+3} ions as follows: we assumed that the fraction, ξ, of the total recombination rate ($\alpha^{rec}_{\rm SII}$ or $\alpha^{rec}_{\rm SIII}$), which populates metastable levels of Sulphur is the same fraction as found for Oxygen. For instance, for a 10 000 K plasma this fraction, $\xi^{S_0}_{\rm OIII}$, in the case of level $^1S_0$ of O III (responsible for the emission of the [O III] λ4363Å line) is 2.2% of $\alpha^{rec}_{\rm OIV}$.

c) An option is offered to scale the He abundance in function of the oxygen abundance, in accordance to the equation:

$$\mathrm{He/H} = 0.06623 + 0.0315\left(\frac{\mathrm{O/H}}{5.75\times10^{-4}}\right), \tag{A1}$$

which follows a suggestion from David Nicholls (private communication, ANU). It differs from equation 4 of Nicholls et al. (2017) as it behaves linearly down to primordial abundances. If we assume the O/H ratio given by the solar abundance set of Asplund et al. (2006), the He/H ratio[16] derived is 0.093. Beyond solar metallicities, it remains an open question to what extent the He/H ratio of the ISM from nuclear regions exceeds the solar neighborhood value. Equation A1 is intended as an exploratory tool to study the impact of using above solar He/H ratios when modelling the emission plasma from a metallicity enriched interstellar medium. The value of He/H = 0.12 referred to in § 4 is based on our adopted abundance set of $Z_{\rm tot} = 2.5$, which has O/H = 9.8×10^{-4} as defined in § 4. The inferred He/H ratio differs slightly from the value of 0.107 obtained using equation 4 of Nicholls et al. (2017).

[16]The solar He/H ratio adopted by Ri14 with CLOUDY is 0.103.

REFERENCES

Asplund, M., Grevesse, N., & Jacques Sauval, A. 2006, Nucl. Phys. A, 777, 1, https://doi.org/10.1016/j.nuclphysa.2005.06.010

Baldwin, J., Ferland, G., Korista, K., & Verner, D. 1995, ApJ, 455, 119, https://doi.org/10.1086/309827

Ballero, S. K., Matteucci, F., Ciotti, L., Calura, F., & Padovani, P. 2008, A&A, 478, 335, https://doi.org/10.1051/0004-6361:20078663

Baskin, A. & Laor, A. 2005, MNRAS, 358, 1043, https://doi.org/10.1111/j.1365-2966.2005.08841.x,[BL05]

Bennert, N., Jungwiert, B., Komossa, S., Haas, M., & Chini, R. 2006a, A&A, 459, 55, https://doi.org/10.1051/0004-6361:20065477

_________. 2006b, A&A, 456, 953, https://doi.org/10.1051/0004-6361:20065319,[Be06b]

_________. 2006c, NewAR, 50, 708, https://doi.org/10.1016/j.newar.2006.06.026

Binette, L., Matadamas, R., Hägele, G. F., et al. 2012, A&A, 547, 29, https://doi.org/10.1051/0004-6361/201219515

Binette, L., Villar Martín, M., Magris C., G., et al. 2022, RMxAA, 58, 133, https://doi.org/10.22201/ia.01851101p.2022.58.01.11,[BVM]

Binette, L., Wilson, A. S., Raga, A., & Storchi-Bergmann, T. 1997, A&A, 327, 909

Binette, L., Wilson, A. S., & Storchi-Bergmann, T. 1996, A&A, 312, 365, [BWS]

Cheng, H., Yuan, W., Liu, H.-Y., et al. 2019, MNRAS, 487, 3884, https://doi.org/10.1093/mnras/stz1532

Done, C., Davis, S. W., Jin, C., Blaes, O., & Ward, M. 2012, MNRAS, 420, 1848, https://doi.org/10.1111/j.1365-2966.2011.19779.x

Dopita, M., Rhee, J., Farage, C., et al. 2010, Ap&SS, 327, 245, https://doi.org/10.1007/s10509-010-0335-9

Dopita, M. A., Scharwächter, J., Shastri, P., et al. 2014, A&A, 566, 41, https://doi.org/10.1051/0004-6361/201423467

Dors, O. L., Cardaci, M. V., Hägele, G. F., et al. 2015, MNRAS, 453, 4102, https://doi.org/10.1093/mnras/stv1916

Dors, O. L., Maiolino, R., Cardaci, M. V., et al. 2020, MNRAS, 496, 3209, https://doi.org/10.1093/mnras/staa1781

Ferguson, J. W., Korista, K. T., Baldwin, J. A., & Ferland, G. J. 1997, ApJ, 487, 122, https://doi.org/10.1086/304611,[Fg97]

Fonseca-Faria, M. A., Rodríguez-Ardila, A., Contini, M., & Reynaldi, V. 2021, MNRAS, 506, 3831, https://doi.org/10.1093/mnras/stab1806

Haro-Corzo, S. A. R., Binette, L., Krongold, Y., et al. 2007, ApJ, 662, 145, https://doi.org/10.1086/515565

Korista, K., Baldwin, J., Ferland, G., & Verner, D. 1997, ApJS, 108, 401, https://doi.org/10.1086/312966

Koski, A. T. 1978, ApJ, 223, 56, https://doi.org/10.1086/156235,[Kos78]

Kubota, A. & Done, C. 2018, MNRAS, 480, 1247, https://doi.org/10.1093/mnras/sty1890

Lawrence, A. 2012, MNRAS, 423, 451, https://doi.org/10.1111/j.1365-2966.2012.20889.x,[La12]

Morais, S. G., Humphrey, A., Villar Martín, M., Binette, L., & Silva, M. 2021, MNRAS, 506, 1389, https://doi.org/10.1093/mnras/stab1599

Morganti, R., Robinson, A., Fosbury, R. A. E., et al. 1991, MNRAS, 249, 91, https://doi.org/10.1093/mnras/249.1.91,[Mo91]

Nagao, T., Murayama, T., Shioya, Y., & Taniguchi, Y. 2002, ApJ, 575, 721, https://doi.org/10.1086/341355

Nicholls, D. C., Sutherland, R. S., Dopita, M. A., Kewley, L. J., & Groves, B. A. 2017, MNRAS, 466, 4403, https://doi.org/10.1093/mnras/stw3235

Osterbrock, D. E. 1978, Phys. Scr, 17, 285, https://doi.org/10.1088/0031-8949/17/3/024

Pequignot, D., Petitjean, P., & Boisson, C. 1991, A&A, 251, 680

Piconcelli, E., Jimenez-Bailón, E., Guainazzi, M., et al. 2005, A&A, 432, 15, https://doi.org/10.1051/0004-6361:20041621,[Pi05]

Pringle, J. E. 1981, ARA&A, 19, 137, https://doi.org/10.1146/annurev.aa.19.090181.001033

Richardson, C. T., Allen, J. T., Baldwin, J. A., Hewett, P. C., & Ferland, G. J. 2014, MNRAS, 437, 2376, https://doi.org/10.1093/mnras/stt2056, [Ri14]

Ross, R. R. & Fabian, A. C. 2005, MNRAS, 358, 211, https://doi.org/10.1111/j.1365-2966.2005.08797.x

Scott, J. E., Kriss, G. A., Brotherton, M., et al. 2004, ApJ, 615, 135, https://doi.org/10.1086/422336

Shakura, N. I. & Sunyaev, R. A. 1973, A&A, 24, 337

Storchi-Bergmann, T. & Pastoriza, M. G. 1990, PASP, 102, 1359, https://doi.org/10.1086/132775

Storchi-Bergmann, T., Wilson, A. S., Mulchaey, J. S., & Binette, L. 1996, A&A, 312, 357

Tadhunter, C. N., Fosbury, R. A. E., Binette, L., Danziger, I. J., & Robinson, A. 1987, Natur, 325, 504, https://doi.org/10.1038/325504a0, [Ta87]

Tadhunter, C. N., Metz, S., & Robinson, A. 1994, MNRAS, 268, 989, https://doi.org/10.1093/mnras/268.4.989

Telfer, R. C., Zheng, W., Kriss, G. A., & Davidsen, A. F. 2002, ApJ, 565, 773, https://doi.org/10.1086/324689

Villar-Martín, M., Humphrey, A., Martínez-Sansigre, A., et al. 2008, MNRAS, 390, 218, https://doi.org/10.1111/j.1365-2966.2008.13779.x

Zheng, W., Kriss, G. A., Telfer, R. C., Grimes, J. P., & Davidsen, A. F. 1997, ApJ, 475, 469, https://doi.org/10.1086/303560

L. Binette and Y. Krongold: Instituto de Astronomía, Universidad Nacional Autónoma de México, A.P. 70-264, 04510 México, D.F., México, Apartado Postal 70-264, Ciudad de México, CDMX, C.P. 04510, México.

S. A. R. Haro-Corzo: Escuela Nacional de Estudios Superiores (ENES) Unidad Morelia, UNAM, Antigua Carretera a Patzcuaro No. 8701 Col. Ex Hacienda de San José de la Huerta C.P. 58190 Morelia, Michoacán, México.

A. Humphrey and S. G. Morais: Instituto de Astrofísica e Ciências do Espaço, Universidade do Porto, CAUP, Rua das Estrelas, 4150-762, Porto, Portugal.

A. Humphrey: DTx – Digital Transformation CoLAB, Building 1, Azurém Campus, University of Minho, 4800-058 Guimarães, Portugal.

S. G. Morais: Departamento de Física e Astronomia, Faculdade de Ciências, Universidade do Porto, Rua do Campo Alegre 687, PT4169-007 Porto, Portugal.

Revista Mexicana de Astronomía y Astrofísica, **59**, 123–135 (2023)

https://doi.org/10.22201/ia.01851101p.2023.59.01.09

PHOTOMETRIC STUDY OF TWO CONTACT BINARY SYSTEMS AND A DETACHED LATE DWARF + M DWARF COMPONENTS

R. Michel[1], C. Barani[2], M. Martignoni[3], F. Acerbi[4], and L. Altamirano-Dévora[1,5]

Received July 3 2022; accepted January 2 2023

ABSTRACT

The results of our study of the eclipsing binary systems AF LMi, CzeV188 and CRTS J073333.0+302556 based on new CCD B, V, R_C, I_C complete light curves, are here presented. The short periods of these systems are confirmed and revised. The light curves were modeled using the latest version of the Wilson-Devinney code and, as a result, we found that AF LMi (G3+G9) and CzeV188 (K0+K1) are W UMa-type contact binary systems belonging to the W subclass, showing a shallow degree of fill-out with components in good thermal contact. CRTS J073333.0+302556 is a detached binary system composed by a late dwarf (K8) and an M6 dwarf spectral type components. The asymmetries of the light curves were accounted for with a spot on the surface of one of the component. The absolute elements of the three objects were estimated.

RESUMEN

Se presentan los resultados de nuestro estudio de los sistemas binarios eclipsantes AF LMi, CzeV188 y CRTS J073333.0+302556 los cuales están basados en nuevas curvas de luz completas tomadas con CCD y los filtros B, V, R_C, I_C. Los cortos periodos de estos sistemas se confirman y actualizan. Las curvas de luz han sido modeladas con la última versión del código Wilson-Devinney y, como resultado, encontramos que AF LMi (G3+G9) y CzeV188 (K0+K1) son binarias en contacto del tipo W UMa pertenecientes a la subclase W, presentado un bajo grado de relleno y con las componetes en buen contacto térmico. CRTS J073333.0+302556 es un sistema binario separado compuesto por una enana tardía (K8) y una enana de tipo espectral M6. Las asimetrías encontradas en las curvas de luz fueron tomadas en cuenta con una mancha en la superficie de una de las componentes. Se ha hecho una estimación de los valores absolutos de los parámetros de los tres sistemas.

Key Words: binaries: close — stars: fundamental parameters — stars: individual: AF LMi, CzeV188, CRTS J073333.0+302556 — techniques: photometric

1. INTRODUCTION

Eclipsing binary systems can be divided in three groups, detached, semidetached, and contact, and are important objects for our understanding of the properties of stars, as well as stellar systems. The above sequence can be interpreted as different evolutionary stages, governed by the mass transfer of the massive component. Detached binaries (DB) that are eclipsing, exhibit Algol-type (EA type) light curves and the interactions between their components are quite weak. When one of the components of the detached binary system fills its Roche lobe, mass transfers to its companion start and a semidetached system is formed.

The continuing mass transfer produces the formation of a common envelope around the components with the consequent formation of a contact system (W UMa-type). The semidetached-contact phase is suggested by the thermal relaxation oscillation theory (TRO theory) (Lucy 1976; Flannery 1976; Robertson & Eggleton 1977; Yakut & Eggleton 2005; Li et al. 2008), which predicts that binaries

[1]Instituto de Astronomía, UNAM. Ensenada, México.
[2]Via Molinetto 35, 26845 Triulza di Codogno (LO), Italy.
[3]Stazione Astronomica Betelgeuse, Magnago, Italy.
[4]Via Zoncada 51, 26845 Codogno (LO), Italy.
[5]Universidad Autónoma de Baja California, Ensenada, México.

evolve oscillating in a cycle of contact-semidetached-contact states via mass transfer between the components. Moreover, K-type contact binaries with periods shorter than 0.3 days are important systems for explaining the period cut-off phenomenon (Liu et al. 2014). However, only few systems are well studied, especially those with periods shorter than 0.25 days. AF LMi was reported as variable star by Khruslov (2007) in his second list of new short periodic eclipsing binaries. He proposed its typology of variation as EW, as suggested by only 0.1 mag difference between the minima.

Details about the system CzeV188 were first published in the Open European Journal on Variable Stars (OEJV) nr. 185 (Skarka et al. 2017) where the typology of EW variation was proposed. The present study on this system is interesting because its orbital period is below the period cut-off and because of its K spectral type.

Finally, CRTS J073333.0+302556 was found to be a variable star with a period of 0.267498 days and amplitude of variations of 0.16 mag, in the Catalina Surveys Periodic Variable Star Catalog (Drake et al. 2014).

2. OBSERVATIONS

Observations were done at the San Pedro Martir Observatory (Mexico) with the 0.84-m telescope (an f/15 Ritchey-Chretien), the Mexman filter-wheel and the *Spectral Instruments 1* CCD detector (an e2v CCD42-40 chip with 13.5×13.5 μ^2 pixels, gain of 1.39 e^-/ADU and readout noise of 3.54 e^-). The field of view was $7.6' \times 7.6'$ and binning 2×2 was employed during all the observations.

AF LMi was observed on February 3, 2016 for 0.7h, January 17, 2018 for 4.2h, April 20, 2018 for 2.3h, May 2, 2018 for 5.1h, and April, 15 2021 for 2.8h. Alternated exposures in filters B, V, R_c and I_c, with exposure times of 30, 20, 15 and 15 seconds respectively, were taken in all the observing runs.

CzeV188 was observed on July 2, 2017 for 4.7h, July 4, 2017 for 0.6h, June 12, 2018 for 4.3h, and June 13, 2018 for 0.5h. Alternated exposures in filters B, V, R_c and I_c with exposure times of 40, 20, 15 and 15 seconds respectively, were taken in all the observing runs.

CRTS J073333.0+302556 was observed January 18, 2017 for 4.6h, January 28, 2017 for 7.1h, and February 3, 2017 for 6.1h. Alternated exposures in filters B, V and R_c with exposure times of 80, 30 and 15 seconds respectively, were taken in all the observing runs.

All the images were processed using IRAF[6] routines. Images were bias subtracted and flat field corrected before the instrumental magnitudes were computed with the standard aperture photometry method.

The field stars were also calibrated in the $UBV(RI)_c$ system with the help of Landolt's photometric standards (Landolt 2009). Based on this information we were able to choose comparison stars with colors similar to the variables (making differential extinction corrections negligible). For the case of AF LMi, star 2MASSJ10381377+3219597 ($U = 15.046, B = 15.051, V = 14.429, R = 14.054, I = 13.694$) was employed while 2MASSJ19493362+3141488 ($U = 14.041, B = 13.008, V = 11.773, R = 11.121, I = 10.545$) was used for CzeV188 and 2MASSJ07334403+3024524 ($U = 19.624, B = 18.355, V = 16.933, R = 16.079, I = 15.282$) in the case of CRTS J073333.0+302556. From our observations we determined the apparent magnitude m_v in quadrature for AF LMi while for Cze V188 we calculated the V magnitude using equations (23) of Fukugita et al. (1996)

All the obtained light curves are shown in Figure 6.

Any part of the data can be provided upon request.

3. PERIOD ANALYSIS AND NEW EPHEMERIS

The first ephemeris of AF LMi was proposed by Khruslov (2007) as:

$$
\begin{aligned}
Min.I(HJD) &= 2451475.948 + \\
& 0^d.40660 \times E\,. \qquad (1)
\end{aligned}
$$

Subsequently, the system was observed by the All-Sky Automated Survey for Super Novae, (ASAS-SN) (Shappee et al. 2014; Kochanek et al. 2017), and a more precise period of 0.4065976d was obtained. From our observations we obtained one new time of minimum (ToM) by the fourth-order polynomial fit method.

One ToM was determined for each filter and finally they were conveniently averaged to adopt one ToM per epoch. Another 56 ToMs were obtained from the 1SWASP observations (Butters et al. 2010) and 8 more published in literature, were extracted from the "O-C gateway" database. The whole set of

[6]IRAF is distributed by the National Optical Observatories, operated by the Association of Universities for Research in Astronomy, Inc., under cooperative agreement with the National Science Foundation.

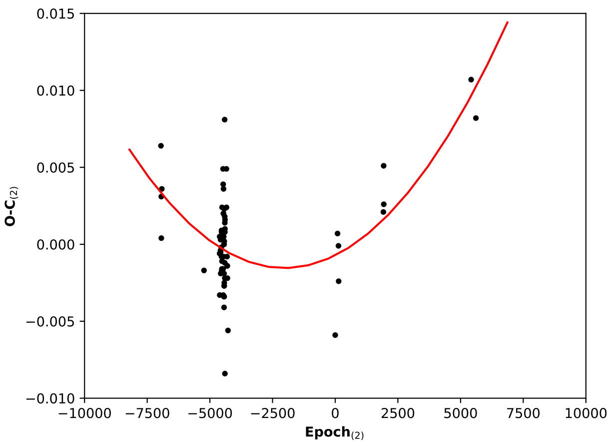

Fig. 1. O-C diagram of AF LMi related to Equation 2. The solid curve shows the second order polynomial fit to the data points. The color figure can be viewed online.

ToMs is listed in Table 1 and was used to determine new ephemeris as follows:

$$Min.I(HJD) = 2455598.8733(8) + 0^d.40659790(2) \times E + 2.016^{-10}(\pm 4.125^{-11}) \times E^2\,, \quad (2)$$

and the construction of the O-C diagram depicted in Figure 1.

The linear square fitting to the O-C data was used to obtain the new ephemeris for all the three systems.

For CzeV188, a period of 0.250295d was firstly proposed by (Skarka et al. 2017). After new observations during the ASAS-SN survey (Shappee et al. 2014; Kochanek et al. 2017), a new period of 0.2474002d was suggested. The ephemeris published in the VSX database is:[7]

$$Min.I(HJD) = 2456149.54952 + 0^d.247306 \times E\,. \quad (3)$$

Using the ToMs obtained from our observations (Table 2) of CzeV188, determined by the polynomial fit method, we can refine its ephemeris as follow:

$$Min.I(HJD) = 2456149.5494(11) + 0^d.2474007(2) \times E\,. \quad (4)$$

[7]The VSX (Variable Star IndeX) database is a web interface accessible to the public, in which one can find an exhaustive set of data for a single variable star. It is managed by the American Association of Variable Star Observers (AAVSO) and to date contains data for more than 2.2 million of variable stars.

From our observations of CRTS J073333.0+302556 we obtained 3 ToMs (Table 3), determined by the fourth-order polynomial fit method, giving a refined ephemeris of:

$$Min.I(HJD) = 2457771.8069(18) + 0^d.2674736(437) \times E\,. \quad (5)$$

4. MODELLING THE LIGHT CURVES

The latest version of the Wilson–Devinney (WD) code (Wilson & Devinney 1971; Wilson 1990; Wilson 1994; Wilson & van Hamme. 2016) was used and, since there are no reported spectroscopic mass-ratios of these systems, the q-search method was applied to find best initial values to be used during the light curve analysis.

The shape of the light curves of AF LMi and CzeV188 are clearly similar to those of W UMa systems, so we started our analysis directly in Mode 3 for overcontact binaries. Since CRTS J073333.0+302556 is a detached system, we used the appropriate Mode 2 in our calculations with no constrain on the potentials. CRTS J073333.0+302556 shows a flat primary eclipse covering approximately 0.040, 0.059 and 0.070 in phase respectively in the B, V and R_C filters.

To determine the mean surface temperature of the hotter star for AF LMi, we took the average value from the temperature indicated in different catalogues: LAMOST DR2 and DR5 catalogs (Luo et al. 2016, Luo et al. 2019), ATLAS all-sky stellar reference catalog (Tonry et al. 2018), Regression of stellar effective temperatures in GaiaDR2 (Bai et al. 2019) and CRTS Variable Sources Catalogue (Marsh et al. 2017). The average is 5700K.

For CzeV188 we used the color index $J - K = 0.524$ reported in the OEJV 185 (Skarka et al. 2017) deriving the temperature from the tables of Worthey & Lee (2011). We also used the regression of stellar effective temperatures in Gaia DR2 (Bai et al. 2019). The average temperature was found to be 5270K.

Finally, for CRTS J073333.0+302556 we used the 4027K temperature value reported by the GAIA DR2 collaboration (Gaia Collaboration 2018).

For the two contact systems, the limb-darkening parameters were interpolated with a square root law from the tables of van Hamme (1993) for $\log(g) = 4.0$ and solar abundances, while for CRTS J073333.0+302556 we used the tables of Claret & Bloemen (2011) again for $\log(g) = 4.0$ and solar abundances. A search for a solution was made

TABLE 1

TIMES OF MINIMA FOR AF LMI

HJD	$Epoch_{(1)}$	$O\text{-}C_{(1)}$	$Epoch_{(2)}$	$O\text{-}C_{(2)}$	Error	Source
2453132.4207	-6951.5	0.0332	-6951.5	0.0064	0.0002	SWASP
2453137.4998	-6939.0	0.0298	-6939.0	0.0031	0.0003	SWASP
2453138.5136	-6936.5	0.0271	-6936.5	0.0004	0.0004	SWASP
2453146.4454	-6917.0	0.0302	-6917.0	0.0036	0.0002	SWASP
2453830.5396	-5234.5	0.0199	-5234.5	-0.0017	0.0004	SWASP
2454083.6474	-4612.0	0.0192	-4612.0	-0.0006	0.0003	SWASP
2454084.6650	-4609.5	0.0203	-4609.5	0.0005	0.0003	SWASP
2454085.6776	-4607.0	0.0164	-4607.0	-0.0033	0.0003	SWASP
2454098.6917	-4575.0	0.0193	-4575.0	-0.0004	0.0002	SWASP
2454099.7088	-4572.5	0.0199	-4572.5	0.0003	0.0002	SWASP
2454100.7245	-4570.0	0.0191	-4570.0	-0.0005	0.0002	SWASP
2454101.7396	-4567.5	0.0177	-4567.5	-0.0019	0.0003	SWASP
2454111.7030	-4543.0	0.0194	-4543.0	-0.0002	0.0002	SWASP
2454114.5485	-4536.0	0.0187	-4536.0	-0.0008	0.0002	SWASP
2454114.7535	-4535.5	0.0204	-4535.5	0.0009	0.0002	SWASP
2454115.5666	-4533.5	0.0203	-4533.5	0.0008	0.0003	SWASP
2454118.6136	-4526.0	0.0178	-4526.0	-0.0017	0.0002	SWASP
2454120.6467	-4521.0	0.0179	-4521.0	-0.0016	0.0003	SWASP
2454122.6801	-4516.0	0.0183	-4516.0	-0.0011	0.0003	SWASP
2454123.7001	-4513.5	0.0218	-4513.5	0.0024	0.0002	SWASP
2454139.5600	-4474.5	0.0243	-4474.5	0.0049	0.0002	SWASP
2454140.5699	-4472.0	0.0177	-4472.0	-0.0016	0.0002	SWASP
2454141.5919	-4469.5	0.0232	-4469.5	0.0039	0.0002	SWASP
2454142.6012	-4467.0	0.0160	-4467.0	-0.0033	0.0003	SWASP
2454145.6560	-4459.5	0.0213	-4459.5	0.0020	0.0002	SWASP
2454146.4692	-4457.5	0.0213	-4457.5	0.0020	0.0003	SWASP
2454147.4873	-4455.0	0.0229	-4455.0	0.0036	0.0003	SWASP
2454147.6862	-4454.5	0.0185	-4454.5	-0.0008	0.0002	SWASP
2454150.5337	-4447.5	0.0198	-4447.5	0.0005	0.0002	SWASP
2454153.5792	-4440.0	0.0158	-4440.0	-0.0034	0.0002	SWASP
2454154.5991	-4437.5	0.0192	-4437.5	0.0000	0.0003	SWASP
2454155.6115	-4435.0	0.0151	-4435.0	-0.0041	0.0003	SWASP
2454156.4269	-4433.0	0.0173	-4433.0	-0.0019	0.0001	SWASP
2454156.6321	-4432.5	0.0192	-4432.5	0.0000	0.0002	SWASP
2454157.6459	-4430.0	0.0165	-4430.0	-0.0027	0.0002	SWASP
2454158.4584	-4428.0	0.0158	-4428.0	-0.0034	0.0001	SWASP
2454158.6624	-4427.5	0.0165	-4427.5	-0.0027	0.0002	SWASP
2454159.4784	-4425.5	0.0193	-4425.5	0.0002	0.0001	SWASP
2454159.6790	-4425.0	0.0166	-4425.0	-0.0025	0.0002	SWASP
2454160.4971	-4423.0	0.0215	-4423.0	0.0023	0.0001	SWASP
2454165.5854	-4410.5	0.0273	-4410.5	0.0081	0.0002	SWASP
2454166.5956	-4408.0	0.0210	-4408.0	0.0018	0.0002	SWASP
2454167.4047	-4406.0	0.0169	-4406.0	-0.0022	0.0003	SWASP
2454167.6091	-4405.5	0.0180	-4405.5	-0.0012	0.0002	SWASP
2454168.4249	-4403.5	0.0206	-4403.5	0.0014	0.0002	SWASP
2454169.4407	-4401.0	0.0199	-4401.0	0.0008	0.0002	SWASP
2454169.6348	-4400.5	0.0107	-4400.5	-0.0084	0.0003	SWASP
2454170.4574	-4398.5	0.0201	-4398.5	0.0010	0.0002	SWASP
2454171.4745	-4396.0	0.0207	-4396.0	0.0016	0.0002	SWASP
2454194.4505	-4339.5	0.0238	-4339.5	0.0049	0.0002	SWASP
2454195.4645	-4337.0	0.0213	-4337.0	0.0024	0.0002	SWASP
2454204.4064	-4315.0	0.0180	-4315.0	-0.0008	0.0002	SWASP
2454206.4388	-4310.0	0.0174	-4310.0	-0.0014	0.0002	SWASP
2454208.4718	-4305.0	0.0174	-4305.0	-0.0014	0.0002	SWASP
2454210.5040	-4300.0	0.0166	-4300.0	-0.0022	0.0002	SWASP
2454219.4457	-4278.0	0.0131	-4278.0	-0.0056	0.0002	SWASP
2455958.8674	0.0	0.0000	0.0	-0.0059	0.0001	Diethelm (2012)
2455996.4842	92.5	0.0063	92.5	0.0007	-	Hubscher et al. (2013)
2456011.7308	130.0	0.0054	130.0	-0.0001	-	Diethelm (2012)
2456014.5747	137.0	0.0031	137.0	-0.0024	-	Hubscher et al. (2013)
2456740.3549	1922.0	0.0023	1922.0	0.0021	-	Juryšek et al. (2017)
2456744.6271	1932.5	0.0052	1932.5	0.0051	-	Hubscher & Lehmann (2015)

TABLE 1. CONTINUED

HJD	Epoch$_{(1)}$	O-C$_{(1)}$	Epoch$_{(2)}$	O-C$_{(2)}$	Error	Source
2456746.4543	1937.0	0.0027	1937.0	0.0026	-	Juryšek et al. (2017)
2458163.4530	5422.0	0.0004	5422.0	0.0107	-	Lienhard (2018)
2458240.7039	5612.0	-0.0027	5612.0	0.0082	-	This paper

TABLE 2

TIMES OF MINIMA FOR CZEV188

HJD	Epoch$_{(4)}$	O-C$_{(4)}$	Error	Source
2457936.8949	7224.5	-0.0009	0.0002	This paper
2458281.8967	8619.0	0.0007	0.0020	This paper

TABLE 3

TIMES OF MINIMA FOR CRTS J073333.0+302556

HJD	Epoch$_{(5)}$	O-C$_{(5)}$	Error	Source
2457771.8063	0.0	-0.0006	0.0021	This paper
2457781.7049	37.0	0.0015	0.0015	This paper
2457787.8544	60.0	-0.0009	0.0044	This paper

for several fixed values of the mass-ratio q using as adjustable parameters the inclination of the systems i, the mean temperature of the secondaries T_2, the surface potentials Ω_1=Ω_2 for the contact systems, but Ω_1 and Ω_2 individually for the detached one, and the monochromatic luminosities of the primaries L_1. The behavior of the q-search for all the systems is shown in Figure 2.

The value of q corresponding to the minimum of Σ (the mean residuals for input data) was included in the list of the adjustable parameters and a more detailed analysis was performed simultaneously for all the available light curves for AF LMi and CzeV188 and separately for the light curves of CRTS J073333.0+302556. The amplitude of the light curve of CRTS J073333.0+302556 decreases with the increase of the wavelength: 0.44 mags in the B filter, 0.30 in the V filter and 0.22 in the R filter, suggesting an increase in the contribution of the cooler (secondary) component to the system's total light (Zakirov & Shevchenko 1982). The strong wavelength dependency of the primary minima of CRTS J073333.0+302556 prevent us from dealing simultaneously with the light curves. Moreover, the light curves were treated with the Iglewicz and Hoaglin's test (Iglewicz & Hoaglin 1993) in order to exclude some deviating points.

For all the three systems, it was necessary to add a spot on the surface of one component to obtain a best fit of the data.

The WD code provides the "probable" errors of the adjustable parameters, which are derived by

TABLE 4

LIGHT CURVES SOLUTION FOR AF LMI AND CZEV188

	AF LMi	Error	CzeV188	Error
i (°)	76.085	0.578	73.879	0.578
T_1 (K)	5700	fixed	5270	fixed
T_2 (K)	5379	57	5152	86
$\Omega_1 = \Omega_2$	8.103	0.287	8.763	0.116
q	4.300	0.115	4.760	0.087
f	0.296	0.012	0.162	0.009
L_{1B}	0.263	0.020	0.210	0.009
L_{2B}	0.677	0.013	0.734	0.001
L_{1V}	0.249	0.011	0.206	0.006
L_{2V}	0.685	0.012	0.743	0.001
L_{1R}	0.242	0.012	0.203	0.003
L_{2R}	0.700	0.008	0.747	0.001
L_{1I}	0.243	0.010	0.201	0.001
L_{2I}	0.705	0.007	0.753	0.001
Primary				
r (pole)	0.2540	0.0007	0.2418	0.0007
r (side)	0.2658	0.0008	0.2523	0.0008
r (back)	0.3087	0.0017	0.2899	0.0016
Secondary				
r (pole)	0.4856	0.0004	0.4887	0.0004
r (side)	0.5289	0.0005	0.5235	0.0006
r (back)	0.5557	0.0007	0.5570	0.0008
lat spot (°)	74.21	1.5	79.58	1.7
long spot (°)	226.43	1.1	301.33	0.8
Radius (°)	17.56	0.5	30.15	0.7
Temp. Fact.	0.91	0.06	0.97	0.03
Star	2		1	
Σ	0.001795		0.000769	

the differential correction routine. It is known that they are unrealistically small. With the purpose of obtaining an independent estimate of the uncertainties of these parameters, we approached the problem through the Markov Chain Monte Carlo (MCMC) procedure. We generated many different data samples of the free parameters; the correlations among them from MCMC simulations and histograms of individual parameter distributions for AF LMi, CzeV188 and CRTS J073333.0+302556 are shown in Figures. 3 - 5.

The final light curve solutions, with the uncertainties derived from the MCMC procedure are reported in Tables 4 and 5, while in Figure 6 we present the filtered solution curves overlaying the data and the geometrical surface representations of the systems respectively.

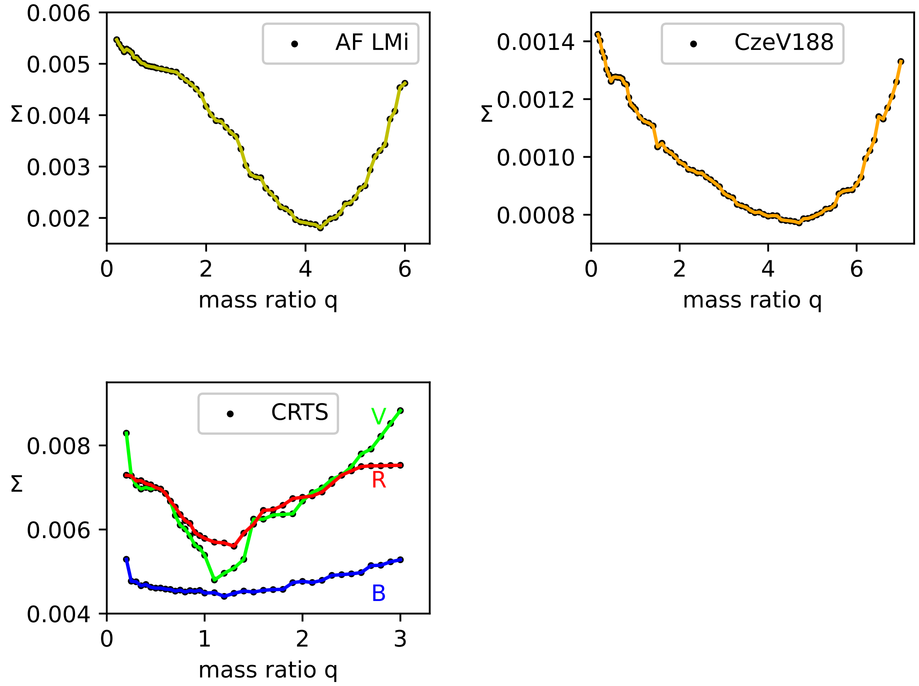

Fig. 2. The relation Σ (the mean residuals for input data) versus mass-ratio q. The color figure can be viewed online.

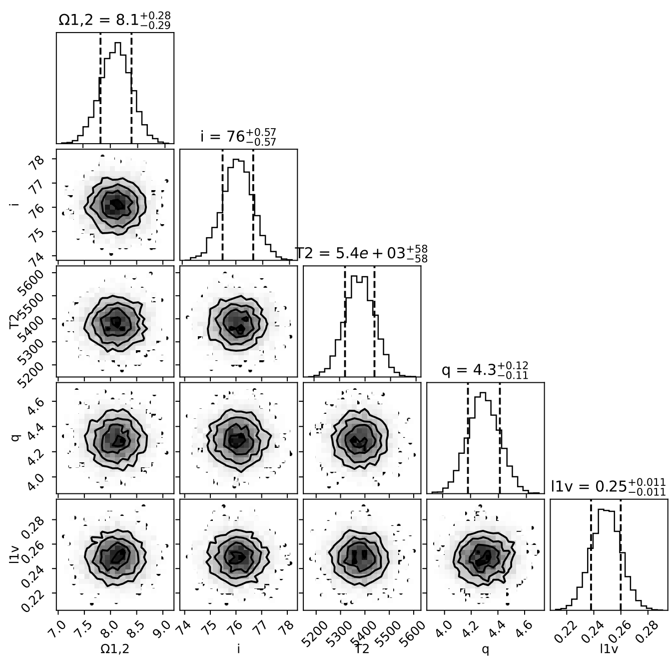

Fig. 3. Parameter correlations resulting from MCMC fit and histograms of individual parameter distributions for AF LMi.

5. ESTIMATION OF THE PHYSICAL PARAMETERS OF AF LMI AND CZEV188 WITH THE GAIA PARALLAX

Physical parameters such as mass, radius and luminosity are very important information for a contact binary system. Here we will introduce how we have estimated the physical parameters of AF LMi and CzeV188, without knowing their radial velocity curves, by using the parallaxes reported by Gaia (Gaia Collaboration et al. 2018). First, we

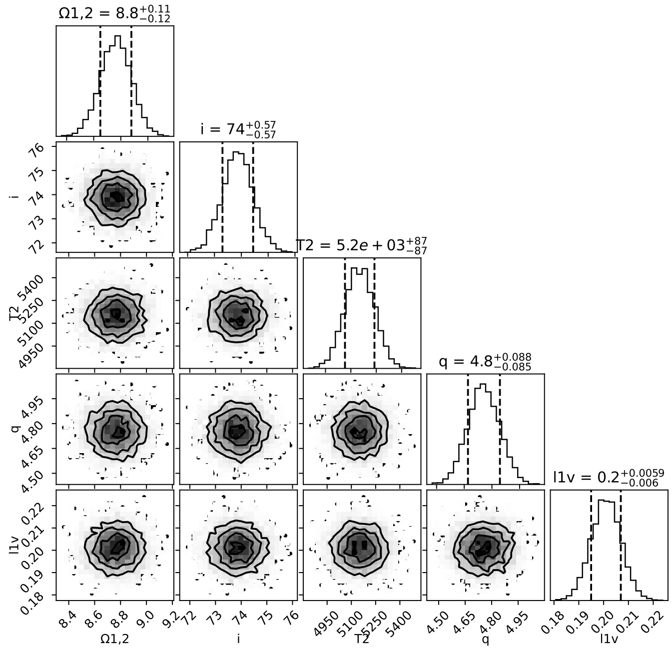

Fig. 4. The same of Figure 3 but for CzeV188.

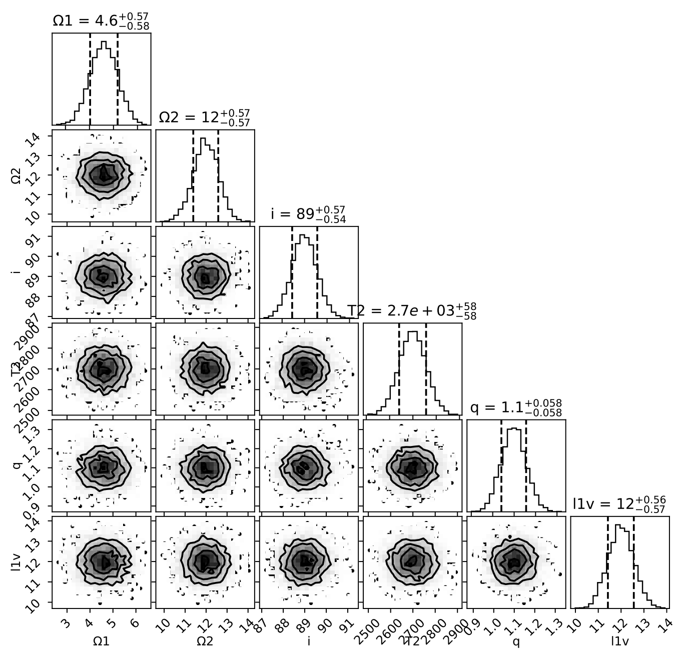

Fig. 5. The same of Figure 3 but for CRTS J073333.0+302556 in V Filter.

calculated the Galactic extinction using two different methods: for AF LMi ($A_v = 0.1892$) the spiral model from Amôres & Lépine (2005) using the code GALEextin.[8] For CzeV188 ($A_v = 0.7285$) we used the methodology of Arenou et al. (1992) since its galactic latitude is between -5° < b < +5°.

[8]http://www.galextin.org/interstellar_extinction.php.

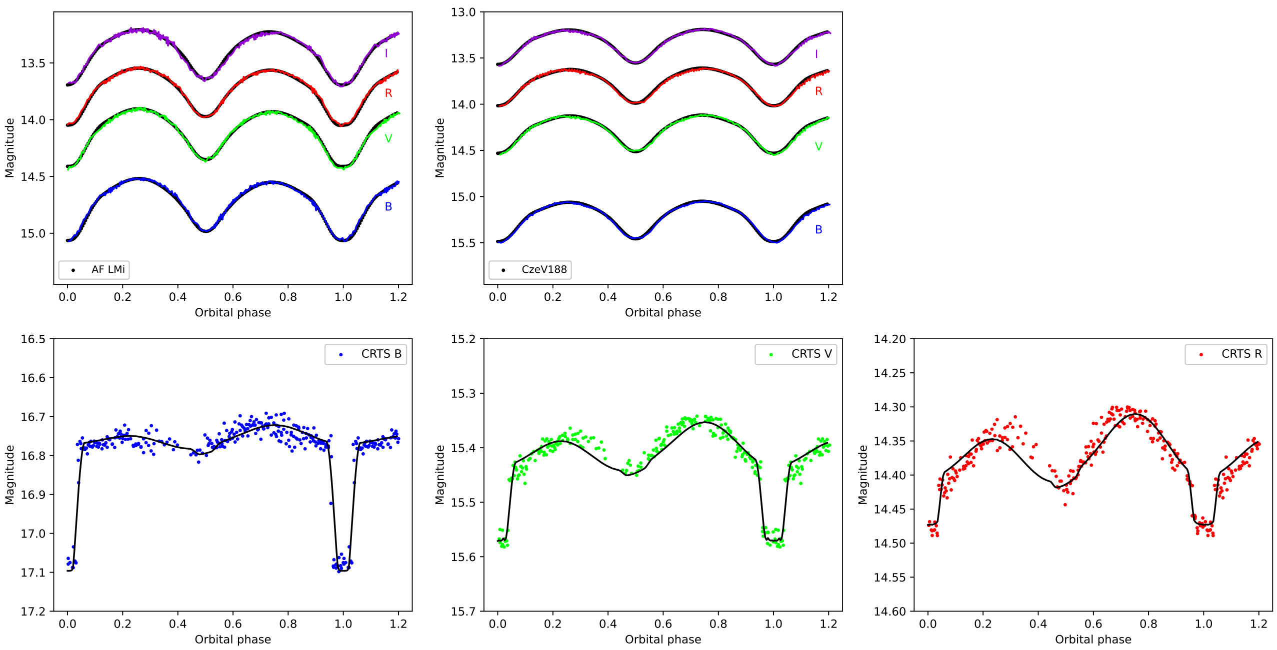

Fig. 6. CCD light curves for the three systems. Points are the original observations, color lines are the theoretical light curves. The color figure can be viewed online.

Knowing the parallax from Gaia, AF LMi p[mas] 0.986±0.017 and distance d_{pc} 1014.2±0.017, CzeV188 p[mas] 2.260±0.013 and d_{pc} 442.46±3.60, we calculated the visual absolute magnitude M_v, the bolometric magnitude M_{bol}, the total luminosity L_{tot} and the individual luminosities $L_{1,2}$ with the following equations (e.g. Chen et al. 2018):

$$M_v = m_v - 5\log(1000/\pi) + 5 - A_v \,, \tag{6}$$

where m_v is the dereddened V magnitude.

$$M_{bol} = M_v + BC \,. \tag{7}$$

Here BC is the star's bolometric correction as interpolated from the Pecaut & Mamajek (2013) tables.

$$\log(L_{tot}/L_\odot) = 0.4(4.74 - M_{bol}) \,, \tag{8}$$

$$L_1 = L_{tot}/(c) \,, \tag{9}$$

where $c = \mathrm{L}_{2V}/\mathrm{L}_{1V}$, see Table 4

$$L_2 = L_{tot} - L_1 \,. \tag{10}$$

The temperatures of the first and second component of the system are known, so we obtained their radii $\mathrm{R}_{1,2}$, the semiaxis, a, and the total mass of the systems from Kepler's third law.

$$R_{1,2}[R_\odot] = L_{1,2}^{(1/2)}/(T_{1,2}/[T_\odot])^2 \,, \tag{11}$$

where $[T_\odot] = 5771.8\mathrm{K}$.

$$a = R_1/r_{1mean}$$

$$M_{tot} = 0.0134(a^3/P^2) \,, \tag{12}$$

where P is the period in days.

Using the value of the mass ratio from the Wilson-Devinney analysis, finally we obtained the masses M_1 and M_2. The values of all parameters are shown in Table 6.

6. ESTIMATION OF THE ABSOLUTE ELEMENTS OF CRTS J073333.0+302556

Due to the lack of radial velocity (RV) solutions, we used empirical relations to determine the absolute parameters of the binary systems. Dimitrov & Kjurkchieva (2015) gave a period - semi-major axis (P,a) relation on the basis of 14 binary stars having $P < 0.27$d which had both RV and photometric solutions, which is approximated by a parabola:

$$a = -1.154 + 14.633 \times P - 10.319 \times P^2,$$

where P is in days and a is in solar radii.

Using the semi-major axis, we can calculate the radii of the binary components as $R_{1,2} = a \times r_{1,2}$ mean, where $r_{1,2}$ mean is the mean fractional radii of the components. Considering a solar temperature of

TABLE 5

LIGHT CURVES SOLUTION FOR CRTS J073333.0+302556

	B Filter	Error	V Filter	Error	R Filter	Error
i (°)	89.204	0.478	89.384	0.577	89.527	0.848
T_1 (K)	4027	fixed	4027	fixed	4027	fixed
T_2 (K)	2903	19	2748	57	2760	8
Ω_1	5.394	0.176	4.602	0.577	4.827	0.105
Ω_2	10.697	1.118	12.004	0.577	19.077	0.506
q	1.2068	0.0068	1.0863	0.0577	1.2961	0.0026
f_1	-0.246	0.007	-0.146	0.004	-0.117	0.008
f_2	-0.600	0.009	-0.660	0.010	-0.764	0.006
L_{1B}	12.177	0.006				
L_{2B}	0.139	0.003				
L_{1V}			12.079	0.573		
L_{2V}			0.071	0.002		
L_{1R}					12.167	0.008
L_{2R}					0.071	0.003
Primary						
r (pole)	0.2354	0.0117	0.2818	0.0085	0.2795	0.0088
r (side)	0.2390	0.0125	0.2887	0.0095	0.2869	0.0098
r (back)	0.2445	0.0140	0.2994	0.0112	0.2996	0.0119
Secondary						
r (pole)	0.1223	0.0140	0.0982	0.0050	0.0711	0.0020
r (side)	0.1225	0.0141	0.0983	0.0051	0.0711	0.0020
r (back)	0.1228	0.0142	0.0984	0.0051	0.0712	0.0020
lat spot (°)	90	fixed	90	fixed	90	fixed
long spot (°)	250.56	1.9	250.34	2.1	250.78	1.7
Radius (°)	25.68	1.3	25.44	0.9	25.12	1.3
Temp. Fact.	0.98	0.04	0.97	0.03	0.97	0.06
Star	1		1		1	

$T_\odot = 5771.8$ K, the luminosities can be calculated using the equation: $L_{1,2} = (R_{1,2}/R_\odot)^2 \times (T_{1,2}/T_\odot)^4$. The mean densities of the binary components were derived from the following equation given by Mochnacki (1981): $\rho_1 = 0.0189/[r^3_{1mean}P^2(1+q)]$ and $\rho_2 = 0.0189q/[r^3_{2mean}P^2(1+q)]$.

All the above calculated values are listed in Table 7.

The results here presented for CRTS J073333.0+302556 are a preliminary solution.

7. DISCUSSION ON THE SYSTEMS

Here we have presented the analysis of filtered CCD light curves of two contact binary systems. For both we calculated the orbital angular momentum J_0 (Eker et al. 2006) and their position in the $\log J_0 - \log M$ diagram. With a value of $\log J_0$ as reported in Table 6, the systems are beyond the curved limit separating the detached and contact systems, in the region of the contact stars, which supports the shallow-contact geometric situation (Figure 8). From Figure 1, the trend of O-C (solid line) shows parabolic compositions with a rate of $dP/dt = 3.61 \times 10^{-7} \pm 7.41^{-8}$ days year^{-1}. This long-term increase can probably be explained by the mass transfer from the less massive star to the more massive star. Then, if we assume conservative mass transfer, the following equation can be used to calculate the mass transfer between the components of AF LMi:

$$\dot{P}/P = -3\dot{M}_1(1/M_1 - 1/M_2). \qquad (13)$$

Combining the parameters (including mass, period and rate of period variation) the rate of mass transfer was determined as

$$dM_1/dt = -1.97 \times 10^{-7} M_\odot \text{ years}^{-1}.$$

TABLE 6

ESTIMATED ABSOLUTE ELEMENTS FOR AF LMI AND CZEV188

Target	$L_1(L_\odot)$	$L_2(L_\odot)$	$R_1(R_\odot)$	$R_2(R_\odot)$	a $(R_\odot)$	$M_1(M_\odot)$	$M_2(M_\odot)$
AF LMi	0.752 ± 0.029	2.064 ± 0.120	0.889 ± 0.017	1.654 ± 0.054	3.219 ± 0.074	0.510 ± 0.170	2.193 ± 0.060
CzeV188	0.267 ± 0.009	0.960 ± 0.034	0.620 ± 0.011	1.230 ± 0.022	2.372 ± 0.042	0.507 ± 0.026	2.413 ± 0.012
	J	$\log J$	J_{lim}	$\log J_{lim}$	Sp. type	$\log \rho_1$(gr/cm^3)	$\log \rho_2$(gr/cm^3)
AF LMi	7.38^{51}	51.87	52.14	1.37^{52}	G3 + G9	0.01	-0.19
CzeV188	6.66^{51}	51.82	52.12	1.62^{52}	K0 + K1	0.48	0.25

Note: Spectral types are according to Pecaut & Mamajek (2013).

TABLE 7

ESTIMATED ABSOLUTE ELEMENTS FOR CRTS J073333.0+302556 (V FILTER)

$L_1(L_\odot)$	$L_2(L_\odot)$	$R_1(R_\odot)$	$R_2(R_\odot)$	a $(R_\odot)$	$M_1(M_\odot)$	$M_2(M_\odot)$
0.084 ± 0.003	0.002 ± 0.001	0.595 ± 0.011	0.199 ± 0.073	2.022 ± 0.001	0.742 ± 0.002	0.891 ± 0.005
J	$\log J$	J_{lim}	$\log J_{lim}$	Sp. type	$\log \rho_1$(gr/cm^3)	$\log \rho_2$(gr/cm^3)
4.13^{51}	51.62	55.21	1.63^{55}	K8 + M6	0.70	2.16

Note: Spectral types are according to Pecaut & Mamajek (2013).

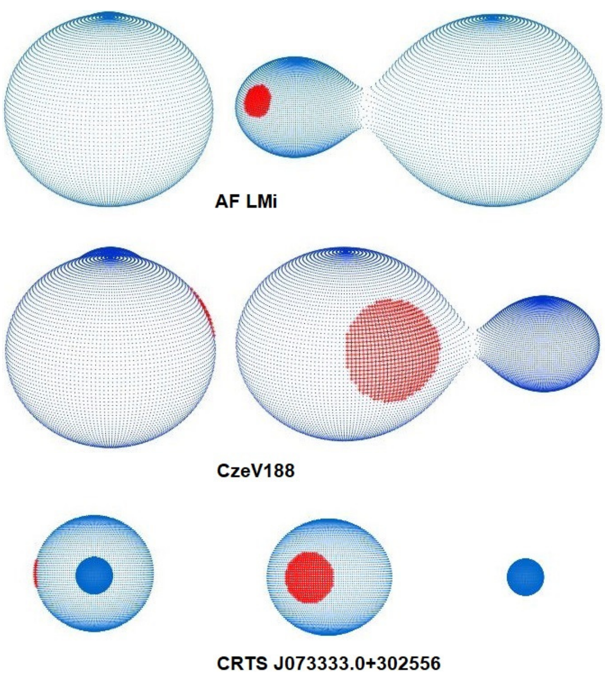

Fig. 7. The 3D view of the stars. Left at the primary minimum, right at the quadrature. The color figure can be viewed online.

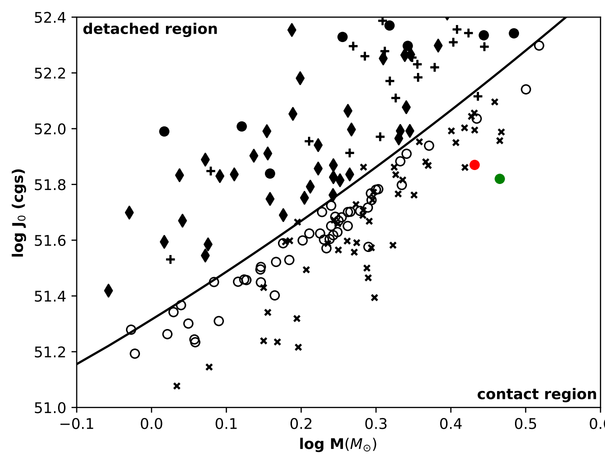

Fig. 8. Position of AF LMi (red dot) and CzeV188 (green dot) in the $\log J_0 - \log M$ diagram. As explained in Figure 1 of the original paper of Eker et al. (2006) symbols mean: Giants (•), Sub-Giants (+), Main-Sequence (♦), A-subtype (×), W-subtype (○). The color figure can be viewed online.

The negative sign indicates that the less massive component M_1 is losing mass, while the more massive component M_2 is gaining mass. As the mass ratio increases, so does the separation between the two components. The degree of contact would decrease, and AF LMi will evolve from the present contact state to the semi-contact or detached binary state.

Because the sums of the mean fractional radii of the components are $r_{mean} = 0.799$ and $r_{mean} = 0.784$, for AF LMi and CzeV188 respectively, they are in a state of marginal contact (Kopal, 1959).

7.1. *AF LMi and CzeV188*

The values of mass ratio found for AF LMi and CzeV188 indicate that they are typical W-subtype contact binaries. A-and W-subtype are two groups of the W UMa systems divided in these subclasses by Binnendijk(1965, 1970). In the A-subtype systems the larger star is the hottest and the primary eclipse is a transit. In W-type the opposite is true: the smaller star is the hottest and the primary eclipse is an occultation. Both types of systems have a shallow fill-out value and a small difference in temperature between the components, i.e good thermal contact, these characteristics are generally accepted for over-contact systems. The O'Connell effect (O'Connell 1951) that explains the different heights of the maxima, is visible; a cool spot on the secondary component of AF LMi and a cool spot on the primary component of CzeV188 (inverse O'Connell effect) were added to obtain the best fit to the light curves. The cool spot, in contrast to the hot spot, is connected with magnetic activity of the same nature as solar magnetic spots (Mullan 1975); the hot spot is generally due to the impact of the mass transferred between the components (Lee et al. 2006). CzeV188, with its short orbital period (<0.3 days) and its spectral type K, suggests that it is near the shortest period limit. Following the work of Qian et al. (2020), who investigated in detail the period-temperature relation using the LAMOST stellar atmospheric parameters and constructed the heat map for this relation as shown in our Figure 9 (Figure 4 in the original paper), it is possible to see that AF LMi (red dot) and CzeV188 (green dot) in this graph are located inside the boundaries for normal EW systems, but with different positions. In fact, the red and blue lines are the boundaries of the normal EW systems. Near the red line are found marginal contact systems, while those close to the blue line are deep contact ones. The objects between the two lines are normal contact EW systems.

AF LMi, with its fill-out factor and the difference in temperature between its component of some hundreds of K, is located near the red border, indicating that it could be either at the end or at the beginning of the contact phase, as predicted by the TRO theory. CzeV188 shows good thermal contact since the difference in temperature between the components is less than 100K. It is located far from the red border and near the blue one. This suggests that it is approaching the final stage of contact binary evolution.

7.2. *CRTS J073333.0+302556*

CRTS J073333.0+302556 is a rare M dwarf detached system with non-degenerate components. As discussed in Becker et al. (2011), the sample of known binary systems composed of two dwarfs is

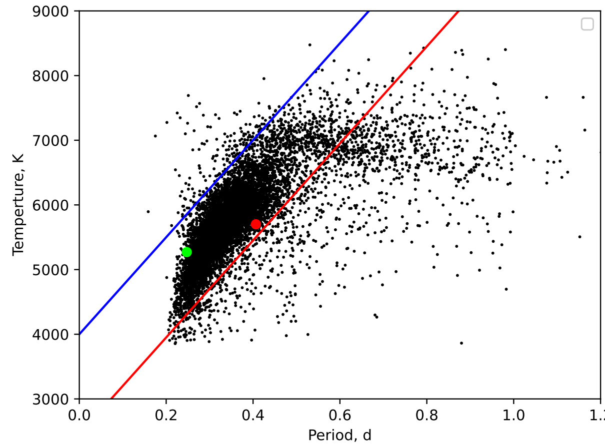

Fig. 9. Correlation between orbital period and temperature based on parameters of 8510 contact binaries from Qian et al. (2020). The position of AF LMi is marked in red, the one of CzeV188 in green. The red and blue lines are the boundaries of normal EWs. The color figure can be viewed online.

very small. Its light curve shows a strong wavelength dependency at the primary minima. The amplitude of the light curve decreases with increasing wavelength; this suggest an increase in the contribution of the cooler (secondary) component to the system's total light (Zakirov & Shevchenko 1982). Also visible is the shallower secondary eclipse, which becomes deeper in the redder bands. In addition it is seen that there is a small difference in the height of the maxima with the secondary higher than the primary, so it was necessary to add a cool spot on the surface of the first component in order to account for this characteristic.

A graphical representation and the Roche geometry of CRTS J073333.0+302556 is depicted in Figure 7.

This work has made use of data from the European Space Agency (ESA) mission Gaia, [9] and processed by the Gaia Data Processing and Analysis Consortium (DPAC).[10]

Use of the International Variable Star Index (VSX) database has been made (operated at AAVSO Cambridge, Massachusetts, USA), as well as of the AAVSO Photometric All-Sky Survey (APASS) funded by the Robert Martin Ayers Sciences Fund. Also, use has been made of the VizieR catalogue access tool, CDS, Strasbourg, France. The original

[9] https://www.cosmos.esa.int/gaia.

[10] https://www.cosmos.esa.int/web/gaia/dpac/consortium.

description of the VizieR service was published in A&AS 143, 23.

Based upon observations carried out at the Observatorio Astronómico Nacional on the Sierra San Pedro Mártir (OAN-SPM), Baja California, México.

We would like to thank the anonymous referee for all her/his very useful comments and corrections which have improved the quality of this paper.

REFERENCES

Amôres, E. B. & Lépine, J. R. D. 2005, AJ, 130, 659, https://doi.org/10.1086/430957

Arenou, F., Grenon, M., & Gomez, A. 1992, A&Ap, 258, 104

Bai, Y., Liu, J., Bai, Z., Wang, S., & Fan, D. 2019, AJ, 158, 93

Becker, A. C., Bochanski, J. J., Hawley, S. L., et al. 2011, ApJ, 731, 17, https://doi.org/10.1088/0004-637X/731/1/17

Binnendijk, L. 1965, VeBam, 27, 36

__________. 1970, VA, 12, 217, https://doi.org/10.1016/0083-6656(70)90041-3

Butters, O. W., West, R. G., Anderson, D. R., et al. 2010, A&Ap, 520, 10, https://doi.org/10.1051/0004-6361/201015655

Chen, X., Deng, L., de Grijs, R., Wang, S., & Feng, Y. 2018, ApJ, 859, 140, https://doi.org/10.3847/1538-4357/aabe83

Claret, A. & Bloemen, S. 2011, A&Ap, 529, 75, https://doi.org/10.1051/0004-6361/201116451

Diethelm, R. 2012, IBVS, 6029, 1

Dimitrov, D. P. & Kjurkchieva, D. P. 2015, MNRAS, 448, 2890, https://doi.org/10.1093/mnras/stv147

Drake, A. J., Graham, M. J., Djorgovski, S. G., et al. 2014, ApJS, 213, 9, https://doi.org/10.1088/0067-0049/213/1/9

Eker, Z., Demircan, O., Bilir, S., & Karataş, Y. 2006, MNRAS, 373, 1483, https://doi.org/10.1111/j.1365-2966.2006.11073.x

Flannery, B. P. 1976, ApJ, 205, 217, https://doi.org/10.1086/154266

Fukugita, M., Ichikawa, T., Gunn, J. E., et al. 1996, AJ, 111, 1748, https://doi.org/10.1086/117915

Gaia Collaboration, Brown, A. G. A., Vallenari, A., et al. 2018, A&Ap, 616, 1, https://doi.org/10.1051/0004-6361/201833051

Hubscher, J., Braune, W., & Lehmann, P. B. 2013, IBVS, 6048, 1

Hubscher, J. & Lehmann, P. B. 2015, IBVS, 6149, 1

Juryšek, J., Hoňková, K., Šmelcer, L., et al. 2017, OEJV, 179, 1

Kochanek, C. S., Shappee, B. J., Stanek, K. Z., et al. 2017, PASP, 129, 104502, https://doi.org/10.1088/1538-3873/aa80d9

Kopal, Z. 1959, Close Binary Systems, The International Astrophysics Series (London: Chapman & Hall)

Khruslov, A. V. 2007, PZP, 7, 6

Iglewicz, B., & Hoaglin, D., 1993, The ASQC Basic References in Quality Control: Statistical Techniques in How to Detect and Handle Outliers, ed. E. F. Mykytka (Milwaukee, WI: ASQC Quality Press)

Gaia Collaboration. 2018, VizieR Online Data Catalog, I/345

Landolt, A. U. 2009, AJ, 137, 4186, https://doi.org/10.1088/0004-6256/137/5/4186

Lee, J.-W., Lee, C.-U., Kim, C.-H., & Kang, Y.,-W. 2006, JKAS, 39, 41, https://doi.org/10.5303/JKAS.2006.39.2.041

Li, L., Zhang, F., Han, Z., Jiang, D., & Jiang, D. 2008, MNRAS, 387, 97, https://doi.org/10.1111/j.1365-2966.2008.12736.x

Lienhard, P. 2008, BAV Journal, 31, 19

Liu, N.-P., Qian, S.-B., Soonthornthum, B., et al. 2014, AJ, 147, 41, https://doi.org/10.1088/0004-6256/147/2/41

Lucy, L. B. 1976, ApJ, 205, 208, https://doi.org/10.1086/154265

Luo, A.-L., Zhao, Y.-H., Zhao, G., et al. 2016, VizieR Online Data Catalog, V/149

__________. 2019, VizieR Online Data Catalog, V/164

Marsh, F. M., Prince, T. A., Mahabal, A. A., et al. 2017, MNRAS, 465, 4678, https://doi.org/10.1093/mnras/stw2110

Milano, L. & Russo, G. 1983, MNRAS, 203, 235, https://doi.org/10.1093/mnras/203.2.235

Mochnacki, S. W. 1981, ApJ, 245, 650, https://doi.org/10.1086/158841

Mullan, D. J. 1975, ApJ, 198, 563, https://doi.org/10.1086/153635

O'Connell, D. J. K. 1951, Publications of the Riverview College Observatory, 2, 85

Pecaut, M. J. & Mamajek, E. E. 2013, ApJS, 208, 9, https://doi.org/10.1088/0067-0049/208/1/9

Qian, S.-B., Zhu, L.-Y., Liu, L., et al. 2020, RAA, 20, 163, https://doi.org/10.1088/1674-4527/20/10/163

Robertson, J. A. & Eggleton, P. P. 1977, MNRAS, 179, 359, https://doi.org/10.1093/mnras/179.3.359

Shappee, B. J., Prieto, J. L., Grupe, D., et al. 2014, ApJ, 788, 48, https://doi.org/10.1088/0004-637X/788/1/48

Skarka, M., Mašek, M., Brát, L., et al. 2017, OEJV, 185, 1

Svechnikov, M. A. & Taidakova, T. A. 1984, SvA, 28, 84

Tonry, J. L., Denneau, L., Flewelling, H., et al. 2018, ApJ, 867, 105, https://doi.org/10.3847/1538-4357/aae386

van Hamme, W. 1993, AJ, 106, 2096, https://doi.org/10.1086/116788

Wilson, R. E. & Devinney, E. J. 1971, ApJ, 166, 605, https://doi.org/10.1086/150986

Wilson, R. E. 1990, ApJ, 356, 613, https://doi.org/10.1086/168867

__________. 1994, PASP, 106, 921, https://doi.org/10.1086/133464

Wilson, R. E. & van Hamme, W. 2016, Computing Binary Stars Observables. <ftp.astro.ufl.edu>, directory pub/wilson/lcdc2015

Worthey, G. & Lee, H.-ch. 2011, ApJS, 193, 1, https://doi.org/10.1088/0067-0049/193/1/1

Yakut, K. & Eggleton, P. P. 2005, ApJ, 629, 1055, https://doi.org/10.1086/431300

Zakirov, M. M. & Shevchenko, V. S. 1982, PZ, 21, 629

F. Acerbi: Via Zoncada 51, Codogno, LO, 26845, Italy (acerbifr@tin.it).

L. Altamirano-Dévora: Carretera Tijuana-Ensenada 3917, 22860 Ensenada, BC, Mexico (altamirano.l18@gmail.com).

C. Barani: Via Molinetto 35, Triulza di Codogno, LO, 26845, Italy (cvbarani@alice.it).

M. Martignoni: Via Don G. Minzoni 26/D, Magnago, MI, 20020, Italy (massimiliano.martignoni@outlook.it).

R. Michel: Instituto de Astronomia, UNAM. A.P. 877, 22800 Ensenada, BC, Mexico (rmm@astro.unam.mx).

Revista Mexicana de Astronomía y Astrofísica, **59**, 137–150 (2023)

https://doi.org/10.22201/ia.01851101p.2023.59.01.10

PHOTOMETRIC ANALYSIS OF ECLIPSING BINARIES: VY UMI, RU UMI AND GSC 04364-00648

V. Kudak[1], Š.Parimucha[2], V. Perig[1], and P. Gajdoš[2]

Received June 15 2022; accepted February 13 2023

ABSTRACT

We present the photometric analysis of *BVR* and *TESS* light curves of three eclipsing binaries, together with their period changes considering archival data and new minima times from our and *TESS* observations. For the first time we detected wave-like variations with low-amplitude in $O-C$ residua of RU UMi, which can be interpreted as a consequence of the light-time effect caused by the 3rd component with period 7370 days. The period increase detected in the VY UMi system corresponds to mass transfer from the secondary to the primary component. For the GSC 04364-00648 binary system we find quadratic changes on the $O-C$ diagram, which correspond to a period decrease. We cannot make assumptions about their nature, mainly due to short time of observation and uneven coverage of $O-C$ diagram. We also determined the absolute parameter of their components using the photometric solution and *GAIA* distances.

RESUMEN

Presentamos el análisis fotométrico de las curvas de luz *BVR* y *TESS*, y de los cambios de período de tres binarias eclipsantes, a partir de datos de archivo y nuevos datos de los mínimos de nuestras observaciones y de *TESS*. Detectamos por primera vez variaciones ondulatorias de baja amplitud en los residuos $O-C$ de RU UMi, que pueden ser consecuencia del efecto de tiempo de luz causado por la tercera componente, con un período de 7370 días. El aumento del período en VY UMi corresponde a la transferencia de masa de la secundaria a la primaria. En GSC 04364-00648 encontramos cambios cuadráticos en el diagrama $O-C$, que corresponden a una disminución del período. No podemos proponer hipótesis sobre su naturaleza debido al corto tiempo de observación y a la cobertura inhomogénea en el diagrama $O-C$. Determinamos los parámetros absolutos de las componentes mediante la solución fotométrica y las distancias de *GAIA*.

Key Words: binaries: close — binaries: eclipsing — stars: individual: RU UMi, VY UMi, GSC 04364-00648 — stars: mass-loss

1. INTRODUCTION

Eclipsing binary stars are systems where the components are mutually obscured for the observer during their motion around a common centre of mass. It is a very important group of variable stars with specific and well-recognized light-curves, whose shapes depend on the physical properties of the components and their geometrical configuration (Hilditch 2001; Prša 2018; Čokina et al. 2021).

Analysis of light-curves of eclipsing binaries can reveal, among other aspects, the relative dimensions of stars, their effective temperatures, orbital inclination, the eccentricity of the orbit, and potential spots on their surfaces. Together with radial velocities obtained from spectroscopic observations, we can determine the masses of the components, their radii and luminosities, and the dimension of their orbit. These parameters can be also estimated if we know the distance and the amount of interstellar extinction to the stars.

The shapes of the components in binary stars are described by Roche geometry (e.g Prša 2018). Ac-

[1]Laboratory of space researches, Uzhhorod National University, Uzhhorod, Ukraine.
[2]Institute of Physics, Faculty of Science, P.J. Šafárik University, Košice, Slovakia.

cording to this, three configurations of binaries are possible: detached (both components are in their Roche lobes), semidetached (one component fills its Roche lobe), and contact, where both components overfill their Roche lobes. All this is reflected in the light-curves and also has other observational consequences, like a period change due to mass transfer, angular momentum loss (e.g. Yang et al. 2009) and/or magnetic braking (Applegate 1992).

We now know more than 500 000 eclipsing binaries (Watson et al. 2006), and in the era of large photometric surveys (e.g. Ivezić et al. 2019) one can expect the discovery of several million new eclipsing binaries. But only a very small fraction of them (less than 1%) have calculated parameters. It is a big challenge for data analysis in the near future.

In this paper, we want to make a small contribution to the knowledge of eclipsing binary stars by a photometry study and period analysis of three eclipsing binaries; two of them were not studied in detail up to now in the literature, while for 3rd we indicate the possible presence of a 3rd body according to the $O-C$ diagram.

RU UMi (TYC 4402-504-1) was for the first time mentioned as an eclipsing binary of Algol type by Strohmeier & Bauernfeind (1968). They analysed sky-patrol plates taken from 1931 through 1959. Wood (1971) presented the first photometric solution and concluded that both stars are oversize for their masses and that the object may be a contact system of W UMa type. Other photometric solutions by Nha (1973) and de Bernardi & Scaltriti (1977) suggested that the system was close to contact, while Kaluzny (1985) modeled previous data and concluded that the system was quite close to a semidetached configuration. It was supported by Okazaki et al. (1988), Bell et al. (1993) and Zhu et al. (2006). The radial velocities for the primary component were published by Okazaki et al. (1988) and for both components by Maxted & Hilditch (1996). They found that mass ratios in the range $0.32 < q < 0.40$ provide a good solution to the light curves.

Zhu et al. (2006) published $O-C$ period analysis of up to date minima times observations and suggested a continuous period decrease at a rate $dP/dt = -1.72 \times 10^{-8}\,\mathrm{d\,yr^{-1}}$ caused by a transfer of matter from the secondary to the primary component. Lee et al. (2008) explained the secular period decrease by angular momentum loss (AML) due to magnetic braking alone or, more convincingly, by a combination of AML and mass transfer from the less massive secondary to the more massive primary. The distance to the system is 283.0±1.2 pc (Babusiaux et al. 2022). RU UMi was observed in 5 sectors during *TESS* mission (Ricker 2014).

VY UMi (GSC 04568-00313) was discovered as a variable star by Strohmeier (1958). The first ephemeris for this eclipsing binary was published by Otero & Dubovsky (2004). The distance to the system is 164.5±0.3 pc (Babusiaux et al. 2022). VY UMi has no published photometric solution of the light-curve or period analysis up to now. Meanwhile, the object was observed in 13 sectors during the *TESS* mission, so it is an interesting system for our research.

GSC 04364-00648 (TYC 4364-648-1) was mentioned as a variable in the Wide-field Infrared Survey Explorer (WISE) Catalog of Periodic Variable Stars by Chen et al. (2018) with a period 0.8628506 d. The distance to the system was determined to be 512.5±4.8 pc (Babusiaux et al. 2022). The system has observations from 3 *TESS* mission sectors. No other analysis of this eclipsing binary has been published.

2. OBSERVATIONS AND DATA REDUCTION

All new CCD observations of eclipsing binary systems presented in this work were carried out at the Derenivka Observatory of Uzhhorod National University, Ukraine (Lat: 48.563 N; Long: 22.453 E, MPC code K99) and Kolonica Astronomical Observatory (KAO) of the P. J. Šafárik University, Košice, Slovakia (Lat: 48.950 N; Lon: 22.266 E). Measurements were collected from March 2021 to October 2021.

In the Derenivka Observatory, we used a 400 mm Newton-type telescope with a focal ratio of f/4.4 equipped with FLI PL9000 CCD camera array (3056×3056, pixel size $12\mu m$) with BVR Bessel photometric filters. The field of view of such configuration of the system is $1.21^\circ \times 1.21^\circ$. Observations at KAO were made by the PlaneWave CDK20 telescope with a main mirror diameter of 508 mm and a focal ratio of f/6.8 at the Cassegrain focus. The telescope is equipped with a G4-16000 CCD camera array (4096×4096, pixel size $9\mu m$) with $UBVRI$ Bessel photometric filters. The field of view of the system is $37' \times 37'$. The detailed journal of our CCD observation is given in Table 1.

The CCD images were calibrated (bias and dark subtraction, flat-field correction) utilizing the software package CoLiTecVS (Savanevych et al. 2017; Parimucha et al. 2019). This package was also used for aperture photometry, calculation of differential magnitudes according to artificial comparison stars,

TABLE 1

THE JOURNAL OF OUR CCD OBSERVATIONS

System	Date	Time(UT)	Phase[a]	Filters
RU UMi	Mar 03 21	17:24 - 23:05	0.646 - 0.097	BVR
	Sep 06 21	20:43 - 01:00	0.151 - 0.490	BVR
	Sep 09 21	17:53 - 00:48	0.640 - 0.190	BVR
	Sep 12 21	17:53 - 21:49	0.356 - 0.669	BVR
VY UMi	Mar 24 21	18:36 - 03:35	0.729 - 0.878	BVR
	Oct 28 21	16:47 - 01:12	0.430 - 0.509	BVR
	Oct 29 21[b]	18:50 - 03:03	0.767 - 0.819	BVR
GSC 04364-00648	Apr 04 21	18:28 - 03:02	0.469 - 0.883	BVR
	Apr 08 21	18:27 - 23:34	0.104 - 0.351	BVR
	Apr 10 21	18:28 - 02:47	0.422 - 0.824	BVR
	May 08 21	19:11 - 01:52	0.908 - 0.230	BVR
	Jun 08 21	20:00 - 00:51	0.875 - 0.109	BVR

[a]Phase is calculated according to ephemeris determined in § 3.
[b]Observation made at KAO.
[c]Photometrical data are available from the first author upon request.

as well as calibration to the standard photometric system. The comparison stars used for the determination of artificial ones were selected manually according to their similarity to the studied binaries (brightness, distance in the sky). This approach significantly improves the quality of photometric measurements. Due to unstable night-to-night observing conditions, the average precision of our measurements varied ≈0.01-0.05 mag in the V and R filters and ≈0.03-0.08 mag in the B filter. The comparison stars used in our study are listed in Table 2, together with their magnitudes from the NOMAD catalogue (Zacharias et al. 2004, 2005).

The resulting light-curves of all eclipsing binaries are depicted in Figure 1. The light-curves were phased according to ephemerides determined from $O-C$ variations analyzed in the next chapter. Magnitudes on Figure 1 have tiny systematic shifts according to APASS magnitudes that are comparable to the level of observation errors.

3. ANALYSIS OF PERIOD CHANGES

In our analysis of period changes of all systems we have considered all available published minima times as can be found in the $O-C$ gateway[3] as well as minima times from our (weighted averages from BVR light curves) and *TESS* observations.

Our new minima times were calculated following the phenomenological method described in Mikulášek (2015). This method gives realistic and statistically significant errors in determining minima times. Newly calculated minima times from our and *TESS* observations are listed in Tables 7-10.

Although the first minima times of RU UMi were obtained at the beginning of the previous century and cover almost the whole observed range, many of them are useless for detailed analysis. Photographic and visual estimates have a large scatter and one can expect large internal errors. We decided to use only archived photoelectric and CCD minima times obtained since 1990 and minima times determined from our CCD and *TESS* light curves. Their precision is in the range of 10^{-4} days. A weighted least-squares solution using all selected minima (weights were calculated as $1/\sigma^2$, where σ is a published or determined error of the minimum) leads to the following linear ephemeris of the RU UMi system (errors of parameters are given in parenthesis):

$$\text{Min I} = \text{HJD } 2452500.0931(4) + 0^d.52492591(9) \times E. \qquad (1)$$

This ephemeris was used to create the $O-C$ diagram displayed in Figure 2. The inspection of $O-C$ residua uncovers their low-amplitude, wave-like variations. They can be explained by the light-time effect caused by another invisible body orbiting a common center of the mass. To find the parameters of this orbit, we used the package OCFit[4] (Gajdoš & Parimucha 2019). We found a 3$^{\rm rd}$ body orbiting the eclipsing system with a period of 7370 days (about 20.2 years) on a slightly eccentric orbit. The resulting parameters of its orbit are listed in Table 3. We did not detect any secular quadratic period changes in the data used in our analysis, which contradicts the findings of Zhu et al. (2006) and Lee et al. (2008).

VY UMi has several CCD minima times published from 1999 and few visual minima times, which were omitted from our analysis. The linear ephemeris determined from a weighted least-squares solution (as in the previous case) is:

$$\text{Min I} = \text{HJD } 24552500.0090(7) + 0^d.3254048(4) \times E. \qquad (2)$$

The eclipsing binary GSC 04364-0064 has no published minima times. For our analysis we have used minima times determined from *TESS* observations and 2 of our new minima times. A weighted least-squares solution using all minima (weights were calculated as in the previous cases) leads to the linear ephemeris:

$$\text{Min I} = \text{HJD } 24559309.7281(3) + 0^d.862851(5) \times E. \qquad (3)$$

Ephemerides (2) and (3) were used to create the $O-C$ diagrams of VY UMi and GSC 04364-0064 as displayed in Figure 2. We can clearly see that, in

[3]`http://var2.astro.cz/ocgate/`.

[4]`https://github.com/pavolgaj/OCFit`.

TABLE 2

STARS USED FOR A DETERMINATION OF ARTIFICIAL COMPARISON STARS

System	Comparison stars NOMAD	Coordinates $\alpha(2000)$	$\delta(2000)$	B	V	R
RU UMi	1596-0121876	13:38:09.84	+69:41:12.9	10.8230	10.066	9.580
	1596-0122007	13:40:43.97	+69:36:34.7	9.769	9.349	9.070
	1599-0114087	13:42:10.79	+69:59:01.9	10.410	9.923	9.590
VY UMi	1666-0084341	17:16:16.99	+76:37:00.25	11.725	10.338	9.470
	1668-0086624	17:14:20.44	+76:52:34.29	11.313	10.602	10.130
	1667-0084244	17:15:37.39	+76:42:45.44	12.036	11.589	11.290
GSC	1611-0075943	07:19:59.44	+71:08:30.09	12.288	11.841	11.540
04364-0064	1610-0077383	07:19:58.36	+71:05:32.56	11.157	10.646	10.310

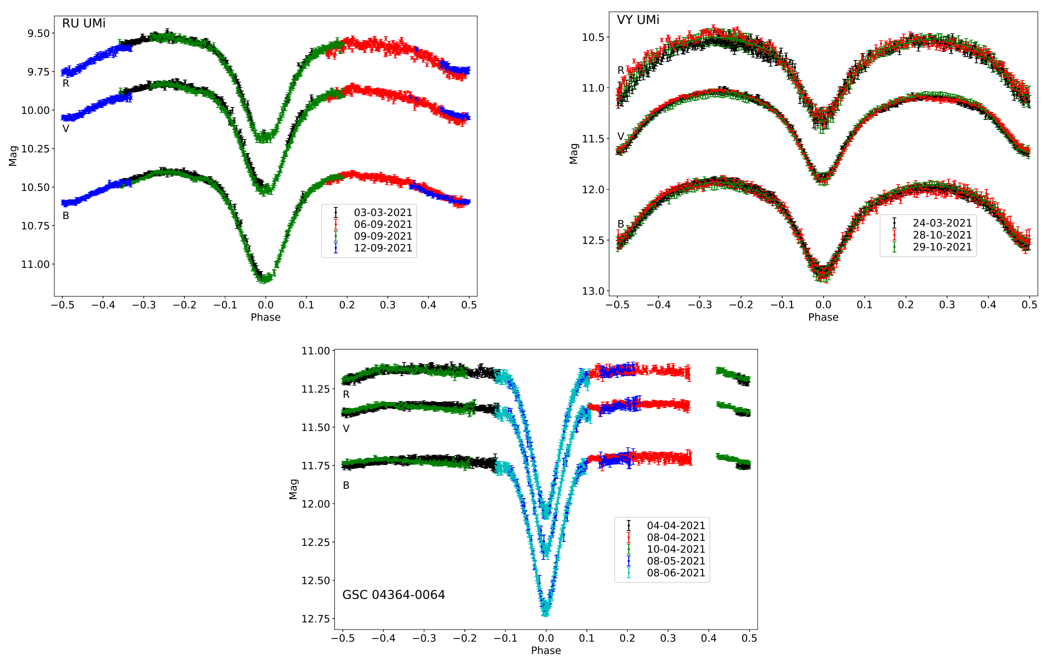

Fig. 1. Phased light curves of RU UMi, VY UMi and GSC 04364-00648 in BVR pass bands by dates of observations. The phases are calculated according to the ephemerides determined in § 3. The color figure can be viewed online.

both cases, quadratic variations are detected, which indicate mass transfer between components and/or magnetic braking. The quadratic ephemerides of both systems are given in Table 3.

4. LIGHT CURVE ANALYSIS

For the analysis of the light curves of all three systems, we have relied on the ELISa[5] code (Čokina et al. 2021). It is a cross-platform Python software package dedicated to modeling close eclipsing binaries including surface features such as spots and pulsations. ELISa utilizes modern approaches to the EB modeling with an emphasis on computational speed, while maintaining a sufficient level of precision to process a ground-based and space-based observation. It was designed for easy use even by a not very experienced user. In this paper, we take advantage of its capability to model the light curves of close eclipsing binaries with the built-in capability to solve an inverse problem using a least squares thrust region reflective algorithm and Markov Chain Monte-Carlo (MCMC) methods (for references see Čokina et al. 2021).

[5] https://github.com/mikecokina/elisa.

TABLE 3

PARAMETERS OF PERIOD CHANGES DETECTED IN THE STUDIED ECLIPSING SYSTEMS

	RU UMi	VY UMi	GSC 04364-00648
P[d]	–	0.3254004(4)	0.862839(1)
T_0	–	2452500.0469(38)	2459309.7273(2)
Q[d]	–	$1.14(3)\times10^{-10}$	$-2.67(2)\times10^{-8}$
P_3[d]	7370(42)	–	–
T_{0_3}	2458984(55)	–	–
e_3	0.199(1)	–	–
$\omega_3[^\circ]$	116(3)	–	–
$a_{12}\sin i_3$ [AU]	0.247(2)	–	–
$f(m_3)$ [$M_\odot$]	$3.69(8)\times10^{-5}$	–	–

P, T_0, Q are period, reference minimum time and quadratic term. P_3, T_{0_3}, e_3, ω_3, $a_{12}\sin i_3$ and $f(m_3)$ describe parameters of the 3rd body orbit, period, time of periastron passage, eccentricity, argument of periastron, projection of semi-major axis and mass function.

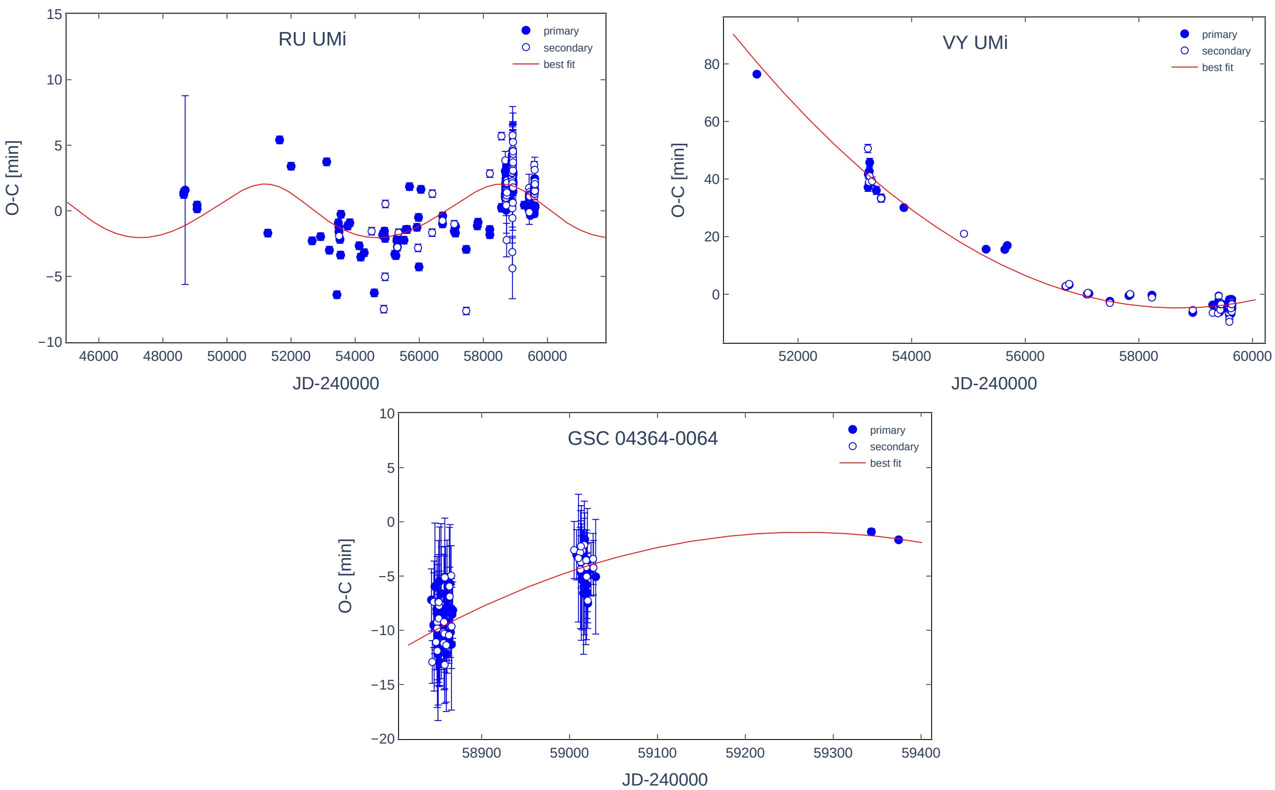

Fig. 2. $O-C$ diagrams of studied systems according to linear ephemeris in § 3. The color figure can be viewed online.

At the beginning of the fitting process, it is necessary to prepare the input data. ELISa requires phased light curves with normalized flux. All our phased observations in all pass bands were transformed to flux and normalized according to flux in the maxima, and were simultaneously fitted by the least-squares method to find the global optimal solution. Subsequently, MCMC sampling was used to produce 1σ confidence intervals of the fitted system's parameters.

Each system was fitted with a model containing 5 free parameters: orbital inclination i, photometric mass ratio q_p, surface potentials of both components Ω_1 and Ω_2 and the effective temperature of the sec-

TABLE 4

PHOTOMETRIC PARAMETERS OF THE STUDIED SYSTEMS

	RU UMi		VY UMi		GSC 04364-00648	
	Primary	Secondary	Primary	Secondary	Primary	Secondary
i [deg]	$83.4^{+0.15}_{-0.22}$		$85.1^{+0.22}_{-0.25}$		$76.9^{+0.20}_{-0.21}$	
q_p (M_2/M_1)	$0.341^{+0.010}_{-0.006}$		$0.536^{+0.023}_{-0.025}$		$0.440^{+0.014}_{-0.015}$	
T [K]	7420^a	4885^{+148}_{-201}	5340^a	4850^{+240}_{-250}	7970^a	4065^{+44}_{-49}
Ω	$2.632^{+0.013}_{-0.007}$	$2.568^{+0.037}_{-0.019}$	$2.821^{+0.034}_{-0.036}$		$4.138^{+0.033}_{-0.033}$	$2.767^{+0.032}_{-0.030}$
l^V/l^V_{tot}	$0.93^{+0.02}_{-0.03}$	$0.07^{+0.09}_{-0.10}$	$0.68^{+0.09}_{-0.10}$	$0.32^{+0.06}_{-0.07}$	$0.92^{+0.05}_{-0.06}$	$0.08^{+0.03}_{-0.03}$
Ω_{crit}	$2.553^{+0.022}_{-0.012}$		$2.943^{+0.032}_{-0.00.035}$		$2.760^{+0.029}_{-0.028}$	
R^{eq}[SMA]	$0.457^{+0.001}_{-0.002}$	$0.286^{+0.001}_{-0.001}$	$0.465^{+0.002}_{-0.001}$	$0.357^{+0.001}_{-0.001}$	$0.273^{+0.002}_{-0.001}$	$0.308^{+0.002}_{-0.002}$

[a]Temperatures of the primary component for all systems were adopted from Babusiaux et al. (2022).

ondary component T_2^{eff}. Temperatures of the primary component T_1^{eff} for all systems were adopted from Babusiaux et al. (2022) and were fixed during the fitting process, while temperatures of the secondary component were fitted with no restrictions.

For the components with convective envelopes (effective temperatures bellow ≈7000 K), the albedos A_1, A_2 of components were set to 0.6 (Ruciński 1969) and the gravity darkening factors, g_1 and g_2 to 0.32 (Lucy 1967). In the case of radiative envelope (above ≈7000 K), the values of albedo and gravity darkening factor were both set to 1.0. Castelli & Kurucz (2003) models of stellar atmospheres were used. The linear limb darkening coefficients for each component were interpolated from the van Hamme (1993) tables.

The weights of individual data points were established as $1/\sigma^2$, where σ is the standard error of point derived during photometric measurement. Initially, the least-squares algorithm was used with suitable initial parameters to find an approximate solution, and then the parameter space near the solution was explored with MCMC sampler with 500 walkers and 500 iterations with the prior 300 iterations discarded as they belonged to the thermalization stage of the sampling.

The resulting as well as the derived parameters of all systems, like relative luminosities of the components in the V filter $l^V_{1,2}/l^V_{tot}$, a critical potential Ω_{crit}, a corresponding equivalent radius R^{eq} in SMA units (semi-major axis), are listed in Table 4. The best-fit models with observed LCs and resulting flat chains displayed in the form of the corner plot are shown in Figure 3, and 3D models with the surface temperature distributions are shown in Figure 4.

TABLE 5

PARAMETERS OF THE SPECTROSCOPIC ORBIT*

M_1 $[M_\odot]$	$2.65^{+0.11}_{-0.16}$	K_1 $[km/s]$	$96.5^{+6.4}_{-5.9}$
M_2 $[M_\odot]$	$0.85^{+0.12}_{-0.10}$	K_1 $[km/s]$	$301.6^{+10.8}_{-8.3}$
R_1 $[R_\odot]$	$1.89^{+0.7}_{-0.4}$	q	$0.32^{+0.02}_{-0.02}$
R_2 $[R_\odot]$	$1.18^{+0.4}_{-0.3}$	$a \sin i$ $[R_\odot]$	$4.13^{+0.11}_{-0.08}$
L_1 $[L_\odot]$	$9.61^{+2.51}_{-1.48}$	γ $[km/s]$	$-21.0^{+3.8}_{-4.0}$
L_2 $[L_\odot]$	$0.71^{+0.16}_{-0.12}$		
a $[R_\odot]$	$4.15^{+0.12}_{-0.09}$		

*And absolute parameters of RU UMi system derived from radial velocity and light curve solutions.

5. ABSOLUTE PARAMETERS OF THE SYSTEMS

The absolute parameters of the binary components, like their masses $M_{1,2}$, radii $R_{1,2}$, luminosities $L_{1,2}$ and semi-major axis of the orbit a, can be mainly determined by the combination of the photometric solution and an analysis of the radial velocity curve. Radial velocities are available only for the system RU UMi (Okazaki et al. 1988; Maxted & Hilditch 1996). We used their measurements and re-analyzed them with the ELISa code (assuming circular orbit) and determined orbital and absolute parameters of the components, as listed in Table 5.

But if we know the distance to an object from independent measurements (e.g parallaxes from *GAIA* measurements), we can find absolute parameters from properties of binary derived from photometric solution and using basic relationships, described in the following text.

Let us assume that we have calculated q_p, i, $T_{1,2}$, $R^{eq}_{1,2}$ and $l^V_{1,2}/l^V_{tot}$ from the analysis of the light curves and we know the standard V magnitude of the system in phase 0.25. The absolute magnitude M_V of

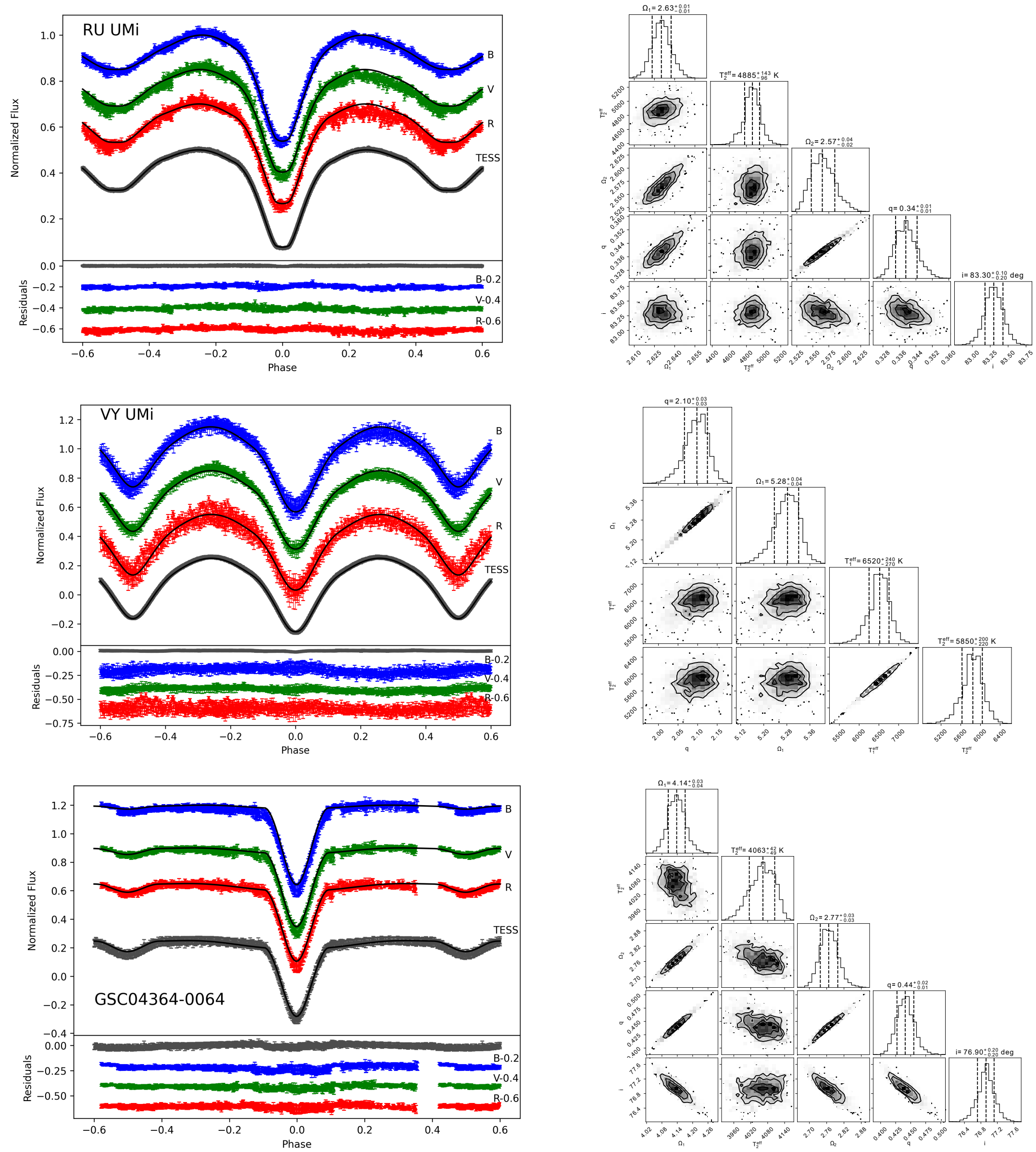

Fig. 3. The synthetic model fitted on observational data of (from top) RU UMi, VY UMi and GSC 04364-0064 together with the corresponding results of the MCMC sampling displayed in the form of the corner plot. The color figure can be viewed online.

the system we can find from equation

$$M^V = V - 5\log(d) + 5 - A^V, \tag{4}$$

where d is the distance and the extinction coefficient A^V can be determined from the dust map in Green et al. (2019). The absolute magnitudes of each component can be found from relation

$$M^V_{1,2} - M^V = -2.5\log\frac{l^V_{1,2}}{l^V_{tot}}. \tag{5}$$

The corresponding bolometric magnitude is

$$M^{Bol}_{1,2} = M^V_{1,2} + BC, \tag{6}$$

where the bolometric correction is taken from Eker et al. (2020). If we assume that the bolometric magnitude of the Sun is $M^{Bol}_{\odot}$=4.73 mag (Torres 2010), the luminosities of the components can be found from

$$M^{Bol}_{1,2} - M^{Bol}_{\odot} = -2.5\log\frac{L_{1,2}}{L_{\odot}}, \tag{7}$$

TABLE 6

ABSOLUTE PARAMETERS OF THE STUDIED SYSTEMS DERIVED FROM THEIR DISTANCES AND PHOTOMETRIC SOLUTIONS

	RU UMi		VY UMi		GSC 04364-00648	
	Primary	Secondary	Primary	Secondary	Primary	Secondary
M [$M_\odot$]	1.90(21)	0.64(17)	0.97(15)	0.52(18)	2.54(42)	1.12(31)
R [$R_\odot$]	1.55(11)	1.16(9)	0.96(2)	0.87(2)	1.22(3)	2.25(5)
L [$L_\odot$]	6.61(1.47)	0.69(14)	0.67(10)	0.38(11)	5.40(1.34)	1.24(23)
a [$R_\odot$]	3.74(37)		2.27(21)		5.88(79)	
A^V [mag]	0.0		0.0		0.03(3)	
M^{Bol} [mag]	2.67(7)	5.12(13)	5.16(8)	5.75(14)	2.89(8)	4.49(11)
BC [mag]	0.06	-0.31	-0.082	-0.30	0.03	-1.03
d [pc]	283.0(1.2)		164.5(3)		512.5(4.8)	

and the corresponding radii are

$$R_{1,2} = \sqrt{\frac{L_{1,2}}{4\pi\sigma T_{1,2}^4}}. \tag{8}$$

The distance between components can be found using their equivalent radii $R_{1,2}^{eq}$

$$a = \frac{1}{2}\left(\frac{R_1}{R_1^{eq}} + \frac{R_2}{R_2^{eq}}\right). \tag{9}$$

The total mass $M_1 + M_2$ of the system can be derived using Kepler's 3$^{\rm rd}$ law

$$\frac{a^3}{P^2} = \frac{G(M_1 + M_2)}{4\pi^2}, \tag{10}$$

and individual masses can be found from the mass ratio q_p.

The absolute parameters for the studied objects determined by the method described above are listed in Table 6. The uncertainties of the parameters were calculated considering the errors of the light curve solutions of the systems and errors in their distances.

6. DISCUSSION AND CONCLUSIONS

In our study, we have presented the photometric analysis of multi-color BVR and *TESS* photometry of three eclipsing binaries, RU UMi, VY UMi and GSC 04364-00648, for the first time for the last two systems. We have also analyzed their period variations considering archival data and our new minima times. The presented photometry solutions, mainly for VY UMi and GSC 04364-00648, has some small disagreements with observations; the residuals at some phases show up to 0.1 deviations in normalized flux value. These issues can be caused by spots, weather conditions, etc. They are really small, and we cannot even try to explain what phenomena they are caused by. Future observation is needed for this purpose.

RU UMi has been studied in the past years by several authors. Recently, Lee et al. (2008) analyzed period variations, fitted light-curve and determined absolute parameters of the components from the radial velocities solution. From their period analysis they concluded that long-term period changes can be caused by the combination of angular momentum loss (AML) and mass transfer from the less massive secondary to the more massive primary. In our period analysis, we used only minima times obtained from ground-based photoelectric and CCD observations, as well as satellite observations from *TESS*, where we can expect higher precision with respect to older visual and photographic observations. We detected wave-like variations with low amplitude ($\approx$ 5 minutes) in $O - C$ residua. They can be interpreted as a consequence of the light-time effect caused by the 3$^{\rm rd}$ invisible component. From the parameters listed in Table 3 we can see that the orbital period of the 3$^{\rm rd}$ body is 7370 days and the orbit is slightly eccentric. According to the mass function of the 3$^{\rm rd}$ body $f(m_3)$ and masses of the binary components (see Table 6), we can find that the minimum mass of the 3$^{\rm rd}$ component in the case of an edge-on orbit ($\sin i_3 = 1$) should be M_3=0.063(16)$M_\odot \approx 60M_J$. It corresponds to a low massive red dwarf or more probably (due to its mass), it is a brown dwarf (Joergens 2014) with very low luminosity. This is supported also by the results of the photometric solution, where no 3$^{\rm rd}$ light was detected. Photometric analysis of BVR and *TESS* light curves confirmed previous findings that RU UMi is a near contact system with a secondary component that almost fulfills its Roche lobe.

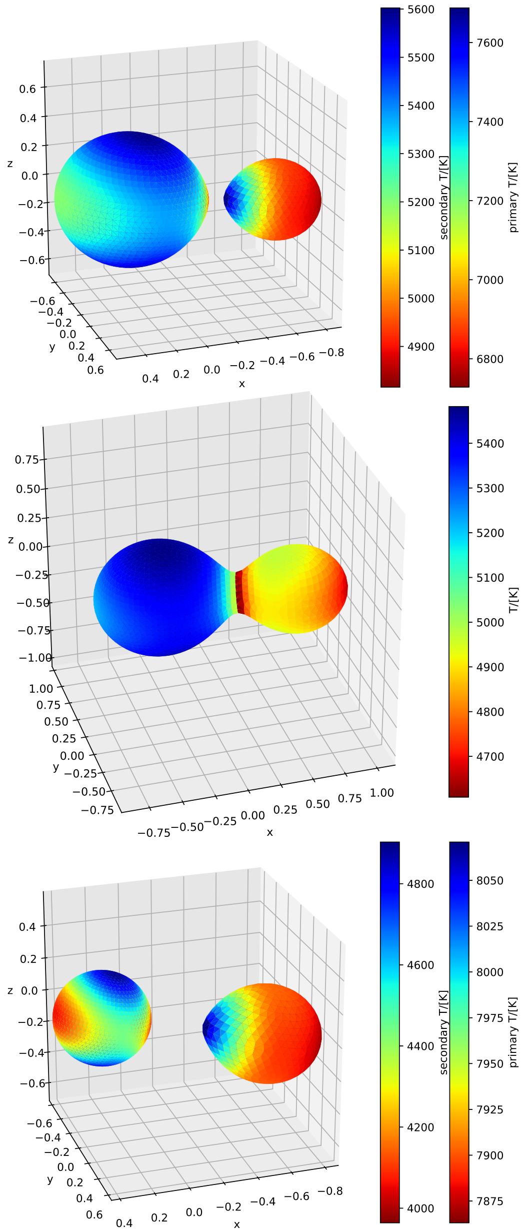

Fig. 4. 3D models with the surface temperature distributions of (from top) RU UMi, VY UMi and GSC 04364-0064. The color figure can be viewed online.

We were not able to find any satisfactory LC solution with spot(s) (not even *TESS* LC) as was done by Lee et al. (2008), although some wave-like variation is visible in the residuals in Figure 3. We can explain it by the temporal evolution of the spot, when the spot parameters, such as diameter, temperature and position on the star's surface, are changing over decades. Our absolute parameters of components determined from the radial velocity solution are a little larger than presented in Lee et al. (2008). On the other hand, the absolute parameters determined from *GAIA* parallax are smaller than previously determined and correspond to an A6V primary component and an evolved K5 star secondary. This differences deserve deeper analysis, because many factors can affect the results. One of them is the mass ratio, which has strong influence on the partial dimensions of the components as well on the inclination, due to the $q-i$ correlation. Terrell & Wilson (2005) showed that the photometric mass ratio for semi-detached and over-contact binaries is often overestimated for partial eclipses. Recently Terrell (2022) noted that not properly modeled third light will lead to mass ratios that are too low. Our solution of RU UMi show no third light and no total eclipses on the LCs (just like other stars). The presented photometric mass ratios q_p have to be considered as a high estimates and this affects also the determination of absolute parameters from distances.

Photometric analysis of VY UMi showed that the system is a typical W UMa type overcontact binary with a more massive primary component (q_p=0.535). Its orbital period and the determined temperatures of both components place the system in the W-type subclass of overcontact binaries. The detected parabolic period change reflected on the $O-C$ diagram can be explained by the mass transfer from a less massive star to a more massive one. The period increase with a rate of $2.56(9)\times10^{-7}$ d/yr^{-1} detected in the VY UMi system corresponds to mass transfer from the secondary to the primary component.

The first photometric solution of the GSC 04364-00648 light curves revealed that the system is semi-detached binary, where a cool secondary component almost fills its Roche lobe, as detected in some other near-contact systems, like EG Cep (Djurašević et al. 2013) or CR Tau (Kudak et al. 2021). Although we can see some quadratic changes on the $O-C$ diagram, which corresponds to a period decrease with a high rate of $-2.26(5)\times10^{-5}$ d/yr^{-1}, we cannot make strict conclusions about period variations in the system, mainly due to the short time (2019-2021) and uneven coverage of the $O-C$ diagram. We have to wait for other observations to confirm or disprove this trend.

This work was supported by Ukrainian National Grant 0122U000937 and by the Slovak Research and Development Agency under contract No. APVV-20-0148. The research of P.G. was supported by the internal grant No. VVGS-PF-2021-2087 of the Faculty of Science, P. J. Šafárik University in Košice.

APPENDIX

TABLE 7

RU UMI TIMES OF MINIMA DETERMINED FROM TESS LIGHT CURVES*

BJD	BJD	BJD	BJD	BJD	BJD	BJD
58683.4591(5)	58706.2924(2)	58730.7012(1)	58886.8666(2)	58910.7460(11)	59428.8517(1)	59585.0166(2)
58683.7210(10)	58706.5541(1)	58730.9632(2)	58887.1296(1)	58911.0137(7)	59429.1138(2)	59585.5416(2)
58683.9827(1)	58706.8163(2)	58731.2262(9)	58887.3914(2)	58911.2710(10)	59429.3768(1)	59585.8049(2)
58684.2447(2)	58707.0794(1)	58731.4882(2)	58887.6544(1)	58911.5387(7)	59429.6388(2)	59586.0665(2)
58684.5074(1)	58707.3413(2)	58731.7511(1)	58887.9164(2)	58911.7950(20)	59429.9018(1)	59586.3312(2)
58684.7694(2)	58707.6043(1)	58732.0130(21)	58888.1793(1)	58913.9016(3)	59430.1637(2)	59586.5911(2)
58685.0323(1)	58707.8672(2)	58732.2761(1)	58888.4413(2)	58914.1627(2)	59430.4267(1)	59586.8546(2)
58685.2944(2)	58708.1292(1)	58732.5380(20)	58888.7046(1)	58914.4261(2)	59430.6886(2)	59587.1164(2)
58685.5573(1)	58708.3912(2)	58732.8008(1)	58888.9664(2)	58914.6877(2)	59430.9515(1)	59587.3796(2)
58685.8194(2)	58708.6541(1)	58733.0630(21)	58889.2293(1)	58914.9513(3)	59431.2135(2)	59587.6413(2)
58686.0823(1)	58708.9161(2)	58733.3253(2)	58889.4912(2)	58915.2128(2)	59431.4764(1)	59587.9044(2)
58686.3443(2)	58709.1791(1)	58733.5904(2)	58889.7543(1)	58915.4765(3)	59431.7385(2)	59588.1662(2)
58686.6071(1)	58709.4411(2)	58733.8509(1)	58890.0161(2)	58915.7377(1)	59432.0014(1)	59588.4297(2)
58686.8692(2)	58709.7040(1)	58734.1127(2)	58890.2793(1)	58916.0014(3)	59432.2631(1)	59588.6911(2)
58687.1321(1)	58709.9671(2)	58734.3757(1)	58890.5410(21)	58916.2626(1)	59432.5255(6)	59588.9543(2)
58687.3941(2)	58711.8037(1)	58734.6377(2)	58890.8042(1)	58916.5259(4)	59433.8383(2)	59589.2161(2)
58687.6569(1)	58712.0657(2)	58734.9006(1)	58891.0661(2)	58916.7789(8)	59434.1010(10)	59589.4791(2)
58688.1820(12)	58712.3286(1)	58735.1626(2)	58891.3293(1)	58917.0450(9)	59434.3631(2)	59589.7410(20)
58688.4440(23)	58712.5906(2)	58735.4257(1)	58891.5913(1)	58917.3119(7)	59434.6260(10)	59590.0042(2)
58688.7068(1)	58712.8536(1)	58735.6874(2)	58891.8539(1)	58917.5720(11)	59434.8880(21)	59590.2660(20)
58688.9690(21)	58713.1156(2)	58735.9504(1)	58892.1159(2)	58917.8376(6)	59435.1510(9)	59590.5291(2)
58689.2316(1)	58713.3785(1)	58736.2125(2)	58892.3788(1)	58918.0950(21)	59435.4130(22)	59590.7908(2)
58689.4937(2)	58713.6405(2)	58736.4755(1)	58892.6407(2)	58918.3627(7)	59435.6760(10)	59591.0541(2)
58689.7567(1)	58713.9036(1)	58736.7374(2)	58892.9037(1)	58918.8876(7)	59435.9379(2)	59591.3158(2)
58690.0188(2)	58714.1654(2)	58737.0004(1)	58893.1657(2)	58919.1440(20)	59436.2008(1)	59591.5790(20)
58690.2813(1)	58714.4286(1)	58870.8572(3)	58893.4289(1)	58919.4125(7)	59436.4628(2)	59591.8407(2)
58690.5437(2)	58714.6905(2)	58871.1191(2)	58893.6906(2)	58920.2051(9)	59436.7257(1)	59592.1039(2)
58690.8065(1)	58714.9533(1)	58871.3818(1)	58893.9536(1)	58920.7190(20)	59436.9877(2)	59592.3656(2)
58691.0687(2)	58715.2165(2)	58871.6437(2)	58894.2156(2)	58920.9868(7)	59437.2507(1)	59592.6290(20)
58691.3313(1)	58715.4772(3)	58871.9065(1)	58894.4786(1)	58921.2450(21)	59437.5127(2)	59594.2037(2)
58691.5935(2)	58716.0030(10)	58872.1686(2)	58894.7404(2)	58921.5123(7)	59437.7756(1)	59594.4653(2)
58691.8563(1)	58716.2651(2)	58872.4315(1)	58895.0033(1)	58921.7690(20)	59438.0377(2)	59594.7287(2)
58692.1184(2)	58716.5281(1)	58872.6935(2)	58895.2654(2)	58922.0371(7)	59438.3006(1)	59594.9902(2)
58692.3850(20)	58716.7901(2)	58872.9569(2)	58895.5285(1)	58922.2950(21)	59438.5625(2)	59595.2537(2)
58692.6441(2)	58717.0529(1)	58873.2186(2)	58895.7904(2)	58922.5621(7)	59438.8254(1)	59595.5152(2)
58692.9063(1)	58717.3150(24)	58873.4816(1)	58896.0534(1)	58922.8190(20)	59439.0874(2)	59595.7789(2)
58693.1684(2)	58717.5779(1)	58873.7435(2)	58896.3154(1)	58923.0864(7)	59439.3504(1)	59596.0401(2)
58693.4313(1)	58717.8400(21)	58874.0064(1)	58896.5783(1)	58923.3430(22)	59439.6124(2)	59596.3035(2)
58693.6934(2)	58718.1031(1)	58874.2683(2)	58896.8402(2)	58923.8690(20)	59439.8754(1)	59596.5651(2)
58693.9559(1)	58718.3648(2)	58874.5313(1)	58897.1032(1)	58924.1364(7)	59440.1374(2)	59596.8285(1)
58694.2182(2)	58718.6278(1)	58874.7932(2)	58897.3653(2)	58924.3940(21)	59440.4003(1)	59597.0899(2)
58694.4807(1)	58718.8898(2)	58875.0564(1)	58897.6277(1)	58924.6619(7)	59440.6622(2)	59597.3534(2)
58694.7431(2)	58719.1527(1)	58875.3182(2)	58899.4663(1)	58924.9190(20)	59440.9250(10)	59597.6149(2)
58695.0062(1)	58719.4159(2)	58875.5813(1)	58899.7285(3)	58925.1867(7)	59441.1872(2)	59597.8782(2)
58695.2681(2)	58719.6771(2)	58875.8430(20)	58899.9897(2)	58925.4440(21)	59441.7120(20)	59598.1398(2)
58695.5308(1)	58719.9590(20)	58876.1061(1)	58900.2535(3)	58925.9690(20)	59441.9750(10)	59598.4031(2)
58695.7930(22)	58720.2025(1)	58876.3679(1)	58900.5156(2)	58926.2364(8)	59442.2370(20)	59598.6647(2)
58696.0559(1)	58720.4646(2)	58876.6317(6)	58900.7786(3)	58926.4860(10)	59442.7619(2)	59598.9282(2)
58697.6307(1)	58720.7277(1)	58876.8921(3)	58901.0399(1)	59420.1901(2)	59443.0250(10)	59599.1897(2)
58697.8928(2)	58720.9896(2)	58877.1560(12)	58901.3032(3)	59420.4530(10)	59443.2868(2)	59599.4528(2)
58698.1556(9)	58721.2525(1)	58877.4178(2)	58901.5648(1)	59420.7150(20)	59443.5498(1)	59599.7146(2)
58698.4177(2)	58721.5145(2)	58877.6809(1)	58901.8268(4)	59420.9779(9)	59443.8117(2)	59599.9780(20)
58698.6805(1)	58721.7773(1)	58877.9427(2)	58902.0899(1)	59421.2399(2)	59444.0746(1)	59600.2408(3)
58698.9425(2)	58722.0394(2)	58878.2058(1)	58902.3519(3)	59421.5030(10)	59444.3367(2)	59600.7660(10)
58699.2056(1)	58722.3024(1)	58878.4677(2)	58902.6069(6)	59421.7650(20)	59444.5996(1)	59601.0278(2)
58699.4674(2)	58722.5642(2)	58878.7308(1)	58902.8732(8)	59422.0278(1)	59444.8616(2)	59601.2894(2)
58699.7303(1)	58722.8273(1)	58878.9927(2)	58903.1397(6)	59422.2898(2)	59445.1246(1)	59601.5529(2)
58699.9923(2)	58723.0893(2)	58879.2555(1)	58903.4005(9)	59422.5527(1)	59445.3865(2)	59601.8143(2)
58700.2553(1)	58723.3520(12)	58879.5176(2)	58903.6752(8)	59422.8147(2)	59445.6495(1)	59602.0777(2)
58700.5173(2)	58723.6155(2)	58879.7806(1)	58903.9267(4)	59423.0777(1)	59445.9114(2)	59602.3393(2)
58700.7803(1)	58725.1890(23)	58880.0425(2)	58904.1896(1)	59423.3397(2)	59446.1744(1)	59602.6026(2)

*Errors are in parenthesis.

TABLE 7. CONTINUED

RU UMI TIMES OF MINIMA DETERMINED FROM TESS LIGHT CURVES*

BJD	BJD	BJD	BJD	BJD	BJD	BJD
58701.0422(2)	58725.4521(1)	58880.3056(1)	58904.4516(4)	59423.6027(1)	59446.4364(2)	59602.8642(2)
58701.3053(1)	58725.7154(2)	58880.5674(2)	58904.7147(1)	59423.8646(2)	59580.0305(1)	59603.1274(2)
58701.5570(11)	58725.9739(9)	58880.8305(1)	58904.9773(3)	59424.1275(1)	59580.2920(20)	59603.3891(2)
58701.8292(3)	58726.2402(1)	58881.0923(2)	58905.2393(1)	59424.3894(2)	59580.5558(2)	59603.6525(2)
58702.0927(2)	58726.5019(1)	58881.3554(1)	58905.5015(4)	59424.6525(1)	59580.8172(2)	59603.9141(2)
58702.3552(1)	58726.7639(2)	58881.6173(2)	58906.0240(9)	59424.9144(2)	59581.0806(2)	59604.1773(2)
58702.6170(20)	58727.0268(1)	58881.8804(1)	58906.5460(22)	59425.1773(1)	59581.3422(2)	59604.4390(20)
58702.8797(1)	58727.2888(2)	58882.1422(2)	58906.8143(7)	59425.4394(2)	59581.6057(2)	59604.7026(1)
58703.1419(2)	58727.5517(1)	58882.4053(1)	58907.0720(11)	59425.7022(1)	59581.8670(20)	59604.9638(2)
58703.4050(1)	58727.8136(2)	58882.6668(1)	58907.3392(6)	59425.9640(10)	59582.1305(2)	59605.2275(2)
58703.6669(2)	58728.0766(1)	58882.9380(10)	58907.5960(22)	59426.2276(7)	59582.3920(20)	59605.4888(2)
58703.9298(1)	58728.3386(2)	58883.1923(2)	58907.8639(6)	59426.4890(20)	59582.6552(2)	59605.7526(2)
58704.1918(2)	58728.6015(1)	58883.4553(1)	58908.1210(19)	59426.7521(1)	59582.9169(2)	59606.0138(2)
58704.4548(1)	58728.8633(2)	58883.7169(1)	58908.3891(6)	59427.0141(2)	59583.1802(2)	59606.2774(2)
58704.7168(2)	58729.1258(4)	58885.2924(1)	58908.6470(10)	59427.2771(1)	59583.4419(2)	59606.5387(2)
58704.9797(1)	58729.3882(3)	58885.5549(1)	58909.1720(11)	59427.5390(19)	59583.7054(2)	
58705.2418(2)	58729.6514(1)	58885.8167(2)	58909.6960(22)	59427.8019(1)	59583.9668(2)	
58705.5044(1)	58729.9134(2)	58886.0798(1)	58909.9638(6)	59428.0640(20)	59584.2301(2)	
58705.7660(1)	58730.1763(1)	58886.3415(2)	58910.2220(10)	59428.3270(10)	59584.4918(2)	
58706.0289(2)	58730.4383(2)	58886.6049(1)	58910.4888(7)	59428.5889(2)	59584.7552(2)	

*Errors are in parenthesis.

TABLE 8

VY UMI TIMES OF MINIMA DETERMINED FROM TESS LIGHT CURVES*

BJD	BJD	BJD	BJD	BJD	BJD	BJD
59390.7777(4)	59406.5601(1)	59423.1556(1)	59439.1004(1)	59586.9968(2)	59602.7798(1)	59619.5379(2)
59390.9408(1)	59406.7234(1)	59423.3189(1)	59439.2638(1)	59587.1606(1)	59602.9422(1)	59619.7013(1)
59391.1038(1)	59406.8855(1)	59423.4809(1)	59439.4256(1)	59587.3229(2)	59603.1054(1)	59619.8635(2)
59391.2662(9)	59407.0486(1)	59423.6442(1)	59439.5892(1)	59587.4858(1)	59603.2671(1)	59620.0265(1)
59391.4289(2)	59407.2108(1)	59423.8064(1)	59439.7511(1)	59587.6475(2)	59603.4307(1)	59620.1888(2)
59391.5915(1)	59407.3742(6)	59423.9697(1)	59439.9134(6)	59587.8113(1)	59603.5931(2)	59620.3517(1)
59391.7547(1)	59407.5363(1)	59424.1318(1)	59440.0763(3)	59587.9738(2)	59603.7562(1)	59620.5133(2)
59391.9169(1)	59407.6994(1)	59424.2951(1)	59440.2385(5)	59588.1367(1)	59603.9184(1)	59620.6776(1)
59392.0801(1)	59407.8616(1)	59424.4572(1)	59440.4021(1)	59588.2990(20)	59604.0816(1)	59620.8388(2)
59392.2424(1)	59408.0249(1)	59424.6205(1)	59440.5653(1)	59588.4624(1)	59604.2432(2)	59621.0027(1)
59392.4057(1)	59408.1872(1)	59424.7823(1)	59440.7273(1)	59588.6246(2)	59604.4070(10)	59621.1641(2)
59392.5679(1)	59408.3502(1)	59424.9458(1)	59440.8908(4)	59588.7877(1)	59604.5693(2)	59621.3282(1)
59392.7308(1)	59408.5126(1)	59425.1076(1)	59441.0528(1)	59588.9499(2)	59604.7324(1)	59623.7672(3)
59392.8932(1)	59408.6759(1)	59425.2713(1)	59441.2162(1)	59589.1131(1)	59604.8948(2)	59623.9314(1)
59393.0563(1)	59408.8379(1)	59425.4330(1)	59441.3783(8)	59589.2746(2)	59605.0579(1)	59624.0937(2)
59393.2186(1)	59409.0012(1)	59425.5967(1)	59441.5415(1)	59589.4384(1)	59605.2201(2)	59624.2567(1)
59393.3817(1)	59409.1633(7)	59425.7585(1)	59441.7035(1)	59589.6001(2)	59605.3833(1)	59624.4181(2)
59393.5440(1)	59409.3265(5)	59425.9221(1)	59441.8670(1)	59589.7640(10)	59605.5454(1)	59624.5821(1)
59393.7071(1)	59409.4887(1)	59426.0814(7)	59442.0290(1)	59589.9254(2)	59605.7087(1)	59624.7435(2)
59393.8695(1)	59409.8141(8)	59426.2465(6)	59442.1924(1)	59590.0894(1)	59605.8704(1)	59624.9080(10)
59394.0326(1)	59409.9773(1)	59426.4062(7)	59442.3543(9)	59590.2510(20)	59606.0341(1)	59625.0699(2)
59394.1949(1)	59410.1395(1)	59426.5724(2)	59442.5177(1)	59590.4148(1)	59606.1958(1)	59625.2333(1)
59394.3579(6)	59410.3029(1)	59426.7349(1)	59442.6798(1)	59590.5763(2)	59606.3593(1)	59625.3954(2)
59394.5203(1)	59410.4649(1)	59426.8984(1)	59442.8432(1)	59590.7402(1)	59606.5210(21)	59625.5582(1)
59394.6834(1)	59410.6282(1)	59427.0602(1)	59443.0053(8)	59590.9025(2)	59606.6845(1)	59625.7198(2)
59394.8458(1)	59410.7903(1)	59427.2239(2)	59443.1686(1)	59591.0655(1)	59606.8457(6)	59625.8842(1)
59395.0089(1)	59410.9536(1)	59427.3855(8)	59443.3307(1)	59591.2270(22)	59608.7994(5)	59626.0452(2)
59395.1711(1)	59411.1158(8)	59427.5491(1)	59443.4936(2)	59591.3909(1)	59608.9619(6)	59626.2091(1)
59395.3340(1)	59411.2790(1)	59427.7110(1)	59443.6561(1)	59591.5524(2)	59609.1250(20)	59626.3716(2)
59395.4964(1)	59411.4411(1)	59427.8745(1)	59443.8194(1)	59591.7167(1)	59609.2881(1)	59626.5349(1)
59395.6595(1)	59411.6045(1)	59428.0365(1)	59443.9814(1)	59591.8786(2)	59609.4504(2)	59626.6960(20)
59395.8218(1)	59411.7662(1)	59428.1999(1)	59444.1450(20)	59592.0418(1)	59609.6136(1)	59626.8599(1)
59395.9849(7)	59411.9293(5)	59428.3618(1)	59444.3068(1)	59592.2041(2)	59609.7759(2)	59627.0214(2)
59396.1472(1)	59412.2538(5)	59428.5254(4)	59444.4702(1)	59592.3671(1)	59609.9389(1)	59627.1854(1)
59396.3105(6)	59412.4174(1)	59428.6871(1)	59444.6322(1)	59592.5294(2)	59610.1014(2)	59627.3469(2)
59396.4726(1)	59412.5807(1)	59428.8502(2)	59444.7956(4)	59592.6923(1)	59610.2643(1)	59627.5107(1)

*Errors are in parenthesis.

TABLE 8. CONTINUED

VY UMI TIMES OF MINIMA DETERMINED FROM TESS LIGHT CURVES*

BJD	BJD	BJD	BJD	BJD	BJD	BJD
59396.6359(1)	59412.7423(1)	59429.0128(1)	59444.9575(1)	59592.8531(7)	59610.4258(2)	59627.6733(2)
59396.7979(1)	59412.9060(1)	59429.1762(1)	59445.1211(1)	59594.1564(2)	59610.5896(10)	59627.8365(1)
59396.9612(1)	59413.0683(1)	59429.3381(1)	59445.2829(1)	59594.3195(1)	59610.7512(2)	59627.9986(3)
59397.1235(1)	59413.2315(1)	59429.5013(1)	59445.4465(1)	59594.4818(2)	59610.9151(1)	59628.1617(1)
59397.2868(8)	59413.3933(1)	59429.6636(1)	59445.6085(1)	59594.6448(1)	59611.0776(2)	59628.3240(20)
59397.4484(8)	59413.5568(1)	59429.8271(1)	59445.7719(1)	59594.8071(2)	59611.2406(1)	59628.4874(1)
59397.6121(5)	59413.7187(1)	59429.9891(1)	59445.9338(1)	59594.9701(1)	59611.4029(2)	59628.6495(2)
59397.7769(8)	59413.8823(1)	59430.1524(1)	59446.0972(1)	59595.1324(1)	59611.5659(1)	59628.8123(1)
59397.9374(1)	59414.0444(1)	59430.3143(1)	59446.2594(1)	59595.2957(1)	59611.7274(2)	59628.9748(3)
59398.0996(1)	59414.2076(1)	59430.4778(6)	59446.4218(3)	59595.4574(1)	59611.8914(1)	59629.1382(1)
59398.2627(1)	59414.3698(1)	59430.6397(1)	59579.8384(5)	59595.6210(1)	59612.0537(2)	59629.3015(7)
59398.4249(1)	59414.5330(1)	59430.8032(1)	59580.0012(5)	59595.7833(2)	59612.2168(1)	59629.6234(8)
59398.5883(1)	59414.6951(1)	59430.9652(1)	59580.1634(2)	59595.9464(1)	59612.3791(2)	59629.7886(1)
59398.7504(1)	59414.8587(2)	59431.1286(1)	59580.3274(1)	59596.1089(2)	59612.5422(1)	59630.1141(1)
59398.9137(1)	59415.0204(1)	59431.2905(1)	59580.4896(2)	59596.2717(1)	59612.7036(2)	59630.2754(2)
59399.0757(1)	59415.1837(1)	59431.4540(1)	59580.6528(1)	59596.4342(1)	59612.8676(1)	59630.4395(1)
59399.2389(1)	59415.5093(1)	59431.6159(1)	59580.8150(20)	59596.5971(1)	59613.0299(2)	59630.6018(2)
59399.4011(1)	59415.6712(1)	59431.7795(1)	59580.9779(1)	59596.7596(1)	59613.1929(1)	59630.7651(1)
59399.5645(1)	59415.8346(1)	59431.9413(1)	59581.1396(2)	59596.9225(1)	59613.3554(2)	59630.9274(2)
59399.7266(1)	59415.9966(1)	59432.1048(1)	59581.3035(1)	59597.0850(21)	59613.5184(1)	59631.0902(1)
59399.8894(1)	59416.1601(1)	59432.2669(1)	59581.4649(2)	59597.2479(1)	59613.6799(2)	59631.2528(3)
59400.0519(9)	59416.3219(1)	59432.4311(4)	59581.6291(1)	59597.4104(1)	59613.8436(8)	59631.4158(1)
59400.2153(1)	59416.4851(2)	59433.8933(5)	59581.7912(2)	59597.5735(1)	59614.0052(3)	59631.5770(29)
59400.3774(1)	59416.6475(1)	59434.0574(1)	59581.9541(1)	59597.7352(1)	59614.1695(1)	59631.7413(1)
59400.5406(1)	59416.8109(1)	59434.2193(1)	59582.1166(2)	59597.8988(1)	59614.3307(3)	59631.9035(2)
59400.7028(1)	59416.9728(8)	59434.3823(2)	59582.2799(1)	59598.0612(2)	59614.4938(2)	59632.0666(1)
59401.0281(1)	59417.1365(2)	59434.5448(1)	59582.4412(2)	59598.2242(1)	59614.6582(4)	59632.2277(3)
59401.1915(1)	59417.2979(1)	59434.7082(1)	59582.6052(1)	59598.3865(1)	59615.1456(1)	59632.3921(1)
59401.3535(1)	59417.4616(1)	59434.8701(1)	59582.7674(2)	59598.5496(9)	59615.3078(2)	59632.5532(3)
59401.5168(1)	59417.6237(1)	59435.0337(1)	59582.9306(1)	59598.7114(1)	59615.4707(1)	59632.7176(1)
59401.6789(1)	59417.7871(1)	59435.1954(1)	59583.0928(2)	59598.8751(1)	59615.6333(2)	59632.8798(2)
59401.8423(1)	59417.9489(1)	59435.3589(1)	59583.2558(1)	59599.0375(2)	59615.7960(10)	59633.0428(1)
59402.0044(1)	59418.1126(2)	59435.5209(1)	59583.4182(2)	59599.2005(1)	59615.9575(2)	59633.2052(3)
59402.1675(1)	59418.2743(1)	59435.6843(1)	59583.5813(1)	59599.3628(1)	59616.1219(1)	59633.3679(1)
59402.3297(1)	59418.4379(1)	59435.8461(1)	59583.7427(2)	59599.5258(1)	59616.2839(2)	59633.5306(3)
59402.4929(1)	59418.5990(20)	59436.0097(1)	59583.9066(1)	59599.6876(2)	59616.4469(1)	59633.6938(1)
59402.6551(1)	59420.2257(4)	59436.1718(1)	59584.0691(2)	59599.8513(1)	59616.6093(2)	59633.8548(2)
59402.8185(1)	59420.3904(1)	59436.3351(1)	59584.2322(1)	59600.0136(1)	59616.7726(1)	59634.0191(1)
59402.9807(1)	59420.5522(1)	59436.4972(1)	59584.3944(2)	59600.1756(3)	59616.9348(2)	59634.1814(3)
59403.1442(2)	59420.7157(4)	59436.6606(1)	59584.5575(1)	59600.3387(4)	59617.0980(10)	59634.3442(1)
59403.3060(1)	59420.8776(1)	59436.8224(1)	59584.7199(2)	59600.5006(5)	59617.2602(2)	59634.5068(3)
59403.4694(1)	59421.0412(1)	59436.9859(1)	59584.8830(10)	59600.6648(5)	59617.4234(1)	59634.6695(1)
59403.6312(1)	59421.2028(1)	59437.1478(1)	59585.0452(2)	59600.8274(1)	59617.5856(2)	59634.8311(2)
59403.7945(1)	59421.3664(1)	59437.3113(1)	59585.2083(1)	59600.9891(2)	59617.7485(9)	59634.9950(10)
59403.9568(1)	59421.5285(1)	59437.4734(1)	59585.3706(2)	59601.1529(1)	59617.9110(20)	59635.1576(2)
59404.1201(1)	59421.6919(1)	59437.6367(1)	59585.5337(1)	59601.3146(2)	59618.0741(1)	59635.3204(1)
59404.2819(8)	59421.8538(1)	59437.7987(1)	59585.6960(21)	59601.4783(1)	59618.2355(2)	59635.4831(3)
59405.4201(5)	59422.0172(1)	59437.9621(1)	59585.8591(1)	59601.6406(2)	59618.3995(1)	59635.6457(1)
59405.5834(1)	59422.1790(1)	59438.1242(1)	59586.0213(2)	59601.8038(1)	59618.5617(2)	59635.8090(10)
59405.7470(1)	59422.3428(1)	59438.2875(1)	59586.1834(5)	59601.9651(2)	59618.7251(1)	
59405.9091(1)	59422.5048(1)	59438.4496(1)	59586.3450(28)	59602.1290(1)	59618.8873(2)	
59406.0724(6)	59422.6680(1)	59438.6129(1)	59586.5115(5)	59602.2913(1)	59619.0501(1)	
59406.2347(1)	59422.8298(1)	59438.7748(1)	59586.6721(2)	59602.4545(9)	59619.2117(2)	
59406.3979(1)	59422.9935(1)	59438.9384(1)	59586.8353(1)	59602.6169(2)	59619.3758(1)	

*Errors are in parenthesis.

TABLE 9

GSC 04364-0064 TIMES OF MINIMA DETERMINED FROM TESS LIGHT CURVES*

BJD	BJD	BJD	BJD	BJD	BJD	BJD
58842.925(2)	58848.963(1)	58851.983(4)	58858.454(2)	58864.494(2)	59014.199(3)	59019.375(4)
58843.356(4)	58849.391(4)	58851.985(3)	58858.886(3)	58864.926(3)	59014.632(1)	59019.809(2)
58843.786(1)	58849.394(4)	58852.414(1)	58859.749(4)	58865.789(3)	59014.634(1)	59020.241(3)
58845.512(2)	58849.826(2)	58852.415(2)	58860.609(4)	58867.085(2)	59015.498(2)	59020.672(1)
58845.513(1)	58849.827(1)	58852.844(4)	58861.473(4)	59011.179(2)	59015.923(4)	59020.674(2)
58845.937(4)	58850.259(4)	58853.709(4)	58862.338(4)	59012.045(2)	59016.789(4)	59021.534(2)
58845.945(4)	58850.687(2)	58854.140(8)	58862.767(2)	59012.476(4)	59017.648(4)	59026.712(1)
58846.374(2)	58850.688(2)	58856.727(2)	58862.768(2)	59012.906(2)	59018.085(2)	59029.729(4)
58846.376(2)	58851.119(4)	58857.158(4)	58863.199(4)	59012.907(2)	59018.086(2)	59031.888(2)
58846.804(4)	58851.552(1)	58857.593(2)	58863.634(2)	59013.335(4)	59018.514(3)	59033.614(2)
58848.101(2)	58851.553(2)	58858.022(4)	58864.065(4)	59013.773(2)	59018.946(2)	59034.481(2)

*Errors are in parenthesis.

TABLE 10

OBSERVED TIMES OF MINIMA OF SELECTED EB SYSTEMS*

Name	BJD	Name	BJD
RU UMi	59277.4101(2)	VY UMi	59516.3846(2)
RU UMi	59467.4327(1)	VY UMi	59517.3604(1)
VY UMi	59298.3633(2)	VY UMi	59517.5219(1)
VY UMi	59298.5245(2)	GSC 04364-0064	59343.3781(2)
VY UMi	59516.2200(3)	GSC 04364-0064	59374.4401(1)

*Errors are in parenthesis.

REFERENCES

Applegate, J. H. 1992, ApJ, 385, 621, https://doi.org/10.1086/170967

Babusiaux, C., Fabricius, C., Khanna, S., et al. 2022, arXiv:2206.05989, https://doi.org/10.48550/arXiv.2206.05989

Bell, S. A., Hilditch, R. W., & Edwin, R. P. 1993, MNRAS, 260, 478, https://doi.org/10.1093/mnras/260.3.478

Castelli, F. & Kurucz, R. L. 2003, IAU 210, Modelling of Stellar Atmospheres, ed. N. Piskunov, W. W. Weiss, & D. F. Gray, 20, https://doi.org/10.48550/arXiv.astro-ph/0405087

Chen, X., Wang, S., Deng, L., de Grijs, R., & Yang, M. 2018, ApJS, 237, 28, https://doi.org/10.3847/1538-4365/aad32b

Čokina, M., Fedurco, M., & Parimucha, Š. 2021, A&A, 652, 156, https://doi.org/10.1051/0004-6361/202039171

de Bernardi, C. & Scaltriti, F. 1977, Acta Astron., 27, 187

Djurašević, G., Baştürk, Ö., Latković, O., et al. 2013, AJ, 145, 80, https://doi.org/10.1088/0004-6256/145/3/80

Eker, Z., Soydugan, F., Bilir, S., et al. 2020, MNRAS, 496, 3887, https://doi.org/10.1093/mnras/staa1659

Gajdoš, P. & Parimucha, Š. 2019, OEJV, 197, 71

Green, G. M., Schlafly, E., Zucker, C., Speagle, J. S., & Finkbeiner, D. 2019, ApJ, 887, 93, https://doi.org/10.3847/1538-4357/ab5362

Hilditch, R. W. 2001, An Introduction to Close Binary Stars (Cambridge, UK: CUP)

Ivezić, Ž., Kahn, S. M., Tyson, J. A., et al. 2019, ApJ, 873, 111, https://doi.org/10.3847/1538-4357/ab042c

Joergens, V. 2014, ASSL, 50 Years of Brown Dwarfs: From Prediction to Discovery to Forefront of Research, 401, https://doi.org/10.1007/978-3-319-01162-2

Kaluzny, J. 1985, AcA, 35, 327

Kudak, V., Fedurco, M., Perig, V., & Parimucha, Š. 2021, RAA, 21, 174, https://doi.org/10.1088/1674-4527/21/7/174

Lee, J. W., Kim, C.-H., Kim, S.-L., et al. 2008, PASP, 120, 720, https://doi.org/10.1086/589976

Lucy, L. B. 1967, ZA, 65, 89

Maxted, P. F. L. & Hilditch, R. W. 1996, Obs, 116, 288

Mikulášek, Z. 2015, A&A, 584, 8, https://doi.org/10.1051/0004-6361/201425244

Nha, I.-S. 1973, AJ, 78, 107

Okazaki, A., Nakamura, Y., & Yamasaki, A. 1988, PASJ, 40, 79

Otero, S. A. & Dubovsky, P. A. 2004, IBVS, 5570, 1,

Parimucha, Š., Savanevych, V. E., Briukhovetskyi, O. B., et al. COSka, 49, 151

Prša, A. 2018, Modeling and Analysis of Eclipsing Binary Stars; The theory and design principles of PHOEBE (Bristol, UK: IOP Publishing), https://doi.org/10.1088/978-0-7503-1287-5

Ricker, G. R. 2014, JAVSO, 42, 234
Ruciński, S. M. 1969, AcA, 19, 245
Savanevych, V. E., Briukhovetskyi, O. B., Khlamov, S. V., et al. 2017, OAP, 30, 194, https://doi.org/10.18524/1810-4215.2017.30.114495
Strohmeier, W. 1958, KVB, 23
Strohmeier, W. & Bauernfeind, H. 1968, BamVe, 7, 72
Terrell, D. 2022, Galaxies, 10, 8, https://doi.org/10.3390/galaxies10010008
Terrell, D. & Wilson, R. E. 2005, Ap&SS, 296, 221, https://doi.org/10.1007/s10509-005-4449-4
Torres, G. 2010, AJ, 140, 1158, https://doi.org/10.1088/0004-6256/140/5/1158
van Hamme, W. 1993, AJ, 106, 2096, https://doi.org/10.1086/116788
Watson, C. L., Henden, A. A., & Price, A. 2006, ASS, 25, 47
Wood, D. B. 1971, PASP, 83, 286
Yang, Y. G., Lü, G. L., Yin, X. G., Zhu, C. H., & Nakajima, K. 2009, AJ, 137, 236, https://doi.org/10.1088/0004-6256/137/1/236
Zacharias, N., Monet, D. G., Levine, S. E., et al. 2004, AAS, 205, 4815
_________. 2005, VizieR On-line Data Catalog: 1/297
Zhu, L.-Y., Qian, S.-B., & Xiang, F.-Y. 2006, PASJ, 58, 361, https://doi.org/10.1093/pasj/58.2.361

P. Gajdoš and Š. Parimucha: Institute of Physics, Faculty of Science, P. J. Šafárik University, Košice, Park Angelinum 9, 04001, Slovakia (stefan.parimucha@upjs.sk).

V. Kudak and V. Perig: Laboratory of space researches, Uzhhorod National University, Uzhhorod, Daleka Str., 2A, 88000, Ukraine (lab-space@uzhnu.edu.ua).

La *Revista Mexicana de Astronomía y Astrofísica*, fundada en 1974, publica trabajos originales de investigación en todas las ramas de la astronomía, astrofísica y temas vinculados a éstas. Se editan dos números por año y su distribución es gratuita a todas las instituciones relacionadas con los campos cubiertos por esta revista.

La política editorial de la *RMxAA* consiste en enviar a arbitrar los artículos recibidos a especialistas en el campo. Los interesados en publicar en nuestra revista deberán enviar por correo electrónico, a la dirección rmaa@astro.unam.mx, la versión completa de su artículo en formato PostScript o PDF y el archivo LaTeX. Estos archivos deberán ir acompañados de una carta de presentación. Todos los trabajos deben ser preparados en inglés usando la versión más reciente del macro en LaTeX de la *RMxAA* "rmaa.cls" (disponible en https://www.irya.unam.mx/rmaa/). Se requiere un "Abstract" no mayor que 12 líneas, y un "Resumen" en español (este último podrá ser provisto por los editores de ser necesario); también se incluirán de 1 a 6 palabras clave ("Keywords") de la lista de las revistas astronómicas internacionales. Se requiere que cada tabla incluida en el texto esté numerada y con título; las figuras deberán estar en formato PostScript (.ps) o PostScript encapsulado (.eps), estar numeradas y con leyenda explicativa. Se requiere que cada tabla y figura estén mencionadas en el texto. El estilo de las referencias sigue las normas astronómicas internacionales recientes. Para mayor información sobre el estilo de la *RMxAA* se puede consultar el archivo de ejemplo que viene incluido en los macros. La publicación es gratuita para los autores.

En 1995 se inició la Serie de Conferencias de la *Revista Mexicana de Astronomía y Astrofísica*, dedicada a la publicación de las memorias de reuniones astrónomicas efectuadas en México y en otros países del continente. Hasta 1994 las memorias de reuniones astronómicas de la región se publicaron como volúmenes especiales de la *RMxAA*.

Las condiciones de publicación de cada volumen de las memorias de conferencias serán el resultado de un convenio establecido entre la *RMxAC* y los organizadores de cada evento. Los detalles de la publicación, que incluyen fechas y extensión de los textos, serán anunciados por los editores de cada conferencia. Las contribuciones extensas estarán en inglés con un resumen en español (o portugués en caso de las Reuniones regionales). Los resúmenes de las reuniones que no son temáticas tendrán una extensión máxima de 300 palabras incluyendo título, autores y afiliación; serán exclusivamente en inglés. Los macros LaTeX para las memorias se encuentran en http://www.astroscu.unam.mx/~rmaa. Todas las contribuciones y resúmenes deberán estar en estos formatos.

Se concede permiso a los autores de artículos y libros científi-cos para citar trabajos publicados en la *RMxAA* y en la *RMxAC* siempre y cuando se dé la referencia completa. También se permite la reproducción de figuras y tablas bajo las mismas condiciones.

La *RMxAA* aparece indexada en Current Contents, Science Citation Index, Astronomy and Astrophysics Abstracts, Physics Briefs, Publicaciones Científicas en América Latina, Astronomy and Astrophysics Monthly Index, PERIODICA, RedALyC, Latindex y SciELO.

The *Revista Mexicana de Astronomía y Astrofísica*, founded in 1974, publishes original research papers in all branches of astronomy, astrophysics and closely related fields. Two numbers per year are issued and are distributed free of charge to all institutions engaged in the fields covered by the *RMxAA*.

All papers received by the *RMxAA* are sent to a specialist in the field for refereeing. Authors interested in publishing in the *RMxAA* should send their papers to the e-mail address rmaa@astro.unam.mx, in PostScript or PDF format, along with the LaTeX file. A submission letter should also be sent. Papers should be prepared in English, using the most recent version of the *RMxAA* LaTeX document class "rmaa.cls" (available from https://www.irya.unam.mx/rmaa/). An "Abstract" of at most 12 lines is required, as well as a "Resumen" in Spanish. The latter can be provided by the Editors, if necessary. A total of six or fewer "Keywords", taken from the lists of international astronomical journals should be included. Tables should be numbered and include a title. Figures should be submitted in PostScript (.ps) or Encapsulated PostScript (.eps) format, should be numbered, and should include a caption. Both tables and figures should be mentioned in the text. The style of the references follows recent international astronomical usage. For more information about the style norms of *RMxAA* please consult the example included in the LaTeX package. Publication in *RMxAA* is free of charge to authors.

The Conference Series of *Revista Mexicana de Astronomía y Astrofísica* was founded in 1995 to publish the proceedings of astronomical meetings held in Mexico and other countries throughout the continent. Until 1994 such proceedings had been published as special issues of *Revista Mexicana de Astronomía y Astrofísica*.

Conditions of publication of proceedings of each conference will be the result of a mutual agreement between the *RMxAC* and the organizing committee. Details of publication, including length of papers, will be announced by the editors of each event. The extensive contributions should be in English, and should include an abstract in Spanish (or Portuguese for regional meetings). The abstracts of non-thematic meetings should not exceed 300 words including title, authors, and affiliation; they should be exclusively in English. The LaTeX templates specially prepared for proceedings can be obtained at http://www.astroscu.unam.mx/~rmaa; all papers should be submitted in this format.

Authors of scientific papers and books may quote articles published both in *RMxAA* and *RMxAC* provided that a complete reference to the source is given. Reproduction of figures and tables is also permitted on the same basis.

The *RMxAA* is indexed in Current Contents, Science Citation Index, Astronomy and Astrophysics Abstracts, Physics Briefs, Publicaciones Científicas en América Latina, Astronomy and Astrophysics Monthly Index, PERIODICA, RedALyC, Latindex, and SciELO.